DESY 93-059
May 1993

DESY-93-059

Fermilab Library
0 1160 0029266 8

Emittance Growth and Proton Beam Lifetime in HERA

F. Zimmermann
Fachbereich Physik, Universität Hamburg

ISSN 0418-9833

DESY 93-059
May 1993

ISSN 0418-9833

Emittance Growth and Proton Beam Lifetime in HERA

Dissertation
zur Erlangung des Doktorgrades
des Fachbereichs Physik
der Universität Hamburg

vorgelegt von
Frank Zimmermann
aus Hamburg

Hamburg, im März 1993

Gutachter der Dissertation:	Prof. Dr. P. SCHMÜSER Prof. Dr. E. LOHRMANN
Gutachter der Disputation:	Prof. Dr. P. SCHMÜSER Prof. Dr. Dr. h.c. G.-A. VOSS
Datum der Disputation:	27.04.1993
Sprecher des Fachbereichs Physik und Vorsitzender des Promotionsausschusses:	Prof. Dr. G. MACK

Abstract

In this thesis physical processes are investigated which affect the proton beam size and lifetime in HERA. Among these are the effect of the nonlinear persistent-current field errors, the beam-beam interaction, and various multiple scattering processes.

In the HERA proton ring persistent-current field errors may strongly limit the dynamic aperture at injection energy. Techniques of particle tracking and tracking data analysis are described, which allow to estimate and to correct the harmful effect of the measured multipole errors. Special emphasis is put on Lyapunov exponent methods and map tracking.

An additional reduction of the dynamic aperture is observed if the betatron tune is harmonically modulated. A tune modulation is for instance caused by magnet power supply ripple. The magnitude of actual modulation amplitudes is estimated and existing theories of the impact of tune modulation on high-order resonances are further developed. Resonance parameters for a typical working point are evaluated by differential-algebra and normal-form procedures. Subsequently, amplitude-dependent emittance growth rates are derived for the HERA proton ring at injection energy.

At 820 GeV, the beam-beam interaction limits the luminosity and the beam lifetime. The theory of tune modulation proposed can likewise be applied in the presence of beam-beam forces, for which the resonance parameters are calculated analytically. Again predictions of emittance growth rates are obtained.

Furthermore, the emittance growth and the beam lifetime caused by multiple proton-electron scattering and by residual gas scattering are estimated, the latter for several vacuum chamber geometries and including coupling.

The importance of the different processes is compared, both at 40 GeV and at 820 GeV, and viewed in relation to other phenomena that may influence the beam emittance and lifetime, such as intra-beam scattering.

Kurzfassung

In dieser Arbeit werden physikalische Prozesse untersucht, die zu einer Beschränkung der Strahllebensdauer und zu einem Anwachsen der Strahl- oder Einteilchen-Emittanz im HERA-Protonen-Ring führen können. Zu diesen gehören der Einfluß der nichtlinearen Feldfehler in den supraleitenden Magneten, die Strahl-Strahl-Wechselwirkung sowie verschiedene Vielfachstreuprozesse.

Feldfehler der supraleitenden Magnete bestimmen die dynamische Apertur bei Injektionsenergie. Die erwartete Apertur läßt sich mit Hilfe von speziellen Simulationsprogrammen ermitteln, die die Bahn eines einzelnen Teilchens im Speicherring über viele Umläufe hinweg verfolgen. Ein Hauptproblem bei dieser Vorgehensweise ist der große Bedarf an Rechenzeit. Diese kann verkürzt werden, entweder indem man das Modell des Beschleunigers vereinfacht oder indem man die Auswertung der Simulationsdaten so verfeinert, daß aus dem Verhalten einer Trajektorie über eine kleine Zeitdauer bereits auf potentielle Instabiliät und späteren Teilchenverlust geschlossen werden kann. Zum ersten Ansatz gehört der Versuch, das Beschleuniger-Modell durch eine Taylor-Reihe zu ersetzen, zum zweiten die Ermittlung des Lyapunov-Exponenten, der ein Maß für die Chaotizität einer Trajektorie darstellt.

Eine harmonische Modulation der Betatronfrequenz führt zu einer merklichen, zusätzlichen Verkleinerung der dynamischen Apertur. Frequenzänderungen dieser Art werden beispielsweise durch Stromschwankungen der Magnet-Netzgeräte verursacht. Die Größenordnung der zu erwartenden Modulationsamplituden wird abgeschätzt und es wird eine Theorie vorgestellt, die den Einfluß von Frequenz-Modulationen auf Resonanzen höherer Ordnung quantitativ beschreibt. Diese Theorie wird auf den HERA-Protonen-Ring mit nichtlinearen Feldfehlern bei Injektionsenergie angewandt. Benötigt werden hierzu bestimmte Parameter der Resonanzen hoher Ordung, die mit differentieller Algebra und Normalform-Transformationen ermittelt werden. Unter Verwendung der Resonanzparameter werden Emittanzanwachsraten als Funktion der Teilchenamplitude vorhergesagt.

Während des Luminositätsbetriebes bei einer Protonenenergie von 820 GeV erweist sich die Strahl-Strahl-Wechselwirkung als der dominierende Prozeß, der die Protonenstrahllebensdauer beschränkt. Unter der plausiblen Annahme, daß auch hier eine harmonische Modulation der Betatronfrequenz den Effekt der reinen Strahl-Strahl-Wechselwirkung deutlich verstärkt, läßt sich dieselbe Theorie wie für die nichtlinearen Magnetfelder bei 40 GeV anwenden. In diesem Fall werden die Resonanzparameter analytisch berechnet. Wiederum werden amplitudenabhängige Anwachsraten der Emittanz bestimmt.

Des weiteren werden zwei Vielfachstreuprozesse näher untersucht, und zwar Coulomb-Streuung zwischen Protonen und Elektronen und zwischen Protonen und dem Restgas. Die Restgasstreuung wird, ausgehend von einer Fokker-Planck-Gleichung, für verschiedene Vakuumkammergeometrien und unter Berücksichtigung von Kopplung behandelt. Das entsprechende Protonen-Emittanzwachstum wird berechnet.

Die verschiedenen betrachteten Prozesse bei Injektionsenergie und bei Luminositätsbetrieb werden hinsichtlich ihrer Bedeutung miteinander und mit anderen Effekten verglichen, welche die Strahlgröße und Strahllebensdauer beeinflussen.

Contents

1 Introduction **1**
1.1 Motivation 1
1.2 Outline 2

2 Particle Tracking Methods **3**
2.1 Introduction 3
2.2 Lyapunov Exponent 3
2.3 Map Tracking 8
2.3.1 Tracking with Truncated Taylor Maps 8
2.3.2 Irwin Factorization 16
2.3.3 Reliability and Computing Time 20

3 Tune Modulation **23**
3.1 Introduction 23
3.2 Single Resonance 24
3.3 Single Resonance with Modulation 25
3.4 Island Width of Sidebands 26
3.5 Chaotic Region and Diffusion Rate 26
3.6 Diffusion Rate for a Two-Dimensional Map 30
3.7 Adiabatic Trapping 32
3.8 Small Angle Approximation 32
3.9 Two Degrees of Freedom 33
3.10 Width of the Stochastic Layer 35
3.11 Phase Diagrams 38
3.12 Octupole Kick Map 40
3.13 Chaotic Fraction of Phase Space 46
3.14 Diffusion Model 47

4 Modulation Amplitudes **49**
4.1 Origin of Power Supply Ripple 49
4.2 Simple Model of the Main Circuit 49
4.3 Transmission Line Characteristics 52
4.4 The Quadrupoles of the Interaction Region 52
4.5 Shielding by the Beam Pipe 53
4.6 Ground Motion Effects 54
4.7 Modulation Amplitudes 56

5 Dynamic Aperture **57**
5.1 Effect of the Persistent-Current Field Errors 57
5.2 Tracking Studies including Tune Modulation 58
5.3 Parameters of High-Order Resonances 63
5.4 Emittance Growth Rates 74
5.5 Range of Validity of the Model 76

6 Beam-Beam Interaction **79**
6.1 Model 79
6.2 Hamiltonian 80
6.3 Tune Shift and its Derivatives 81
6.4 Driving Term 82
6.5 Chaotic Fraction of Phase Space 82
6.6 Emittance Growth Rates 85
6.7 Off-Center Collisions 86

7 Multiple Proton-Electron Scattering **89**
7.1 Emittance Growth Rate 89

8 Residual Gas Scattering **91**
8.1 Introduction 91
8.2 Lifetime for One Degree of Freedom 91
8.3 Lifetime for Two Degrees of Freedom 92
8.4 Lifetime on the Coupling Resonance 93
8.5 Comparison with Experimental Observations 94
8.6 Estimate of Emittance Growth Rates 95
8.7 Nuclear Interactions 97

9 Comparison of Lifetime Limiting Processes **98**
9.1 Intra-Beam Scattering 98
9.2 Tune Modulation and Field Errors at 40 GeV 99
9.3 Gas Scattering and Proton-Electron Scattering 100
9.4 Tune Modulation and Beam-Beam Interaction 100
9.5 Comparison of Growth Rates 101

10 Conclusions **106**

A Differential Algebra and Normal-Form Methods **110**
A.1 Introduction 110
A.2 Examples of Differential-Algebra Operations 111
A.3 Normal-Form Analysis 113
A.4 Example of a Normal-Form Transformation 114
A.5 Comparison of the Map and the Hamiltonian 115
A.5.1 Hamiltonian 116
A.5.2 Lie-Algebraic Treatment 116
A.6 Examples of Normal-Form Results 117
A.7 Description of the Beam-Beam Interaction by Differential Algebra 122

B Parameters of High-Order Resonances in HERA **124**

C Jacobi-Anger Expansion 127

D Melnikov-Arnold Integral 128

E Fokker-Planck Equation 129

F Diffusion Equation 131

List of Commonly Used Symbols

a_{xz}	—	position-independent transverse amplitude
$< a_{xz} >_N$	—	running average transverse amplitude
α	—	fine structure constant *or* exponent in the diffusion coefficient *or* phase of the tune modulation
$A_{x,z}$	—	horizontal or vertical acceptance
A^{-1}	—	normal-form transformation
b	—	impact parameter
B	—	magnetic field
β	—	beta function
c	—	velocity of light *or* parameter in the diffusion coefficient
D	—	diffusion coefficient *or* dispersion function
$(\frac{\delta a_{xz}}{a_{xz}})_N$	—	relative average amplitude error per turn computed from the first N turns
ΔI_{tot}	—	total width of a resonance island
$\frac{\overline{(\Delta\epsilon)^2}}{\Delta t}$	—	diffusion rate in the chaotic region
$< \frac{\overline{(\Delta\epsilon)^2}}{\Delta t} >_{\mathrm{global}}$	—	global emittance growth rate
$< \frac{\overline{\Delta\epsilon}}{\Delta t} >$	—	locally averaged emittance growth rate
$\frac{\Delta p}{p}$	—	relative momentum deviation
Δx	—	horizontal displacement of the beams at the interaction point
ϵ	—	total transverse emittance of a single trajectory ($= \epsilon_x + \epsilon_z$)
ϵ_x	—	horizontal emittance of a single trajectory
ϵ_z	—	vertical emittance of a single trajectory
$\bar{\epsilon}$	—	beam emittance corresponding to 86% of the distribution (or to 2σ)
η	—	relative energy deviation ($= \Delta E/E$)
f_{rev}	—	revolution frequency
g	—	detuning term
γ	—	relativistic gamma factor ($= E/(m_0c^2)$)
h	—	driving term of a resonance *or* Planck's constant
H	—	Hamiltonian
I	—	action variable *or* electric current
I_r	—	value of action variable at the resonance
J	—	action variable
k	—	subscript *or* integer in the resonance condition $kQ_x + lQ_z = p$.
κ	—	ratio of modulation frequency Q_m and island tune Q_I
l	—	superscript *or* integer in the resonance condition $kQ_x + lQ_z = p$.
λ	—	Lyapunov exponent *or* separation constant
M	—	truncated Taylor map
n	—	superscript *or* integer in the resonance condition $nQ = p$.

N	—	normalized Taylor map
p	—	momentum *or* integer in the resonance condition $kQ_x + lQ_z = p$.
ϕ	—	angle variable, phase function of betatron oscillations
q	—	amplitude of tune modulation *or* four-momentum transfer
Q	—	betatron tune
Q_I	—	island tune
Q_m	—	frequency of tune modulation in units of the revolution frequency f_{rev}
$\tilde{Q}$	—	shielding factor
r	—	aperture *or* transverse amplitude
σ	—	standard deviation of the beam distribution *or* longitudinal distance from the bunch center
T	—	temperature *or* coefficient in a Taylor expansion
θ	—	scattering angle *or* azimuth angle around the machine
w	—	relative width of the stochastic layer
x	—	horizontal coordinate
x'	—	horizontal angle
ξ	—	chromaticity
$\tilde{\xi}$	—	beam-beam tune shift
y	—	either horizontal or vertical coordinate
y'	—	either horizontal or vertical angle
z	—	vertical coordinate
z'	—	vertical angle
$: :$	—	Poisson bracket operator

Chapter 1

Introduction

1.1 Motivation

The HERA proton ring at DESY in Hamburg is the second large superconducting storage ring that has come into operation. It was expected, and it has been partly verified in the first years of its operation, that the beam lifetime and performance of this storage ring will be limited by single particle nonlinear beam dynamics and not by collective effects. In this respect, two unique features distinguish HERA from all other operating colliders.

Firstly, the persistent-current nonlinear field errors, the time-dependence of which proved to be harmful in the first superconducting accelerator, the Fermilab Tevatron, are potentially more dangerous for HERA due to the larger ratio of the maximum dipole field to the field at injection B_{max}/B_{inj} which is about 20 as compared to 6 for the Tevatron. At the injection energy of 40 GeV the relative size of the nonlinear field errors is significantly increased. In addition the size of the injected beam is also larger. Therefore the impact of the persistent-current induced field errors on the dynamic aperture was a question of considerable concern.

Consequently, strong effort has been devoted to detailed magnet measurements [1], a dedicated local correction scheme [2], comprehensive simulation studies [3, 4], a reference magnet system allowing a permanent control of the time dependence of the dipole and sextupole field errors, and to the invention of special magnet 'massage' cycles to achieve reproducibility. Following this recipe it has proved possible to inject a proton beam into HERA with a reasonable lifetime of about ten hours [5]. Nevertheless there is evidence for a dynamic aperture limitation inside the physical aperture.

Secondly, HERA is the first collider in which two beams with different particles and not necessarily equal beam sizes are stored in two separated rings and brought into collision. Preliminary experience suggests that the forces induced by the electron beam may strongly affect the proton beam lifetime [6].

In this thesis several aspects of amplitude growth resulting from nonlinear dynamics, i. e. from the persistent-current field errors and from the beam-beam interaction, are discussed, with special emphasis on the effect of an additional external tune modulation.

A second class of processes causing amplitude growth are multiple scattering phenomena. The protons suffer small angle Coulomb scattering by atoms of the residual gas, by electrons of the opposite bunch and by other protons in the same bunch. The first two effects are analysed in detail, partly stimulated by the suspicion that multiple proton-gas scattering might have been the origin of an unexplained lifetime limitation in spring 1991.

1.2 Outline

The structure of this thesis is as follows.

Chapter 2 is concerned with new tracking methods and tracking data analysis. The techniques described are employed in the evaluation of the dynamic aperture of the HERA proton ring.

In chapter 3, a theory of the effect of tune modulation in a nonlinear Hamiltonian system is developed. A criterion for the onset of chaos is derived in terms of island tune, resonance order, modulation amplitude and modulation frequency. The relative harmfulness of different modulation frequencies on the beam dynamics is quantified by a sensitivity function Γ which measures the chaotic fraction of phase space. Moreover, an approximate expression for the amplitude growth rate caused by tune modulation is presented. The theory outlined can be applied to analyse the effect of the persistent-current field errors as well as the beam-beam interaction.

In chapter 4, the frequency-dependent tune-modulation amplitudes due to power supply ripple are estimated both at 40 GeV and at 820 GeV.

The dynamic aperture of the HERA proton ring at injection energy is calculated in chapter 5, from a simulation of particle motion taking into account the multipole contents of each individual magnet. The inclusion of tune modulation leads to a further reduction of the acceptance. To understand the effect of tune modulation quantitatively, the island parameters of high-order resonances are extracted for three typical working points, making use of differential algebra and normal-form methods. Subsequently, the chaotic fraction of phase space and the expected amplitude growth rates are evaluated. The analytically predicted dynamic acceptance is in quantitive agreement with the tracking results. Its value and the calculated transverse diffusion rates can be compared with the acceptance and the diffusion coefficient measured in the proton ring.

In chapter 6, the influence of tune modulation on the beam-beam interaction is discussed. Again the general theory, as developed in chapter 3, provides an estimate for the diffusion rate, which is strongly dependent on the resonance order.

Chapter 7 addresses another aspect of the beam-beam interaction in HERA. The amplitude growth due to multiple proton-electron scattering is calculated to determine if this effect is important and should be taken into account in simulation studies of the beam-beam interaction.

Stimulated by the lifetime limitation observed in the first commissioning run of the proton ring the effect of residual gas scattering is analysed in detail in chapter 8. The lifetime caused by multiple gas scattering is deduced for several operating and boundary conditions starting from a Fokker-Planck equation. It is compared with the beam loss rate due to nuclear interactions.

In chapter 9, the amplitude growth rates for the different processes under investigation are compared and viewed in relation to other phenomena that affect the beam size and lifetime, such as intra-beam scattering.

Finally the results are summarized and some conclusions are drawn in chapter 10.

In appendix A, an overview is presented of differential algebra and differential-algebra based normal-form algorithms. Both mathematical tools considerably facilitate the postprocessing analysis of tracking results, provide a substantial increase in computing speed and, even more important, permit an analytical treatment of the beam dynamics as a supplement to numerical multi-turn-tracking.

Chapter 2

Particle Tracking Methods

2.1 Introduction

The dynamic aperture is defined as the border in phase space inside which particle motion is stable for a sufficiently large number of turns around the storage ring. For superconducting hadron colliders the aperture can be strongly limited at injection energy due to the field errors caused by persistent currents in the magnets. In HERA the minimum time needed to inject 210 bunches is about 20 minutes, corresponding to $6 \cdot 10^7$ turns. Tracking studies with the present computer systems fall short of this number of revolutions by almost a factor 100. There are two possible approaches to overcome this problem:

- The tracking data for a smaller number of turns are analysed in such a way as to detect potentially unstable trajectories, which may result in a particle loss after a much longer time period. A promising approach of this category is based on a calculation of Lyapunov exponents and the determination of the border between regular and chaotic motion, which can be viewed as a good estimate value for the actual dynamic acceptance. Here $10^3 - 10^4$ turns are usually sufficient to yield fairly accurate results.

- The employed model of the accelerator is simplified. For instance the complete storage ring can be replaced by a Taylor map representation [11]. Such a Taylor map can easily be extracted from a standard tracking code with the methods of differential algebra [12]. In order to avoid artificial emittance growth in the simulation [13], the Taylor map must be modified by some symplectification scheme, for instance by performing a kick factorization [14]. Following this approach a gain in computational speed by a factor 10–20 is possible. It is evident that the Taylor map tracking can also be analysed with respect to chaotic motion, thereby further reducing the required computing time.

In the following the two approaches are discussed in more detail.

2.2 Lyapunov Exponent

A sensitive measure of local instabilities in phase space is the Lyapunov exponent which characterizes the rate of divergence of initially close trajectories. For regular motion the distance d in phase space between two tracks grows linearly with the number of turns N, when averaged over long periods of time

$$d(N) \propto N.$$

Chaotic motion is characterized by an exponential growth of this distance

$$d(N) \propto e^{\lambda N},$$

where λ is called Lyapunov exponent (see for instance [17]). Its formal definition reads

$$\lambda \equiv \lim_{N\to\infty} \lim_{d(0)\to 0} \frac{1}{N} \ln \frac{d(N)}{d(0)}. \tag{2.1}$$

and is independent of the measure of d, i. e. the value of λ does not depend on the choice of metric for the phase space [8]. It should be noted that the Lyapunov exponent λ is zero for a regular trajectory.

A general particle trajectory is described by the six canonical coordinates $x, p_x, z, p_z, \sigma, \eta$ [7]. Here x and z are the horizontal and vertical displacement from the design orbit, σ is the longitudinal distance from the bunch center and η the relative energy deviation. The canonically conjugate momenta to x and z are denoted by p_x and p_z. In linear approximation the six-dimensional phase space coordinates after N turns are related to the initial values through the N-turn Jacobian matrix J_N,

$$J_N \equiv \frac{\partial(x, z, \sigma, p_x, p_z, \eta)_N}{\partial(x, z, \sigma, p_x, p_z, \eta)_0}. \tag{2.2}$$

The limit of vanishing initial distance $d(0) \to 0$ in (2.1) can be performed exactly [8], leading to an alternative expression in which the Lyapunov exponent is given in terms of the largest eigenvalue $EV_{N,\max}$ of the Jacobian matrix J_N:

$$\lambda \equiv \lim_{N\to\infty} \lambda_N \equiv \lim_{N\to\infty} \frac{1}{N} \ln |EV_{N,\max}|. \tag{2.3}$$

The modulus of the largest eigenvalue $EV_{N,\max}$ shows the same behavior as a function of N as the distance $d(N)$. That means, for a regular trajectory a linear increase with the number of turns is observed, and for chaotic motion the eigenvalue increases exponentially.

At this point it is appropriate to review some basic concepts of accelerator physics [9, 10]. The equations of motion can be solved exactly for a model of the storage ring consisting only of dipoles, quadrupoles and drift spaces, hereafter referred to as 'linear storage ring'. Without coupling between the three planes of motion a particle performs a betatron oscillation of the form

$$y = \sqrt{\epsilon_y \beta_y(s)} \cos(\phi_y(s) + \phi_{y0}), \tag{2.4}$$

where y denotes either the horizontal or the vertical displacement with respect to the reference orbit and the coordinate s is the path length along that orbit. The linear storage ring is completely characterized by the *beta function* $\beta_y(s)$, which is a periodic function

$$\beta_y(s) = \beta_y(s + C), \tag{2.5}$$

C being the circumference of the ring. This function does not only describe the s-periodic part of the oscillation amplitude in (2.4), but it also determines the derivative of the phase function $\phi_y(s)$

$$\frac{d\phi_y(s)}{ds} = \frac{1}{\beta_y(s)}. \tag{2.6}$$

Hence the number of betatron oscillations per turn, called Q-value or *tune*, is given by

$$Q_y = \frac{1}{2\pi} \oint \frac{1}{\beta_y(s)} ds. \tag{2.7}$$

One of the two constants of integration ϵ_y and ϕ_{y0} in (2.4), namely the initial phase ϕ_{y0}, is of no particular importance. The second, ϵ_y, describes the s-independent part of the oscillation amplitude. At a fixed value of s the particle trajectory is restricted to an ellipse in the y-p_y-plane, whose area F is related to ϵ_y by

$$F = \pi \epsilon_y. \tag{2.8}$$

The quantity ϵ_y is called *single-particle emittance* and is quoted in units of mm mrad.

In a linear storage ring the single-particle emittance ϵ_y defined by (2.4) or (2.8) is a constant of motion. The real storage ring is not linear and the actual particle trajectories deviate from the solution (2.4). Nevertheless, because this deviation is small over short periods of time, it is still a fruitful concept to use the linear solution as a parametrization in the tracking analysis. In the presence of nonlinearities, ϵ_y calculated according to (2.4) does not stay constant, but can increase (or decrease) slowly as a function of time. Because the divergence from the linear solution depends strongly on the starting value of ϵ_y itself, the particles inside a bunch will suffer different changes of ϵ_y. In general, the increase of the average value of ϵ_y over the beam distribution differs strongly from the increase experienced by a particle, say, at one or at two standard deviations.

The emittance ϵ_y of a single trajectory, used throughout this thesis, is defined by (2.4) and should be understood simply as a measure of the squared horizontal or vertical oscillation amplitude normalized such as to be independent of the position around the ring. Very often we will quote the sum $\epsilon \equiv \epsilon_x + \epsilon_z$, called the total transverse emittance.

Occasionally also the two-sigma beam emittance is referred to, which is the emittance of a particle trajectory enclosing 86% of the beam in phase space. The two-sigma beam emittance will be denoted by the symbol $\bar{\epsilon}$ and is to be distinguished from the single-particle emittance ϵ defined before, which refers to an arbitrary trajectory.

In the case of a linear storage ring the difference of the phase ϕ_y between two nearby trajectories as a function of the number of turns is a constant, because the local phase advance is given by $1/\beta_y(s)$ for all particles. In a nonlinear system the phase advance depends on the amplitude, and the phase distance $|\phi_{y,1} - \phi_{y,2}|$ grows at least linearly in time.

The use of the Lyapunov method in the postprocessing analysis of tracking data rests on the following observations and hypotheses:

1. The divergence between two particles, as observed in cartesian coordinates, is mainly an information on the phase distance and not on the amplitude evolution. It is therefore advantageous to consider only the phase separation $(\frac{1}{2}\sum_{y=x,z}(\phi_{y,1} - \phi_{y,2})^2)^{\frac{1}{2}}$, respectively its three-dimensional generalization, instead of the strongly oscillating cartesian distance between two trajectories.

2. The eigenvalue behavior and the phase divergence are almost identical (Fig. 2.1 a, b and 2.2 a, b). This implies that two-particle-tracking already gives very accurate results and that a sufficiently small initial distance had been chosen, the limitation in this quantity being given by rounding errors.

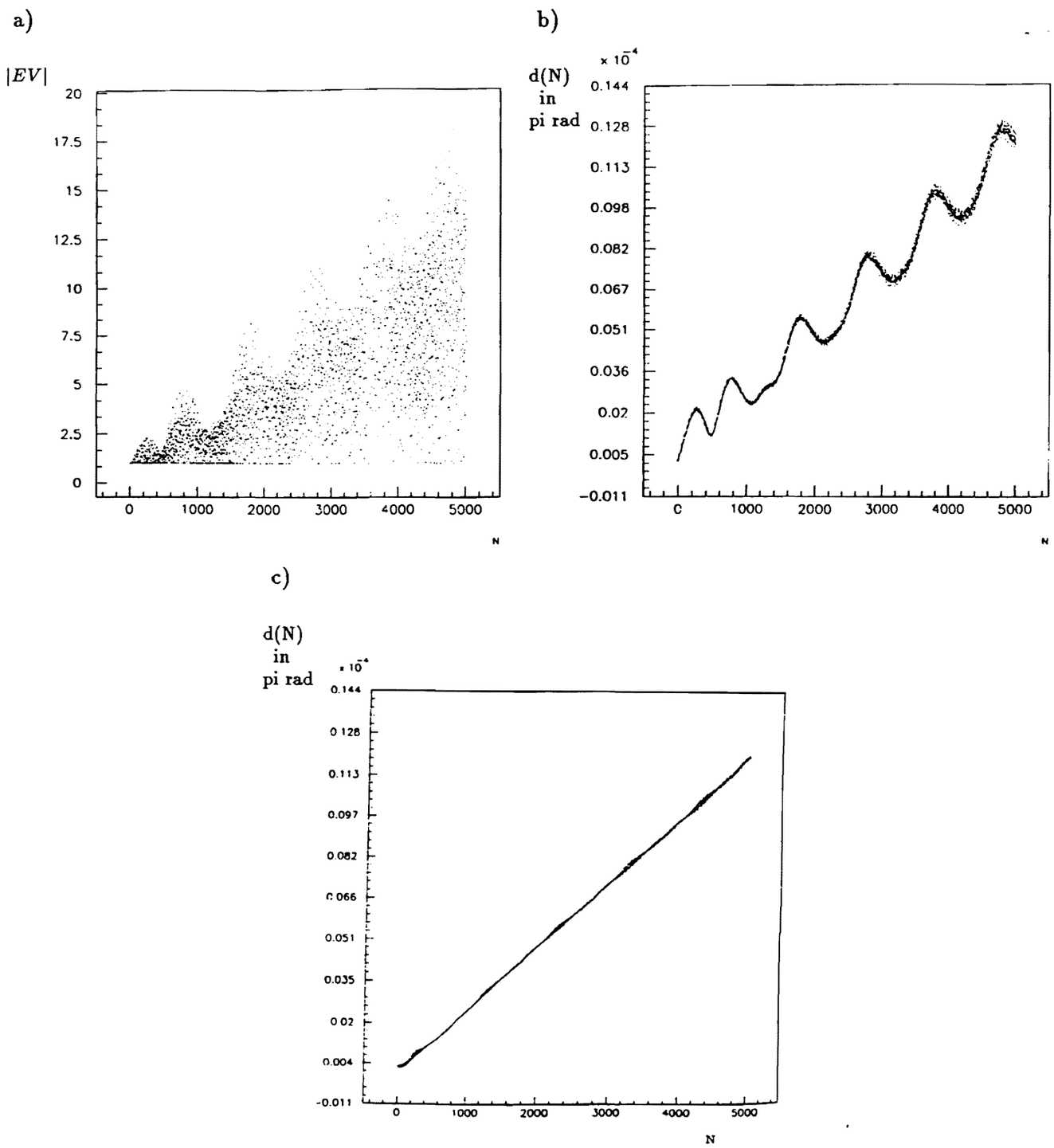

Figure 2.1: Regular trajectory in a HERA-like FODO cell for 5 000 turns; a) maximum eigenvalue, b) phase distance between two nearby particles, c) phase distance between two nearby particles in normal-form coordinates [18].

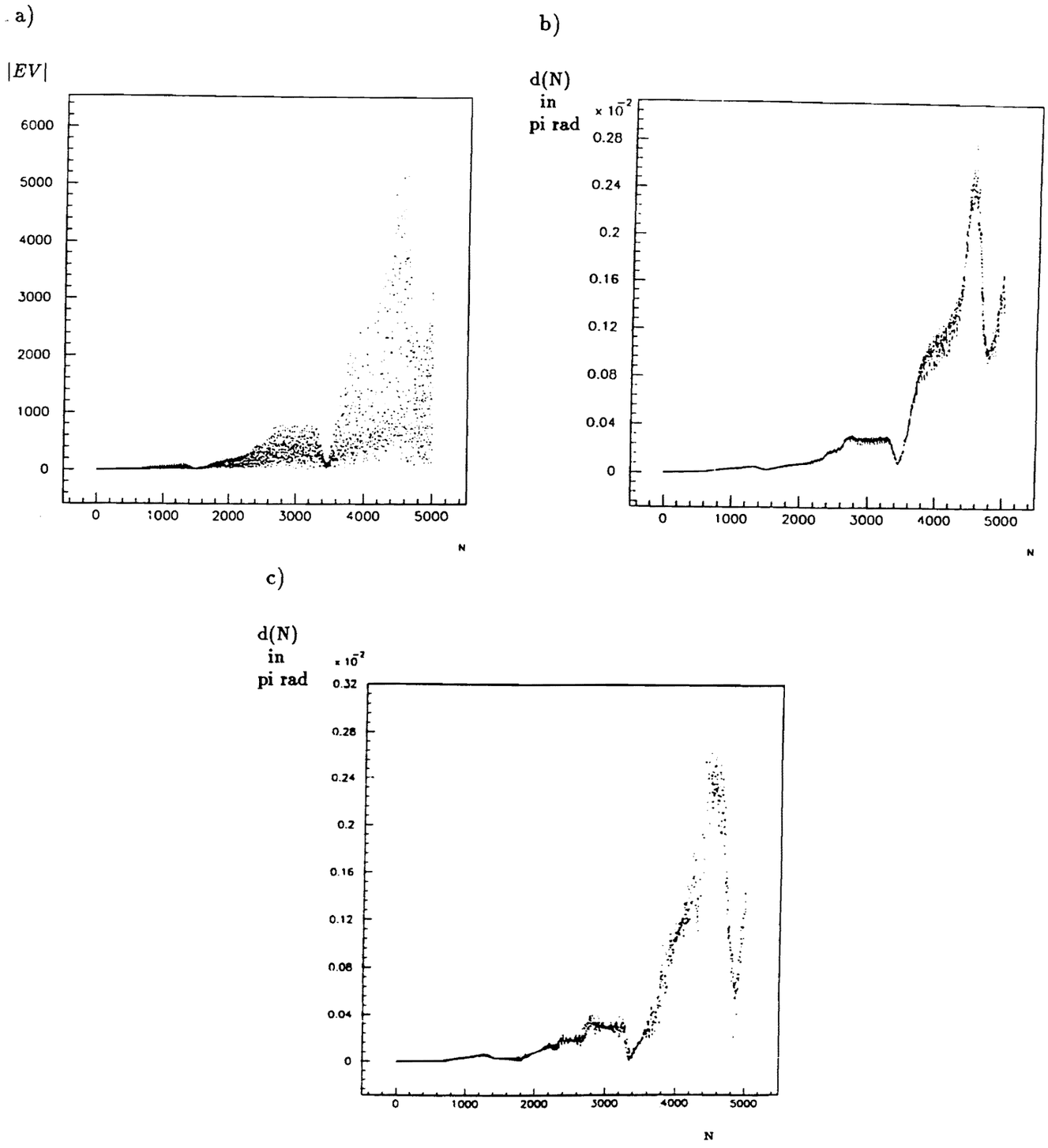

Figure 2.2: Chaotic trajectory in a HERA-like FODO cell for 5 000 turns; a) maximum eigenvalue, b) phase distance between two nearby particles c) phase distance between two nearby particles in normal-form coordinates [18].

3. Considerable improvement can be achieved by investigating the phase distance in a suitably 'normalized' coordinate frame, in which all phase space deformations up to a specific order have been removed. For regular motion the distance between two particles in the normalized coordinates evolves almost free of any disturbing oscillations (Fig. 2.1 b, c), whereas for strongly chaotic trajectories the transformation to new coordinates has virtually no effect (Fig. 2.2 b, c). The increased sensitivity for detecting barely chaotic particles by this method is documented in Fig. 2.3.

4. Particles with positive Lyapunov exponents experience an emittance growth on a longer time scale. Hence an exponential phase separation indicates a long-term amplitude increase and possible final particle loss. This is the main reason for the use of Lyapunov exponents in tracking studies and has been confirmed for all cases under consideration. An example is shown in Fig. 2.4.

2.3 Map Tracking

2.3.1 Tracking with Truncated Taylor Maps

Truncated Taylor maps, which expand the change in the phase space coordinates during one turn around the accelerator in terms of the initial coordinates, provide a promising alternative to element-by-element tracking, hereafter also called direct tracking. A Taylor map representation of a storage ring is obtained from a conventional tracking code by use of an automatic differentiation technique named 'differential algebra' or, briefly, 'DA' [12] (see appendix A). The purpose of map tracking is to increase the computing speed by a significant factor and to access turn numbers which are beyond the capacity of direct tracking. The applicability of map tracking is determined by two conditions. The order of the Taylor map has to be high enough to reproduce the correct dynamic aperture. Simultaneously it has to be so small that the map tracking is still faster than direct tracking. For HERA, a 12th order map requires about the same amount of computing time as direct tracking.

Let us assume that a Taylor map description of the following form has been extracted from a conventional tracking code like SIXTRACK [19]

$$v_j^f = T^1_{jk} v_k^i + T^2_{jk_1k_2} v^i_{k_1} v^i_{k_2} + \ldots \equiv M_j(\vec{v}^i), \tag{2.9}$$

where the subscripts j or k denote the components of the phase space coordinate vector $\vec{v} \equiv (x, z, \sigma, p_x, p_z, \eta)$ and the superscripts i or f refer to the initial and final coordinates, respectively.

For the comparison of map tracking and direct tracking it is useful to introduce the notion of a normalized *transverse amplitude* a_{xz}. This is defined in the following way. We construct a linear transformation A_2, which brings the linear part of the map M (2.9) into a particularly simple form [23]. The transformation is written as

$$\tilde{M} = A_2 M A_2^{-1}, \tag{2.10}$$

where the new map has been called $\tilde{M}$. In the transformed coordinate frame the Taylor expansion reads

$$\tilde{v}_j^f = \tilde{T}^1_{jk} \tilde{v}_k^i + \tilde{T}^2_{jk_1k_2} \tilde{v}^i_{k_1} \tilde{v}^i_{k_2} + \ldots \equiv \tilde{M}_j(\vec{\tilde{v}}^i). \tag{2.11}$$

The linear part $\tilde{T}^1$ of the transformed map is a rotation in each plane of motion

$$\begin{pmatrix} \tilde{y} \\ \tilde{p}_y \end{pmatrix}^f = \begin{pmatrix} \cos 2\pi Q_y & \sin 2\pi Q_y \\ -\sin 2\pi Q_y & \cos 2\pi Q_y \end{pmatrix} \begin{pmatrix} \tilde{y} \\ \tilde{p}_y \end{pmatrix}^i, \tag{2.12}$$

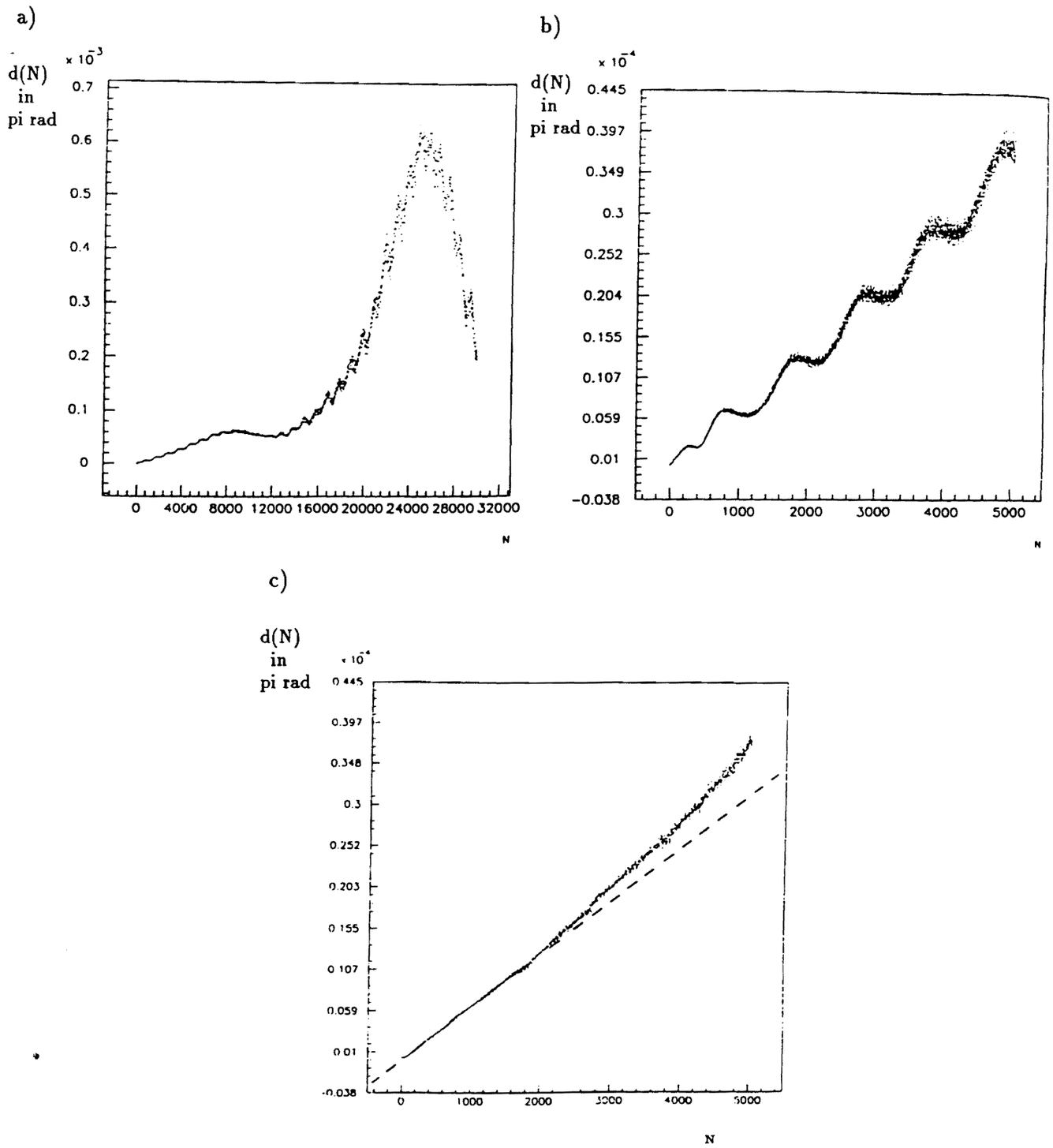

Figure 2.3: Barely chaotic trajectory in a HERA-like FODO cell; a) phase distance between two nearby particles for 30 000 turns, b) phase distance between two nearby particles for 5 000 turns, c) phase distance between two nearby particles in normal-form coordinates for 5 000 turns (the change of the slope indicates chaotic motion) [18].

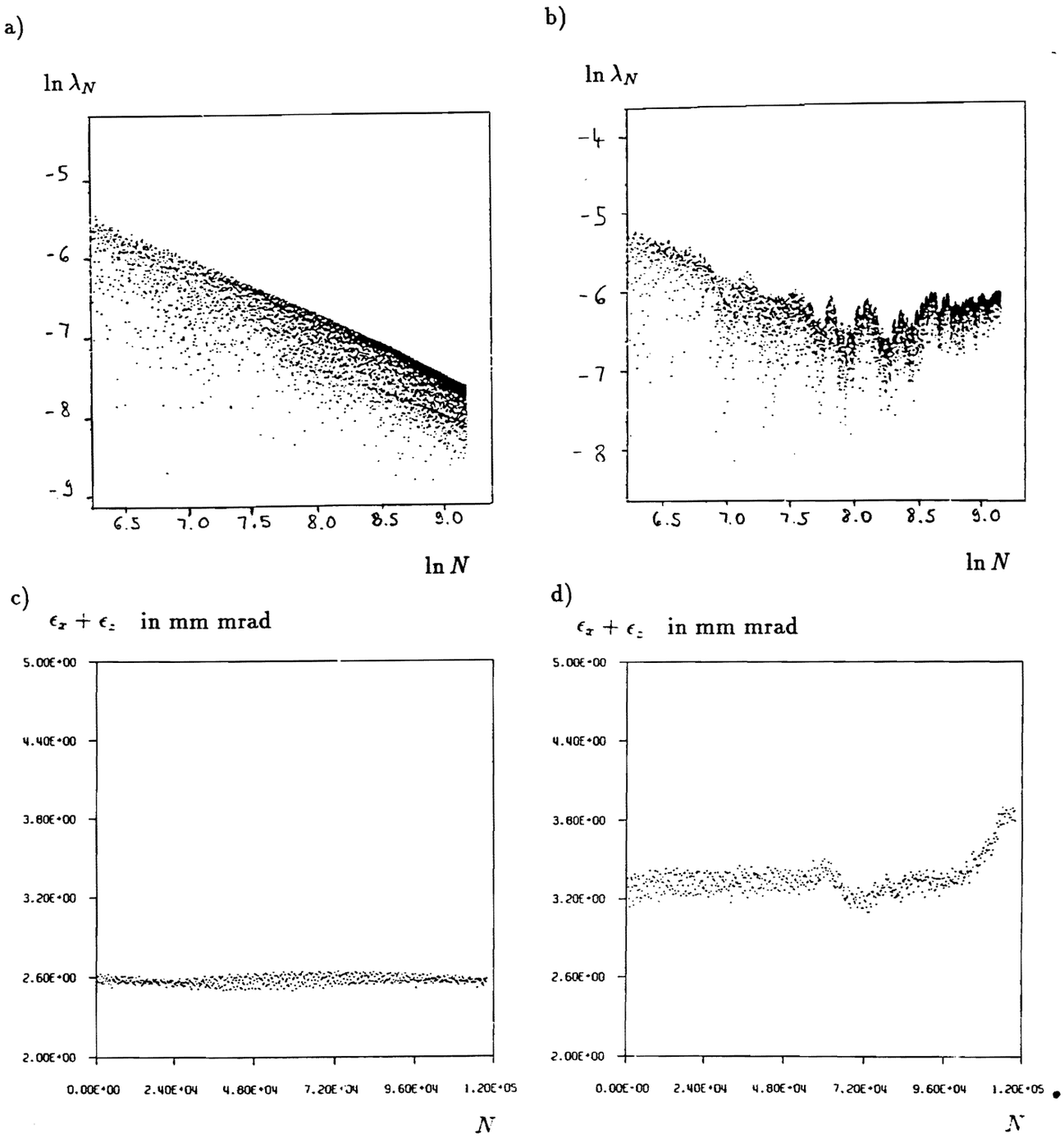

Figure 2.4: Lyapunov exponent for a regular and a chaotic trajectory in HERA and the corresponding emittance evolution; a) and b) $\ln \lambda_N$ as a function of $\ln N$ for 10 000 turns at a starting amplitude of 11.9 mm and 13.5 mm (β = 76 m), respectively, with $\Delta p/p = 10^{-3}$; c) and d) transverse emittance $\epsilon_x + \epsilon_z$ over 120 000 revolutions for the same two trajectories; each dot represents the maximum value during 200 turns.

where $(\tilde{y}, \tilde{p}_y)$ denotes the position and momentum in either one of the three degrees of freedom. In the new coordinate frame the motion is linearly decoupled. Furthermore, the linear transformation $\tilde{T}^1$ is independent of the beta function. If we define a horizontal and a vertical amplitude $a_{x,z}$ by

$$a_x \equiv \sqrt{\tilde{x}^2 + \tilde{x}'^2} \qquad \text{and} \qquad a_z \equiv \sqrt{\tilde{z}^2 + \tilde{z}'^2}, \tag{2.13}$$

the total transverse amplitude a_{xz} is given by

$$a_{xz} \equiv \sqrt{a_x^2 + a_z^2}. \tag{2.14}$$

For an ideal accelerator without linear coupling between the three degrees of freedom the transverse amplitude can be written in terms of the transverse emittance as

$$a_{xz} = \sqrt{\epsilon_x + \epsilon_z} \qquad \text{(without linear coupling).} \tag{2.15}$$

A convenient measure for the deviation between direct tracking and map tracking is the average relative amplitude error per turn $(\delta a_{xz}/a_{xz})_N$. Denoting the average value over the first N turns by brackets '$< \ldots >_N$', also called running average value in the following, the average relative amplitude error per turn computed from N turns is defined by

$$\left(\frac{\delta a_{xz}}{a_{xz}}\right)_N \equiv \frac{< a_{xz}^{map} >_N - < a_{xz}^{dir.} >_N}{N < a_{xz}^{dir.} >_N}. \tag{2.16}$$

Here the superscripts *map* and *dir.* refer to map tracking and direct tracking, respectively. Usually, the right hand side approaches a constant value after a few thousand turns. Only at very large amplitudes the relative amplitude error is not well defined, because the amplitude deviation increases rapidly and nonlinearly with the number of turns, so that the right hand side of (2.16) does not converge as a function of turn number N.

In Fig. 2.5 the absolute value of the relative error $(\delta a_{xz}/a_{xz})_N$ is depicted for tracking with a 7th and an 11th order map in the case of HERA and for tracking with an 11th order map of the proposed Large Hadron Collider LHC [24]. The much better agreement between map tracking and direct tracking for HERA is clearly visible. The dynamic aperture of the LHC is at about $a_{xz} \approx 0.772$ mm$^{\frac{1}{2}}$ mrad$^{\frac{1}{2}}$ for an initial relative momentum deviation $\Delta p/p = 10^{-3}$ — 77% of the bucket height — and that of HERA is close to $a_{xz} \approx 1.3$ mm$^{\frac{1}{2}}$ mrad$^{\frac{1}{2}}$ for a momentum deviation $\Delta p/p = 3.5 \cdot 10^{-4}$ — about 50% of the bucket height for the design radio frequency voltage of 26.4 kV. Comparing the relative amplitude error per turn at the respective dynamic aperture limit, a 7th order Taylor map gives a ten times smaller error for HERA than an 11th order map for the LHC.

A short digression on some parameters of HERA and the LHC can explain the significant difference in the applicability of map tracking. A set of parameters for both accelerators is listed in Table 2.1. The injection energy for the LHC of 450 GeV is 11 times higher than that of HERA and, provided the performance of the preaccelerators is similar, the beam emittance is smaller by about the same factor. Most importantly, made possible by the smaller beam size the inner diameter of the superconducting magnet coils is reduced by a factor two third for the LHC.

Parameter	HERA	LHC
Normalized Emittance $\bar{\epsilon}_N \equiv \gamma\bar{\epsilon}\ (2\sigma)$	15 mm mrad	15 mm mrad
Unnormalized Emittance $\bar{\epsilon}\ (2\sigma)$	0.4 mm mrad	0.03 mm mrad
Injection Energy	40 GeV	450 GeV
Maximal Beta in the Arc	76 m	167 m
Number of FODO Cells	95	224
Coil Diameter in sc. Magnets	75 mm	50 mm
Bucket Height $(\Delta p)/p$	$7 \cdot 10^{-4}$	$1.3 \cdot 10^{-3}$

Table 2.1: Comparison of parameters for HERA and the model of the LHC.

HERA and LHC Multipole Errors						
	Dipole Magnets				Quadrupole Magnets	
	HERA		LHC		HERA	
coefficient	average	sigma	average	sigma	average	sigma
Normal Components						
b_3	−32	3.2	−20.9	10.6	0.02	0.17
b_4	0.09	0.36	0.8	2.3	0.05	0.09
b_5	12	1.04	18	8.6	0.02	0.08
b_6	−0.1	0.34	–	–	−2.4	0.2
b_7	−2.0	0.53	34	4.9	0.02	0.05
b_8	0.14	0.41	–	–	−0.17*	0.45*
b_9	0.44	0.48	52	7.6	0.30*	0.88*
b_{10}	−0.13	0.53	–	–	3.04*	0.89*
Skew Components						
a_3	−0.36	0.71	–	–	0.05	0.18
a_4	0.86	1.25	–	–	−0.01	0.13
a_5	0.23	0.66	–	–	−0.02	0.13
a_6	−0.70	0.56	–	–	−0.02	0.15
a_7	−0.20	0.54	–	–	0.01	0.06
a_8	0.24	0.39	–	–	−0.56*	0.53*
a_9	0.10	0.67	–	–	−0.46*	0.50*
a_{10}	−0.26	0.50	–	–	0.26*	0.72*

Table 2.2: Normal and skew multipole components for the superconducting magnets in the models of HERA [25] and the LHC [24]. All multipole values are quoted for a radius $r_0 = 25$ mm in units of 10^{-4} relative to the main dipole field B_0. In the model of the LHC no field errors in the quadrupoles and no skew components in the dipole magnets have been taken into account. * Due to a faulty database the multipole coefficients of order 8 to 10 for the quadrupole magnets in this model of HERA are a factor 10 larger than the actually measured values.

Table 2.2 shows the average value and the rms-deviation of the multipole coefficients for the superconducting magnets in HERA and in the model of the LHC. The skew and normal multipole components a_n and b_n, quoted in Table 2.2, are defined by the complex equation

$$B_z + iB_x = B_0 \sum_{n=1}^{\infty} (b_n + ia_n)(x + iz)^{n-1}/r_0^{(n-1)}, \tag{2.17}$$

where B_0 is the main dipole field and r_0 is a reference radius.

Because of the smaller magnet and coil dimensions the multipole coefficients for the LHC are much larger than for HERA. The unlike size of the nonlinear field errors is reflected in the average magnitude of the Taylor map coefficients. As an illustration the absolute values of the Taylor map coefficients averaged over all coefficients of the same order n are plotted versus the order n in Fig. 2.6, both for HERA and for the LHC. They differ by about a factor 10 000 for the high-order terms which explains the different accuracy of map tracking in Fig. 2.5. Moreover, the Taylor map coefficients reflect the build-up of nonlinear field errors around the storage ring. A general $2n$-pole contributes primarily to the coefficients of order $(n-1)$ in the Taylor map. For example, the uncompensated systematic 20-pole component of the superconducting HERA quadrupoles gives rise to a sharp peak value for the Taylor map coefficients of 9th order. Because multipole errors beyond 20-poles are not used in the simulation, all coefficients of order higher than nine are solely due to an interference between lower order multipoles. Therefore the magnitude of these coefficients decreases rapidly.

If one wants to use Taylor maps for multi-turn tracking studies, the long-term evolution of the transverse amplitude is an important question to be addressed. Fig. 2.7 presents a typical behavior close to the dynamic aperture in HERA for three different orders (7, 9 and 11) of the Taylor map and an initial relative momentum deviation of $3.5 \cdot 10^{-4}$. Depicted is the *running average* amplitude $< a_{xz} >_N \equiv \frac{1}{N} \sum_{i=1}^{N} a_{xz}(i)$, for which the extant amplitude oscillations tend towards zero, as a function of turn number N. The map tracking amplitude deviates from the direct tracking amplitude, which is constant over this number of turns, in a linear and regular way. Depending on the chosen order of the map, one finds both regular decreases and growths. Increasing the order of the map by two units, reduces the deviation by a factor of about eight. The reason for the deviation is that a truncated Taylor map is in general not symplectic.

Denoting the Jacobian matrix of the map M (2.9) by J,

$$J_{jk}(\vec{v}^i) \equiv \frac{\partial M_j(\vec{v}^i)}{\partial v_k^i}, \tag{2.18}$$

the map M is *symplectic*, if and only if the condition

$$J^t S J = S \tag{2.19}$$

holds for any set of initial coordinates $\vec{v}^i$. The 6x6 matrix S is defined by

$$S \equiv \begin{pmatrix} 0 & I \\ -I & 0 \end{pmatrix}, \tag{2.20}$$

where I denotes the 3x3 unit matrix.

In general, because the map M and its Jacobian matrix are polynomial expressions, the symplecticity condition cannot be fulfilled everywhere in phase space.

It can be shown [20] that symplecticity is a necessary and sufficient condition for a transformation to be canonical. Therefore truncated Taylor maps are not canonical and do in

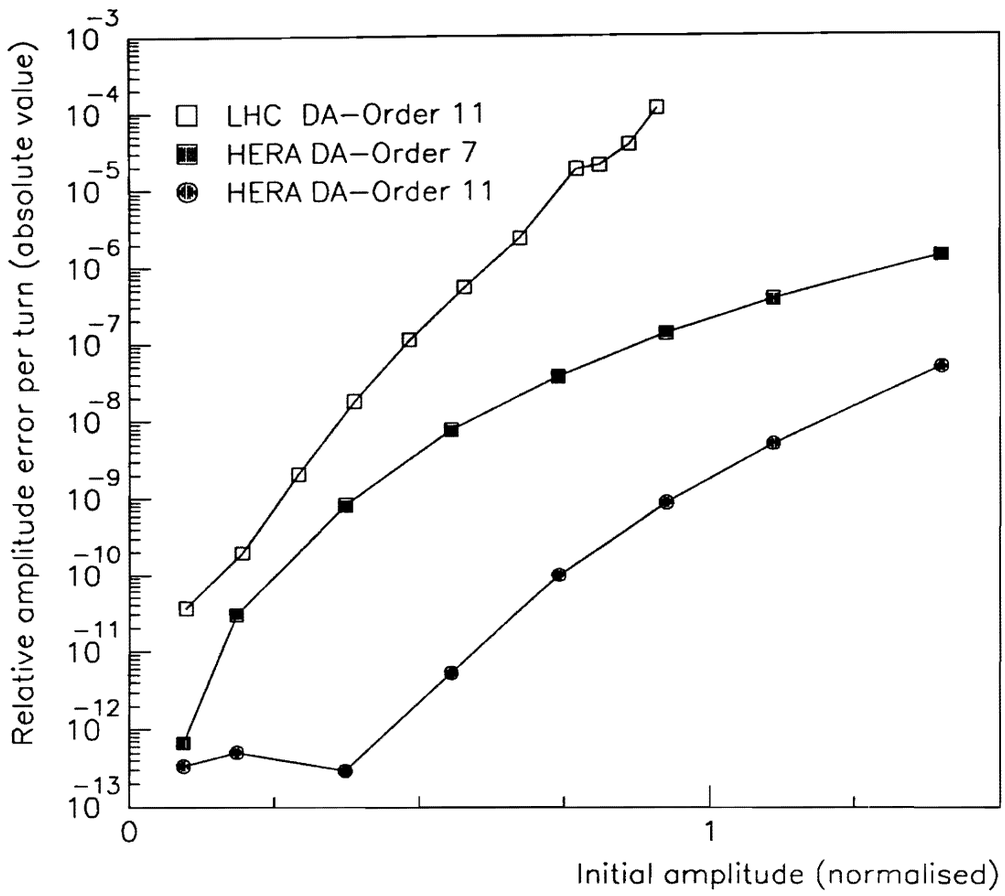

Figure 2.5: Absolute value of the average relative amplitude error per turn, as deduced from tracking over 20 000 turns, for various starting amplitudes and orders of the Taylor map. The dynamic aperture in the LHC is at about 0.77 $\mathrm{mm}^{\frac{1}{2}}$ $\mathrm{mrad}^{\frac{1}{2}}$ for an initial momentum deviation of 10^{-3} as compared with an aperture of 1.3 $\mathrm{mm}^{\frac{1}{2}}$ $\mathrm{mrad}^{\frac{1}{2}}$ for a momentum deviation $3.5 \cdot 10^{-4}$ in HERA. A 7th order map provides a better description of HERA than an 11th order map of the LHC.

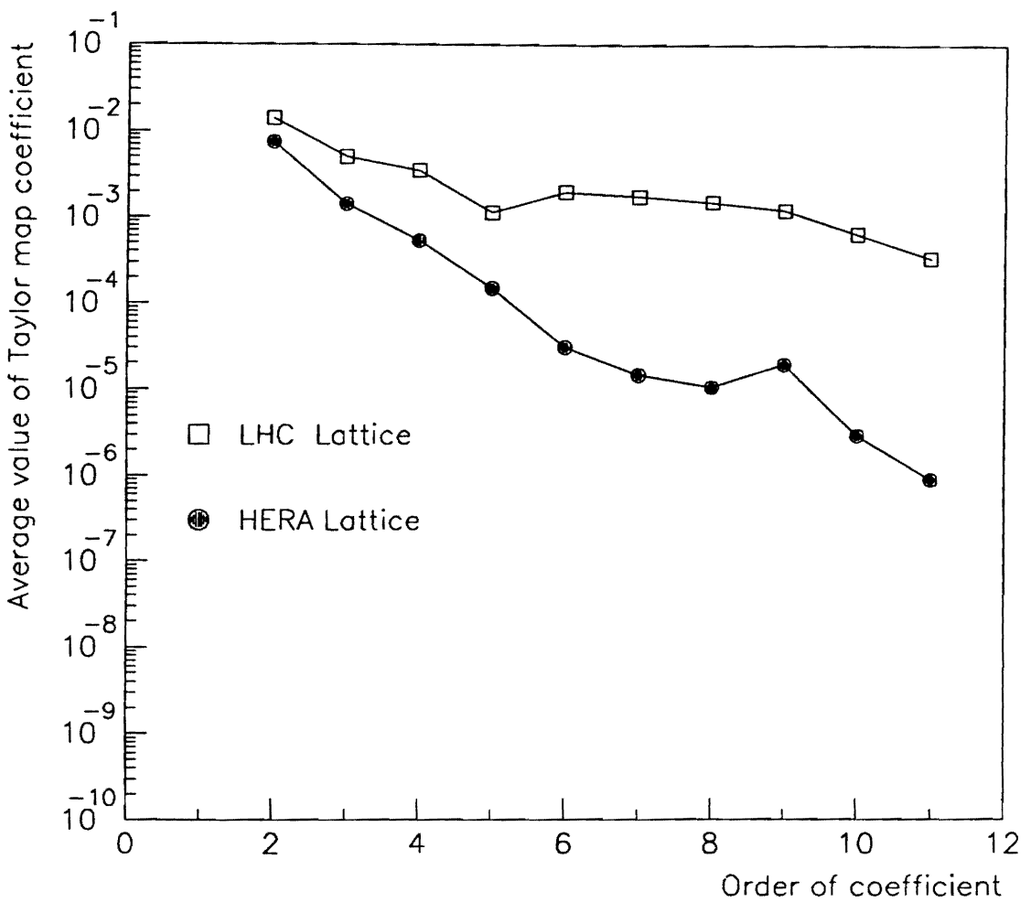

Figure 2.6: The absolute value of the Taylor map coefficients averaged over all terms of the same oder n in units of (mm mrad)$^{\frac{1-n}{2}}$ versus the order n of the coefficients.

particular not conserve the volume in phase space. As a result tracking with these maps leads to the artificial emittance growth or decrease observed in Fig. 2.7.

It should be emphasized that despite of its manifest non-symplecticity a truncated Taylor map may contain an almost exact description of the resonance parameters and of the amplitude-dependent tunes (see chapter 5).

2.3.2 Irwin Factorization

In this section we describe a promising scheme to 'symplectify' a truncated Taylor map. The aim is to modify the Taylor map in such a way that is still agrees with the direct tracking over a few turns, but does not show the artificial emittance growth due to the truncation. A Taylor map $\tilde{M}$ (2.11) can be transformed into the following form [20]

$$\tilde{M} = Re^{:f_3:}e^{:f_4:}\dots e^{:f_{n_o}:} + \mathcal{O}(n_o), \tag{2.21}$$

where R is a rotation and the f_n are homogeneous polynomials of order n in $\vec{x}$ and $\vec{p}$. The colon represents the Poisson bracket operator, which is defined by

$$:f:g \equiv [f,g] \equiv \frac{\partial f}{\partial \vec{x}}\frac{\partial g}{\partial \vec{p}} - \frac{\partial f}{\partial \vec{p}}\frac{\partial g}{\partial \vec{x}}$$

for two arbitrary functions f and g of the phase space variables [20]. Here the derivatives $\partial/\partial\vec{x}$ and $\partial/\partial\vec{p}$ denote the nabla operators ∇_x and ∇_p. The polynomials f_n can be chosen in such a way, that the expression (2.21) agrees with the original Taylor map up to order (n_o-1). This representation, called Dragt-Finn factorization [20], is exactly symplectic, because it is formulated in terms of Lie generators. If applied to an initial coordinate the Dragt-Finn factorization generally gives rise to an infinite series, which means that it cannot be evaluated exactly. To bypass this problem another factorization has been suggested by Irwin [14]. Equation (2.21) is rewritten as

$$\tilde{M} = Re^{:g_1:}e^{:g_2:}\dots e^{:g_K:} + \mathcal{O}(n_o), \tag{2.22}$$

where the $e^{:g_n:}$ are 'kicks', for which the exponential series terminates after the second term,

$$e^{:g_n:}\vec{x} \equiv \vec{x} + [g_n,\vec{x}] + \tfrac{1}{2}[g_n,[g_n,\vec{x}]] + \dots \stackrel{!}{=} \vec{x} - \frac{\partial g_n}{\partial \vec{p}} \tag{2.23}$$

$$e^{:g_n:}\vec{p} \equiv \vec{p} + [g_n,\vec{p}] + \tfrac{1}{2}[g_n,[g_n,\vec{p}]] + \dots \stackrel{!}{=} \vec{p} + \frac{\partial g_n}{\partial \vec{x}}. \tag{2.24}$$

In other words, all multiple Poisson brackets in (2.23) and (2.24) vanish. The expression on the right hand side of (2.22) is called kick factorization or Irwin factorization. Also the 'kick map' (2.22) agrees with the Taylor map $\tilde{M}$ up to order $(n_o - 1)$. In a six-dimensional kick factorization the k-th Irwin polynomial g_k is defined by

$$g_k = \sum_{l+m+n\le n_o} \beta_k^{l,m,n} x_k^l y_k^m z_k^n, \tag{2.25}$$

where x_k, y_k and z_k have the form

$$x_k = \cos\theta_{xk}x + \sin\theta_{xk}p_x, \dots \tag{2.26}$$

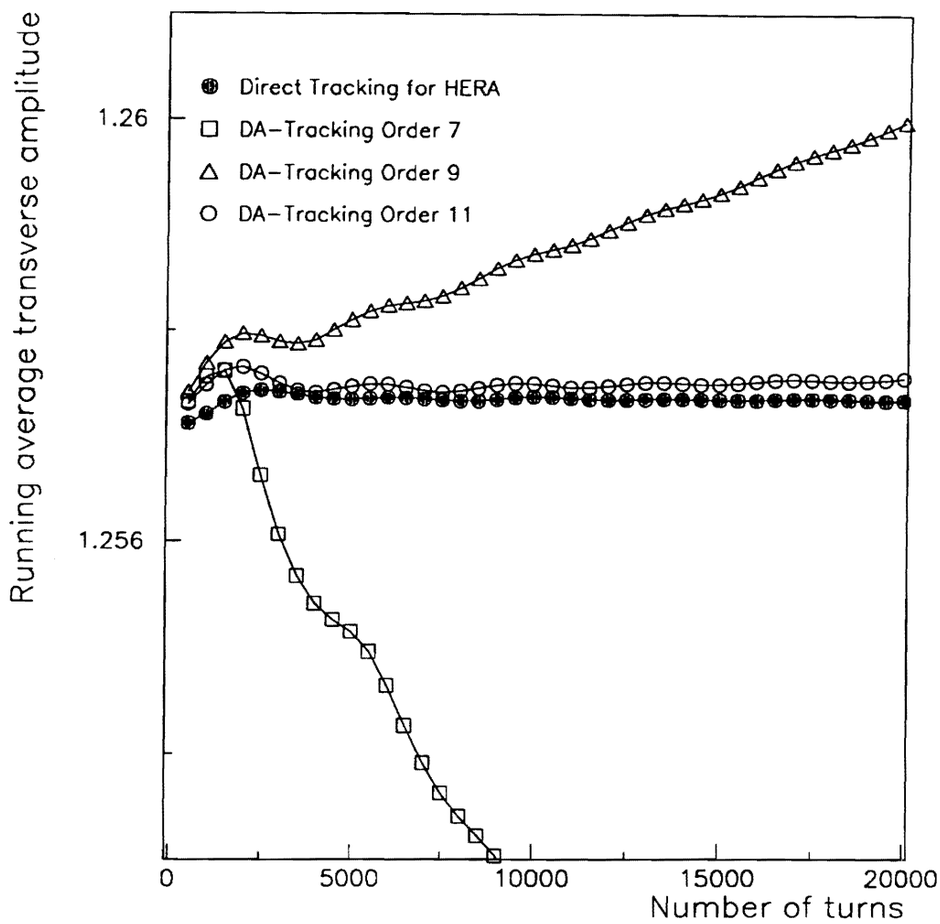

Figure 2.7: Evolution of the transverse amplitude as a function of turn number N for an initial amplitude close to the dynamic aperture of HERA using Taylor map tracking of various order. Shown is the running average amplitude $< a_{xz} >_N \equiv \frac{1}{N}\sum_{i=1}^{N} a_{xz}(i)$ in $\mathrm{mm}^{\frac{1}{2}}$ $\mathrm{mrad}^{\frac{1}{2}}$, computed from the first N turns. In direct tracking the amplitude is perfectly constant, while with map tracking the amplitude grows or shrinks approximately linearly with time. The magnitude of the deviation depends sensitively on the order of the used map. Despite of this divergence, the Taylor maps of order 7–11 and the direct tracking predict the same amplitude threshold of chaos, computed from 20 000 turns by the Lyapunov exponent method (compare Table 2.3).

Here, exceptionally, 'y' denotes the vertical and 'z' the longitudinal plane of motion. For three degrees of freedom, that is for the description of coupled synchro-betatron motion, the minimum number of kicks K required to ensure agreement with the Taylor map $\tilde{M}$ of order $(n_o - 1)$ is given by

$$K = \left\{ \begin{array}{c} (n_o+3)^3/27 \\ (n_o+4)^2(n_o+1)/27 \\ (n_o+2)^2(n_o+5)/27 \end{array} \right\}, \text{ if } \left\{ \begin{array}{c} n_o/3 \\ (n_o+1)/3 \\ (n_o+2)/3 \end{array} \right\} \text{ is an integer.} \tag{2.27}$$

The angles θ_{xk}, θ_{yk}, θ_{zk} can be chosen either by a special algorithm [14] or by a random number generator [21]. In general some freedom is left for the choice of the kick strengths $\beta_k^{l,n,m}$ to reproduce a specific monomial in the original map. The Irwin scheme uses Lagrange multipliers to minimize the quantity $\sum_{k=1,K}(\beta_k^{l,m,n})^2$. Thereby the Irwin polynomials become uniquely defined. To avoid an accidentally large kick strength due to an unlucky choice of rotation angles, it is advisable not to work with the minimum number of kicks.

In the Irwin factorization the original DA map is cast into a form which is identical to the original map in the low order terms, which is symplectic and which can be evaluated exactly. The only potential problem, inherent in every factorization scheme, is the introduction of spurious high-order terms: The evaluation of the Irwin factorization gives rise to new terms up to order $(n_o - 1)^K$, which may be widely different from the equivalent terms in the element-by-element tracking.

Thus an application of the Irwin factorization relies on two premises. Firstly, the high-order terms in the direct tracking must have no influence on the dynamic aperture, because they are not represented in the Taylor map. This requirement has to be satisfied by any scheme that involves a truncated Taylor map. Secondly, the nonlinear kicks, which are determined such as to yield the correct low order terms, cause high-order nonlinearities, which likewise must not change the dynamic aperture. One might suspect that the second requirement is much more difficult to guarantee than the first one, in view of the fact that the Irwin scheme replaces an accelerator model containing very many, say 1000, multipole kicks by a new model with only 80 nonlinear kicks.

A seventh order six-dimensional Irwin factorization [1], consisting of 80 kicks (the minimum number is 48), is a factor of two faster than direct tracking for HERA. Therefore this is the highest order for which a six-dimensional kick factorization is useful concerning speed.

In Figure 2.7 the amplitude behavior close to the dynamic aperture in HERA was shown, that was obtained by tracking with truncated Taylor maps of various orders. Fig. 2.8 presents the result of the Irwin scheme for the same starting coordinates. The tracking is now perfectly symplectic, which is reflected by the constant average amplitude. However, the oscillation frequency perceptible in the running average amplitude as a function of turn number differs from the corresponding frequency in the direct tracking. The difference can be ascribed to the spurious high-order terms.

It is important to note here that a dependence on the longitudinal coordinate exists only in the accelerating sections, which are described by a single cavity in the model of HERA. Hence, if the tracking through this cavity is performed separately at the end of each turn, the number of independent variables can be reduced from six to five. This provides the possibility of a four-dimensional kick factorization with momentum-dependent coefficients [22], which hereafter is

[1] To avoid confusion the specified order always refers to the equivalent map and not to the order of the Lie generators, which is higher by one.

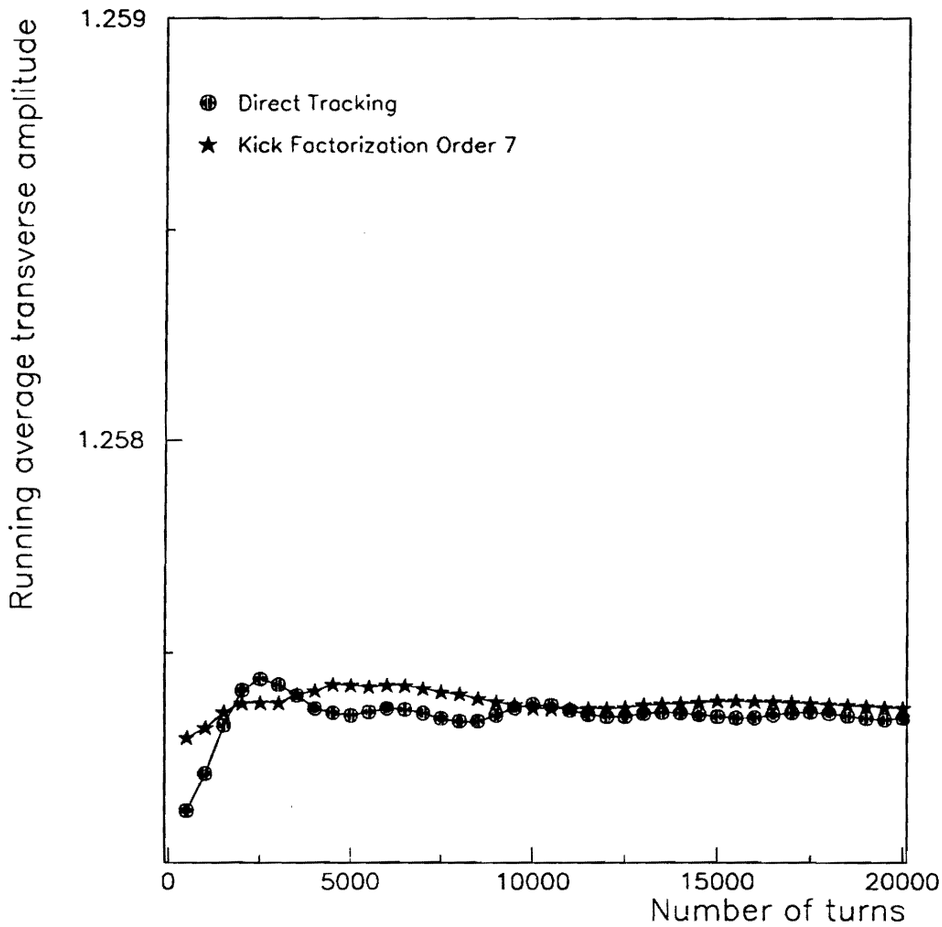

Figure 2.8: Evolution of the amplitude as a function of turn number N for an initial amplitude close to the dynamic aperture of HERA using a 7th order Irwin factorization. Shown is the running average amplitude $< a_{xz} >_N \equiv \frac{1}{N}\sum_{i=1}^{N} a_{xz}(i)$ in $\mathrm{mm}^{\frac{1}{2}} \cdot \mathrm{mrad}^{\frac{1}{2}}$, computed from the first N turns. This trajectory has the same initial coordinates as the one depicted in Fig. 2.7.

called (4+1)-dimensional. In analogy to (2.25) the k-th Irwin polynomial is written as

$$g_k = \sum_{l+m \leq n_o} \beta_k^{l,m}(\eta) x_k^l y_k^m, \tag{2.28}$$

where now the coefficients $\beta_k^{l,m}$ are of the form

$$\beta_k^{l,m}(\eta) = \beta_{k,0}^{l,m} + \beta_{k,1}^{l,m}\eta + \beta_{k,2}^{l,m}\eta^2 + \ldots \tag{2.29}$$

The $\beta_{k,i}^{l,m}$ are determined for each order of η exactly as in a 4-dimensional problem. The expansion in η need not necessarily be performed to the order n_o of the transverse factorization and may even change for different values of $(l+m)$ [22]. It can be expected that a cubic expansion in η is usually sufficient. Not included in the Irwin polynomials g_k such obtained is the purely η-dependent part, which affects only the transformation of σ. This term has to be extracted from the Taylor map directly.

The minimum number of kicks required by a 4-dimensional factorization of order $(n_o - 1)$ is

$$K = \left\{ \begin{array}{c} (n_o+2)^2/4 \\ (n_o+3)(n_o+1)/4 \end{array} \right\}, \text{ if } \left\{ \begin{array}{c} n_o/2 \\ (n_o+1)/2 \end{array} \right\} \text{is an integer.} \tag{2.30}$$

and thus only 49 kicks are needed for a (4+1)-dimensional kick factorization of 11th order as compared with 48 kicks for a full 6-dimensional factorization of 7th order. A significant reduction of computing time is therefore to be expected, but the (4+1)-dimensional kick factorization has not yet been implemented.

2.3.3 Reliability and Computing Time

Map tracking for HERA is reliable even for maps of order as low as seven. Analysis of the Lyapunov exponent over 20 000 turns yields the same onset of chaos for direct tracking and map tracking of orders 7, 9 and 11 without symplectification. If one considers the first 50 000 turns, the 7th order map starts to fail and predicts a dynamic aperture which is too low by about 10 %. As far as the short-term particle loss is concerned, a fairly large spread of values is observed with the different tracking schemes. This is not surprising, because at larger amplitudes the deviation between map tracking and direct tracking becomes stronger and nonlinear as a function of the turn number. The amplitude thresholds for the onset of chaos and for the short term particle loss predicted by Taylor maps of various order are summarized in Table 2.3.

Table 2.4 shows the computing time required to track 20 000 turns in HERA and indicates that the use of Taylor maps can increase the tracking speed by a factor 10–25. Included in the table is the possibility to treat the cavity separately at the end of each turn. This option, denoted by '6x5', increases the speed by about a factor of two for pure map tracking. In addition it permits the (4+1)-dimensional kick factorization discussed above. An estimate of the computing time for this refined factorization can be obtained by a simple scaling law. In first approximation the computing time is proportional to the number of kicks and to the number of monomials in each Irwin polynomial. The latter is $(n_{o4+1}+1)$ and $(n_{o6}+1)(n_{o6}+2)/2$ for the four- and for the six-dimensional factorization, respectively. Considering (2.27) and (2.30), we then expect [2]

$$\tau_{4+1}^{comp} \approx \frac{27}{2} \frac{(n_{o4+1}+2)^2}{(n_{o6}+3)^3} \frac{(n_{o4+1}+1)}{(n_{o6}+2)(n_{o6}+1)} \tau_6^{comp}, \tag{2.31}$$

[2]Note that (2.31) underestimates the actual computing time, because neither the transformation of σ nor the individual terms in $\beta_k^{l,m}(\eta)$, corresponding to different powers of η, are taken into account.

method	onset of chaos for 20 000 turns	onset of chaos for 50 000 turns	particle loss before 20 000 turns
Direct Tracking			2.22
11th Order Taylor Map		1.34	1.86
9th Order Taylor Map	1.34		1.86
7th Order Taylor Map		1.19	3.73
7th Order Kick Factorization		1.34	2.80

Table 2.3: Onset of chaos and 'short-term' particle loss predicted by the different tracking schemes for HERA; quoted are normalized amplitudes in units of $\mathrm{mm}^{\frac{1}{2}}\ \mathrm{mrad}^{\frac{1}{2}}$. The amplitude threshold of chaos is reproduced very accurately in all cases, except for the 7th order map tracking over 50 000 turns. A large spread of values is, however, observed for the amplitude, at which a particle loss occurs in less than 20 000 turns.

where τ^{comp} denotes the computing time and $(n_o - 1)$ the order of the equivalent map. According to this rule of thumb the (4+1)-dimensional scheme is faster than the 6-dimensional factorization by a factor 10 for 7th order and by a factor 18 for 11th order.

In view of Table 2.4, the kick factorization appears a promising alternative to pure map tracking. For studies of the LHC, a symplectification of the Taylor map is unavoidable and the Irwin scheme is even more attractive than for HERA [13, 15, 16].

An estimate of the dynamic aperture is provided by the Lyapunov-exponent method, which requires tracking over 10 000 or 20 000 turns (see section 2.2). Since the Lyapunov exponent of a trajectory in HERA can be obtained by a 7th order Taylor map, for this particular application the tracking speed can be increased by a factor 25.

The reduction of computing time for map tracking facilitates scans in parameter values and allows detailed studies on the effect of tune modulation. Two comments may help to clarify these possibilities:

Firstly, the effect of tune modulation due to a periodic ripple of the quadrupole strengths could, in principle, be simulated by using several Taylor maps in the map tracking, where each map were calculated for a slightly different strength of the quadrupole magnets. Fortunately, direct tracking studies suggest (compare also section 5.2) that tune modulation can be added in a much easier way, namely as a linear rotation with varying angle applied after each turn. This procedure permits a simple inclusion of tune modulation in the case of map tracking.

Secondly, a parameter-dependence can already be included while extracting the map [12], so that the Taylor map does not only depend on the phase space coordinates but also on a set of parameters, for instance on the strength of a correction magnet. An alternative method to consider tune modulation is, therefore, to define the focusing strength of a quadrupole family as a parameter of the Taylor map.

The important conclusion is that only a single map is needed for most applications.

method	computing time
Direct Tracking	**520 s**
11th Order Taylor Map	300 s
11th Order Taylor Map 6x5	150 s
9th Order Taylor Map	120 s
9th Order Taylor Map 6x5	60 s
7th Order Taylor Map	44 s
7th Order Taylor Map 6x5	**22 s**
11th Order (4+1)-dim. Kick Factorization	$\sim$ 90 s
7th Order 6-dim. Kick Factorization	300 s
7th Order (4+1)-dim. Kick Factorization	$\sim$ 30 s

Table 2.4: Comparison of the computing time required by different tracking schemes to simulate six-dimensional particle motion over 20 000 turns in HERA. The speed of the (4+1)-dimensional kick factorization is estimated by (2.31). All values refer to the IBM ES 9000/900 at CERN.

Chapter 3

Tune Modulation

3.1 Introduction

The inclusion of tune modulation in tracking simulations of HERA can lead to a large reduction of the dynamic aperture (see also chapter 5). A typical emittance evolution of a chaotic trajectory in the presence of tune modulation is shown in Fig. 3.1. Clearly visible are step-like changes of the emittance, which occur in intervals corresponding to the modulation period. It should be noted that this trajectory lies inside a region where the motion is regular in the absence of tune modulation.

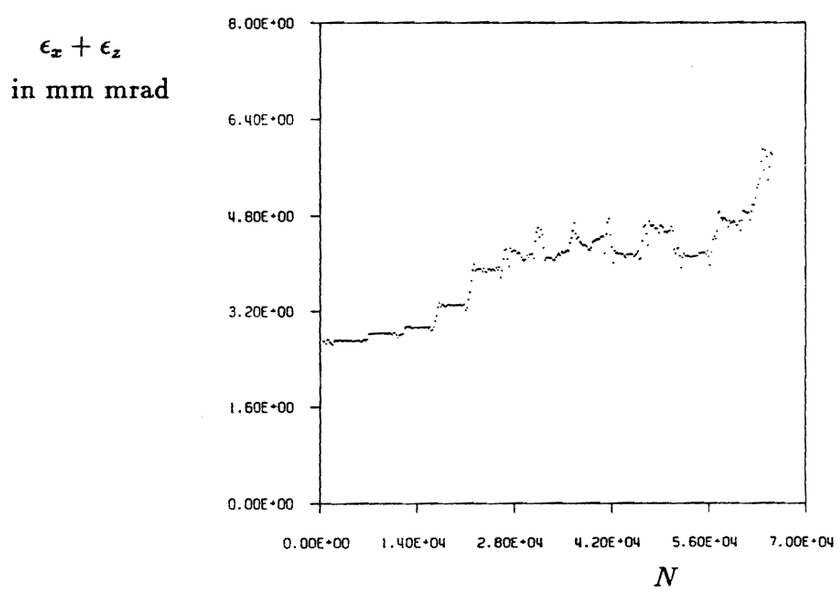

Figure 3.1: Transverse emittance $\epsilon_x + \epsilon_z$ for 70 000 revolutions in HERA at a starting amplitude of 11.0 mm ($\beta = 76$ m). Each dot represents the maximum value during 200 turns. The step-like changes coincide with the tune modulation period of 5 000 turns, which corresponds to a frequency of 10 Hz. The modulation amplitude is $q_x = q_z = 0.001$.

In the following a theory of tune modulation is developed which applies to dynamic aperture problems as well as to the beam-beam interaction. There are many origins of tune modulation in a storage ring:

- Synchrotron oscillations together with a nonzero chromaticity. The design synchrotron frequency for HERA is 14 Hz at injection and 78 Hz under luminosity conditions.
- Power supply ripple at multiples of 50 Hz.
- Standing waves in the main superconducting magnet circuit. The fundamental mode has a frequency of about 15.6 Hz [34]. It has been conjectured that such waves might be excited during the acceleration.
- Ground waves and mechanical vibrations of the magnets. Typical frequencies are between 2 and 20 Hz.

The expected tune modulation amplitudes can almost reach the same order of magnitude as the proton beam-beam tune shift and therefore their impact on the beam stability should be understood. The above list may suffice to motivate the detailed theoretical study in the next sections.

3.2 Single Resonance

As a starting point some basic quantities for a nonlinear Hamiltonian system in the absence of tune modulation are defined. If the motion is dominated by a single resonance

$$nQ - p \approx 0$$

the Hamiltonian for one degree of freedom is approximately given by

$$H(I, \phi, \theta) = IQ_0 + g(I) + h(I)\cos(n\phi - p\theta), \tag{3.1}$$

where $g(I)$ and $h(I)$ denote in general nonlinear functions of the action I, which are called detuning and driving term, respectively. Of importance for HERA is the case of several isolated weak resonances, for which $g(I) \gg h(I)$. From (3.1), the amplitude-dependent tune is [1]

$$Q(I) = Q_0 + \frac{dg}{dI}(I) \approx \phi'. \tag{3.2}$$

The resonance condition is fulfilled at a certain action value I_r defined by $nQ(I_r) = p$. If equation (3.1) is expanded around the resonant value I_r, a further approximation is possible, which reads

$$K(\Delta, \tilde{\phi}) = \frac{1}{2}\left(\frac{d^2g}{dI^2}(I_r)\right)\Delta^2 + h(I_r)\cos n\tilde{\phi}, \tag{3.3}$$

where the new momentum and phase variables are defined by

$$\Delta \equiv I - I_r, \tilde{\phi} \equiv \phi - \frac{p}{n}\theta.$$

Equation (3.3) is recognized as the Hamiltonian of a nonlinear pendulum. The total width of the pendulum separatrix is given by

$$\Delta I_{\text{tot}} = 2\Delta_{\text{max}} = 4\sqrt{\left|\frac{h(I_r)}{\frac{d^2g}{dI^2}(I_r)}\right|}. \tag{3.4}$$

[1] A prime denotes the derivative with respect to theta.

For small oscillations around $\bar{\phi}_r = \pi/n$, (3.3) can be expanded up to quadratic terms, $\cos n\bar{\phi} \approx -1+\frac{1}{2}n^2(\bar{\phi}-\bar{\phi}_r)^2$. This yields the frequency at which particles inside a resonance island oscillate around the elliptic fixed point,

$$Q_I = n\sqrt{\left|h(I_r)\frac{d^2g}{dI^2}(I_r)\right|}. \tag{3.5}$$

The frequency Q_I is called the 'island tune' [36].

3.3 Single Resonance with Modulation

In the presence of tune modulation the Hamiltonian assumes the form

$$H(I,\phi,\theta) = IQ_0 + g(I) + h(I)\cos\left(n\phi + \frac{nq}{Q_m}\sin(Q_m\theta+\alpha) - p\theta\right), \tag{3.6}$$

where q is the modulation amplitude, Q_m the modulation frequency and α an arbitrary phase. Equation (3.6) differs from the Hamiltonian (3.1) only by the additional term $\frac{nq}{Q_m}\sin(Q_m\theta+\alpha)$ in the argument of the cosine. The contribution of the tune modulation to the total Hamiltonian becomes more explicit by means of a canonical transformation from I,ϕ to $\bar{I},\bar{\phi}$ with the generating function

$$F_2(\bar{I},\phi) = \bar{I}\phi + \frac{q}{Q_m}\sin(Q_m\theta+\alpha)\bar{I}. \tag{3.7}$$

The transformation is

$$\bar{\phi} = \frac{\partial F_2}{\partial \bar{I}} = \phi + \frac{q}{Q_m}\sin(Q_m\theta+\alpha) \tag{3.8}$$

$$I = \frac{\partial F_2}{\partial \phi} = \bar{I} \tag{3.9}$$

and the new Hamiltonian reads (compare also [36])

$$\bar{H} = H + \frac{\partial F_2}{\partial \theta} = Q_0\bar{I} + g(\bar{I}) + h(\bar{I})\cos(n\bar{\phi} - p\theta) + q\cos(Q_m\theta+\alpha)\bar{I}. \tag{3.10}$$

The last term describes the tune modulation. For this Hamiltonian we have

$$\bar{\phi}' = \frac{\partial\bar{\phi}}{\partial\theta} = \frac{\partial\bar{H}}{\partial\bar{I}} \approx Q_0 + \frac{\partial g}{\partial\bar{I}}(\bar{I}) + q\cos(Q_m\theta+\alpha). \tag{3.11}$$

Transforming again to the nonlinear pendulum variables

$$\bar{\Delta} = \bar{I} - \bar{I}_r, \bar{\bar{\phi}} = \bar{\phi} - \frac{p}{n}\theta$$

one obtains

$$\bar{K}(\bar{\Delta},\bar{\bar{\phi}},\theta) = \frac{1}{2}\frac{d^2g}{d\bar{I}^2}(\bar{I}_r)\bar{\Delta}^2 + h(\bar{I}_r)\cos n\bar{\bar{\phi}} + q\cos(Q_m\theta+\alpha)\bar{\Delta}, \tag{3.12}$$

which is the same as equation (3.3) plus an additional term that is linear in $\bar{\Delta}$.

3.4 Island Width of Sidebands

Equation (3.6) can be expanded into Bessel functions using the Jacobi-Anger identity [36, 37] (see appendix C)

$$\cos\left(n\phi + \frac{nq}{Q_m}\sin(Q_m\theta + \alpha) - p\theta\right) = \sum_{j=-\infty}^{\infty} J_j\left(\frac{nq}{Q_m}\right)\cos(n\phi + jQ_m\theta - p\theta + j\alpha). \tag{3.13}$$

Inserting this expansion into (3.6) we get the generalized resonance condition in the presence of tune modulation

$$nQ(I_r^j) + jQ_m - p = 0 \tag{3.14}$$

For each fundamental resonance $nQ - p = 0$ a set of sideband resonances with $j \neq 0$ is generated. From

$$Q(I_r^j) = Q_0 + \frac{dg}{dI}(I_r^j) = \frac{p}{n} - \frac{j}{n}Q_m \tag{3.15}$$

and

$$\frac{dg}{dI}(I_r^j) \approx \frac{dg}{dI}(I_r) + \frac{d^2g}{dI^2}(I_r)\cdot j\delta I,$$

the distance δI between two sideband resonances is

$$\delta I \approx \frac{Q_m}{n\frac{d^2g}{dI^2}(I_r)}. \tag{3.16}$$

The width of the sideband separatrices is obtained by replacing $h(I_r)$ by $h(I_r)J_j(\frac{nq}{Q_m})$ in the formula for the non-modulated case (3.4)

$$\Delta I_{\text{tot}}^j = 4\sqrt{\left|\frac{h(I_r)J_j(\frac{nq}{Q_m})}{\frac{d^2g}{dI^2}(I_r)}\right|} \tag{3.17}$$

3.5 Chaotic Region and Diffusion Rate

As a rule of thumb the Bessel function in (3.17) can have a significant value only, if its argument is larger than the order, i. e. if

$$\frac{nq}{Q_m} > j \tag{3.18}$$

In that case the Bessel functions may be approximated by their rms values for large arguments [38]

$$J_j(x) \approx \frac{1}{\sqrt{\pi x}}. \tag{3.19}$$

From (3.17) we then get (with Q_I as defined in (3.5))

$$\Delta I_{\text{tot}}^j \approx 4\frac{Q_I}{n}\left(\frac{Q_m}{qn\pi}\right)^{\frac{1}{4}}\frac{1}{\frac{d^2g}{dI^2}(I_r)}. \tag{3.20}$$

Following [39] we expect global chaos, if the distance between two sidebands δI (3.16) is smaller than the width of the resonances ΔI_{tot}^j, i. e. if

$$\frac{Q_m}{n\frac{d^2g}{dI^2}(I_r)} < 4\frac{Q_I}{n}\left(\frac{Q_m}{qn\pi}\right)^{\frac{1}{4}}\frac{1}{\frac{d^2g}{dI^2}(I_r)}. \tag{3.21}$$

Therefore the condition for chaos becomes [36]

$$\boxed{\frac{Q_m^{\frac{3}{4}}(nq)^{\frac{1}{4}}}{Q_I} \leq \frac{4}{\pi^{\frac{1}{4}}}} \tag{3.22}$$

Note that (3.18) has been assumed in deriving (3.22). Fig. 3.2 a) and b) illustrate the validity of (3.18) and (3.19). For the two modulation frequencies $Q_m = 0.04$ and $Q_m = 0.1$ the location of the sideband resonances is depicted as a function of the modulation amplitude q. The chosen resonance parameters $n = 4$, $\frac{d^2g}{dI^2}(I_r) = 1$ and $Q_I = 4\sqrt{h(I_r)} = 0.049$ refer to the phase diagram shown in Fig. 3.4.

In Fig. 3.2, the island sizes ΔI^j_{tot} are computed by the exact expression (3.17). Action values in the hatched area lie inside of some resonance island, whereas action values in the white regions are outside of any island. Hence, if there is no white space between two sidebands, these do overlap. The centers of the sidebands are separated by $\delta I = Q_m/4$. They are closer and resonance overlap is, therefore, more probable for the smaller modulation frequency Q_m, in Fig. 3.2 a). The curves drawn in both figures represent equation (3.18), which appears a good approximation to the number of sizable sidebands. As expected, this number grows about linearly with the modulation amplitude q.

The overlap criterion (3.22) predicts a threshold of resonance overlap at modulation amplitudes $q \approx 1.8$ or $q \approx 0.12$ for the modulation frequencies of Fig. 3.2 a) and b), respectively. For larger modulation amplitudes no sideband overlap is expected, since the island size shrinks as a function of q, which is described by (3.17) and (3.19). Fig. 3.2 a) shows that the sideband resonances overlap at least up to the modulation amplitude $q = 1$, in agreement with (3.22). In Fig. 3.2 b), the resonances become separated beyond about $q \approx 0.1 - 0.15$. This value is consistent with the prediction of (3.22), indicated by a straight vertical line, and thus corroborates (3.19).

If the inequalities (3.18) and (3.22) are fulfilled, we are in the chaotic region. Here an estimate of the 'diffusion' speed can be obtained in the following manner [40, 41]. Starting from the unperturbed Hamiltonian

$$H(I, \phi, \theta) = IQ_0 + g(I) + h(I)\cos(n\phi - p\theta)$$

and the corresponding equation of motion for the action

$$\frac{dI}{d\theta} = -\frac{\partial H}{\partial \phi} = nh(I)\sin(n\phi - p\theta) \tag{3.23}$$

we derive the increase in action (or emittance $\epsilon \equiv 2I$) during a single crossing of the fundamental resonance. Integration of equation (3.23) yields

$$\int_{I_1}^{I_2} \frac{dI}{h(I)} = \int_{\theta_1}^{\theta_2} n\sin(n\phi - p\theta)d\theta. \tag{3.24}$$

The integral on the right hand side can be calculated as demonstrated in [42]. The main contribution comes from the neighborhood of the 'stationary phase' ϕ_0 [2], where

$$\frac{\partial}{\partial\theta}(n\phi - p\theta)\Big|_{\phi=\phi_0,\,\theta=\theta_0} = 0. \tag{3.25}$$

[2]The 'method of stationary phase' is described for example in [43].

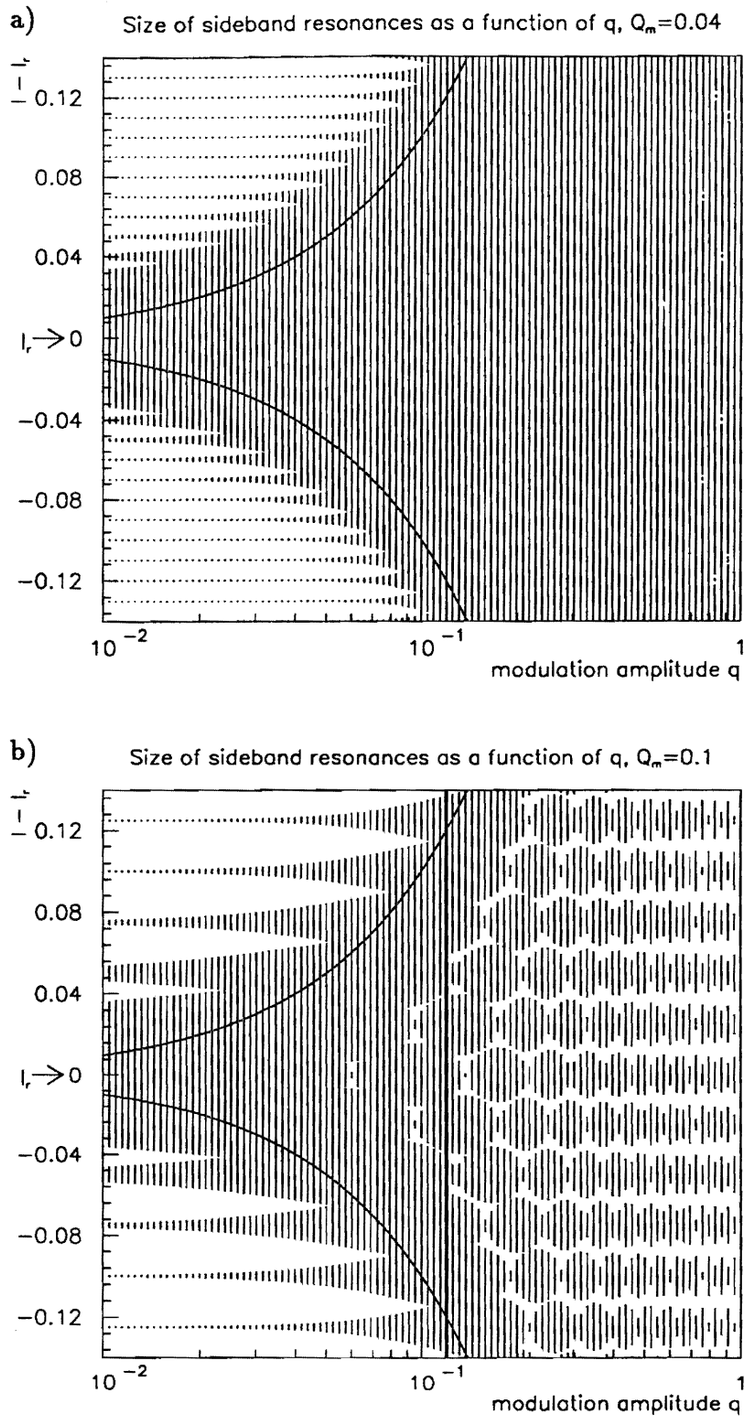

Figure 3.2: Location of the sideband islands with respect to the fundamental resonance as a function of the modulation amplitude q. The island sizes ΔI^j_{tot} are derived from (3.17) for the resonance parameters $n = 4$, $d^2g/dI^2(I_r) = 1$ and $Q_I = 4\sqrt{h(I_r)} = 0.049$. (The corresponding phase diagram is shown in Fig. 3.4.) Action values in the hatched area are inside of some resonance island. Two sideband resonances overlap, if they are not separated by a white region. The two diagrams refer to different modulation frequencies: a) $Q_m = 0.04$, b) $Q_m = 0.1$. According to (3.22), resonance overlap is expected only for modulation amplitudes $q < 1.8$ or $q < 0.12$ in case a) and b), respectively. In b), this limit is depicted by the straight vertical line. The solid curves represent (3.18), which approximates the number of sizable sidebands.

A second order Taylor expansion around the phase ϕ_0

$$\phi \approx \phi_0 + \frac{1}{2}\frac{\partial \phi}{\partial \theta^2}\bigg|_{\theta_0} (\theta - \theta_0)^2 \equiv \phi_0 + \frac{1}{2}\phi_0''(\theta - \theta_0)^2 \tag{3.26}$$

leads to

$$\int_{\theta_1}^{\theta_2} \sin(n\phi - p\theta)d\theta \approx \sin n\psi_0 \int_{\theta_1}^{\theta_2} \cos\left\{\frac{n\phi_0''}{2}(\theta - \theta_0)^2\right\} d\theta + \cos n\psi_0 \int_{\theta_1}^{\theta_2} \sin\left\{\frac{n\phi_0''}{2}(\theta - \theta_0)^2\right\} d\theta\,, \tag{3.27}$$

where, for brevity, a new phase variable $\psi_0 \equiv \phi_0 - \theta_0 p/n$ has been introduced. The remaining integrals are Fresnel integrals and can be solved. Assuming that the intervals $|\theta_1 - \theta_0|$ and $|\theta_2 - \theta_0|$ are sufficiently large [42], the maximum value (as a function of ψ_0) of the integral (3.27) is given by

$$\sqrt{\frac{2\pi}{n|\phi_0''|}} \tag{3.28}$$

and its average absolute value is

$$\sqrt{\frac{8}{\pi n|\phi_0''|}}. \tag{3.29}$$

The average value will be used in our further discussion. Returning to (3.24) we find

$$\Delta I_{\text{single}} \equiv |I_2 - I_1| \approx nh(I_r) \cdot \sqrt{\frac{8}{\pi n|\phi_0''|}}, \tag{3.30}$$

under the assumption $h(I) \approx h(I_r) =$ constant. We now remember that the motion is assumed to be chaotic. Thus the phase correlation is lost between subsequent resonance crossings and the action increase can be described by a random walk process. Then the mean square uncertainty in the action after N resonance crossings grows as

$$\overline{(\Delta I)^2} = N(\Delta I_{\text{single}})^2. \tag{3.31}$$

Taking into account the tune modulation, the modulus of the second derivative of the phase is replaced by its average value

$$|\phi_0''| \approx \frac{2}{\pi} q Q_m. \tag{3.32}$$

Since the number of resonance crossings after a time Δt is

$$N = 2Q_m f_{rev} \Delta t \tag{3.33}$$

(two crossings per modulation period), we obtain

$$\boxed{\frac{\overline{(\Delta\epsilon)^2}}{\Delta t} = 32\frac{f_{rev} n h^2(I_r)}{q},} \tag{3.34}$$

where $\epsilon \equiv 2I$ denotes the single-particle emittance. The diffusion coefficient $D \equiv \frac{1}{2}\overline{(\Delta\epsilon)^2}/(\Delta t)$ is inversely proportional to the modulation amplitude q and independent of the modulation frequency Q_m.

3.6 Diffusion Rate for a Two-Dimensional Map

To examine the validity of (3.34) a numerical simulation is performed for a two-dimensional map consisting of a rotation

$$\begin{pmatrix} x \\ p \end{pmatrix}_f = \begin{pmatrix} \cos 2\pi Q & \sin 2\pi Q \\ -\sin 2\pi Q & \cos 2\pi Q \end{pmatrix} \begin{pmatrix} x \\ p \end{pmatrix}_i, \tag{3.35}$$

where Q depends on the amplitude in the form

$$Q = Q_0 + \frac{\alpha}{4}(x_i^2 + p_i^2)^2, \tag{3.36}$$

and an octupolar kick

$$p_f = p_i - x_i^3 \tag{3.37}$$

The corresponding Hamiltonian is

$$H = \left(Q_0 - \frac{1}{4}\right) I + \frac{\alpha}{3} I^3 + \frac{1}{16\pi} I^2 \cos 4\phi + \frac{3}{16\pi} I^2 + \frac{4}{16\pi} I^2 \cos 2\phi, \tag{3.38}$$

with the usual definition of I and ϕ

$$x = \sqrt{2I}\cos\phi \quad \text{and} \quad p = -\sqrt{2I}\sin\phi. \tag{3.39}$$

If the tune is close to the resonance $4Q \approx 1$ and if, furthermore, $\alpha \gg 1$, the last two terms in the Hamiltonian may be disregarded and the driving term of the fourth integer resonance

$$h(I) = \frac{1}{16\pi} I^2 \tag{3.40}$$

is much smaller than the detuning function

$$g(I) = \frac{\alpha}{3} I^3. \tag{3.41}$$

The case $h(I) \ll g(I)$ is typical for a storage ring, where one stays away from strong low-order resonances. Note that the absolute value of detuning and driving terms can be changed by a scale transformation. Let us choose $Q_0 = 0.23$ and $\alpha = 1000$. The condition $\partial H/\partial I = 0$ then leads to the resonant action value

$$I_r \approx \sqrt{\frac{1}{\alpha}\left(\frac{1}{4} - Q_0\right)} \approx 4.5 \cdot 10^{-3} \tag{3.42}$$

and the elliptic fixed points are located at

$$x_r = p_r = \sqrt{I_r} \approx 6.7 \cdot 10^{-2}. \tag{3.43}$$

The island tune (3.5) is

$$Q_I = 4\sqrt{\frac{2\alpha I_r^3}{16\pi}} \approx 7.6 \cdot 10^{-3}. \tag{3.44}$$

An additional tune modulation with amplitude $q \approx 0.1$ and frequency $Q_m \approx 6.25 \cdot 10^{-3}$, not too far from the island tune, destroys the resonance island chain and gives rise to global chaos in agreement with (3.22). An ensemble of 200 particles is placed inside the chaotic region with a tiny initial spread in position of 10^{-7}. The evolution of the rms-emittance-spread of this ensemble is shown in Fig. 3.3 as a function of the turn number for two different modulation amplitudes. After a transient period of about 2000 turns, in which the initially very close particles lose their phase correlation, the evolution is well described by (3.34). In particular, it is verified that the diffusion rate is inversely proportional to the modulation amplitude q.

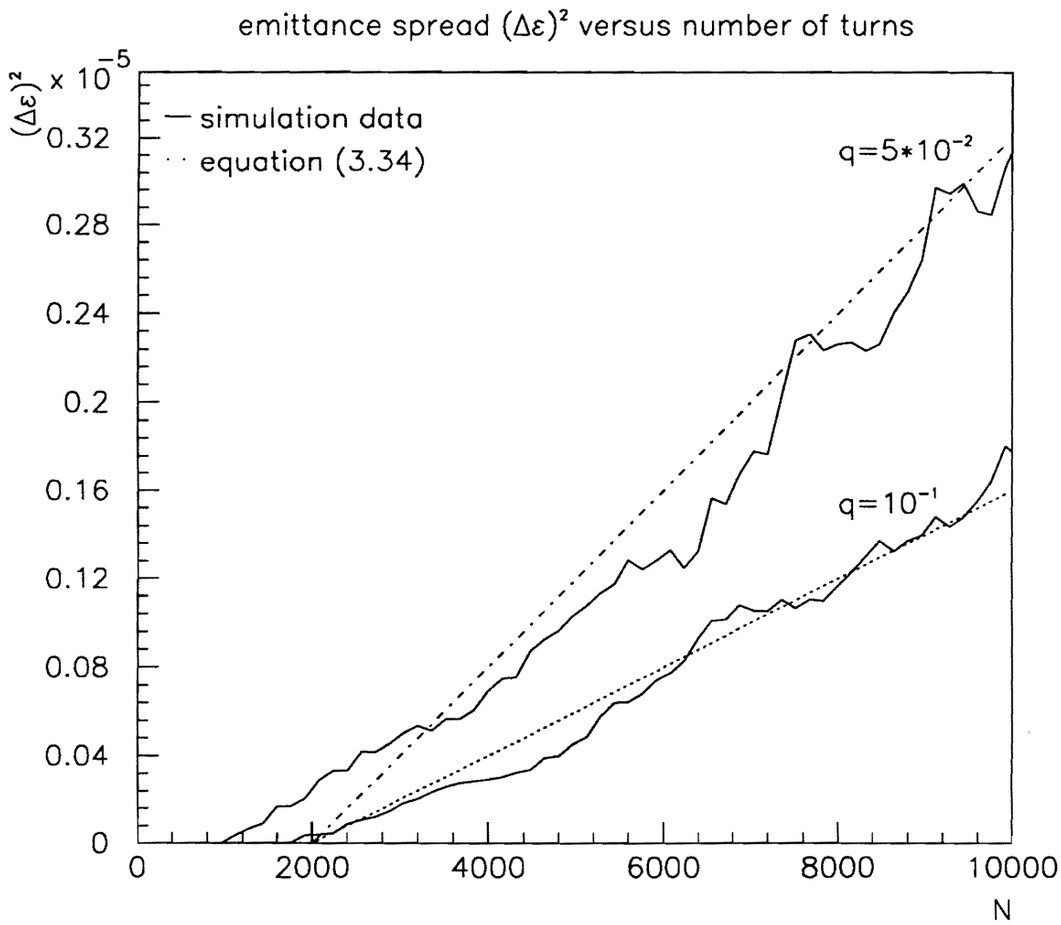

Figure 3.3: Emittance spread for 200 chaotic trajectories of the two-dimensional map (3.35)–(3.37) as a function of the number of turns.

3.7 Adiabatic Trapping

If the modulation frequency Q_m is held constant, equation (3.22) determines a maximum value of the modulation amplitude q below which the motion is chaotic. Here and in the next section, a complementary mimimum value of the modulation amplitude q is derived and justified.

For a constant tune the position of the resonance islands is uniquely determined. If a tune modulation is added, however, the resonance islands change their location in phase space with the periodicity of the modulation cycle. Provided that the frequency of the tune modulation is sufficiently small, particles initially close to the center of the islands move with the islands, returning to the vicinity of their initial position once every modulation period. In this case the tune modulation is called adiabatic [44].

The adiabatic boundary can be derived from the intuitive condition [40, 41]

$$\left\{\begin{array}{c}\text{action change rate}\\ \text{of island center due to}\\ \text{the slow tune variation}\end{array}\right\} < \left\{\begin{array}{c}\text{action change rate}\\ \text{caused by the motion}\\ \text{around the resonance}\end{array}\right\} \tag{3.45}$$

The maximum change rate of the action value for the island center is obtained from the action-dependence of the tune in the following way

$$\phi_r' \approx Q_0 + \frac{dg}{dI}(I_r) \tag{3.46}$$

$$\phi_r'' \approx \frac{d^2g}{dI^2}(I_r)\frac{dI_r}{d\theta}. \tag{3.47}$$

$$\left.\frac{dI_r}{d\theta}\right|_{\max} = \frac{|\phi_r''|_{\max}}{\left|\frac{d^2g}{dI^2}(I_r)\right|} = \frac{qQ_m}{\left|\frac{d^2g}{dI^2}(I_r)\right|} \tag{3.48}$$

According to (3.10) the action change during the motion around the resonance center is

$$\frac{dI}{d\theta} = h(I_r)n\sin(n\bar{\phi} - p\theta) \approx h(I_r)\cdot n \tag{3.49}$$

(here it has been assumed $\sin(n\bar{\phi}-p\theta) \approx 1$, for a trajectory half-way between stable and unstable fixed points). By means of equations (3.45), (3.48) and (3.49) the adiabaticity condition reads

$$qQ_m < \frac{d^2g}{dI^2}(I_r)\cdot h(I_r)\cdot n,$$

or, using the island tune (3.5),

$$\left|\frac{qQ_m}{Q_I^2}\right| < \frac{1}{n}. \tag{3.50}$$

It should be mentioned that equation (3.50) agrees with the condition, that the fixed point of the 0th sideband becomes unstable in the limit of small modulation frequency [36].

3.8 Small Angle Approximation

For small oscillations around the stable fixed points the $\cos n\phi$-term in (3.12) can be expanded and the Hamiltonian is approximated as follows [3] [36]

$$K(\Delta,\phi) = \frac{1}{2}\frac{d^2g}{dI^2}(I_r)\Delta^2 + h(I_r)\frac{1}{2}(n\phi)^2 + q\cos(Q_m\theta + \alpha)\bar{\Delta}. \tag{3.51}$$

[3] For convenience, the definition of the phase ϕ is changed by π/n and the superscripts of (3.12) are dropped.

In this approximation the nonlinear pendulum of equation (3.3) has been replaced by a harmonic oscillator. From (3.51) we have the equations of motion

$$\dot{\Delta} = -hn^2\phi \qquad \text{and} \qquad \dot{\phi} = \frac{d^2g}{dI^2}\Delta + q\cos(Q_m\theta + \alpha).$$

$$\text{So} \qquad \ddot{\Delta} + Q_I^2\Delta = -\frac{qQ_I^2}{\frac{d^2g}{dI^2}}\cos(Q_m\theta + \alpha). \tag{3.52}$$

This is the equation of a driven harmonic oscillator. An analogous equation is satisfied by ϕ

$$\ddot{\phi} + Q_I^2\phi = -qQ_m\sin(Q_m\theta + \alpha). \tag{3.53}$$

A special solution is

$$\phi = -\frac{Q_m^2}{Q_I^2 - Q_m^2}\frac{q}{Q_m}\sin(Q_m\theta + \alpha) \tag{3.54}$$

and

$$\Delta = -\frac{Q_I^2}{Q_I^2 - Q_m^2}\frac{q}{\frac{d^2g}{dI^2}}\cos(Q_m\theta + \alpha). \tag{3.55}$$

The prerequisite for this approximation has been given in [36] as

$$\boxed{\left|\frac{qQ_m}{Q_I^2 - Q_m^2}\right| < \frac{1}{n}.} \tag{3.56}$$

This can be obtained from (3.54), if one requires

$$n\phi \ll 1,$$

on which the quadratic expansion of the cosine in (3.12) was based.

Equation (3.56) has a different physical interpretation in the high and in the low frequency limit. For small modulation frequencies Q_m, (3.56) becomes identical to (3.50), which represents the adiabatic boundary. In the limit of large modulation frequencies, (3.56) approaches (3.18) for $j = 1$, which specifies the border where the first sideband resonance starts to be important.

3.9 Two Degrees of Freedom

The theory of tune modulation outlined above suits also the more general situation of resonances for two degrees of freedom, if the appropriate replacements are made in the previous formulae. The Hamiltonian

$$H(I_x, I_z, \phi_x, \phi_z, \theta) = I_xQ_{x0} + I_zQ_{z0} + g(I_x, I_z) + h(I_x, I_z)\cos(k\phi_x + l\phi_z - p\theta). \tag{3.57}$$

describes the effect of a single resonance $kQ_x + lQ_z - p \approx 0$. By means of the generating function

$$F(\bar{I}_x, \bar{I}_z, \phi_x, \phi_z, \theta) = (k\phi_x + l\phi_z - p\theta)\bar{I}_x + \phi_z\bar{I}_z \tag{3.58}$$

new canonical variables $\bar{\phi}_x, \bar{\phi}_z, \bar{I}_x, \bar{I}_z$ are introduced according to

$$\bar{\phi}_x = \frac{\partial F}{\partial \bar{I}_x} = k\phi_x + l\phi_z - p\theta \quad , \quad \bar{\phi}_z = \frac{\partial F}{\partial \bar{I}_z} = \phi_z \tag{3.59}$$

$$I_x = \frac{\partial F}{\partial \phi_x} = k\bar{I}_x \quad , \quad I_z = \frac{\partial F}{\partial \phi_z} = l\bar{I}_x + \bar{I}_z \tag{3.60}$$

and the transformed Hamiltonian $\bar{H}$ reads

$$\bar{H}(\bar{I}_x, \bar{I}_z, \bar{\phi}_x) = (kQ_{x0} + lQ_{z0} - p)\bar{I}_x + \bar{I}_z Q_{z0} + \bar{g}(\bar{I}_x, \bar{I}_z) + \bar{h}(\bar{I}_x, \bar{I}_z)\cos(\bar{\phi}_x). \tag{3.61}$$

The barred functions $\bar{g}$ and $\bar{h}$ are related to the old ones by

$$\bar{g}(\bar{I}_x, \bar{I}_z) \equiv g(k\bar{I}_x, l\bar{I}_x + \bar{I}_z) = g(I_x, I_z) \tag{3.62}$$

$$\bar{h}(\bar{I}_x, \bar{I}_z) \equiv h(k\bar{I}_x, l\bar{I}_x + \bar{I}_z) = h(I_x, I_z). \tag{3.63}$$

The new Hamiltonian virtually describes a system of one degree of freedom, because the action $\bar{I}_z$ is an invariant of the motion. The $\bar{I}_z$-$\bar{\phi}_z$-plane will, therefore, be disregarded in our further discussion. In the remaining $\bar{I}_x$-$\bar{\phi}_x$-plane the motion close to the resonance is approximated by a nonlinear pendulum similar to (3.3),

$$\bar{K}(\bar{\Delta}, \bar{\phi}) = \frac{1}{2}\frac{d^2\bar{g}}{d\bar{I}_x^2}(\bar{I}_{x,r}, \bar{I}_{z,r})\bar{\Delta}_x^2 + \bar{h}(\bar{I}_{x,r}, \bar{I}_{z,r})\cos\bar{\phi}_x, \tag{3.64}$$

where we have defined the new momentum $\bar{\Delta}_x$ as the deviation from the resonant value,

$$\bar{\Delta}_x = \bar{I}_x - \bar{I}_{x,r}. \tag{3.65}$$

This pendulum equation is almost the same as that derived by a different approach in [45]. According to equation (3.5) the island tune of a resonance for two degrees of freedom is given by

$$\begin{aligned} Q_{I,2d} &= \sqrt{\frac{\partial^2\bar{g}(\bar{I}_x, \bar{I}_z)}{\partial \bar{I}_x^2}\bar{h}(\bar{I}_x, \bar{I}_z)} \\ &= \sqrt{\left[k^2\frac{\partial^2 g(I_{x,r}, I_{z,r})}{\partial I_x^2} + 2kl\frac{\partial^2 g(I_{x,r}, I_{z,r})}{\partial I_x I_z} + l^2\frac{\partial^2 g(I_{x,r}, I_{z,r})}{\partial I_z^2}\right] h(I_{x,r}, I_{z,r})}, \end{aligned} \tag{3.66}$$

where use has been made of (3.62) and (3.63) to convert the expression to the original variables.

As usual the total width of the resonance island is deduced from the pendulum Hamiltonian (see also (3.4))

$$\Delta\bar{I}_{x,\mathrm{tot}} = 2\bar{\Delta}_{x,max} = 4\sqrt{\left|\frac{\bar{h}(\bar{I}_{x,r}, \bar{I}_{z,r})}{\frac{\partial^2\bar{g}}{\partial \bar{I}_{x,r}^2}(\bar{I}_{x,r}, \bar{I}_{z,r})}\right|} \tag{3.67}$$

The translation into the original action space with the help of the transformation (3.60) gives

$$\Delta I_{\mathrm{tot}} = \sqrt{\Delta I_x^2 + \Delta I_z^2} = \sqrt{l^2 + k^2}\,\Delta\bar{I}_{x,\mathrm{tot}}. \tag{3.68}$$

Hence the total island width for two degrees of freedom is

$$\boxed{\Delta I_{\text{tot}} = \frac{4Q_{I,2d}\sqrt{l^2+k^2}}{|l^2\frac{\partial^2 g}{\partial I_z^2} + 2kl\frac{\partial^2 g}{\partial I_x \partial I_z} + k^2\frac{\partial^2 g}{\partial I_x^2}|}} \tag{3.69}$$

Tune modulation is introduced in analogy to (3.10). An additional term linear in $I_{x,z}$ is added to the single-resonance Hamiltonian (3.57), yielding

$$\begin{aligned} H(I_x, I_z, \phi_x, \phi_z, \theta) &= I_x Q_{x0} + I_z Q_{z0} + g(I_x, I_z) + h(I_x, I_z)\cos(k\phi_x + l\phi_z - p\theta) + \\ &\quad + q(I_x + I_z)\cos(Q_m\theta + \alpha), \end{aligned} \tag{3.70}$$

where we have assumed, for simplicity, that both tunes are modulated with the same frequency Q_m and amplitude q. Performing the same canonical transformation as above the pendulum approximation leads to (compare (3.12))

$$\bar{K}(\bar{\Delta}, \bar{\bar{\phi}}, \theta) = \frac{1}{2}\frac{d^2\bar{g}}{d\bar{I}_x^2}(\bar{I}_{x,r}, \bar{I}_{z,r})\bar{\Delta}_x^2 + h(\bar{I}_{x,r}, \bar{I}_{z,r})\cos\bar{\phi}_x + q\bar{\Delta}_x(k+l)\cos(Q_m\theta + \alpha). \tag{3.71}$$

Under our assumption that both tunes are modulated with the same frequency Q_m and amplitude q, equations (3.18),(3.22),(3.56) and (3.50) are still valid, if one uses the general island tune (3.66) and if one replaces n by $k+l$. The latter substitution indicates that difference resonances are less affected by the tune modulation than sum resonances.

The mean emittance growth in the chaotic region close to a single resonance has been calculated for one degree of freedom in section 3.5 (3.34). It can easily be generalized to two degrees of freedom, and reads then

$$\frac{\overline{(\Delta(\epsilon_x + \epsilon_z))^2}}{\Delta t} = 32\frac{f_{rev}(k+l)h^2(I_{x,r}, I_{z,r})}{q}. \tag{3.72}$$

Again we find that only the substitution $n \to k+l$ is required to generalize the result for one degree of freedom.

3.10 Width of the Stochastic Layer

The effect of tune modulation as a function of resonance order, island tune, modulation amplitude and modulation frequency can be estimated in an alternative way. The basic procedure, developed in [39], is to construct a discrete mapping for the motion near the separatrix. The threshold of chaos for this map yields the width of the stochastic layer, which is a quantitative measure of the chaotic part of the phase space close to a resonance. Our starting point is a Hamiltonian of the form (3.71)

$$H(\Delta, \phi, \theta) = \frac{1}{2}\frac{d^2 g}{dI^2}\Delta^2 - h\cos\phi + q(k+l)\Delta\cos(Q_m\theta + \alpha). \tag{3.73}$$

The unperturbed Hamiltonian

$$H_0(\Delta, \phi) = \frac{1}{2}\frac{d^2 g}{dI^2}\Delta^2 - h\cos\phi \tag{3.74}$$

has stable fixed points at $\phi = 2k\pi, \Delta = 0$ and unstable fixed points at $\phi = (2k+1)\pi, \Delta = 0$. The motion on the separatrix is given by [46]

$$\phi_{sx} = 4 \arctan e^{Q_I \theta} - \pi, \tag{3.75}$$

where we have used the island tune defined in equation (3.5). The change in H_0 during a half period of the oscillation can be approximated by integrating $dH_0/d\theta \equiv [H_0, q \cdot (k+l) \cdot \Delta \cos(Q_m \theta + \alpha)]$ along the separatrix trajectory, which is denoted by the subscript 'sx'

$$\begin{aligned}
\Delta H_0 &\approx h \frac{(k+l)q}{2} \int_{-\infty}^{\infty} d\theta [\sin(\phi_{sx} - Q_m\theta - \alpha) + \sin(\phi_{sx} + Q_m\theta + \alpha)] && (3.76)\\
&= h \frac{(k+l)q}{2Q_m} \kappa \int_{-\infty}^{\infty} ds [\sin(\phi_{sx} - \kappa s - \alpha) + \sin(\phi_{sx} + \kappa s + \alpha)] && (3.77)\\
&= -h \frac{(k+l)q}{2Q_m} \kappa \sin\alpha \int_{-\infty}^{\infty} ds [\cos(\phi_{sx} - \kappa s) - \cos(\phi_{sx} + \kappa s)]. && (3.78)
\end{aligned}$$

Here we have changed the integration variable from θ to $s = \theta \cdot Q_I$ and have introduced the dimensionless quantity

$$\kappa \equiv \frac{Q_m}{Q_I}. \tag{3.79}$$

The integrals on the right hand side are known as Melnikov-Arnold integrals [39, 46, 47, 48] and can be evaluated (see appendix B). We are then led to the following solution

$$\Delta H_0 = -h\kappa \frac{(k+l)q}{2Q_m} \cdot (\mathcal{A}_2(\kappa) - \mathcal{A}_2(-\kappa)) \cdot \sin\alpha, \tag{3.80}$$

$\mathcal{A}_2$ being defined in appendix B. Denoting the relative energy deviation from the separatrix by w,

$$w \equiv \frac{H_0 - h}{h},$$

(3.80) can also be written as

$$\boxed{\bar{w} = w - \kappa \frac{(k+l)q}{2Q_m} \cdot (\mathcal{A}_2(\kappa) - \mathcal{A}_2(-\kappa)) \cdot \sin\alpha.} \tag{3.81}$$

A canonical variable conjugate to w is the phase α. In order to construct a map also the change in α has to be calculated. The oscillation frequency in the vicinity of the separatrix is given by [39]

$$Q(w) \approx \frac{\pi Q_I}{\ln(\frac{32}{|w|})}. \tag{3.82}$$

Hence the change of α during a half period of the oscillation is

$$\boxed{\bar{\alpha} \approx \alpha + \pi \frac{Q_m}{Q(\bar{w})} \approx \alpha + \frac{Q_m}{Q_I} \ln \frac{32}{|\bar{w}|}.} \tag{3.83}$$

Note that the argument of the logarithm is the transformed variable $\bar{w}$ and not the initial w, which means that (3.81) and (3.83) are applied successively. The Jacobian determinant of

either part is one and therefore the total map is symplectic. The trace of the Jacobian matrix for this map is calculated as

$$\mathrm{Tr}J(\alpha, w) = 2 + f\frac{\kappa}{|\bar{w}|}\cos\alpha, \tag{3.84}$$

with the abbreviation

$$f \equiv \frac{(k+l)q}{2Q_I}(\mathcal{A}_2(\kappa) - \mathcal{A}_2(-\kappa)). \tag{3.85}$$

A fixed point is stable if the absolute value of the trace is smaller than two, otherwise it is unstable. In our case the fixed points are given by (with m_r and n_r being natural numbers)

$$\begin{aligned} |w_r| &= 32 \cdot e^{-\frac{2\pi m_r}{\kappa}} \\ \alpha_r &= n_r \pi. \end{aligned}$$

If f is a positive quantity, the fixed points $\alpha = n_r\pi$ with n_r even are always unstable. However for an uneven n_r instability occurs only if

$$|w| < \frac{\kappa f}{4}. \tag{3.86}$$

In order to proceed further we have to insert the solution of the Melnikov-Arnold integral $\mathcal{A}_2$, [39, 46] (appendix D)

$$\mathcal{A}_2(\kappa) = 4\pi\kappa\frac{e^{\frac{\pi\kappa}{2}}}{\sinh(\pi\kappa)}, \tag{3.87}$$

into (3.85). According to (3.86) the width of the stochastic layer is then written as

$$\boxed{w_{sl} = \pi\kappa^3\frac{(k+l)q}{Q_m}\frac{\sinh(\frac{\pi\kappa}{2})}{\sinh(\pi\kappa)}.} \tag{3.88}$$

The value of w_{sl} is proportional to the fraction of area of the resonance island which becomes chaotic due to the external tune modulation. For a large ratio $Q_m/Q_I \equiv \kappa \gg 1$, the width of the chaotic layer decreases exponentially as a function of the modulation frequency.

Instead of founding our argumentation on the stability of the fixed points we can derive the width of the stochastic layer in an alternative way. If f defined by (3.85) is sufficiently small, it is possible to linearize the mapping in w (but not in α) around a resonant value w_r. (3.81) and (3.83) are then transformed into

$$\bar{I} = I + K\sin\alpha \tag{3.89}$$

$$\bar{\alpha} = \alpha + \bar{I}, \tag{3.90}$$

where we have introduced the new variable

$$I \equiv -\kappa\left(\frac{w - w_r}{w_r}\right) \tag{3.91}$$

and the parameter

$$K \equiv \frac{\kappa f}{w_r}. \tag{3.92}$$

Equations (3.89) and (3.90) constitute the 'standard mapping', which is of fundamental importance in the theory of nonlinear resonances. The onset of global chaos for this mapping occurs at a critical value $K \approx 1$ [39]. Hence the width of the stochastic layer is approximately

$$|w_{sl}| \approx \kappa f, \tag{3.93}$$

which differs from (3.86) only by a factor four. In the following we will drop the subscript and write w instead of w_{sl} for the expression on the right hand side of (3.88).

3.11 Phase Diagrams

In the parameter space of tune modulation, areas with distinct dynamical behavior can be graphically represented, which leads to 'phase diagrams' as proposed in [36]. The borderlines given by the inequalities (3.22) and (3.56)

$$\boxed{\begin{aligned} \frac{Q_m^{\frac{3}{4}}(nq)^{\frac{1}{4}}}{Q_I} &= \frac{4}{\pi^{\frac{1}{4}}} \\ \left|\frac{qQ_m}{Q_I^2 - Q_m^2}\right| &= \frac{1}{n}. \end{aligned}} \tag{3.94}$$

describe approximate boundaries between regions with qualitatively different behavior in the (q, Q_m)-plane. The unperturbed system is defined by only two parameters, the island tune Q_I and the order n of the resonance [4]. A typical phase diagram is shown in Fig. 3.4 (solid curves), for the values $Q_I = 0.049$ and $n = 4$ of the octupole kick map studied in section 3.12. The four different regions in the phase diagram can be interpreted as follows:

1. At small modulation amplitudes and small modulation frequencies the adiabaticity condition holds and the particles are stable.

2. For small modulation amplitudes and large modulation frequencies the sideband islands cover only a very small fraction of phase space. Thus the majority of particles is not affected by the tune modulation. This region is characterized by 'rapid phase oscillations'.

3. If the modulation amplitude is increased, the sideband islands gain importance. For large modulation frequency these islands are separated from each other and the motion is still regular.

4. For large modulation amplitudes the sidebands start to overlap below some critical modulation frequency, giving rise to global chaos. It is this region of the phase diagram (in the left upper corner) where emittance growth processes and proton losses occur.

The particle loss is due to a 'diffusion' process in the chaotic region, which is described by (3.34)

$$\boxed{\frac{\overline{(\Delta\epsilon)^2}}{\Delta t} = 32\frac{f_{rev} n h^2(I_r)}{q}.} \tag{3.95}$$

[4] As mentioned, in the more general two-dimensional case n has to be replaced by $k + l$.

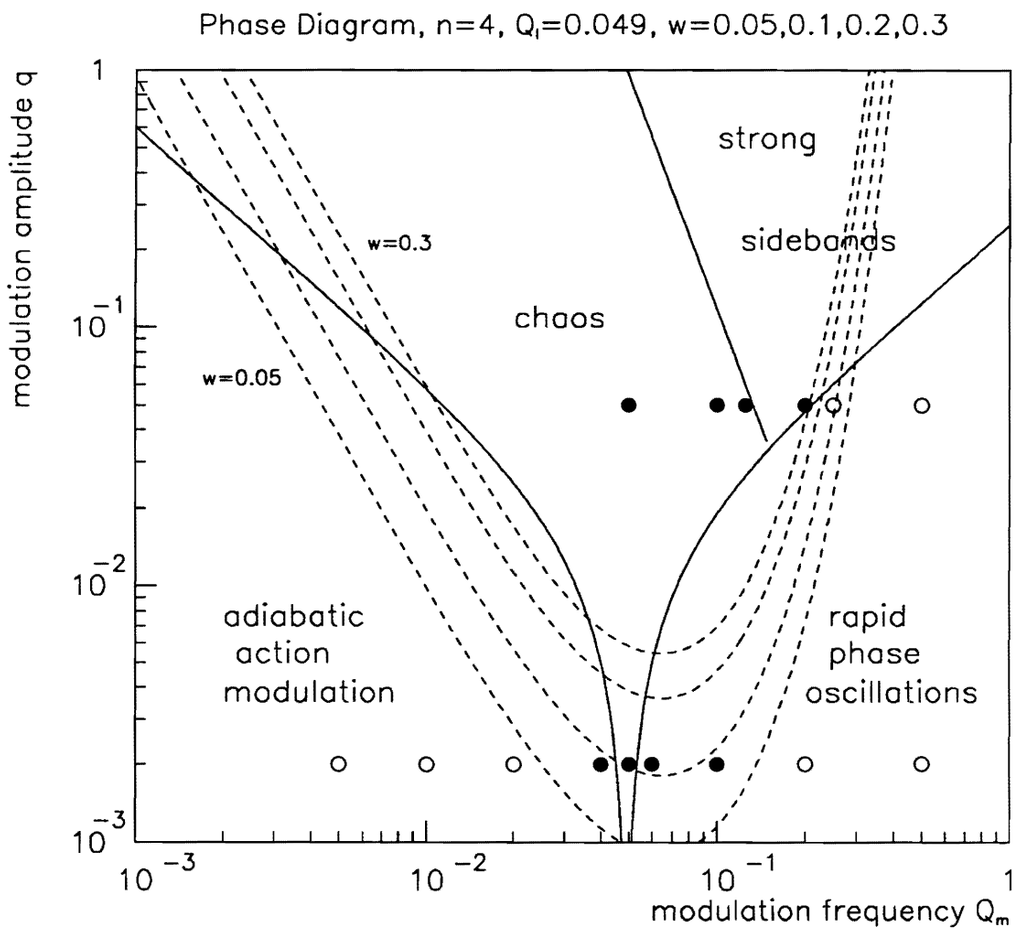

Figure 3.4: Phase diagram for the island tune $Q_I = 0.049$ and the resonance order $n = 4$ according to (3.94) (solid curves) and contour lines (3.96) with $w = 0.05, 0.1, 0.2, 0.3$ (dotted lines). The small closed and open circles refer to strongly chaotic and to almost undisturbed cases, respectively, as found in simulation studies with an octupole kick map (section 3.12). The phase space diagrams corresponding to the circles (from left to right) are depicted in Fig. 3.5 b)–j) and Fig. 3.8 a)–f).

The local diffusion rate is independent of the modulation frequency.

We now propose an alternative phase diagram, which is derived from equation (3.88)

$$\boxed{w \equiv \pi n q \frac{Q_m^2}{Q_I^3} \frac{\sinh(\frac{\pi Q_m}{2Q_I})}{\sinh(\frac{\pi Q_m}{Q_I})} \stackrel{!}{=} w_0.} \tag{3.96}$$

The contour line $w = w_0$, for a properly chosen constant w_0, can be used to define a border between chaotic and regular regions. Contour lines for $w_0 = 0.05, 0.1, 0.2$ and 0.3 are shown as dotted curves in Fig. 3.4. While the chaotic regions predicted by (3.94) and (3.96) agree approximately, there are still a few important differences:

a) Equations (3.94) describe a resonance-like behavior at $Q_m \approx Q_I$, whereas according to equation (3.96) the modulation amplitude has to exceed a certain threshold to be harmful. The prediction of (3.94), that an arbitrarily small modulation amplitude may cause global chaos, seems to be unrealistic.

b) The maximum response to tune modulation is either at $Q_m = Q_I$ (3.94) or at $Q_m \approx 1.35 \cdot Q_I$ (maximum value of width w in (3.96)).

c) The first equation of (3.94) implies that a reduction of the modulation amplitude may lead from regular to chaotic motion.

d) The boundary of the chaotic region is defined by only one equation if one applies the stochastic layer argumentation (3.96).

In order to study these questions more deeply the effect of tune modulation on a simple octupole kick map is examined in the next section.

3.12 Octupole Kick Map

The two-dimensional map that we want to study consists of a rotation

$$\begin{pmatrix} x \\ p \end{pmatrix}_f = \begin{pmatrix} \cos 2\pi Q & \sin 2\pi Q \\ -\sin 2\pi Q & \cos 2\pi Q \end{pmatrix} \begin{pmatrix} x \\ p \end{pmatrix}_i \tag{3.97}$$

and an octupolar kick

$$p_f = p_i - x_i^3. \tag{3.98}$$

The equivalent Hamiltonian is

$$H(x, p, \theta) = \frac{1}{2} Q(x^2 + p^2) + \frac{1}{4} x^4 \delta(\theta). \tag{3.99}$$

Action and angle variables I and ϕ are introduced by the usual relations

$$x = \sqrt{2I} \cos \phi \quad \text{and} \quad p = -\sqrt{2I} \sin \phi. \tag{3.100}$$

Near the fourth integer resonance $4Q \approx 1$ the total Hamiltonian is approximated by

$$H(I, \tilde{\phi}) \approx \left(Q - \frac{1}{4}\right) I + \frac{3}{16\pi} I^2 + \frac{1}{16\pi} I^2 \cos(4\tilde{\phi}). \tag{3.101}$$

We readily identify the characteristic quantities

$$g(I) = \frac{3}{16\pi} I^2 \tag{3.102}$$

$$h(I) = \frac{1}{16\pi} I^2 \tag{3.103}$$

$$n = 4. \tag{3.104}$$

Choosing $Q = 0.23$, the resonant action value is $I_r = 4\pi(\frac{1}{4} - Q) \approx 0.25$ and the island tune is approximately

$$Q_I = n\sqrt{\frac{d^2 g}{dI^2}(I_r)h(I_r)} \approx 0.049. \tag{3.105}$$

The phase diagram of this situation is shown in Fig. 3.4. We investigate two special cases. Firstly, we examine the behavior for the comparatively small modulation amplitude $q = 0.002$. In Fig. 3.5 phase space diagrams for ten different modulation frequencies are presented. Each diagram shows six different trajectories plotted once every modulation period (stroboscopic plot). The corresponding positions in the phase diagram are indicated by the lower row of circles in Fig. 3.4. It is evident from the diagrams that the small angle boundary (3.94) considerably underestimates the size of the chaotic region: The second equation of (3.94) predicts chaos only in the very small range $0.045 < Q_m < 0.053$. However, chaotic trajectories occupy large phase-space areas roughly for $\frac{1}{4}Q_I < Q_m < 4Q_I$. These limits would be described by (3.96) with $w_0 \approx 0.01$ as can be seen from Fig. 3.6 depicting the stochastic width (3.96) as a function of the modulation frequency. The stochastic width w is maximal at $Q_m \approx 0.066$ and thus in a region which should be regular according to (3.94).

Another point of interest is the border derived from the resonance overlap criterion (3.22). We choose the modulation amplitude $q = 0.05$, which is larger than the value $q^* \approx 0.033$ at the intersection of the two phase boundary lines (3.94). Fig. 3.7 shows the width of the stochastic layer as a function of the modulation frequency for this value of q.

In Fig. 3.7 the chaotic width w becomes too large at modulation frequencies close to the island tune for the predicted value to be accurate. Since the stochastic layer extends to both sides of the separatrix only half of it lies inside the resonance island. A reasonable upper limit for the parameter w is therefore two, which would describe a situation where the complete resonance island is chaotic. Hence the range of validity of formula (3.88) is restricted in a self-consistent way to values of w smaller than two. Far from the separatrix it is no longer possible to approximate the motion by integrating along the separatrix, which was the basic assumption made.

Fig. 3.8 shows phase space diagrams for six different modulation frequencies and a constant modulation amplitude $q = 0.05$. Due to the larger value of q, chaotic particles are lost almost immediately, which leads to a somewhat distinct appearance of the phase space diagrams as compared to Fig. 3.5. The change from chaotic to regular motion occurs at about $Q_m \approx 0.25$. In view of Fig. 3.7, this threshold could be described by (3.96) with $w_0 \approx 0.1$, whereas the first equation of (3.94) predicts the border of global chaos already at $Q_m \approx 0.133$. The six cases examined in Fig. 3.8 are represented by the upper row of circles in the phase diagram 3.4.

It may be concluded that (3.96) represents the border of the chaotic region at least as accurately as the two equations (3.94).

The reader may have noticed, from Fig. 3.5–3.8, that in many cases the fraction of the resonance island destroyed by the tune modulation agrees with (3.96) only within a factor 5–10, where the deviations are both towards too high and towards too low values. Therefore, it

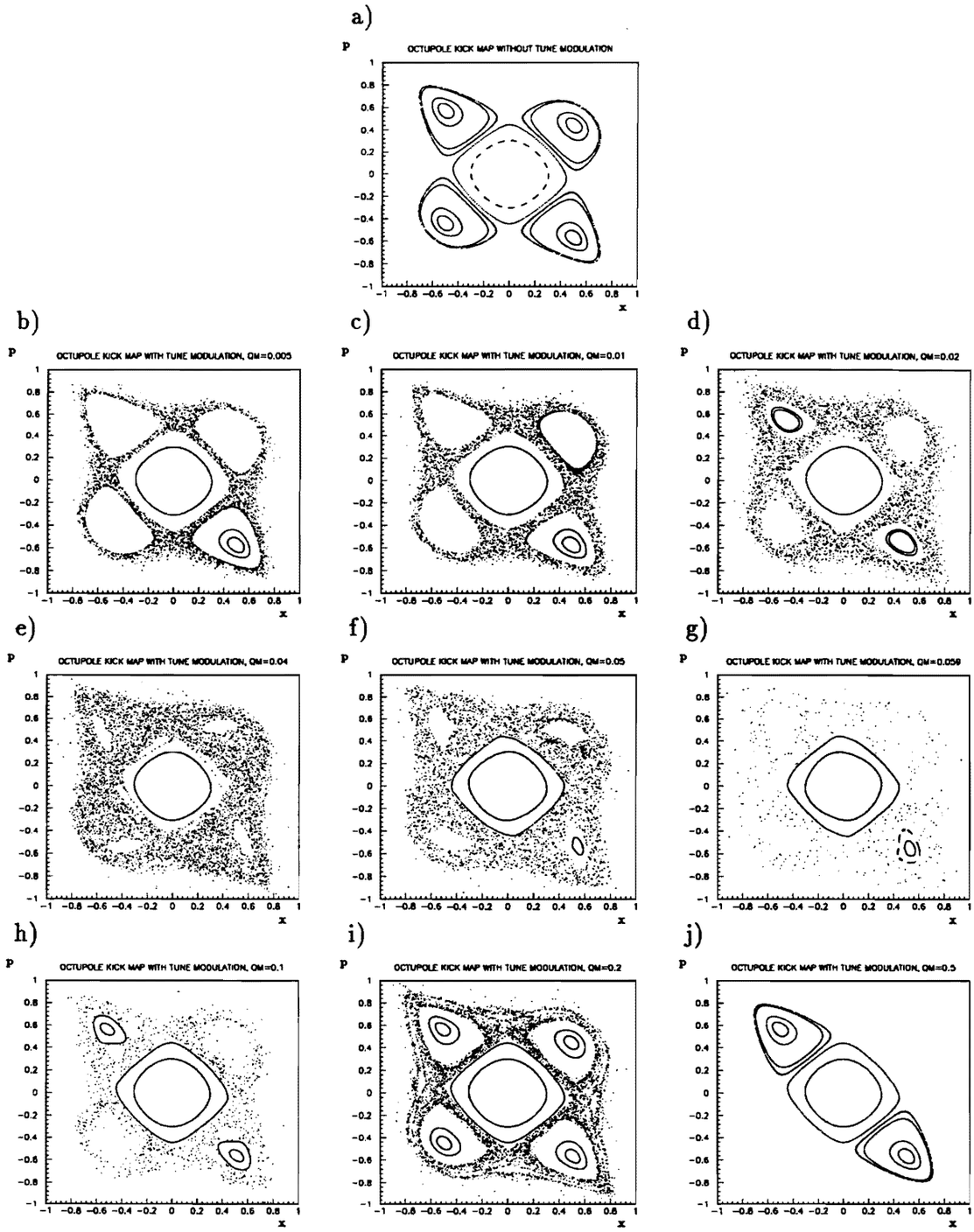

Figure 3.5: Phase space diagrams of six trajectories for the octupole kick map (3.97) and (3.98) with a tune modulation amplitude $q = 0.002$; each diagram corresponds to a different modulation frequency Q_m, namely a) no modulation b) $Q_m = 0.005$, c) $Q_m = 0.01 \approx \frac{1}{5}Q_I$, d) $Q_m = 0.02$, e) $Q_m = 0.04$, f) $Q_m = 0.05 \approx Q_I$, g) $Q_m = 0.06$, h) $Q_m = 0.1$, i) $Q_m = 0.2 \approx 4Q_I$, j) $Q_m = 0.5$.

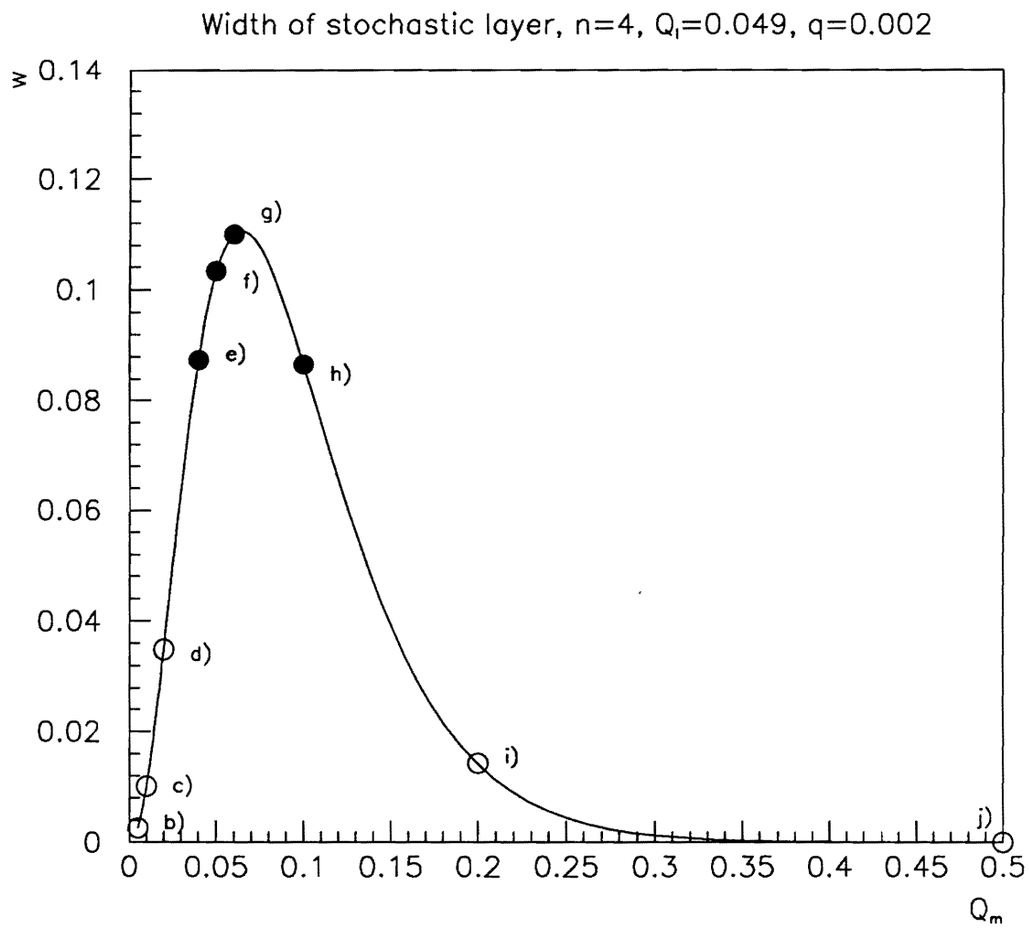

Figure 3.6: Width w of the stochastic layer (3.96) for the simple octupole kick map (3.97) and (3.98) with a modulation amplitude $q = 0.002$ as a function of the modulation frequency Q_m. The open and closed circles refer to the almost undisturbed and to the strongly chaotic phase space diagrams in Fig. 3.5 b)–j), respectively.

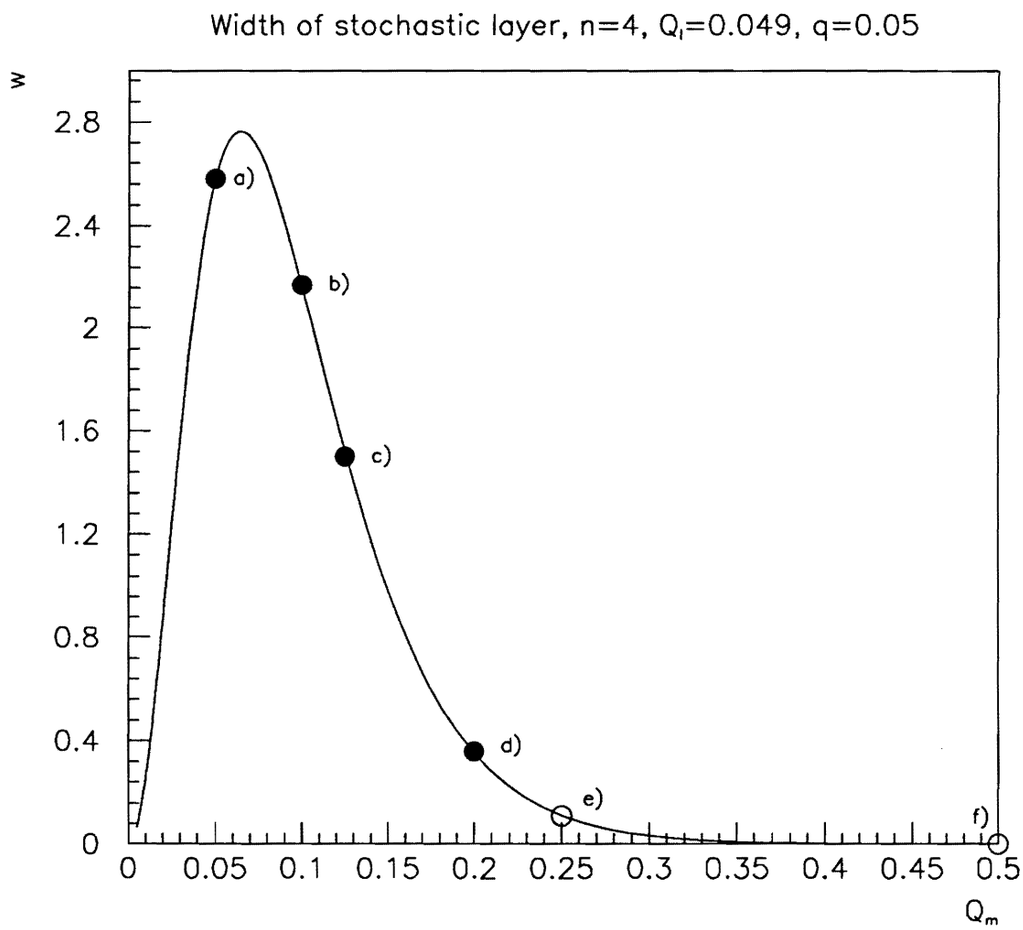

Figure 3.7: Width w of the stochastic layer (3.96) for the simple octupole kick map (3.97) and (3.98) with a tune modulation amplitude $q = 0.05$ as a function of the modulation frequency Q_m. The open and closed circles refer to the almost undisturbed and to the strongly chaotic phase space diagrams in Fig. 3.8 b)–f), respectively.

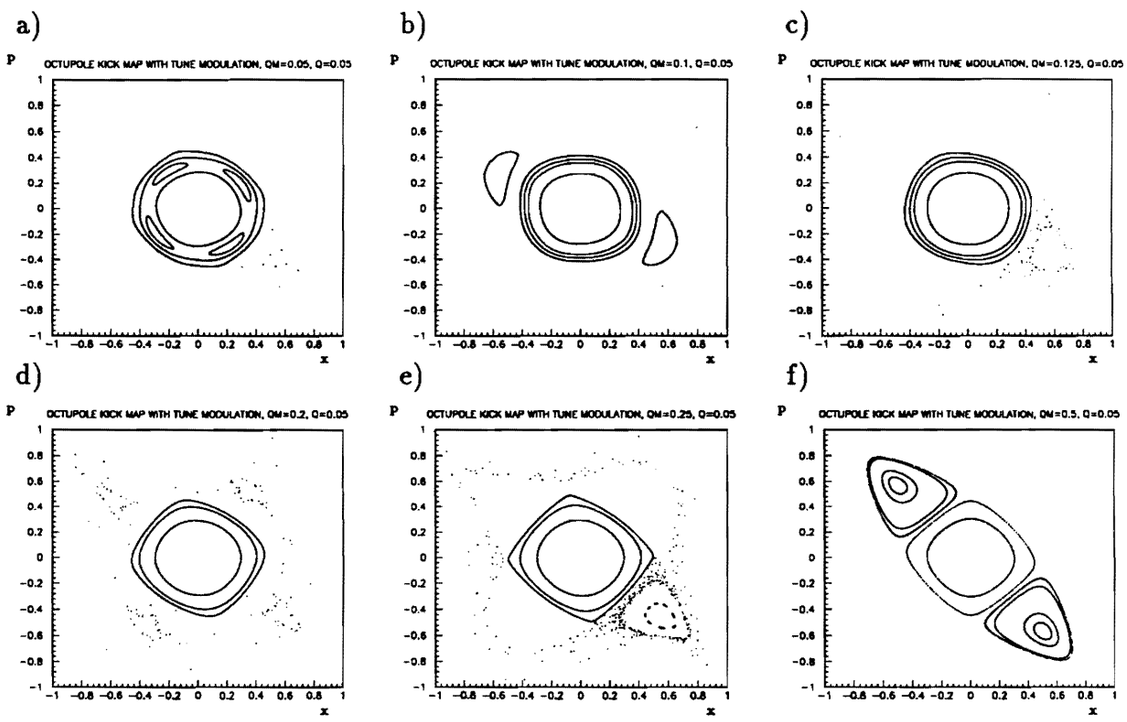

Figure 3.8: Phase space diagrams of six trajectories for the octupole kick map (3.97) and (3.98) with a tune modulation amplitude $q = 0.05$; each diagram corresponds to a different modulation frequency Q_m, namely a) $Q_m = 0.05 \approx Q_I$, b) $Q_m = 0.1$, c) $Q_m = 0.125$, d) $Q_m = 0.2$, e) $Q_m = 0.25 \approx 5Q_I$, f) $Q_m = 0.5$.

is desirable to estimate the magnitude of the deviation to be expected for a typical resonance in HERA and thus of the error in the results of chapter 5.

It has been pointed out [50] that the equations (3.94) and (3.96), describing alternative borders in a phase diagram, can be expressed in terms of two quantities solely, namely by a 'scaled' modulation amplitude $\tilde{q} \equiv nq/Q_m$ and a 'scaled' modulation frequency $\tilde{Q}_m \equiv \kappa \equiv Q_m/Q_I$. Simulations provide strong evidence that the degree of chaoticity is indeed characterized by the two universal parameters $\tilde{q}$ and $\tilde{Q}_m$ and does not depend on the actual values of n and Q_I. Assuming parameters representative for HERA (see chapter 5), here labeled by the superscript H,

$$\begin{aligned} n^H &= 10, \\ Q_I^H &\approx 2 \cdot 10^{-4}, \\ Q_m^H &\approx 10^{-3}, \\ q^H &\approx 10^{-4}, \end{aligned}$$

the scaled parameters are $\tilde{q}^H \approx 1$ and $\tilde{Q}_m^H \approx 5$. The phase space diagram of Fig. 3.8 d) corresponds to about these values, namely to $\tilde{q} \approx 1$ and $\tilde{Q}_m \approx 4$. For this case, Fig. 3.7 predicts a chaotic region whose size is about 40% of the undisturbed island. From comparison of the phase space diagrams in Fig. 3.8 d) and f), about 60-70% of the island is actually destroyed in Fig. 3.8 d). The island tune Q_I for most of the resonances in HERA is smaller than the assumed value $Q_I^H \approx 2 \cdot 10^{-4}$. Fortunately, for a larger ratio Q_m^H/Q_I^H the error of (3.96) decreases. This is illustrated by Fig. 3.8 e), for which the stochastic width is about 15%, in good agreement with Fig. 3.7.

It may, therefore, be expected that, in the results for HERA presented in chapter 5, the error of w is not larger than a factor of two.

3.13 Chaotic Fraction of Phase Space

As a measure of the harmfulness of different tune modulation frequencies for a storage ring such as HERA we introduce a 'sensitivity function' Γ as follows. The product of the total island width and the width of the stochastic layer is summed over all relevant resonances and normalized to the total emittance range. More specifically, the sensitivity is defined by (compare also (3.69) and (3.88))

$$\begin{aligned} \Gamma(Q_m, q) &\equiv \sum_{\text{all resonances } i} 2\Delta I_{\text{tot}}^i \cdot w_i(Q_m, q)/\epsilon_{tot} \\ &= \sum_{\text{all resonances } i} \left(\frac{Q_m}{Q_{I,i}}\right)^2 \frac{\sinh\left(\frac{\pi Q_m}{2Q_{I,i}}\right)}{\sinh\left(\frac{\pi Q_m}{Q_{I,i}}\right)} \frac{\sqrt{l_i^2 + k_i^2}(l_i + k_i) 8\pi q}{\left| l_i^2 \frac{\partial^2 g_i}{\partial I_z^2} + 2k_i l_i \frac{\partial^2 g_i}{\partial I_x \partial I_z} + k_i^2 \frac{\partial^2 g_i}{\partial I_x^2} \right|} \frac{1}{\epsilon_{tot}}, \end{aligned} \tag{3.106}$$

where the subscript 'i' denotes the individual resonances. The function so defined measures the fraction of phase space that becomes chaotic due to the tune modulation. It depends on the modulation frequency Q_m and on the modulation amplitude q.

To estimate the average emittance growth rate, which in general is influenced by several high order resonances, we add the contribution of each resonance, again weighted by the chaotic fraction of the corresponding resonance island and normalized to the total emittance range.

Thus the global emittance growth rate is given by

$$\boxed{\begin{aligned}\left\langle\frac{\overline{(\Delta(\epsilon_x+\epsilon_z))^2}}{\Delta t}\right\rangle_{\text{global}} &\approx \sum_{\text{all resonances } i} 2\cdot\Delta I^i_{\text{tot}}\cdot w_i\cdot\left(\frac{\overline{(\Delta(\epsilon_x+\epsilon_z))^2}}{\Delta t}\right)_i\frac{1}{\epsilon_{\text{tot}}}\\ &= \sum_{\text{all resonances } i}\left(\frac{Q_m}{Q_{I,i}}\right)^2\frac{\sinh\left(\frac{\pi Q_m}{2Q_{I,i}}\right)}{\sinh\left(\frac{\pi Q_m}{Q_{I,i}}\right)}\frac{256\pi\sqrt{k_i^2+l_i^2}(k_i+l_i)^2 f_{rev}h_i^2(I_{x,r,i},I_{z,r,i})}{|l_i^2\frac{\partial^2 g_i}{\partial I_z^2}+2k_il_i\frac{\partial^2 g_i}{\partial I_x\partial I_z}+k_i^2\frac{\partial^2 g_i}{\partial I_x^2}|}\frac{1}{\epsilon_{\text{tot}}},\end{aligned}} \tag{3.107}$$

where the square brackets '< ... >' denote the average over phase space up to a maximum amplitude. The range of validity of this formula will be discussed in chapter 5, where it is used to analyse the dependence of emittance growth rates caused by high order resonances in HERA on the modulation frequency. Note that the average emittance growth rate does not depend on the modulation amplitude q, but does depend strongly on the modulation frequency Q_m, in contrast to the local growth rate (3.72). The insensitivity to q reflects the fact that the fraction of phase space covered with chaotic trajectories increases linearly with the modulation amplitude q, whereas the diffusion rate within this zone decreases as $1/q$ (compare (3.34) and (3.88)).

3.14 Diffusion Model

Let us now assume that the particle distribution function f in the chaotic regions of phase space depends only on the transverse emittance $\epsilon \equiv \epsilon_x + \epsilon_z$ and obeys a diffusion equation of the form (this ansatz is motivated in appendix F)

$$\frac{\partial f}{\partial t} = \frac{\partial}{\partial \epsilon}\left(D(\epsilon)\frac{\partial f}{\partial \epsilon}\right). \tag{3.108}$$

The diffusion coefficient $D(\epsilon)$ is related to the squared emittance change per unit time by the simple formula (see again appendix F)

$$D(\epsilon) = \frac{1}{2}\left\langle\frac{\overline{(\Delta\epsilon)^2}}{\Delta t}\right\rangle. \tag{3.109}$$

Local approximations to this diffusion coefficient can be obtained by considering the individual terms i in the sum of equation (3.107) separately. An approximate value of the diffusion coefficient $D(\epsilon)$ is then given by the average over regular regions with no diffusion and chaotic regions with an emittance growth rate as in (3.72). The range of validity and the interpretation of this mean value are discussed in section 5.5. Instead of the total emittance range ϵ_{tot}, the normalization constant is now the distance between two adjacent resonances $(\epsilon_{i+1} - \epsilon_{i-1})/2$. Consequently, our estimate for the emittance-dependent diffusion coefficient $D(\epsilon)$ reads

$$\begin{aligned}D(\epsilon_i) = \frac{1}{2}\left\langle\frac{\overline{(\Delta(\epsilon_x+\epsilon_z))^2}}{\Delta t}\right\rangle_i &\approx 2\cdot\Delta I^i_{\text{tot}}\cdot w_i\cdot\left(\frac{\overline{(\Delta(\epsilon_x+\epsilon_z))^2}}{\Delta t}\right)_i\frac{1}{\epsilon_{i+1}-\epsilon_{i-1}}\\ &= \left(\frac{Q_m}{Q_{I,i}}\right)^2\frac{\sinh\left(\frac{\pi Q_m}{2Q_{I,i}}\right)}{\sinh\left(\frac{\pi Q_m}{Q_{I,i}}\right)}\frac{256\pi\sqrt{k_i^2+l_i^2}(k_i+l_i)^2 f_{rev}h_i^2(I_{x,r,i},I_{z,r,i})}{|l_i^2\frac{\partial^2 g_i}{\partial I_z^2}+2k_il_i\frac{\partial^2 g_i}{\partial I_x\partial I_z}+k_i^2\frac{\partial^2 g_i}{\partial I_x^2}|}\frac{1}{\epsilon_{i+1}-\epsilon_{i-1}}.\end{aligned} \tag{3.110}$$

Again the index 'i' specifies the individual resonances. In this case the square brackets do not denote an average over the total phase space, but over the region between two resonances. It is reasonable to take into account only resonances 'i' for which the stochastic width does not vanish or, more precisely, for which $Q_m/Q_{I,i} < 50$.

The amplitude-dependent mean emittance growth rate $< \overline{\Delta\epsilon}/\Delta t >$ is obtained from the diffusion coefficient $D(\epsilon)$ by differentiation [5]

$$\left\langle \frac{\overline{\Delta\epsilon}}{\Delta t} \right\rangle \approx \frac{\partial}{\partial\epsilon} D(\epsilon). \tag{3.111}$$

This relation applies not only to purely Hamiltonian systems, but also to multiple scattering (compare chapter 8). In the latter case, $D(\epsilon)$ is a linear function of ϵ and, consequently, $< \overline{\Delta\epsilon}/\Delta t >$ is constant.

[5] It was shown by Landau [46, 49] that this relation is valid for Hamiltonian systems. See also appendix F.

Chapter 4

Modulation Amplitudes

4.1 Origin of Power Supply Ripple

A major source of tune modulation in a storage ring are magnetic field modulations caused by voltage ripple of the magnet power supplies. The voltage ripple is partly due to the design of the rectifiers and partly due to technical imperfections.

The superconducting correction coils in HERA are fed by switched mode power supplies (chopper). These are built as converters on the basis of a pulse width modulation and are driven at a frequency of 14 kHz [51]. Due to the very high frequency their effect on the beam dynamics is negligible, provided that the fractional part of the betatron tune is not too close to the driving frequency of the power supplies, which corresponds to $Q_m \approx 0.296$.

For magnets or magnet chains which are operated at a current higher than $360A$, rectifiers with thyristor bridges are used. The main superconducting circuit is fed by a 24-pulse 4-bridge silicon controlled rectifier (SCR). The expected fundamental ripple frequency is 12 kHz for a perfect balance of the bridge circuit. The circuits of the quadrupoles in the interaction region are powered by 12-pulse (2-bridge) SCRs, for which the lowest unavoidable ripple frequency is 600 Hz. Due to imbalances between individual bridges and thyristors and due to capacitances to ground all harmonics of the fundamental frequency 50 Hz are found in the voltage spectra of the SCRs.

4.2 Simple Model of the Main Circuit

In the HERA ring all superconducting dipoles and quadrupoles are powered in series. As a consequence, a current ripple in the main circuit changes the focusing strength of the quadrupoles as well as the deflecting dipole field. A change in the dipole field leads to a shift in energy and beam orbit. In the arcs the corresponding shift of the tune is compensated by the simultaneous change of the quadrupole strengths. Independent power supplies feed the normal-conducting quadrupoles in the straight sections. Therefore the compensation of the dipole and the quadrupole field variations is not perfect and a net tune modulation results.

To illuminate the relation between power supply ripple and tune modulation, a simplified model of a current ripple $\frac{\Delta I}{I}\cos(\omega_{ripple}t)$ with constant amplitude and phase along the superconducting magnet chain is considered. Three effects contribute to the effective tune modulation, namely

1. the absolute change of the momentum,

2. the orbit change at the position of the sextupoles,

3. the change of the focusing strength of the quadrupoles.

For a low-frequency ripple, $\omega_{ripple} \ll \omega_{sync}$, the energy of the particles follows the change in the external field. The revolution frequency stays constant because the radio frequency (rf) in the cavities is not changed. Hence the change in the velocity is compensated by a change in the path length and we have

$$\frac{\Delta C}{C} = \frac{\Delta v}{v} = \frac{1}{\gamma^2}\frac{\Delta p}{p},$$

where γ is the relativistic $\gamma \equiv (1 - \frac{v^2}{c^2})^{-\frac{1}{2}}$. The relative change in the orbit length is

$$\frac{\Delta C}{C} = \frac{1}{\gamma_{tr}^2}\left(\frac{\Delta p}{p} - \frac{\Delta B}{B}\right).$$

In this section the ripple of the guide field $\frac{\Delta B}{B}$ is assumed to be equal to the current ripple $\frac{\Delta I}{I}$. The transition energy γ_{tr} is the nominal energy at which the change in path length exactly compensates the change in velocity for off-momentum particles. For HERA its value is $\gamma_{tr} \approx 27.7$. The last two equations lead to

$$\frac{\Delta p}{p} = \frac{\gamma^2}{\gamma^2 - \gamma_{tr}^2}\frac{\Delta B}{B}. \tag{4.1}$$

If there were no sextupole coils in the ring, the absolute change in momentum would give rise to a tune modulation amplitude q_I via the natural total chromaticity $\xi_{nat.}^{tot}$

$$q_I = \xi_{nat.}^{tot}\frac{\Delta p}{p} = \xi_{nat.}^{tot}\frac{\gamma^2}{\gamma^2 - \gamma_{tr}^2}\frac{\Delta B}{B}, \tag{4.2}$$

the chromaticity ξ being defined as the change in tune ΔQ per relative momentum deviation,

$$\xi \equiv \frac{\Delta Q}{\Delta p/p}. \tag{4.3}$$

The 'natural' chromaticity $\xi_{nat.}$ is caused by the variation with momentum of the quadrupole focusing strength. It can be expressed as an integral of the quadrupole strength K in units of m^{-2} times the beta function β around the ring,

$$\xi_{nat.}^{tot} \equiv -\frac{1}{4\pi}\oint K\beta\, ds.$$

Sextupole correction coils and sextupole field errors in the superconducting magnets provide a second contribution to the overall chromaticity, which is of opposite sign. The effective sextupole strength around the ring is adjusted such that the total chromaticity

$$\xi^{tot} = \xi_{nat.}^{tot} + \frac{1}{4\pi}\oint mD\beta\, ds \tag{4.4}$$

is close to zero, m being the sextupole strength in units of m^{-3} and D the dispersion function. Hence the horizontal orbit shift in the sextupoles, given by

$$x = D\left(\frac{\Delta p}{p} - \frac{\Delta B}{B}\right) = D\frac{\gamma_{tr}^2}{\gamma^2 - \gamma_{tr}^2}\frac{\Delta B}{B},$$

causes a modulation amplitude q_{II}, which can be written as

$$q_{II} = -\xi_{nat.}^{tot} \frac{\gamma_{tr}^2}{\gamma^2 - \gamma_{tr}^2} \frac{\Delta B}{B}. \tag{4.5}$$

It is convenient to decompose the total natural chromaticity into two parts,

$$\xi_{nat.}^{tot} = \xi_{nat.}^{straight} + \xi_{nat.}^{arc}, \tag{4.6}$$

by means of which the effect of the warm quadrupoles in the straight sections is separated from that of the superconducting quadrupoles in the arcs. The modulation of the focusing strength of the superconducting quadrupoles leads to a modulation amplitude q_{III},

$$q_{III} = \frac{1}{4\pi} \int_{arc} K\beta \, ds \, \frac{\Delta B}{B} = -\xi_{nat.}^{arc} \frac{\Delta B}{B}. \tag{4.7}$$

Adding (4.2), (4.5) and (4.7) the total modulation amplitude q becomes

$$q = |q_I + q_{II} + q_{III}| = |\xi_{nat.}^{straight}| \frac{\Delta B}{B} \qquad \text{for} \qquad \omega_{ripple} \ll \omega_{sync}. \tag{4.8}$$

For frequencies larger than the synchrotron frequency, $\omega_{ripple} \gg \omega_{sync}$, the momentum is approximately constant $\Delta p \approx 0$. Hence, in this case, there is no contribution to the modulation amplitude of the form q_I (4.2). The horizontal orbit change is simply

$$x = -D \frac{\Delta B}{B}$$

and q_{II} (4.5) has to be replaced by

$$q_{IV} = \xi_{nat.}^{tot} \frac{\Delta B}{B}, \tag{4.9}$$

while q_{III} (4.7) also applies to a high-frequency ripple. The total tune modulation amplitude

$$q = |q_{III} + q_{IV}| = |\xi_{nat.}^{straight}| \frac{\Delta B}{B} \qquad \text{for} \qquad \omega_{ripple} \gg \omega_{sync} \tag{4.10}$$

is the same as for a low-frequency ripple (equation (4.8)).

In the HERA proton ring the natural chromaticities at injection energy are about

$$\xi_{nat.}^{tot} = \xi_{nat.}^{arc} + \xi_{nat.}^{straight} \approx -40 \ , \ \xi_{nat.}^{arc} \approx -30 \ , \ \xi_{nat.}^{straight} \approx -10. \tag{4.11}$$

In our simple model, the relation between current ripple and tune modulation amplitude is

$$q \approx |\xi_{nat.}^{straight}| \cdot \frac{\Delta B}{B} \approx 10 \cdot \frac{\Delta B}{B}. \tag{4.12}$$

The amplitude of the 150-Hz field ripple measured in the reference dipole magnets is $\Delta B/B \approx 1.4 \cdot 10^{-6}$ and corresponds to a tune modulation amplitude $q \sim 1.4 \cdot 10^{-5}$, according to (4.12). In reality the amplitude of the current ripple is not constant around the ring and the overall modulation amplitude q is about a factor 3–4 larger (see next section).

It is difficult to relate the observed field ripple to the voltage ripple at the power supply. For example, using $L_{tot} \approx 24$H the estimate $\Delta U = \omega L_{tot} I \frac{\Delta B}{B}$ results in $\Delta U \approx 8V$. In contrast, the power supply specifications allow a maximum ripple amplitude of only 2 Volt [52]. Direct measurements at the power supply show that the actual ripple amplitude is even smaller, namely in the order of 150 mV [53]. Thus an RL-circuit is not an adequate model to describe the superconducting magnet chain.

4.3 Transmission Line Characteristics

In order to properly estimate the actual effect of the magnetic field ripple, the transmission line characteristics of the superconducting magnet string have to be considered. For every ripple frequency a wave pattern builds up along the magnet chain. The corresponding current ripple amplitude at each position in the ring can be computed from the measured 4-pole parameters of dipole and quadrupole magnets. As far as the contribution to the overall tune modulation is concerned the ripple effects in different quadrupole and sextupole magnets partially add and partially cancel each other.

In Fig. 4.1 the tune modulation amplitude expected for a harmonic power supply voltage ripple of amplitude 1 V is shown as a function of the ripple frequency [34]. The amplitude of the 50-Hz ripple was measured to be about 50 mV, which, according to Fig. 4.1, translates into a tune modulation amplitude of $q \sim 3 \cdot 10^{-5}$. The 150-Hz voltage ripple of 150 mV gives rise to a tune modulation of amplitude $q \sim 5 \cdot 10^{-5}$. The large enhancement of the effect of a power supply ripple between 0 and 300 Hz, illustrated by Fig. 4.1, is related to standing wave resonances of the magnet string, which occur at frequencies as low as 15.6 Hz. According to model calculations [54] the eigenmodes of the transmission line may be excited during the ramp. Such an excitation has not yet been measured.

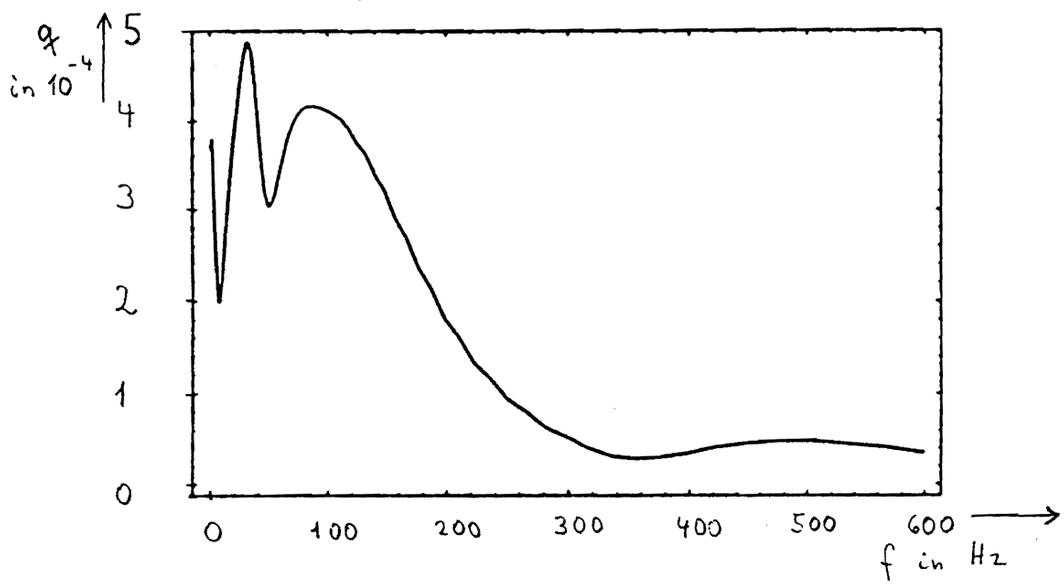

Figure 4.1: Tune modulation amplitude at injection energy as a function of the ripple frequency for a voltage ripple of 1 V at the power supply [34].

4.4 The Quadrupoles of the Interaction Region

At 820 GeV the ripple in the normal-conducting quadrupoles of the interaction regions is the dominant source of tune modulation. While the ripple in the superconducting main circuit is very important at injection energy, its contribution to the total tune modulation is negligible at top energy in view of the much higher dc current.

The vertically focusing interaction-region quadrupole circuit consists of eight magnets (three QS10 and one QR10 on either side of the interaction region). The relative voltage ripple determined for the south interaction region is about 10^{-3} at 50 Hz and $5 \cdot 10^{-3}$ at 600 Hz [55],

where these values apply to luminosity conditions. Fig. 4.2 shows a measurement of the 600-Hz ripple with a relative ripple amplitude of $5 \cdot 10^{-3}$.

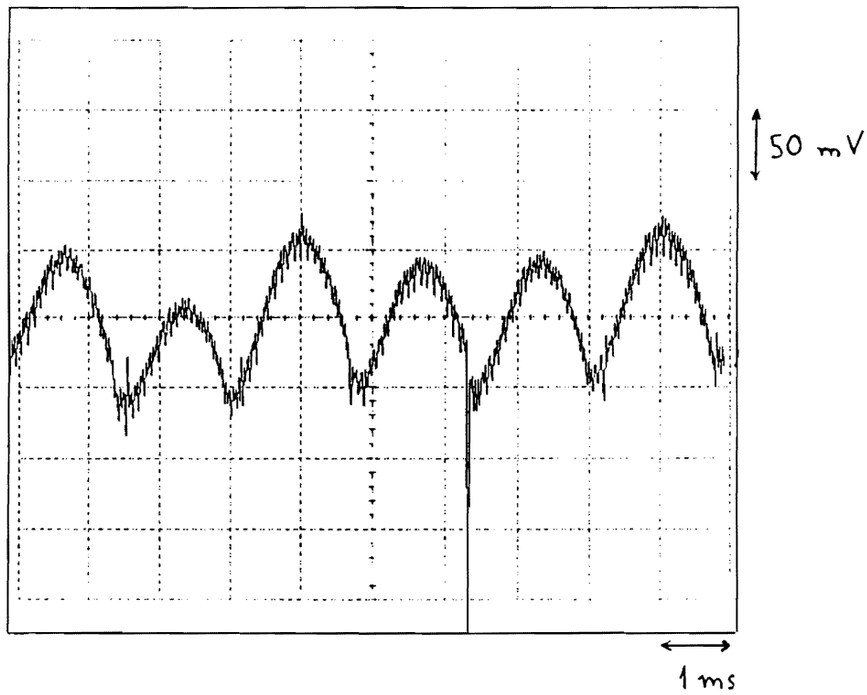

Figure 4.2: Voltage ripple for the power supply Munk 506A/08 feeding the vertically focusing quadrupole circuit in the south. The actual dc voltage of about 650 V corresponds to a value of 10 V in this measurement. The fundamental ripple frequency is 600 Hz as expected for a two-bridge rectifier. Also present is a 50 Hz component, which is, however, not noticeable on this time scale.

A similar number is assumed for the horizontally focusing circuit consisting of three magnets QR14 on both sides of the interaction zone. The current ripple amplitude can be estimated via

$$\frac{\Delta I}{I} = \frac{1}{\sqrt{(\frac{L\omega}{R})^2 + 1}} \frac{\Delta U}{U} \tag{4.13}$$

and the amplitude q of the tune modulation due to the current ripple $\frac{\Delta I}{I}$ is given by

$$q = \frac{1}{4\pi} \int_{quadr.} K\beta \, ds \, \frac{\Delta I}{I}, \tag{4.14}$$

where the integral is over the quadrupole magnets of one circuit. The resistance and inductance of the two circuits are listed in Table 4.1 together with the computed current ripple and tune modulation amplitudes.

4.5 Shielding by the Beam Pipe

The inside of the cold HERA beam pipe is coated with a copper layer of thickness $d = 10\,\mu$m at a radius $r = 27.5$ mm. This layer provides most of the shielding, which can be calculated by

Parameter	horizontal	vertical
$\Delta U/U$(50 Hz)	$\sim 1 \cdot 10^{-3}$	$\sim 1 \cdot 10^{-3}$
$\Delta U/U$(600 Hz)	$\sim 5 \cdot 10^{-3}$	$\sim 5 \cdot 10^{-3}$
Inductance	~ 0.78 H	~ 1.4 H
Resistance	1.22 Ω	1.45 Ω
$\Delta I/I$(50 Hz)	$\sim 5 \cdot 10^{-6}$	$\sim 3 \cdot 10^{-6}$
$\Delta I/I$(600 Hz)	$\sim 2 \cdot 10^{-6}$	$\sim 1.5 \cdot 10^{-6}$
$\int_{quadr.} K ds$	~ 0.12 m^{-1}	~ 0.15 m^{-1}
β	~ 1500 m	~ 1200 m
q (50 Hz)	$\sim 7 \cdot 10^{-5}$	$\sim 4 \cdot 10^{-5}$
q (600 Hz)	$\sim 3 \cdot 10^{-5}$	$\sim 2 \cdot 10^{-5}$

Table 4.1: Current ripple in the interaction region quadrupoles and corresponding tune modulation amplitudes.

solving Maxwell's equations with the appropriate boundary conditions [56, 57]. The frequency-dependent skin depth is given by

$$\delta(f) = \frac{1}{\sqrt{\pi f \mu_0 \sigma}} \,. \tag{4.15}$$

The 'shielding factor' $\tilde{Q} \equiv B_{\text{inside}}/B_{\text{outside}}$ is defined as the ratio of the magnetic field inside the beam pipe and the field in a great distance from it, which is assumed as homogeneous. Introducing the two abbreviations

$$\begin{aligned} k(f) &\equiv \frac{1+i}{\delta(f)} \\ K(f) &\equiv k(f) \cdot (r-d) \,, \end{aligned}$$

the shielding factor can be written in complex form as [56, 57]

$$\tilde{Q}(f) = \left[\cosh(k(f) \cdot d) + 0.5 \left[K(f) + \frac{1}{K(f)}\right] \cdot \sinh(k(f) \cdot d)\right]^{-1} \,. \tag{4.16}$$

In Fig. 4.3 a) the absolute value of $\tilde{Q}(f)$ is plotted in the frequency range from 0 to 15 kHz assuming a conductivity $\sigma_{\text{copper}} \approx 4 \cdot 10^9 \frac{1}{\Omega \text{m}}$ at liquid helium temperature [58]. At 150 Hz, the attenuation factor is only 0.8.

The warm sections of the beam pipe are not coated by copper, but consist of 2 mm thick stainless steel with a conductivity of $\sigma \approx 3 \cdot 10^6 \frac{1}{\Omega \text{m}}$ [58]. At the position of the interaction-region quadrupoles (QR10,QR14) the average beam pipe radius is $r = 29.5$ mm. Fig. 4.3 b) shows that in the frequency range of interest, between 0 Hz and 600 Hz, the warm beam pipe provides virtually no shielding.

4.6 Ground Motion Effects

A tune modulation of low frequency can be caused by ground waves and mechanical vibrations of the magnets. The amplitude of the beam oscillations due to these effects and the impact

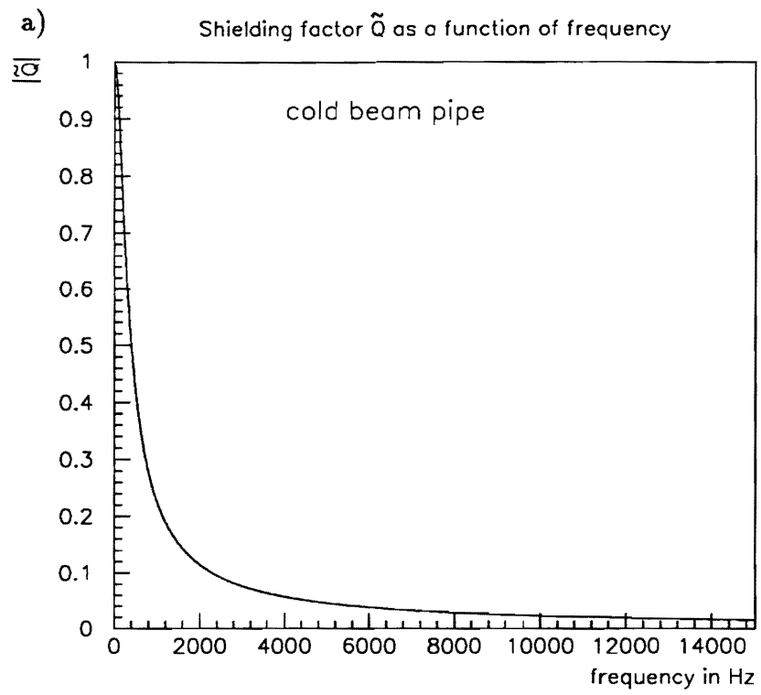

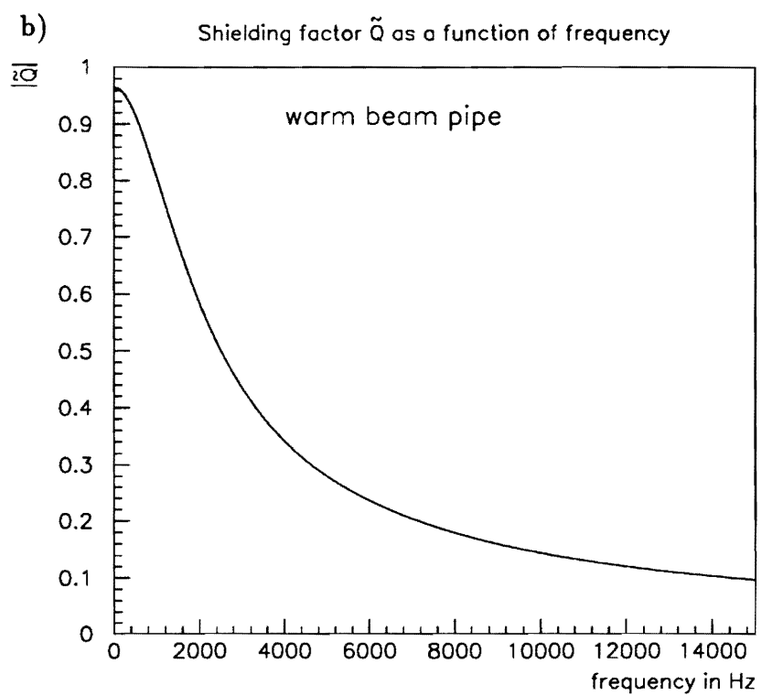

Figure 4.3: Shielding factor $|\tilde{Q}|$ as a function of frequency in Hz for the HERA beam pipe; a) cold beam pipe with $d = 10\mu m$ copper plating, b) warm beam pipe consisting of $d = 2mm$ stainless steel.

on collision alignment in HERA have been an object of vigorous investigations [35]. One may suspect that a part of the low-frequency beam oscillations results in a harmonic tune modulation due to an orbit change at the position of the sextupoles. For instance, assuming a root-mean-square orbit displacement in the arc of $x_{\rm rms} = 0.05$ mm caused by mechanical quadrupole vibrations, a rough estimate of the resulting modulation amplitude is

$$q_{vibration} \approx |\xi_{nat.}| \frac{Q - \{Q\}}{Q} \frac{x_{\rm rms}}{D\sqrt{N_{quad}}}, \tag{4.17}$$

where D is the average dispersion function (about 1.5 m), N_{quad} the number of quadrupoles, $\xi_{nat.} \approx -40$ the natural chromaticity and $Q - \{Q\}$ the fractional part of the betatron tune Q.

The factor $(Q-\{Q\})/Q$ accounts for the oscillatory character of the closed orbit distortions. Over every full betatron wavelength the accumulated tune shift is zero, because orbit displacements of opposite sign in a sextupole compensate each other. Thus in a first approximation only the fractional part of the tune, which corresponds to an incomplete closed orbit oscillation, gives rise to a tune shift. For a typical working point of $Q \approx 31.3$ the suppression factor is about $0.3/31 \approx 10^{-2}$. The square root of the number of quadrupoles ($N_{quad} \approx 200$) enters in (4.17), if there is no correlation between the individual magnets.

A typical number is $q = 10^{-6}$, which is a factor 100 smaller than the modulation amplitudes due to power supply ripple. The dominant frequencies are in the range 2–20 Hz [35].

4.7 Modulation Amplitudes

The results of this chapter can be summarized as follows.

All multiples of 50 Hz are found in the Fourier spectra of voltages and magnetic fields. Of special importance and strength are the 50 Hz and 150 Hz lines at injection energy and the 50 and 600 Hz lines for luminosity conditions.

At injection energy we expect tune modulation amplitudes in the order of 10^{-4}. These are caused by a current ripple in the main superconducting magnet string.

For the luminosity mode the modulation amplitude is of similar size and is primarily due to the normal-conducting quadrupole circuits in the interaction region.

Ground waves and mechanical magnet vibrations may lead to a low-frequency tune modulation (below 20 Hz) whose amplitude is smaller by two orders of magnitude.

Chapter 5

Dynamic Aperture

5.1 Effect of the Persistent-Current Field Errors

Comprehensive tracking calculations have been performed to study the effect of magnetic field errors on the dynamic aperture of HERA at the injection energy of 40 GeV. The measured individual multipole components up to 20-pole of all superconducting dipoles and quadrupoles were taken into account by adding five thin, higher-order lenses to each FODO half cell. The details and methods used in the tracking-data analysis are described elsewhere [60, 63, 4] (see also chapter 2). The simulations provide an estimate of the dynamic aperture, defined by the onset of chaotic particle motion.

The predicted dynamic aperture of the HERA proton ring is shown in Fig. 5.1 as a function of the amplitude of momentum oscillation $\Delta p/p$. The dynamic aperture r is given in units of mm and depends on the beta function β at the point of observation. In this case β is chosen as 76 m, the maximum value in the arcs. A quantity that is closely related to the aperture, but is independent of the point of observation, is the dynamic acceptance $A_{x,z}$, which is defined as the single-particle emittance of the outermost stable trajectory and is quoted in units of mm mrad. The relation between aperture r and acceptance A is

$$A \equiv A_x + A_z = r^2/\beta \qquad \text{or} \qquad r \equiv \sqrt{A \cdot 76\text{m}} \quad , \tag{5.1}$$

where $\beta = 76$ m is the beta function value at the point, to which r refers.

The working point of $Q_x = 31.27$ and $Q_z = 32.30$ chosen for the investigation is close to the actual value used in the HERA operation of 1992. In 1992 the circumferential rf voltage of the 52 MHz system was about 70 kV corresponding to a synchrotron frequency of 22 Hz. This value is also used in the simulation. For a proper bucket matching between PETRA and HERA a smaller rf voltage and synchrotron frequency are required. The design synchrotron frequency is 14 Hz.

The dynamic acceptance expected from the threshold of chaos in the simulation studies is $A \approx 4$ mm mrad for on-momentum particles, equivalent to an aperture of 17.5 mm. The onset of chaos is considerably reduced to about $A = 1.9$ mm mrad or $r = 12$ mm for an initial momentum deviation of $\Delta p/p = 5 \cdot 10^{-4}$, which is about the actual momentum spread of the injected bunch.

Two effects may cause a reduction of the dynamic aperture for off-momentum particles. Firstly, the nonlinear fields are larger on a dispersion orbit than for particles with $\Delta p/p = 0$. However, for a relative momentum deviation of $\Delta p/p = 5 \cdot 10^{-4}$ and an average dispersion function of about 1.5 m in the arc the orbit shift is less than 1 mm. This is much too small to

explain the reduction of aperture noticed in Fig. 5.1. Secondly, large synchrotron oscillations induce a betatron tune modulation via the chromaticity of the storage ring. In the model-calculations the corrected chromaticity is $\xi_x = -1.3$ and $\xi_z = 0.6$. Hence the resulting tune modulation amplitude for a typical off-momentum trajectory is in the order of the momentum spread $5 \cdot 10^{-4}$. The observed reduction of the dynamic aperture for off-momentum particles can mainly be ascribed to the additional tune modulation.

In agreement with this interpretation is the observation that for a circumferential rf voltage of 2 MV (and a different working point $Q_x = 31.15$, $Q_z = 32.18$) the dynamic aperture is reduced by less than 10% in the simulation, for a particle with $\Delta p/p = 5 \cdot 10^{-4}$ [60]. An rf voltage of 2 MV corresponds to a synchrotron frequency of about 120 Hz. As will be shown later a relatively small tune modulation frequency such as the synchrotron frequency of 22 Hz used in 1992 is potentially much more harmful. This can be explained by high-order resonances, which are studied in sections 5.3 and 5.4.

Also shown in Fig. 5.1 is the design beam size, corresponding to two standard deviations σ, and a rough measurement of the actual dynamic aperture in the HERA proton ring. Proton beams that are injected with large transverse oscillations have a lifetime of less than 1 hour, which suggests that the dynamic aperture is smaller than the physical aperture. This is confirmed by beam profile measurements with the residual gas monitors [61]. These indicate that the dynamic aperture is about 1.2 mm mrad, while the linear acceptance as measured by orthogonal orbit bumps is between 2.3 and 3.0 mm mrad. The observed bunch lengths are always smaller than 3 m, which provides an estimate of the dynamic momentum acceptance.

Fig. 5.1 can be compared with Fig. 5.2 presenting the results of a tracking study for a faulty model of HERA, in which the 20-pole coefficients of the quadrupole magnets are a factor of ten larger than the actual values. Hereafter we will occasionally refer to the correct model of HERA as model I and to the faulty one as model II.

While the threshold of chaotic motion for model II is found at about the same amplitude as for the correct model, the stability limit over 20 000 turns for on-momentum trajectories is significantly reduced. This finding can be interpreted as follows. The dynamic aperture, as defined by the border between chaotic and regular trajectories, is so small that it is completely determined by the multipole components of order lower than 20. On the contrary the emittance growth in the chaotic regions of phase space and the border for particle-stability over 20 000 turns are affected by the additional systematic 20-pole coefficient. This multipole component gives rise to a strong detuning at large amplitudes and consequently to more resonance-crossings as well as to enhanced driving terms. This interpretation is confirmed by the results of map tracking for model II, which were reported in chapter 2. A 7th order Taylor map, which does not include the effect of the 20-pole component, yields the same threshold for the onset of chaos as the direct tracking or a Taylor map of 9th order. But both the 9th order map and the direct tracking show a much smaller region of stability over 20 000 turns (see Table 2.3).

For completeness it should be mentioned that in model II also the coefficients a_8–a_{10} and b_8–b_9 of the quadrupole magnets are increased by a factor of 10 (compare Table 2.2). However, only the considerably larger coefficient b_{10} has an influence on the tracking results.

5.2 Tracking Studies including Tune Modulation

According to the last section, the measured dynamic aperture is a factor 1.5–2 smaller than the value expected from simulations which take into account only the nonlinear field errors. A better agreement is obtained if a modest tune modulation is included in the model.

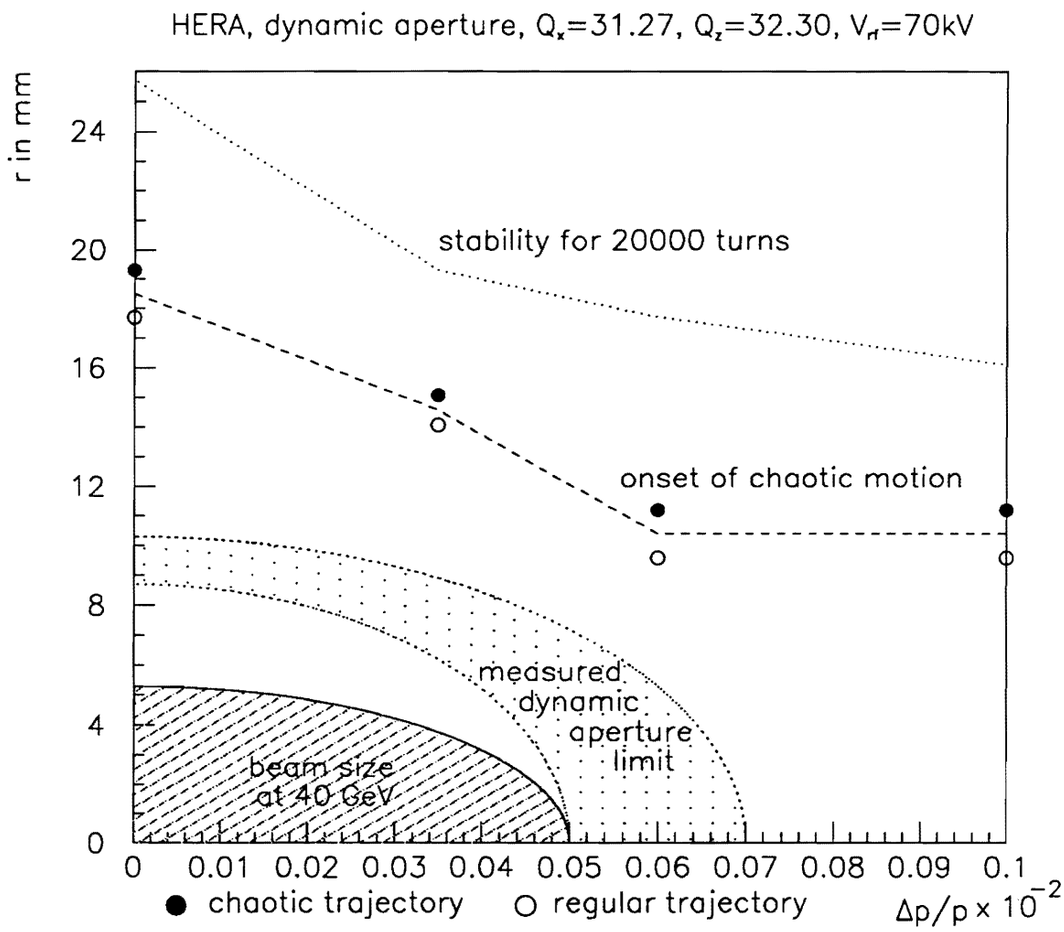

Figure 5.1: Dynamic aperture in the arcs of the HERA proton ring expected from simulation studies for the working point $Q_x = 31.27$, $Q_z = 32.30$ and a circumferential rf voltage of 70 kV. Shown are amplitude values r in mm, defined by the equation $r = \sqrt{\beta(\epsilon_x + \epsilon_z)}$ with $\beta = 76$ m, as a function of the amplitude of momentum oscillations $\Delta p/p$. The underlying model of HERA, which includes the actually measured multipole errors, is referred to as model I in the text. Also indicated is a range of values for the real dynamic aperture measured in 1992. The uncertainty depicted does not refer to the error of the measurement, which is much smaller, but to the variation observed over periods of days or weeks.

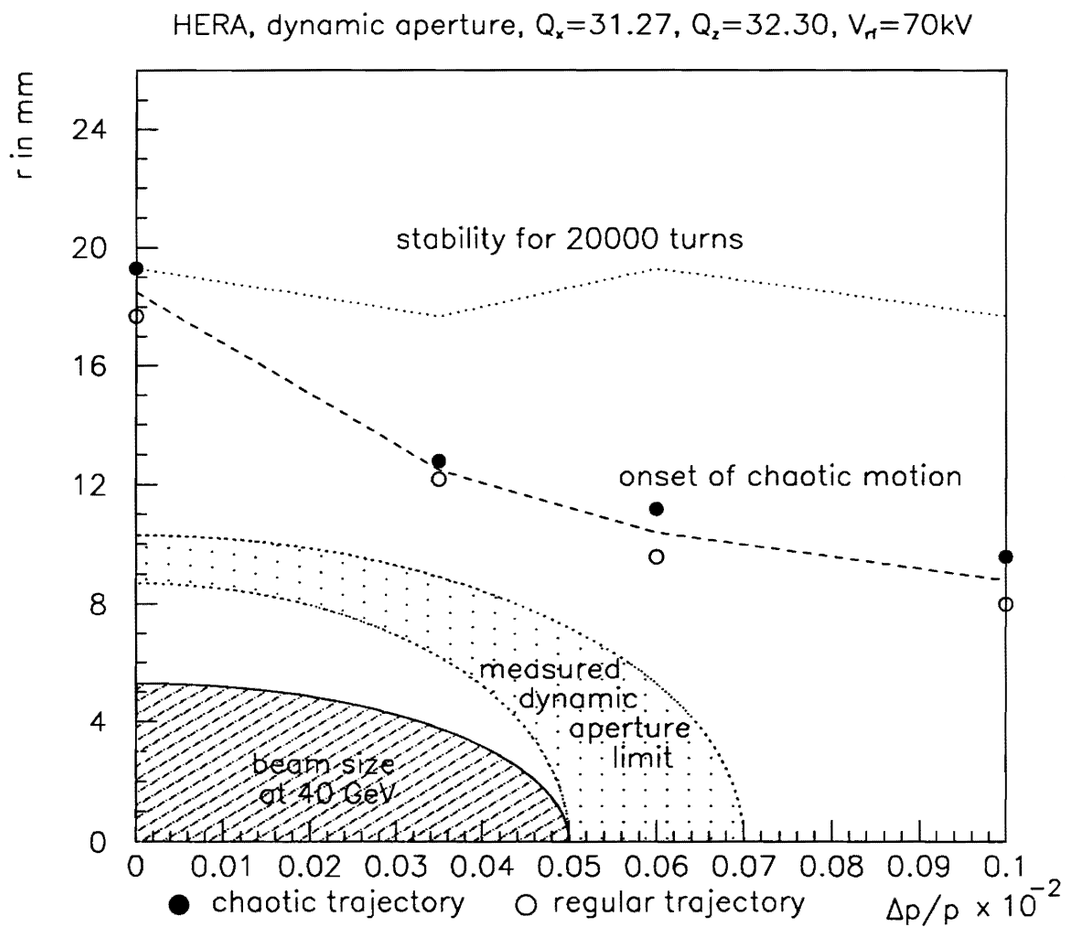

Figure 5.2: Predicted dynamic aperture for model II of HERA, in which the 20-pole coefficients b_{10} of the quadrupole magnets is a factor of ten larger than the measured values. As in the previous figure the aperture r in mm, defined by the equation $r = \sqrt{\beta(\epsilon_x + \epsilon_z)}$ with $\beta = 76$ m, is plotted as a function of the amplitude of momentum oscillations $\Delta p/p$. Also the chosen working point $Q_x = 31.27$, $Q_z = 32.30$ and the rf voltage of 70 kV are the same as in Fig. 5.1.

q	f_q in Hz	acceptance in mm mrad	
		$\Delta p/p = 0$	$\Delta p/p = 10^{-3}$
0	0	4.2	1.9
0.001	10	1.5	—
0.005	10	1.5	—
0.01	10	1.2	0.9
0.005	50	1.9	—
0.01	50	1.9	0.9
0.005	600	3.1	—
0.01	600	3.1	—

Table 5.1: Influence of tune modulation on the dynamic acceptance in HERA at $\Delta p/p = 0$ and $\Delta p/p = 10^{-3}$. The results are obtained by simulations of the six-dimensional motion with uncompensated linear coupling and do not differ for the two models of HERA. The modulation frequency f_q in Hz is related to the modulation tune Q_m by $f_q \equiv Q_m f_{rev}$, where f_{rev} denotes the revolution frequency ($f_{rev} = 47.3$ kHz for HERA).

It is of no great importance in which way the tune modulation is added. The reduction in acceptance is the same, if one either modulates the strength of all quadrupoles or if one simply adds an additional rotation with a modulated angle at the end of each turn, provided that the overall modulation amplitude is the same.

The impact of tune modulation on the dynamic acceptance can be illustrated by the results of two tracking studies:

Table 5.1 shows the reduction in the dynamic acceptance caused by a tune modulation of different frequency and amplitude. The data refer to a simulation performed for uncompensated linear coupling ($\kappa \approx 0.017$, where κ denotes the minimum difference between the two betatron tunes in the case of coupling [62]) and with full synchro-betatron motion. It can be seen that the sensitivity to the modulation frequency is much stronger than the sensitivity to the modulation amplitude and that a ripple of frequency 10–50 Hz can drastically reduce the aperture over a wide range of modulation amplitudes.

The effect of a 50-Hz ripple with an amplitude of 10^{-4} was simulated for pure betatron motion with different emittance ratios in the linearly decoupled accelerator ($\kappa \approx 0.003$). The results of this study are summarized in the two acceptance-diagrams of Fig. 5.3, which represent regular, chaotic and unstable trajectories for the non-modulated case and in the presence of tune modulation, respectively. It can be seen that the tune modulation reduces the aperture by about a factor of two.

In chapter 4 the modulation amplitudes due to power supply ripple have been estimated to be as large as 10^{-4}. The strong effect of tune modulation on the dynamic aperture observed in the tracking studies calls for an analytical study of the chaos-generating process.

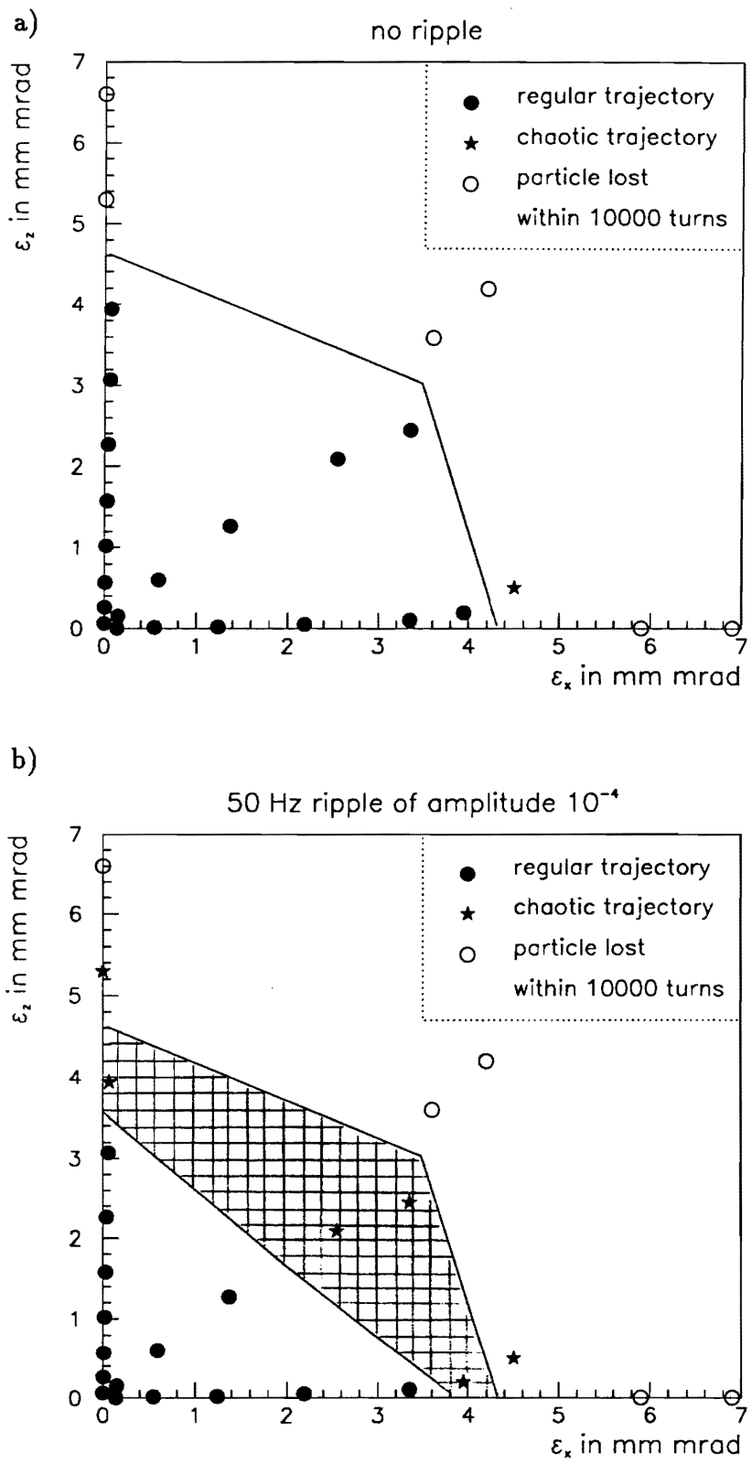

Figure 5.3: Vertical versus horizontal dynamic acceptance for model II of HERA in the case of pure betatron motion with compensated linear coupling; a) no tune modulation, b) 50 Hz tune ripple with amplitude 10^{-4}. The border between regular and chaotic trajectories is hardly affected by the value of the 20-pole coefficient b_{10} and about the same for the model I. Trajectories in the hatched region of diagram b) are chaotic only in the presence of tune modulation.

5.3 Parameters of High-Order Resonances

By a suitable combination of normal-form and factorization processes the parameters of all resonances $kQ_x + lQ_z = p$ up to 11th order can be evaluated inside the dynamic aperture of HERA. The basic procedure consists of two steps [23]. First, a four-dimensional truncated Taylor map of 11th order is extracted from a tracking code by the methods of differential algebra [12]. As a second step differential-algebra based normal-form transformations and Lie-algebraic factorizations are performed [23, 26], which bring the map into a particularly simple form. To illustrate the procedure, an overview of differential algebra and of normal-form methods is presented in appendix A.

An 8th order normal-form transformation for a model of the HERA proton ring still shows considerable deviations from tracking, which indicate that the order 8 is too low. For instance the tune dependence on amplitude is not well reproduced for emittances of about 4 mm mrad (see Fig. 5.4). However, small resonance denominators prevent a 9th order normal-form transformation to converge in the whole amplitude range of interest. A possible way out is to normalize the map M up to 8th order and subsequently to rewrite the remainder as a Dragt-Finn factorization [20], or — in other words — to apply first order perturbation theory in the 8th order normal-form coordinate frame. The original map M is then cast into the following form

$$M = A^{-1} e^{:-2\pi QI + t_3(I) + \ldots + t_8(I):} e^{:f_9(I,\phi):} \ldots e^{:f_{11}(I,\phi):} A + \mathcal{O}(12), \tag{5.2}$$

where the t_n and f_n are polynomials of degree n in $x_k = \sqrt{2I_k}\cos\phi_k$ and $p_k = -\sqrt{2I_k}\sin\phi_k$. '$A$' denotes the 8th order normal-form transformation. The detuning is deduced from the approximate Hamiltonian

$$H_{approx} = A^{-1}\left[QI - \frac{1}{2\pi}\{t_3(I) + \ldots + t_8(I) + < f_9(I,\phi) + \ldots + f_{11}(I,\phi) >_\phi\}\right]. \tag{5.3}$$

Tune curves for model II obtained by this method and those from an 8th and an 11th order normal-form analysis are compared with the tracking data in Fig. 5.4. Here and in the following, the amplitude values refer to the interaction point, where the horizontal and vertical beta function of the injection optics are $\beta_x \approx 28.5$ m and $\beta_z \approx 3.8$ m. The horizontal axis in Fig. 5.4 gives the starting amplitude at this point, the total scale corresponding to an emittance of 4 mm mrad. The initial angles x' and z' are chosen as zero.

In Fig. 5.4 the divergence of the 11th order normal-form analysis and the shortcoming of an 8th order normalization are clearly evident. The combination of a normal-form transformation and a subsequent Dragt-Finn factorization leads to a substantial improvement and reproduces the amplitude-dependent tunes up to the threshold of chaotic motion.

In order to verify the convergence of A^{-1}, the transformation can be directly applied to the tracking data. This is illustrated in Fig. 5.5 for a trajectory with an initial emittance $\epsilon_x \approx 2.2$ mm mrad and $\epsilon_z = 0$ mm mrad. Shown are the usual phase space projections and those in an 8th order normal-form coordinate frame. In the transformed coordinates, the motion in both planes is almost perfectly decoupled and circular. The small, but finite width of the circle in the vertical normal-form plane (Fig. 5.5 d)) is caused by nonlinear terms of order higher than 8 and can only be removed by increasing the order of the transformation.

Fig. 5.6 presents similar phase space plots for an initial vertical emittance of about 4 mm mrad. At this larger amplitude an 8th order transformation is still well behaved. A 9th order normal-form transformation, however, diverges strongly in the vertical plane (Fig. 5.6 f)), where the transformed coordinates become extremely large.

a)

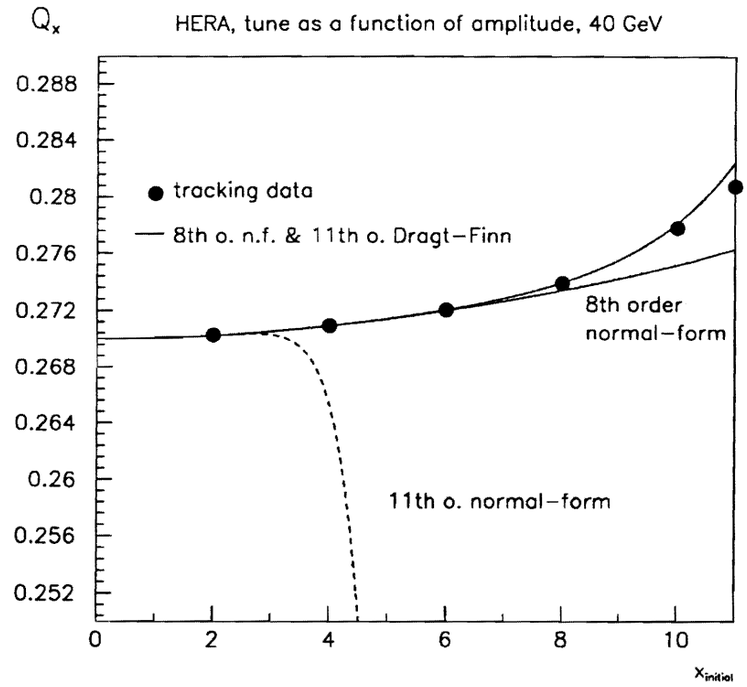

b)

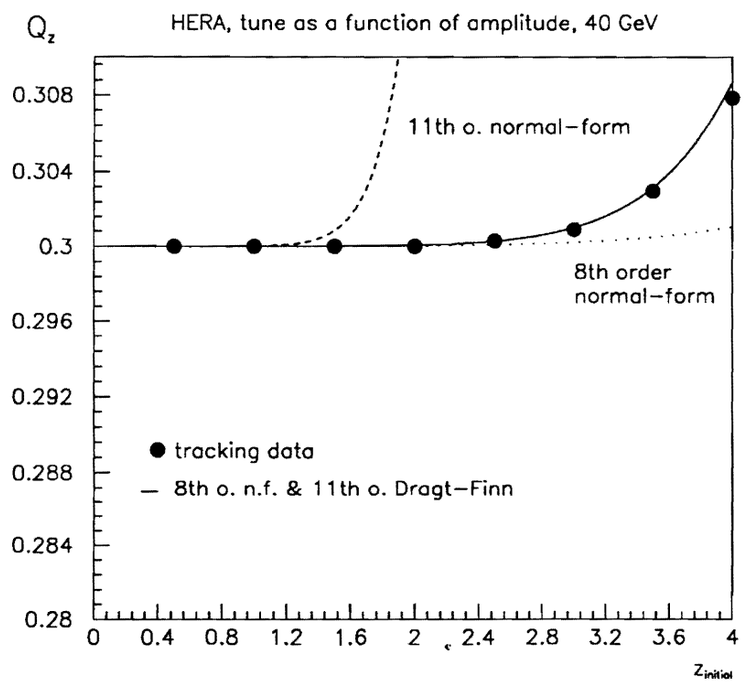

Figure 5.4: a) Horizontal tune Q_x as a function of the starting amplitude x_{start} ($\beta_x = 28.5$ m, $z_{start} = 0$), b) vertical tune Q_z as a function of the starting amplitude z_{start} ($\beta_z = 3.8$ m, $x_{start} = 0$). In both diagrams, the maximum amplitude corresponds to an emittance of about 4 mm mrad.

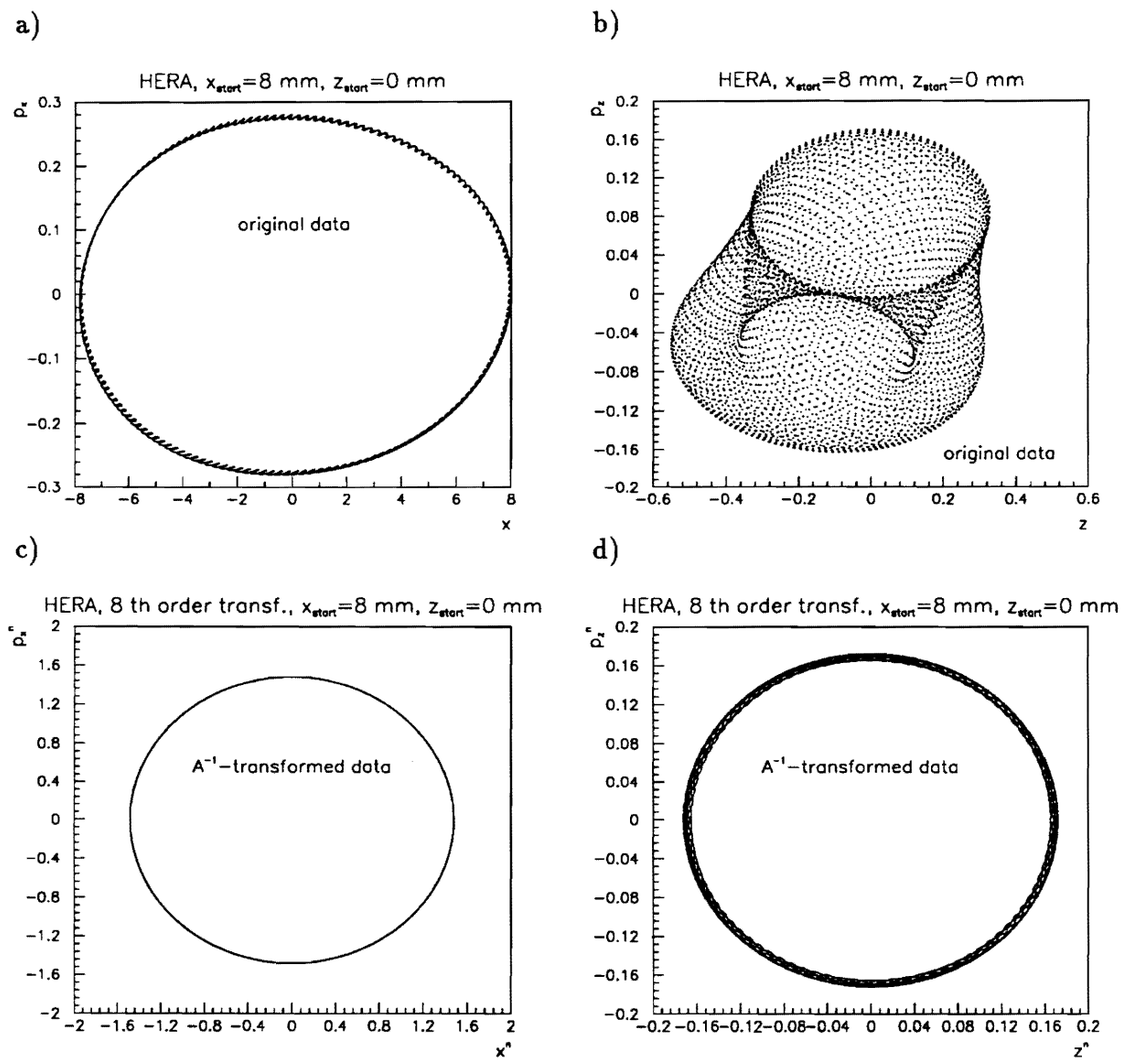

Figure 5.5: Tracking data for HERA at an initial emittance $\epsilon_x \approx 2.2$ mm mrad and $\epsilon_z = 0$ mm mrad; a) original horizontal plane, b) original vertical plane, c) horizontal plane normalized to 8th order, d) vertical plane normalized to 8th order.

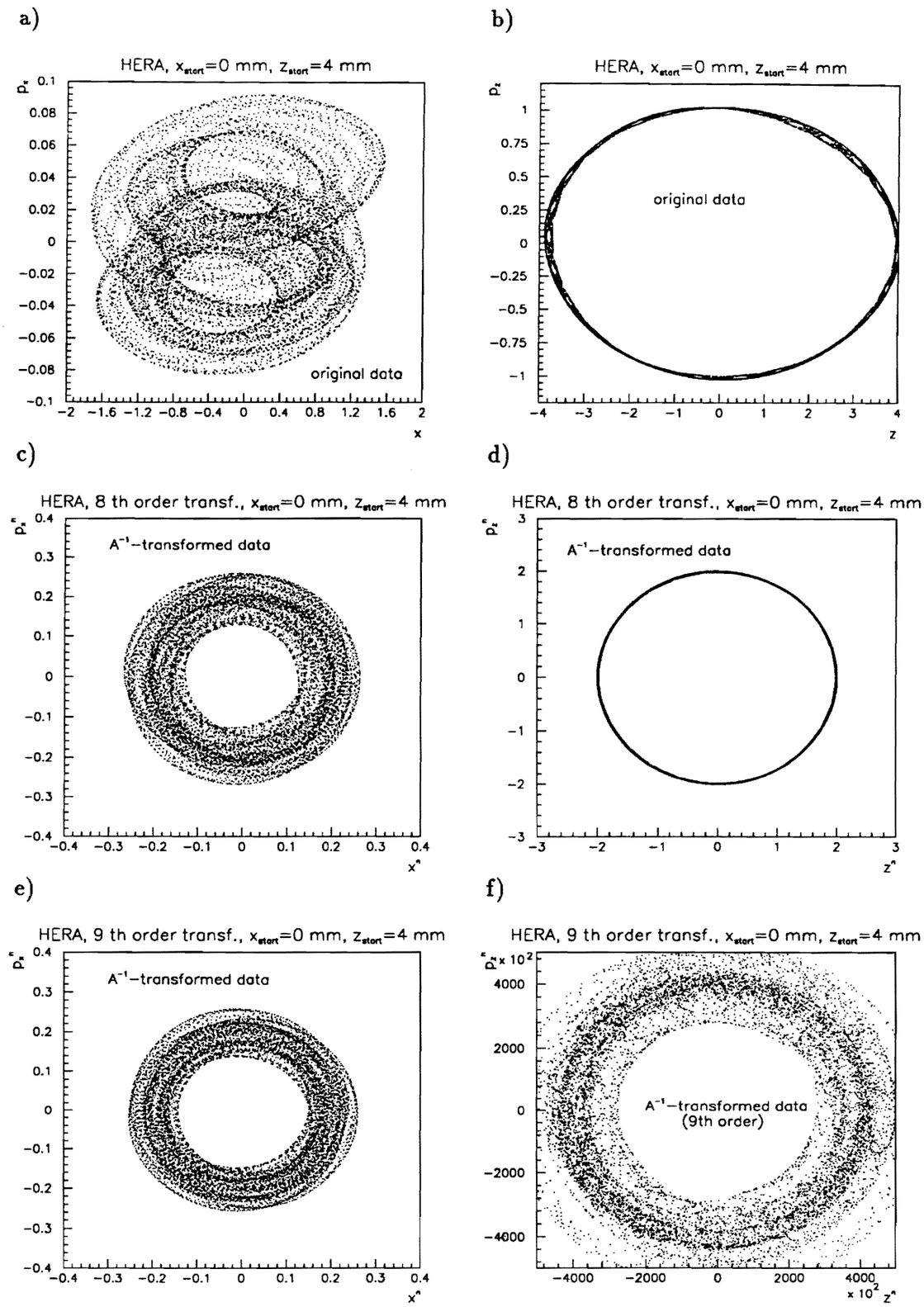

Figure 5.6: Tracking data for HERA at an initial emittance $\epsilon_x = 0$ mm mrad and $\epsilon_z \approx 4$ mm mrad; a)–b) original horizontal and vertical plane, c)–d) horizontal and vertical plane normalized to 8th order, e)–f) horizontal and vertical plane normalized to 9th order. Note the different scale in diagram f).

To identify the relevant high-order resonances the amplitude-dependent tunes are depicted in a tune diagram together with the resonance lines. This is done for three different working points in Fig. 5.7. Shown is the change of the tunes, if the initial emittance is varied between zero and $\epsilon_x = \epsilon_z = 4$ mm mrad. Also represented in the figure are all resonance lines through order 11. For the three working points, it is possible to identify 11, 6 and 11 resonances of order 7 to 11, which are crossed by the tune, if the starting emittance is changed continuously from 0 to 4 mm mrad along the three lines $\epsilon_x = 0$, $\epsilon_z = 0$ and $\epsilon_x = \epsilon_z$.

Fig. 5.8 shows an analogous diagram for model II, where only a single working point is investigated. In this case, 18 resonance-crossings are found. The larger number of resonances crossed can be ascribed to the detuning induced by the additional 20-pole component.

As illustrated in appendix A, the detuning and driving terms $\partial^2 g/\partial I^2$ and h can also be determined by the normal-form analysis. They are evaluated for all resonances crossed in Fig. 5.7. In Table 5.2 the results are listed for one of the working points. A compilation of the resonance-parameters for all three working points is given in appendix B along with normal-form results for model II.

x	z	Resonance	$\partial^2 g/\partial I_x^2$	$\partial^2 g/\partial I_x \partial I_z$	$\partial^2 g/\partial I_z^2$	h	Q_I
0.000	2.720	$-3Q_x + 6Q_z = 100$	$0.5 \cdot 10^{-2}$	$-0.4 \cdot 10^{-2}$	$0.26 \cdot 10^{-3}$	$0.2 \cdot 10^{-10}$	$2 \cdot 10^{-6}$
0.000	2.780	$6Q_x - 2Q_z = 123$	$0.5 \cdot 10^{-2}$	$-0.4 \cdot 10^{-2}$	$0.29 \cdot 10^{-3}$	$0.13 \cdot 10^{-14}$	$1.9 \cdot 10^{-8}$
0.000	2.800	$9Q_x + 2Q_z = 346$	$0.5 \cdot 10^{-2}$	$-0.4 \cdot 10^{-2}$	$0.30 \cdot 10^{-3}$	$0.14 \cdot 10^{-23}$	$6.1 \cdot 10^{-13}$
0.000	2.840	$3Q_x + 4Q_z = 223$	$0.55 \cdot 10^{-2}$	$-0.4 \cdot 10^{-2}$	$0.32 \cdot 10^{-3}$	$0.13 \cdot 10^{-9}$	$2.3 \cdot 10^{-6}$
0.000	3.960	$8Q_x + 3Q_z = 347$	$0.8 \cdot 10^{-2}$	$-0.57 \cdot 10^{-2}$	$0.18 \cdot 10^{-1}$	$0.33 \cdot 10^{-20}$	$2.9 \cdot 10^{-11}$
4.290	0.000	$7Q_x - 3Q_z = 122$	$0.33 \cdot 10^{-2}$	$-0.27 \cdot 10^{-2}$	$-0.71 \cdot 10^{-4}$	$0.9 \cdot 10^{-12}$	$5 \cdot 10^{-7}$
6.105	0.000	$-4Q_x + 7Q_z = 101$	$0.31 \cdot 10^{-2}$	$-0.22 \cdot 10^{-2}$	$-0.17 \cdot 10^{-3}$	$0.3 \cdot 10^{-16}$	$2 \cdot 10^{-9}$
7.150	0.000	$11Q_x = 344$	$0.30 \cdot 10^{-2}$	$-0.20 \cdot 10^{-2}$	$-0.19 \cdot 10^{-3}$	$0.11 \cdot 10^{-7}$	$6.3 \cdot 10^{-5}$
5.720	2.080	$7Q_x - 3Q_z = 122$	$0.39 \cdot 10^{-2}$	$-0.24 \cdot 10^{-2}$	$-0.27 \cdot 10^{-3}$	$0.16 \cdot 10^{-6}$	$2.2 \cdot 10^{-4}$
6.490	2.360	$-4Q_x + 7Q_z = 101$	$0.39 \cdot 10^{-2}$	$-0.21 \cdot 10^{-2}$	$-0.36 \cdot 10^{-3}$	$0.31 \cdot 10^{-6}$	$2.24 \cdot 10^{-4}$
8.415	3.060	$11Q_x = 344$	$0.38 \cdot 10^{-2}$	$-0.13 \cdot 10^{-2}$	$-0.62 \cdot 10^{-3}$	$0.77 \cdot 10^{-7}$	$1.9 \cdot 10^{-4}$

Table 5.2: Characteristics of high-order resonances in HERA as a function of starting amplitudes x and z for the working point $Q_x = 31.27$, $Q_z = 32.30$. At the point of observation $x = 11$ mm or $z = 4$ mm correspond to an emittance of about 4 mm mrad.

According to Tables B.1–B.4 an island tune of $2 \cdot 10^{-4}$ and a resonance order $n = 10$ may be considered typical for large amplitudes. The corresponding phase diagram is depicted in Fig. 5.9. It is evident that tune modulation frequencies above 50 Hz ($Q_m > 10^{-3}$) should be harmless from a sideband-overlap point of view.

Fig. 5.10 shows the island width $\Delta\epsilon_{\text{tot}} \equiv 2\Delta I_{\text{tot}}$, computed from (3.69), as a function of the emittance $\epsilon \equiv \epsilon_x + \epsilon_z$, for the resonances of order 7–11 listed in Tables B.1–B.3 and B.4. The resonance width is approximately parametrized by

$$\Delta\epsilon_{\text{tot}} \approx 2 \cdot 10^{-4} \cdot \epsilon^4 \cdot \ (\text{mm mrad})^{-3}. \tag{5.4}$$

In Fig. 5.11 the absolute width of the stochastic layer $w \cdot \Delta I_{\text{tot}}$ in mm mrad (equations (3.69) and (3.96)) is represented as a function of the modulation frequency for a typical high-order resonance in HERA (10th resonance in Table 5.2). The modulation amplitude $q = 10^{-4}$ assumed can for instance be caused by power supply ripple.

Fig. 5.12 is the same as Fig. 5.11 apart from the larger value of the modulation amplitude $q = 10^{-3}$, which could be due to synchrotron oscillations and a nonzero chromaticity. The design

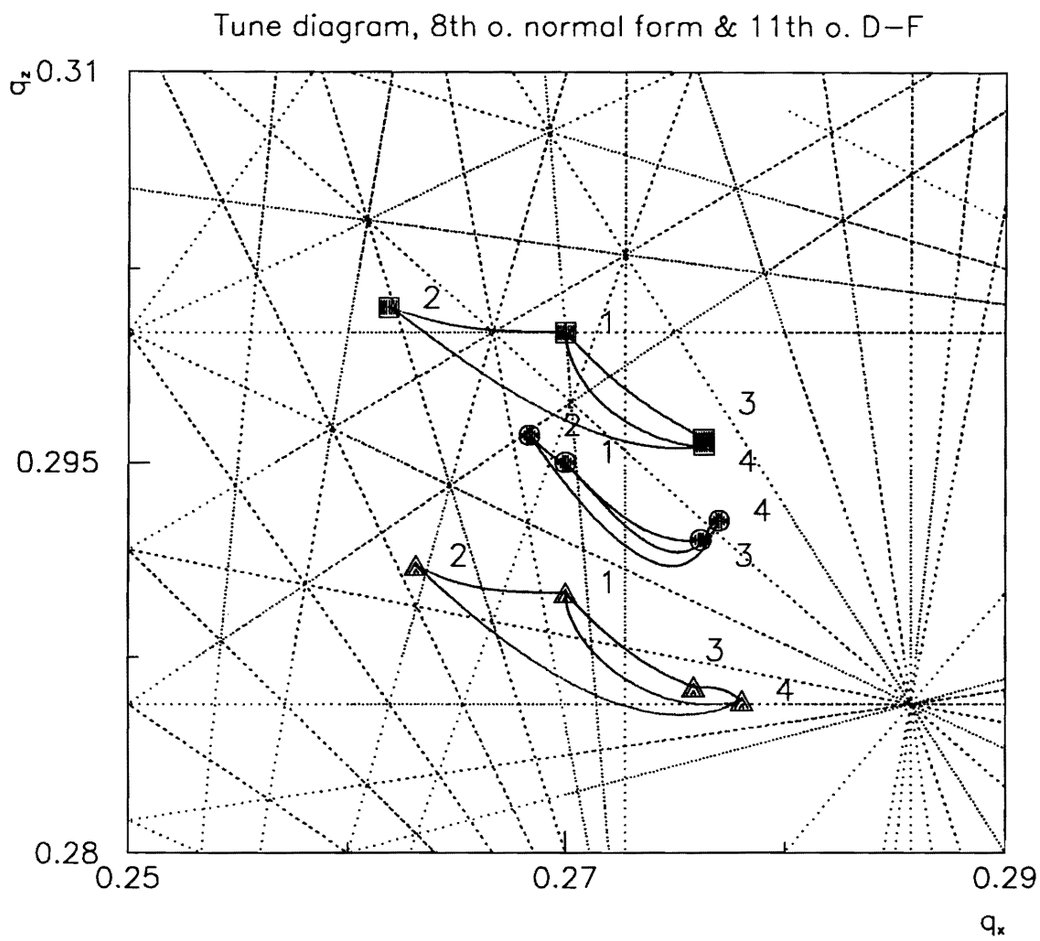

Figure 5.7: Diagram of the amplitude-dependent particle tunes for the HERA proton ring (model I) and of all resonance lines up to order 11. The tunes are obtained by the combined 8th order normal-form analysis / 11th order Dragt-Finn factorization. The numbered dots are tunes for special values of the starting emittances:
1 $\epsilon_x = 0.$, $\epsilon_z = 0$, **2** $\epsilon_x = 0$, $\epsilon_z = 4$ mm mrad,
3 $\epsilon_x = 4$ mm mrad, $\epsilon_z = 0$, **4** $\epsilon_x = 4$ mm mrad, $\epsilon_z = 4$ mm mrad.
The connecting lines correspond to a continuous variation of the initial emittances between these values. The squares, circles and triangles refer to the working points ($Q_x = 31.27$, $Q_z = 32.30$), ($Q_x = 31.27$, $Q_z = 32.295$) and ($Q_x = 31.27$, $Q_z = 32.29$), respectively.

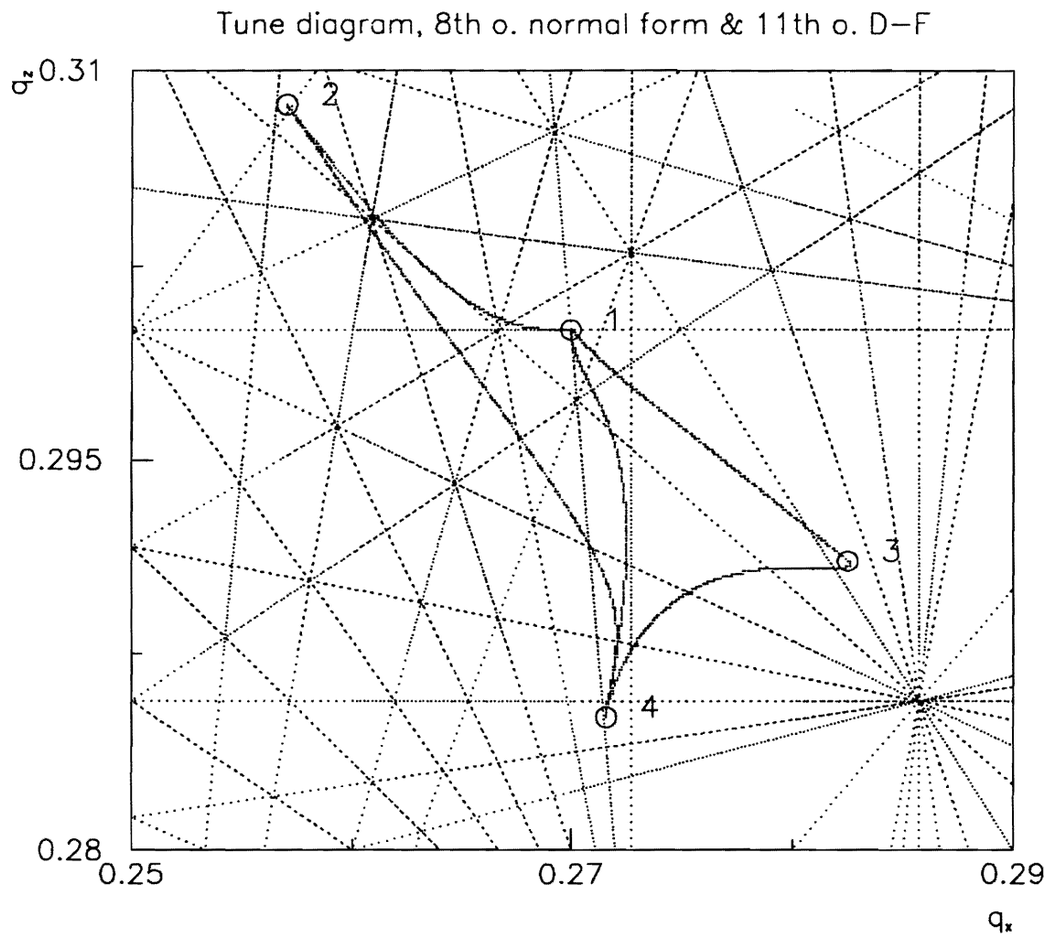

Figure 5.8: Diagram of the amplitude-dependent particle tunes for model II and of all resonance lines up to order 11. The tunes are obtained by the combined 8th order normal-form analysis / 11th order Dragt-Finn factorization. The numbered dots are tunes for special values of the starting emittances:
1 $\epsilon_x = 0$, $\epsilon_z = 0$, **2** $\epsilon_x = 0$, $\epsilon_z = 4$ mm mrad,
3 $\epsilon_x = 4$ mm mrad, $\epsilon_z = 0$, **4** $\epsilon_x = 4$ mm mrad, $\epsilon_z = 4$ mm mrad.
The connecting lines correspond to a continuous variation of the initial emittances between these values. The chosen working point is $Q_x = 31.27$, $Q_z = 32.30$.

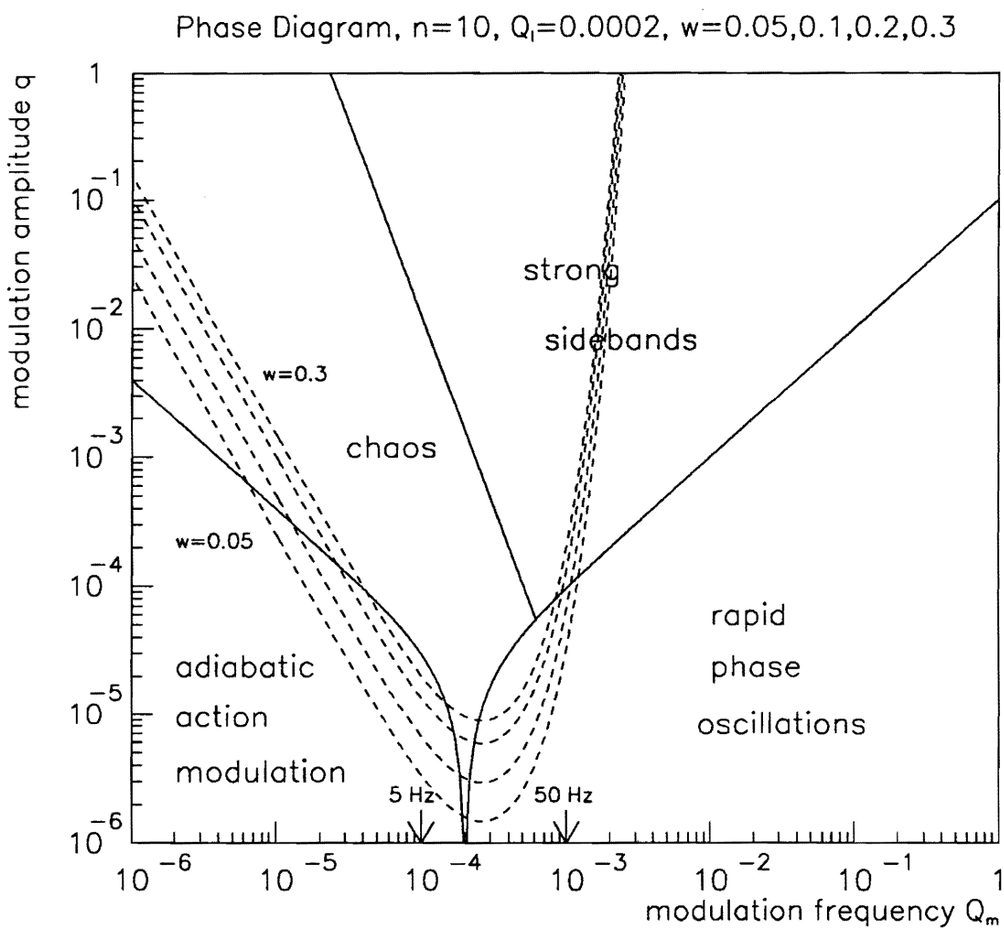

Figure 5.9: Phase diagram for the island tune $Q_I = 2 \cdot 10^{-4}$ and the resonance order $n = 10$ according to (3.94) (solid curves) and contour lines (3.96) for $w = 0.05, 0.1, 0.2, 0.3$ (dotted curves). This diagram represents a typical high-order resonance at injection energy in HERA.

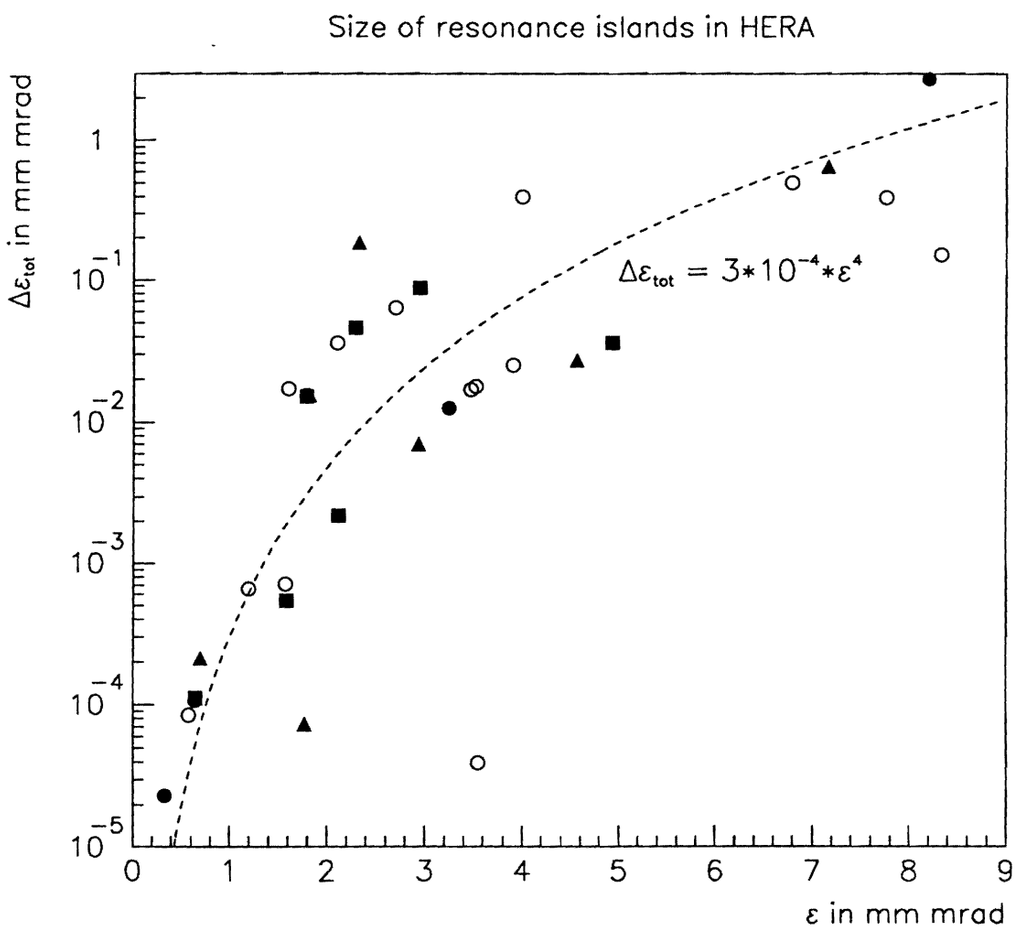

Figure 5.10: Island width $\Delta\epsilon_{tot} \equiv 2\Delta I_{tot}$ (3.69) as a function of the resonant single-particle emittance $\epsilon \equiv \epsilon_x + \epsilon_z$ in units of mm mrad, for the resonances of order 7–11 listed in Tables B.1–B.3 (closed symbols) and B.4 (open circles). The closed squares, circles and triangles refer to the three different working points of Figure 5.7. The dotted curve represents (5.4).

synchrotron frequency of 14 Hz is close to the maximum width of the dotted curve (3.96). For this fairly large value of q it becomes important that the relative width w, computed from (3.96), has an upper limit of about 2. As already mentioned in section 3.12, this limit is related to the complete destruction of the resonance islands. If, for each modulation frequency, the minimum of (3.96) and 2 is chosen as the value of w, we get the solid curve in Fig. 5.12.

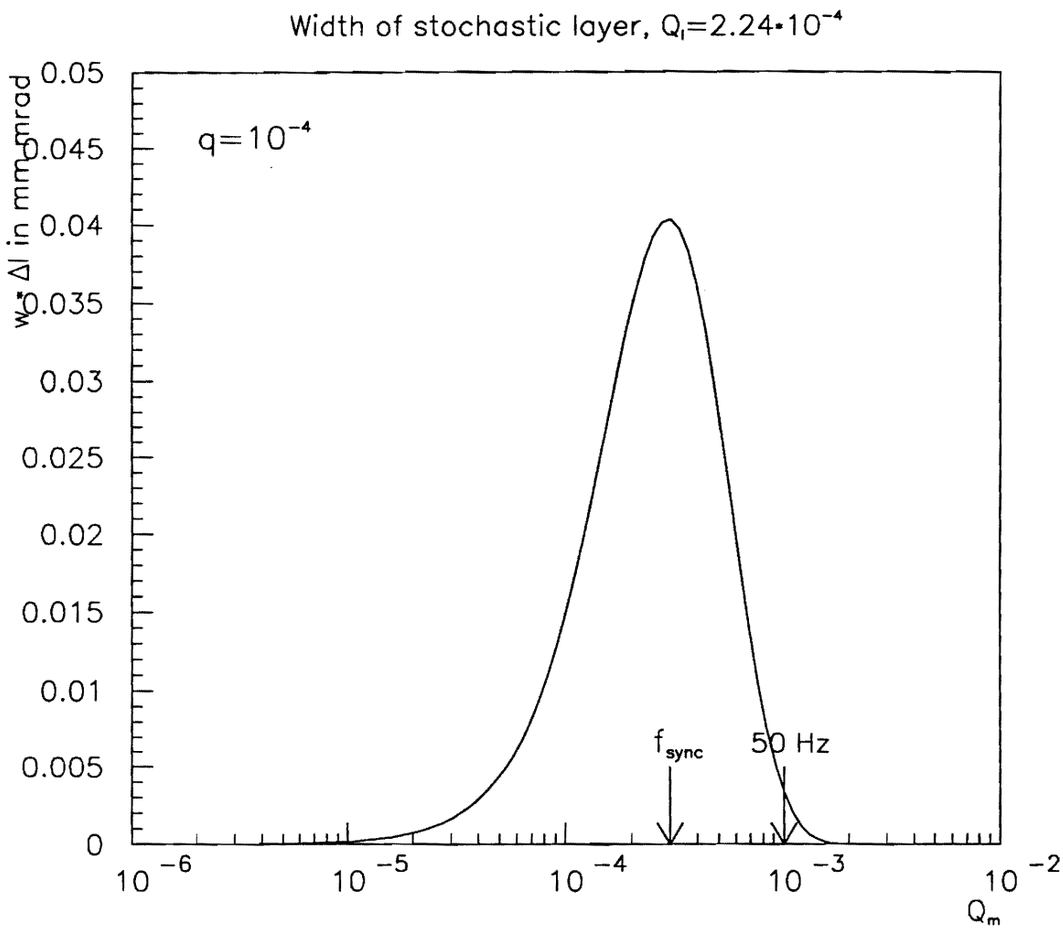

Figure 5.11: Absolute width of the stochastic layer $w \cdot \Delta I_{tot}$ in units of mm mrad according to equations (3.69) and (3.96) as a function of the modulation frequency Q_m for a typical 11th order resonance in HERA. This resonance (10th entry of Table 5.2) is crossed at an emittance value of $\epsilon = \epsilon_x + \epsilon_z \approx 2.95$ mm mrad and has an island tune $Q_I \approx 2.24 \cdot 10^{-4}$. The modulation amplitude $q = 10^{-4}$ is characteristic for the effect of power supply ripple (see chapter 4).

In order to compare the effect of different modulation frequencies in a more quantitative way, the chaotic fraction of phase space Γ (3.106) is calculated for a modulation amplitude $q = 10^{-4}$. To this end the sum in (3.106) is extended over all resonances of Tables B.1–B.3. Fig. 5.13 shows that the sensitivity to tune modulation is highest for modulation frequencies between 5 Hz and 50 Hz. Chaotic trajectories may cover about 10% of the phase space in the

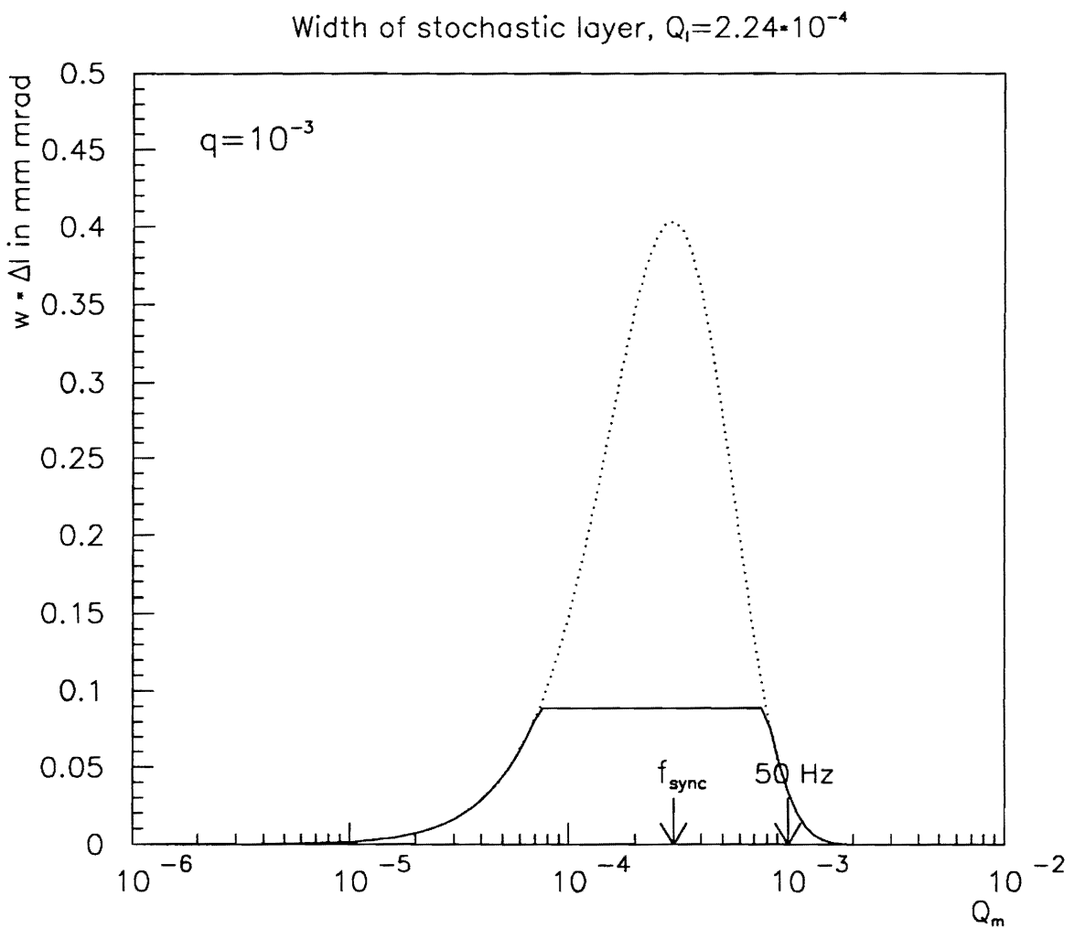

Figure 5.12: Absolute width of the stochastic layer $w \cdot \Delta I_{tot}$ in units of mm mrad for the same resonance as in Fig. 5.11, assuming the larger modulation amplitude $q = 10^{-3}$. A modulation amplitude like this could be caused by synchrotron oscillations and nonzero chromaticity. The dotted curve depicts equation (3.96) solely. The solid curve is obtained by regarding 2 as an upper limit for w, which corresponds to the complete destruction of the resonance island (see also section 3.12).

presence of a 50-Hz power supply ripple. For frequencies above 100 Hz the effect of the tune modulation is negligible.

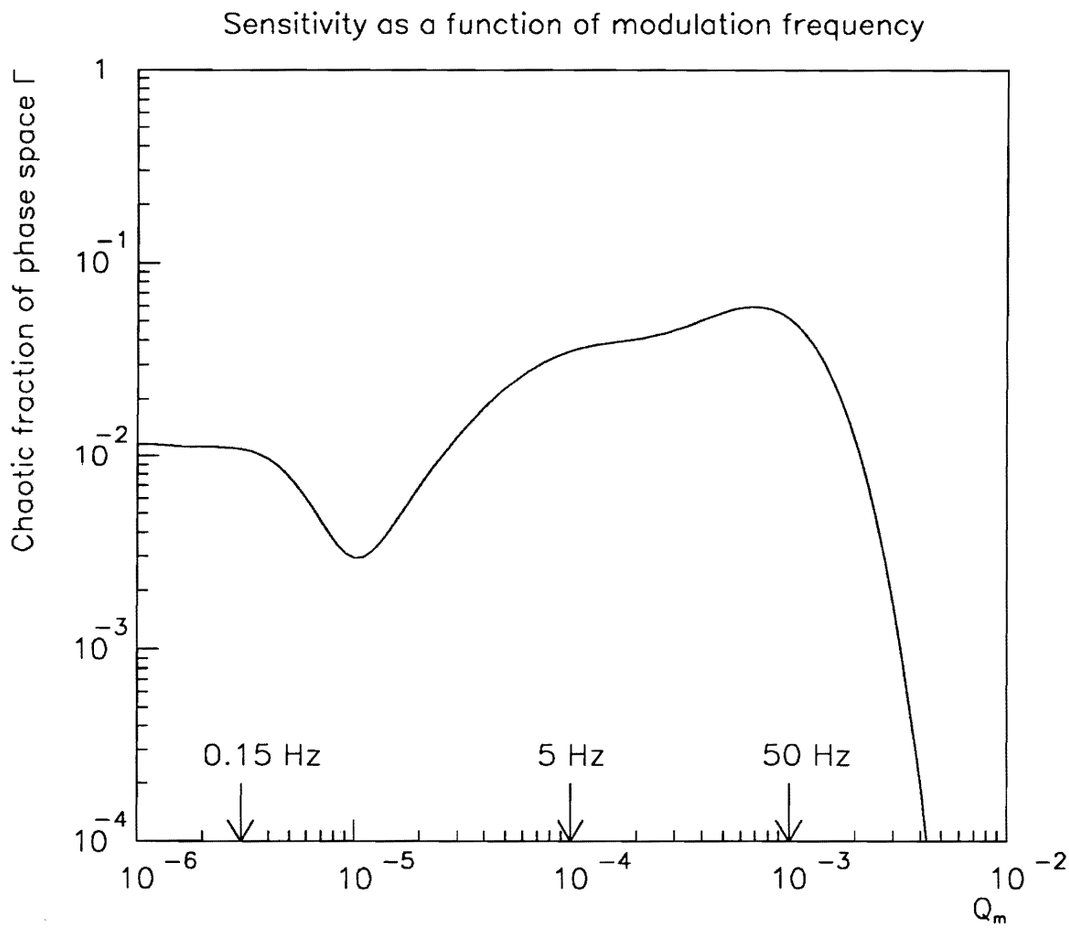

Figure 5.13: Chaotic fraction of phase space Γ (3.106) as a function of the modulation frequency for a constant modulation amplitude $q = 10^{-4}$.

5.4 Emittance Growth Rates

Equation (3.107) may be used to obtain an estimate of the global emittance growth rate caused by high-order resonances under the influence of an external tune modulation. It amounts to computing the weighted sum of the 'local' emittance growth rates near individual resonances. The calculated growth rate (3.107) of the transverse emittance $\epsilon \equiv \epsilon_x + \epsilon_z$ is depicted in Fig. 5.14 for modulation frequencies between 0.05 and 500 Hz, summing over all resonances of Tables B.1–B.3.

The emittance-dependent diffusion coefficient $D(\epsilon)$, defined in (3.110), is shown in Fig. 5.15 for model I and model II assuming a ripple frequency of 50 Hz. Three regions in emittance can

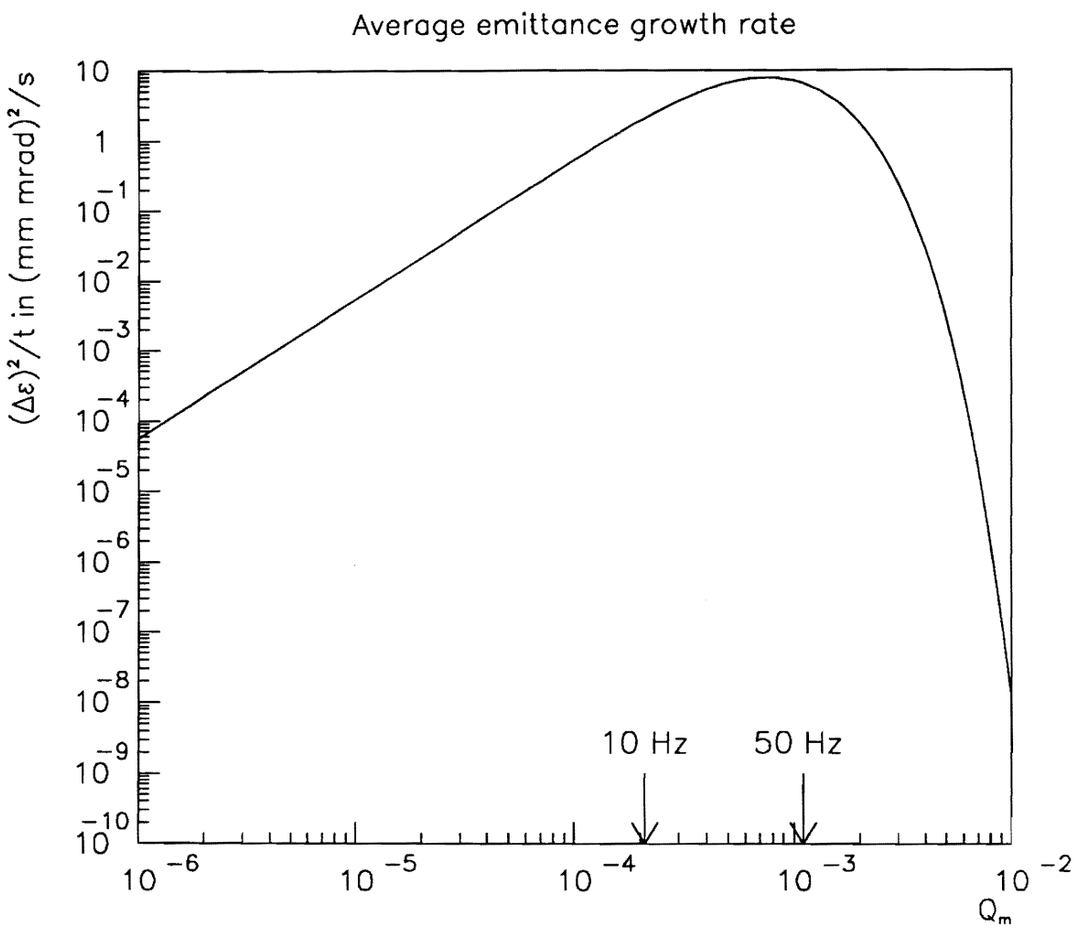

Figure 5.14: Global emittance growth rate $< (\Delta\epsilon)^2/\Delta t >_{\mathbf{global}}$ as a function of the modulation frequency. Note that, according to (3.107), the growth rate does not depend on the modulation amplitude q.

be distinguished:

A threshold ϵ_0 of tune-modulation-induced diffusion is observed at about

$$\epsilon_0 \approx (1 - 1.5) \text{ mm mrad.} \tag{5.5}$$

This threshold can be regarded as an estimate of the dynamic acceptance. Its value is about the same for both investigated models and is in remarkable agreement with the threshold of chaos found in tracking simulations including tune modulation (section 5.2) and with the actually observed acceptance of 1.2 mm mrad (section 5.1).

Beyond about 8 mm mrad in the case of model I and beyond about 4 mm mrad for model II the diffusion coefficient reaches values in the order of 1 (mm mrad)^2/s, which would show up as a rapid particle loss. In fact, these emittance-values are consistent with the stability-limit over 20 000 turns found in six-dimensional tracking studies for the two models (see Figures 5.1 and 5.2).

In an intermediate amplitude range, a possible, very rough parametrization of the diffusion coefficient is

$$D(\epsilon) \sim c \cdot \epsilon^{\alpha}, \tag{5.6}$$

where c is approximately

$$c \approx 5 \cdot 10^{-14} \text{ (mm mrad)}^{2-\alpha} \text{ s}^{-1}. \tag{5.7}$$

The exponent α in (5.6) is of particular interest since the predicted dependence of the diffusion rate on ϵ can directly be compared with collimation studies in the HERA proton ring [64, 65]. From Fig. 5.15 follows

$$\alpha \approx 15. \tag{5.8}$$

Nearly the same values of ϵ_0 and α are obtained for a modulation frequency of 10 Hz. According to (3.111) the locally averaged emittance growth is given by

$$\left\langle \overline{\frac{\Delta\epsilon}{\Delta t}} \right\rangle \approx \alpha c \epsilon^{\alpha-1}, \tag{5.9}$$

leading to

$$\left\langle \overline{\frac{\Delta\epsilon}{\Delta t}} \right\rangle \approx \left\{ \begin{array}{c} 10^{-11} \\ 10^{-8} \\ 2 \cdot 10^{-4} \end{array} \right\} \text{mm mrad s}^{-1} \quad \text{at} \quad \epsilon = \left\{ \begin{array}{c} 1.2 \\ 2.0 \\ 4.0 \end{array} \right\} \text{mm mrad.} \tag{5.10}$$

It should be mentioned, that the large value of the exponent α is consistent with results from a phenomenological analysis of beam profile evolutions observed at the Fermilab Tevatron. For the Tevatron diffusion experiment, the best fit to the measured data was achieved with rapidly growing functions such as $D = D_0\epsilon^{\alpha}$ with $\alpha \geq 6$ [66].

5.5 Range of Validity of the Model

The average value of the diffusion coefficient in the phase space region between two adjacent resonances, defined in (3.110), is suitable for a comparison with multiple scattering processes, that affect all particles equally.

In addition several physical processes give a physical meaning to the phase space average. Some of these are briefly dicussed in this section.

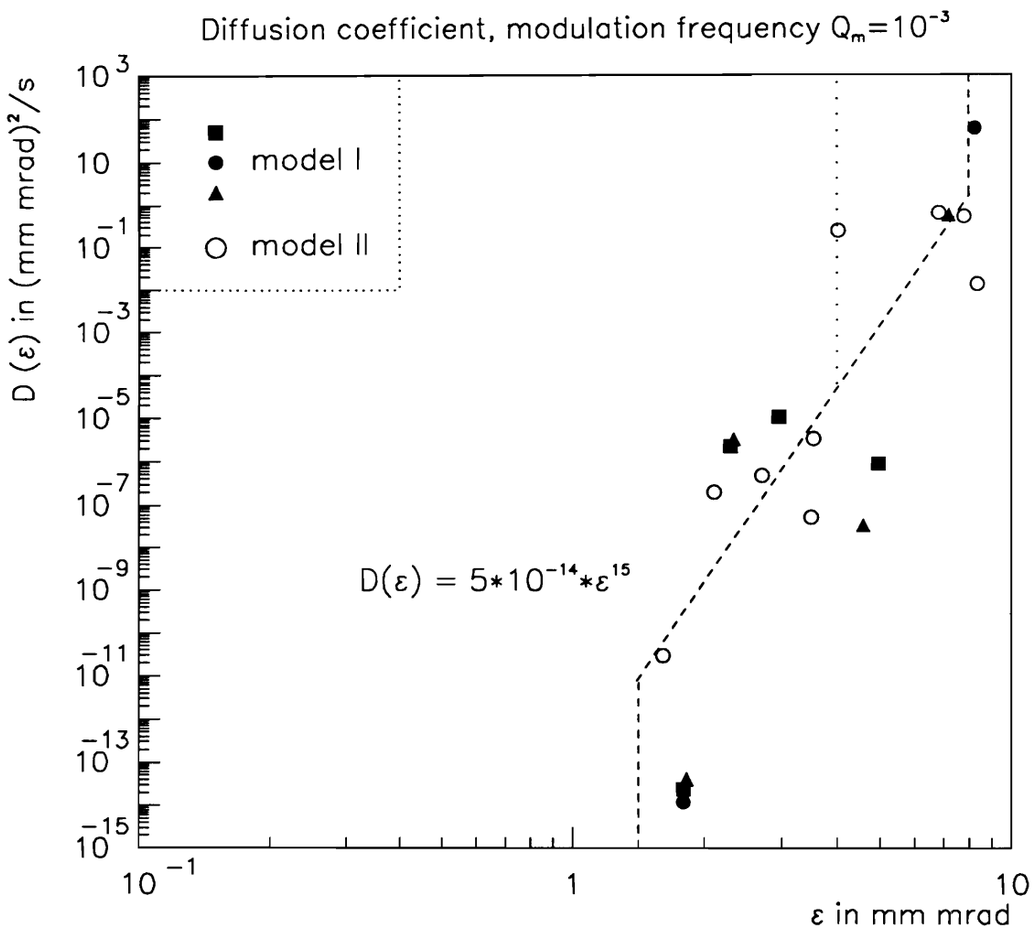

Figure 5.15: Emittance-dependent diffusion coefficient $D(\epsilon)$ (3.110) as a function of the transverse single-particle emittance ϵ in units of mm mrad, for the resonances of Tables B.1–B.3 (closed symbols) and B.4 (open circles). A modulation frequency $Q_m = 10^{-3}$ (corresponding to 50 Hz) is assumed. The closed squares, circles and triangles refer to the three different working points of Figure 5.7. Below $\epsilon_0 \approx 1.4$ mm mrad, demarcated by a vertical dashed line, all trajectories are regular. At 8 or 4 mm mrad, indicated by a dashed and a dotted vertical line, respectively, the diffusion coefficient $D(\epsilon)$ becomes of the order of 1 (mm mrad)$^2/s$. In the intermediate emittance range, $D(\epsilon)$ can be roughly parametrized by an exponentially growing function like (5.6).

Over periods of hours considerable slow changes of orbit and tunes are observed during the operation of HERA. These are mainly due to drifts in the power supplies and to temperature effects. If the tunes change, the resonance islands will alter their position in phase space too. Particles are lost from the chaotic layer and other, previously regular protons are trapped inside the stochastic layer, if the resonance islands move in phase space. Only the particles which are currently inside the chaotic region suffer a diffusion in action. The resulting emittance growth averaged over long time periods equals the emittance growth averaged over the phase space, provided that the change in the island position is faster than the diffusion in the chaotic regions. From this condition we can derive a rough criterion for the range of validity of the model. If we denote the mean change of the machine tune per unit time by $\dot{Q}$, the rate at which the position of the island changes is about

$$\left(\frac{\Delta\epsilon}{\Delta t}\right)_{island-drift} \approx \frac{4}{\frac{\partial^2 g}{\partial I^2}}\dot{Q} \tag{5.11}$$

Typically the tune changes by 10^{-4} during 1 hour. From diagram 5.4, the corresponding emittance change is roughly 0.05 mm mrad. Hence the islands alter their position at a rate

$$\left(\frac{\Delta\epsilon}{\Delta t}\right)_{island-drift} \approx 1.4 \cdot 10^{-5} \text{ mm mrad s}^{-1}. \tag{5.12}$$

For predicted emittance growth rates larger than this value, the validity of the phase space averaging is no longer guaranteed. Using the growth rate (5.9) the drift rate (5.12) can be translated into a 'critical' emittance

$$\epsilon^{critical}_{island-drift} \approx 3.3 \text{ mm mrad}. \tag{5.13}$$

For smaller values of the emittance the phase space average has a physical meaning.

According to Tables B.1–B.3 and Fig. 5.15 the distance between two resonance islands in HERA is about $\delta\epsilon \approx 0.5 - 1.0$ mm mrad. Therefore almost every part of the phase space has been covered by resonance islands roughly after a time $\tau_{ave} \approx \delta\epsilon/(\frac{\Delta\epsilon}{\Delta t})_{island-drift} \approx 10 - 20$ hours.

A second process which can cause an averaging in phase space is residual gas scattering (see section 8). The actual emittance growth due to gas scattering $(\Delta\epsilon/\Delta t)_{res.gas} \approx 1.2 \cdot 10^{-7}$ mm mrad s^{-1} (8.27) is a factor 100 smaller than the critical growth rate (5.12) due to drifts of the resonance islands and is, therefore, of minor importance.

Resonances of order higher than 11 cause tiny chaotic regions everywhere in phase space, which form a dense web of stochastic layers. The 'microchaos' may enhance the phase space averaging effect of the island drifts. It will not be attempted here to quantify this contribution.

Chapter 6

Beam-Beam Interaction

6.1 Model

As shown in appendix A, a Taylor expansion using differential algebra is not adequate for the treatment of the beam-beam interaction. In this chapter, therefore, a different approach is followed, namely the island parameters of high-order resonances for the beam-beam interaction are deduced by first order perturbation theory. To simplify the analysis, we will limit ourselves to the case of round beams. In this special case many results can be stated explicitly without making use of numerical calculations. It is worthwhile to note that the round beam scenario is a viable option for ep collision in HERA [67].

Because of the moderate electron beam-beam tune shift $\bar{\xi}_e \approx 0.01 - 0.02$, no blowup of the electron beam is expected and it is justified to focus the attention on the incoherent single particle dynamics of the protons (weak-strong approximation).

In Table 6.1 a few important beam-beam parameters are listed that are used in our subsequent analysis. The quantities $\bar{\epsilon}_{x,p}$ and $\bar{\epsilon}_{z,p}$ are the two-sigma proton beam emittances at 820 GeV, defined by

$$\bar{\epsilon}_{y,p} = \frac{4\sigma_y^2}{\beta^*_{y,p}} \qquad \text{for} \qquad y = x,\, z. \tag{6.1}$$

Assuming a Gaussian bunch shape the two-sigma emittance corresponds to 86% of the beam. The beam-beam tune shift in Table 6.1 is about four times larger than the one quoted in [67] in order to incorporate the effect of several interaction regions. Almost all quantities of interest, that will be derived, are proportional to the proton beam-beam tune shift $\bar{\xi}_p$ or are independent of it. Hence the extrapolation to other values of $\bar{\xi}_p$ is straightforward.

Parameter	Value
$\sigma^*_{x,e}, \sigma^*_{z,e}$	0.147 mm
$\sigma^*_{x,p}, \sigma^*_{z,p}$	0.146 mm
$\bar{\xi}_{x,p}, \bar{\xi}_{z,p}$	0.0024
$\beta^*_{x,p}, \beta^*_{z,p}$	3.0 m
$\bar{\epsilon}_{x,p}, \bar{\epsilon}_{z,p}$	0.028 mm mrad

Table 6.1: Some beam-beam parameters for the round beam scenario.

The simple model consists of a beam-beam kick and a four-dimensional rotation. Linear coupling between the two transverse planes of motion is disregarded and also the nonlinear magnetic field errors, which are negligible in view of the small transverse beam size at large proton energies.

Our analysis is based on the working hypothesis that an interplay of high-order resonances driven by the beam-beam interaction and an external harmonic tune modulation limits the beam lifetime and leads to particle losses at large amplitudes. Other phenomena, such as a random tune drift, are considered only in so far as they give rise to the averaging in phase space discussed in section 5.5.

6.2 Hamiltonian

The general Hamiltonian reads

$$H(I_x, I_z, \phi_x, \phi_z, \theta) = Q_x I_x + Q_z I_z + V(I_x, I_z, \phi_x, \phi_z) \sum_p e^{ip\theta} \frac{1}{2\pi}. \tag{6.2}$$

The variables $I_{x,z}$ and $\phi_{x,z}$ are related to x and z in the usual way,

$$x = \sqrt{2\beta I_x} \cos\phi_x \text{ and } z = \sqrt{2\beta I_z} \cos\phi_z, \text{ where } \beta \equiv \beta^*_{x,p} = \beta^*_{z,p}. \tag{6.3}$$

The beam-beam potential V is rotationally symmetric and can be obtained by integrating the beam-beam kick

$$V(r) = \frac{8\pi\tilde{\xi}\sigma^2}{\beta} \int_{-\infty}^{r} \frac{1}{\hat{r}}(1 - e^{-\frac{\hat{r}^2}{2\sigma^2}})\, d\hat{r}, \tag{6.4}$$

where $r^2 = x^2 + z^2$ for centered collisions and $\tilde{\xi} \equiv \tilde{\xi}_{x,p} = \tilde{\xi}_{z,p}$. The result can be expressed in terms of the exponential integral Ei,

$$Ei(u) \equiv \int_{-\infty}^{u} \frac{e^{u'}}{u'}\, du' \qquad (u > 0). \tag{6.5}$$

The integral has to be understood as the principal value. Using Ei the potential (6.4) is written as

$$V(x, y) = \frac{4\pi\tilde{\xi}\sigma^2}{\beta} \left[-E_i\left(-\frac{r^2}{2\sigma^2}\right) + \ln\left(\frac{r^2}{2\sigma^2}\right) \right]. \tag{6.6}$$

In the Hamiltonian (6.2) this expression is multiplied by $\sum \delta(\theta + n2\pi) = \sum \exp(ip\theta)/(2\pi)$ to take into account the localisation of the kick. The exponential integral E_1, which is related to the function Ei via [1] [68]

$$Ei(x) = -\frac{1}{2}(E_1(-x + i0) + E_1(-x - i0)) = \gamma + \ln|x| + \sum_{n=1}^{\infty} \frac{x^n}{n \cdot n!}, \tag{6.7}$$

is supported by commercial program libraries [69].

Similar to the treatment of tune modulation and nonlinear magnetic field errors at injection energy, the general Hamiltonian (6.2) is replaced by a single-resonance approximation of the form (3.57)

$$H(I_x, I_z, \phi_x, \phi_z, \theta) = I_x Q_{x,0} + I_z Q_{z,0} + g(I_x, I_z) + h(I_x, I_z) \cos(k\phi_x + l\phi_z - p\theta), \tag{6.8}$$

which will be used in the later analysis. For different resonance orders the tune shifts $\partial g/\partial I_{x,z}$ and the second derivatives of g as well as the driving term h have to be calculated.

[1] The quantity $\gamma \approx 0.57721\ldots$ is Euler's constant.

6.3 Tune Shift and its Derivatives

The tune shift is obtained by taking the derivative of the Hamiltonian (6.2) with respect to the action $I_{x,z}$ and averaging over the angle variables. It reads

$$\frac{\partial g}{\partial I_{x,z}} = \left\langle 4\tilde{\xi}\sigma^2 \frac{1}{r^2}(1 - e^{-\frac{r^2}{2\sigma^2}}) \right\rangle_{\phi_x,\phi_z}, \tag{6.9}$$

where

$$r^2 = x^2 + z^2 = 2\beta(I_x \cos^2\phi_x + I_z \cos^2\phi_z). \tag{6.10}$$

Let us restrict the analysis to the diagonal $I_x = I_z \equiv I$ to represent a typical behavior. In (6.10) only even powers of $\cos\phi_x$ and $\cos\phi_z$ appear. Making use of the general relation

$$\frac{1}{2\pi}\int_0^{2\pi} \cos^{2m}\phi\, d\phi = \frac{1}{2^{2m}}\begin{pmatrix} 2m \\ m \end{pmatrix} \tag{6.11}$$

one can average over both angles and arrive at

$$\frac{\partial g}{\partial I_{x,z}} = 2\tilde{\xi}\left[\frac{1}{2} + \sum_{n=1}^{\infty}\left(\frac{\beta I}{\sigma^2}\right)^n (-1)^n \frac{1}{(n+1)!}\cdot C_n\right] \tag{6.12}$$

where the coefficients C_n are of the form

$$C_n \equiv \frac{1}{2^{2n+2}}\sum_{m=0}^{n}\begin{pmatrix} n \\ m \end{pmatrix}\begin{pmatrix} 2n-2m+2 \\ n-m+1 \end{pmatrix}\begin{pmatrix} 2m \\ m \end{pmatrix} \tag{6.13}$$

The first two terms of the series (6.12) are

$$\frac{\partial g}{\partial I_{x,z}} = \tilde{\xi}\left[1 - \frac{5}{8}\left(\frac{\beta I}{\sigma^2}\right) + \ldots\right] \tag{6.14}$$

The second derivatives of the function $g(I_x, I_z)$ are obtained analogously. Again one has to average over the angles. The result is

$$\begin{aligned} \frac{\partial^2 g}{\partial I_x^2} &= 2\beta\tilde{\xi}\sigma^2 \sum_{n=0}^{\infty}(-1)^n \frac{(\beta I)^n}{(\sigma^2)^{n+2}}\frac{n+1}{(n+2)!}D_n^{xx} \\ \frac{\partial^2 g}{\partial I_x \partial I_z} &= 2\beta\tilde{\xi}\sigma^2 \sum_{n=0}^{\infty}(-1)^n \frac{(\beta I)^n}{(\sigma^2)^{n+2}}\frac{n+1}{(n+2)!}D_n^{xz}, \end{aligned} \tag{6.15}$$

where the coefficients D_n are

$$D_n^{xx} \equiv \frac{1}{2^{2n+4}}\sum_{m=0}^{n}\begin{pmatrix} n \\ m \end{pmatrix}\begin{pmatrix} 2n-2m+4 \\ n-m+2 \end{pmatrix}\begin{pmatrix} 2m \\ m \end{pmatrix} \tag{6.16}$$

$$D_n^{xz} \equiv \frac{1}{2^{2n+4}}\sum_{m=0}^{n}\begin{pmatrix} n \\ m \end{pmatrix}\begin{pmatrix} 2n-2m+2 \\ n-m+1 \end{pmatrix}\begin{pmatrix} 2m+2 \\ m+1 \end{pmatrix} \tag{6.17}$$

6.4 Driving Term

The form of the Hamiltonian already indicates that no odd resonances occur (the Hamiltonian depends only on r^2). Thus we have the resonance condition

$$kQ_x + lQ_z = p \qquad \text{with } k \text{ and } l \text{ even.} \tag{6.18}$$

It is tedious to calculate closed expressions for single resonance driving terms in the same way as for the tune shift and its derivatives [2]. Therefore, to extract Fourier components from the potential

$$U(x,z) = \frac{V(x,z)}{2\pi} = \frac{2\bar{\xi}}{\beta}\left[E_1\left(\frac{r^2}{2\sigma^2}\right) + \ln\left(\frac{r^2}{2\sigma^2}\right)\right] \tag{6.19}$$

we choose a numerical fast Fourier transform (FFT) [69]. The Fourier coefficients are

$$\begin{aligned} U_{kl} &= \frac{1}{(2\pi)^2}\int_0^{2\pi} U(x,z)e^{-ik\phi_x}e^{-il\phi_z}\,d\phi_x\,d\phi_z \\ &\approx \frac{1}{N}\left[\frac{1}{N}\sum_{m,n=0}^{N-1} U(x_{m,n},z_{m,n})e^{-ik2\pi\frac{m}{N}}e^{-il2\pi\frac{n}{N}}\right] \end{aligned} \tag{6.20}$$

The expression in square brackets is calculated by the FFT routine. The driving term h of (6.8) is

$$h(I_x,I_z) = 2|U_{kl}(I_x,I_z)|. \tag{6.21}$$

A further complication arises if a flat electron beam is considered. In this case the beam-beam kick can be expressed by means of the complex error function [32]. In 1992 the aspect ratio of the electron beam in HERA was

$$\sigma_x^e/\sigma_z^e \approx 4\ldots5. \tag{6.22}$$

Extraction of detuning and driving terms for this situation is more involved, but the results will not qualitatively differ from the round beam case and will, therefore, not be presented here.

6.5 Chaotic Fraction of Phase Space

The general procedure to calculate the island tune for a specific resonance consists of several steps, similar to the treatment of resonances in chapter 5:

1. A working point (Q_x, Q_z) is chosen in the tune diagram.
2. The resonance is specified by a pair (k,l) of integer numbers.
3. From the tune shift equation (6.12) the emittance value $\epsilon_x = \epsilon_z$ is computed at which the resonance condition is fulfilled.
4. The second derivatives of g with respect to $I_{x,z}$ are calculated for this emittance using relation (6.15).

[2] After completion of this thesis the author became aware that, for the one-dimensional case, explicit expressions of the driving term h and the detuning term g are stated in [87].

5. Finally the driving term h is calculated by the fast Fourier transform.

Fig. 6.1 compares tracking results with the tune shift calculated from equation (6.12). Not surprisingly, the agreement is good for amplitudes up to about $x = z \approx 3\sigma \approx 0.5$ mm. At larger amplitudes, not shown in the figure, the curve deviates from the tracking data due to a truncation of the infinite sum (6.12) at $n = 26$, which is required to avoid numerical overflow.

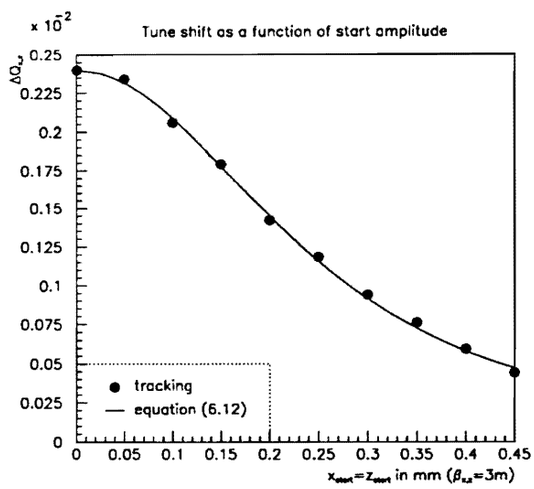

Figure 6.1: Tune shift $\partial g/\partial I_{x,z}$ for the beam-beam interaction.

In Fig. 6.2 the island tune, defined in (3.66), is shown as a function of amplitude for resonances of order 8, 10, 12, 14 and 20. Increasing the resonance order by 2 reduces the island tune by a factor 2 to 10 (dependent on the amplitude value; the largest reduction occurs at small amplitudes).

For all resonances under consideration the island tune stays below 0.001 ($\sim$ 50 Hz). Because both the detuning function g and the driving term h in (6.8) are proportional to the beam-beam tune shift parameter $\tilde{\xi}$, a smaller value of $\tilde{\xi}$ would lead to a further decrease of the island tune. Since the island tune is a measure of the frequency range, in which a harmonic tune modulation gives rise to strong chaos, one can conclude that a tune ripple of 50 Hz or of higher frequency will not dramatically widen the chaotic region for resonances of order 10 or above.

In order to illuminate this topic a little more, a local chaotic fraction of phase space $\tilde{\Gamma}$ is calculated

$$\tilde{\Gamma}(x, Q_m, q) \equiv \Delta I_{tot} \cdot w(x)/(\delta I) = \left(\frac{Q_m}{Q_I(x)}\right)^2 \frac{\sinh\left(\frac{\pi Q_m}{2Q_I(x)}\right)}{\sinh\left(\frac{\pi Q_m}{Q_I(x)}\right)} \frac{4\pi q(l+k)\sqrt{k^2+l^2}}{|(l^2+k^2)\frac{\partial^2 g}{\partial I_x^2} + 2kl\frac{\partial^2 g}{\partial I_x I_z}|} \frac{1}{\delta I} \tag{6.23}$$

Here δI is the distance in action between two adjacent resonances. A realistic value is $\delta I \approx 0.001 - 0.002$ mm mrad. The function $\tilde{\Gamma}$ differs from the sensitivity function Γ (3.106) in that it refers to a single resonance order only and that it also has a dependence on the starting amplitude x.

Fig. 6.3. shows $\tilde{\Gamma}$ as a function of the starting amplitude for different resonance orders. The modulation frequency Q_m is held constant, equal to 10^{-3}, and the modulation amplitude q is 10^{-4}, so that

$$\frac{4\pi q}{\delta I} \approx 1 \text{ mm}^{-1} \text{ mrad}^{-1}. \tag{6.24}$$

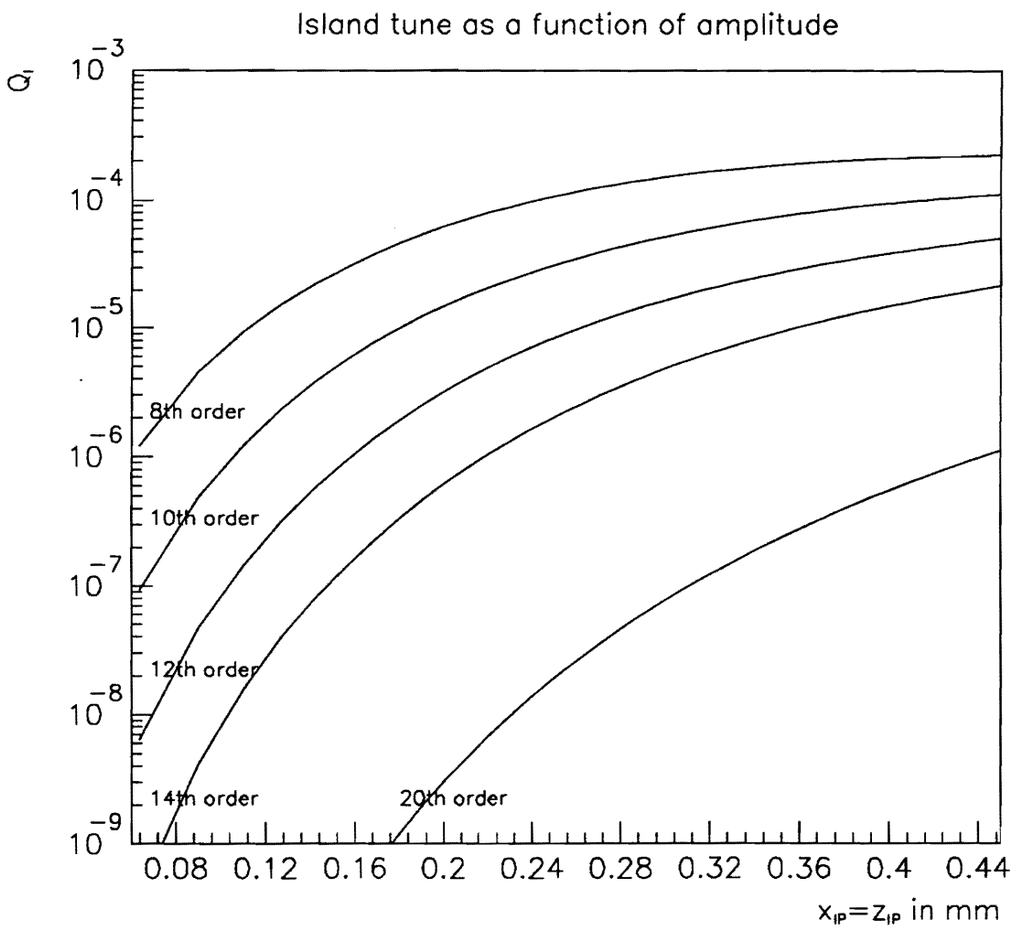

Figure 6.2: Island tunes as a function of the transverse amplitude for resonances of various order.

Fig. 6.3 confirms that, for amplitudes up to 3σ, the resonances of 10th and of higher order

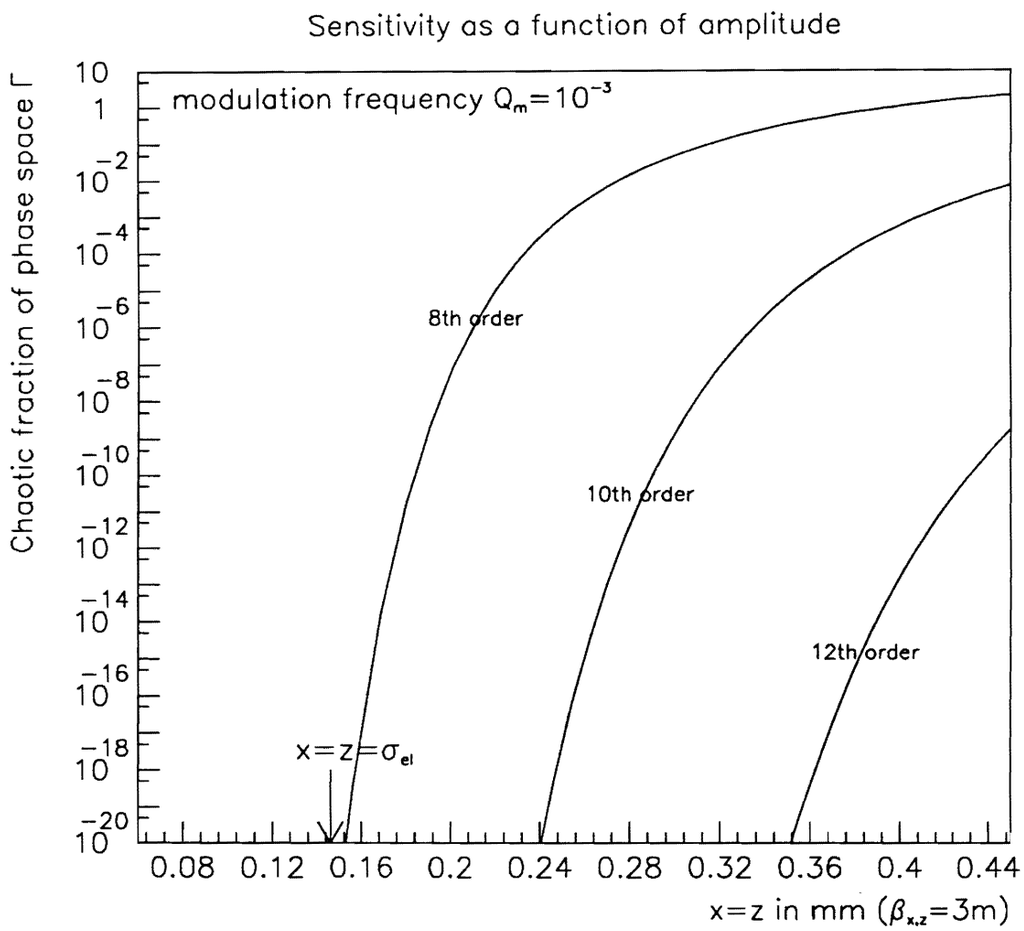

Figure 6.3: Chaotic fraction of phase space $\tilde{\Gamma}$ (6.23) as a function of the transverse amplitude for resonances of various order, assuming a tune modulation of frequency 50 Hz and amplitude 10^{-4}.

should have no strong effect on the particle stability. Note, however, the steep increase of $\tilde{\Gamma}$ for 10th and 12th order resonances, indicating that in the range $3 - 5\sigma$ (0.45 - 0.75 mm) the effect of these resonances may become important.

6.6 Emittance Growth Rates

In close analogy to the discussion in chapter 5, the dependence of the diffusion rate on the transverse emittance $\epsilon \equiv \epsilon_x + \epsilon_z$ is estimated by

$$D(\epsilon) = \left\langle \frac{1}{2}\left(\frac{\overline{(\Delta(\epsilon_x+\epsilon_z))^2}}{\Delta t}\right)\right\rangle \approx \frac{1}{2}\Delta I_{tot}\frac{w}{\delta I}\left(\frac{\overline{(\Delta(\epsilon_x+\epsilon_z))^2}}{\Delta t}\right), \tag{6.25}$$

where the 'local' emittance growth rate is defined in (3.72). In Fig. 6.4 the dependence of the diffusion coefficient $D(\epsilon)$ on the single-particle emittance is weaker than exponential. Thus it is different from the case of multipole errors (Fig. 5.15).

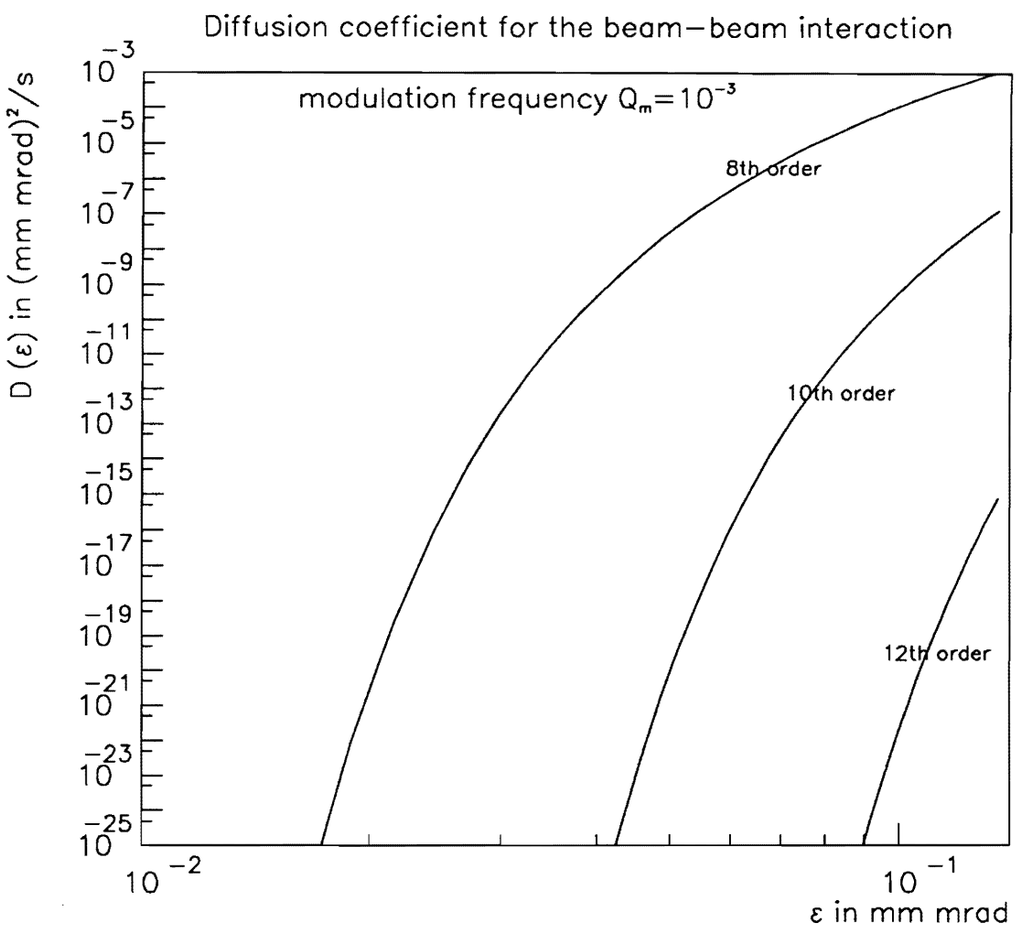

Figure 6.4: Diffusion coefficient $D(\epsilon)$ (6.25) for resonances of various order as a function of the transverse single-particle emittance $\epsilon \equiv \epsilon_x + \epsilon_z$, assuming a modulation frequency of 50 Hz ($Q_m = 10^{-3}$).

Locally it is still possible to approximate $D(\epsilon)$ by an exponential expression $D_0(\epsilon) = c_0\epsilon^{\alpha_0}$ (see also [70]). The subscript 0 indicates the local character of the approximation. Differentiation of $D_0(\epsilon)$ yields the emittance growth rate $< \overline{\Delta\epsilon}/\Delta t >$ at ϵ_0 (compare (3.111) and appendix F). In Table 6.2 results are listed for a single-particle emittance ϵ_0 of about 0.1 mm mrad, corresponding to $x = z \approx 2.7\sigma$.

6.7 Off-Center Collisions

If the beams collide off-center, high-order resonances feed down to lower order. Especially, a non-centered collision leads to an excitation of odd order resonances, whose strengths depend

on the displacement of the two beams. Of special importance is the 7th order odd resonance at $Q_x \approx Q_z \approx 0.286$, which is close to the actual working point of 1992 and has a measurable effect on beam lifetime and background. The beam-beam potential (6.19) also applies in the more general situation of a horizontal displacement Δx, if the horizontal coordinate x in the argument $r^2 = x^2 + z^2$ is replaced by $x + \Delta x$,

$$U(x, z, \Delta x) = \frac{2\tilde{\xi}}{\beta}\left[E_1\left(\frac{x^2 + z^2 + 2\,x\,\Delta x + \Delta x^2}{2\sigma^2}\right) + \ln\left(\frac{x^2 + z^2 + 2\,x\,\Delta x + \Delta x^2}{2\sigma^2}\right)\right]. \quad (6.26)$$

The coordinates x and z are related to $I_{x,z}$ and $\phi_{x,z}$ by (6.3). To study the dependence of the diffusion rate close to this resonance on the displacement between the two beams, the detuning and driving terms have to be evaluated. The second derivatives $\partial^2 U/\partial I_{x,z}^2$ of the potential $U(x, z)$ are computed numerically. Their average values, calculated by a fast Fourier transform [69], are the detuning terms $\partial^2 g/\partial I_{x,z}^2$. Likewise an FFT provides the driving term $h(I_x, I_z)$ as in section 6.4.

A diffusion coefficient $D(\epsilon, \Delta x)$ can be defined in analogy to (6.25), where now the quantities ΔI_{tot}, w and $\overline{(\Delta(\epsilon_x + \epsilon_z))^2}/\Delta t$ depend also on the beam separation Δx. Differentiation of $D(\epsilon)$ yields the amplitude-dependent emittance growth rate (see (3.111)).

In Fig. 6.5 the expected growth rate is depicted as a function of the horizontal displacement Δx of the beams for various starting amplitudes. At the modest amplitude $x = z = 2\sigma_{el}$, in Fig. 6.5 a), the emittance growth rate exceeds that due to intra-beam scattering (9.4), if $\Delta x > 0.1\sigma_{el}$. For this amplitude, the effect of the 14th order resonance is too small to be shown. At a transverse amplitude of $x = z = 4\sigma_{el}$, in Fig. 6.5 b), the growth rate equals that caused by intra-beam scattering for a beam displacement $\Delta x \approx 0.05\sigma_{el}$. The effect of the 14th order resonance can still be neglected. It becomes noticeable at greater transverse amplitudes such as $x = z = 6\sigma_{el}$, shown in Fig. 6.5 c). For beam offsets Δx beyond $0.1\sigma_{el}$, however, the emittance growth resulting from the 7th order resonance exceeds the effect of the 14th order resonance by many orders of magnitude. For still larger transverse amplitudes $x = z$, the emittance growth rate starts to decrease. At $x = z = 8\sigma_{el}$, in Fig. 6.5 d), it is already smaller by about a factor 10^5 than for $x = z = 6\sigma_{el}$.

The maximum tolerable displacement Δx between the electron and the proton beam in HERA is conservatively estimated as

$$\Delta x_{max} \approx 0.1\,\sigma_{el}. \quad (6.27)$$

Resonance order	exponent α_0	coefficient c_0 in $(\text{mm mrad})^{2-\alpha_0}\ \text{s}^{-1}$	$< \Delta\epsilon/\Delta t >$ in mm mrad s^{-1}
8	~ 10	$\sim 10^6$	~ 0.01
10	~ 22	$\sim 10^{13}$	$\sim 2 \cdot 10^{-7}$
12	~ 63	$\sim 10^{41}$	$\sim 6 \cdot 10^{-20}$

Table 6.2: Emittance growth rate $< \overline{\Delta\epsilon}/\Delta t >$ computed by use of (3.111) from the diffusion coefficient $D_0(\epsilon) \approx c_0 \cdot \epsilon^{\alpha_0}$, which is a local approximation to (6.25). The parameters c_0 and α_0 are evaluated at an emittance $\epsilon_0 \approx 0.1$ mm mrad (equivalent to $x \approx z \approx 2.7\sigma$) for resonances of order 8, 10 and 12. The values quoted refer to a modulation frequency of 50 Hz ($Q_m = 10^{-3}$).

For this value the emittance growth rate due to the 7th order resonance, excited by the beam displacement, becomes comparable to that caused by intra-beam scattering and to the effect of the 14th order resonance, which is excited even if the collision is centered.

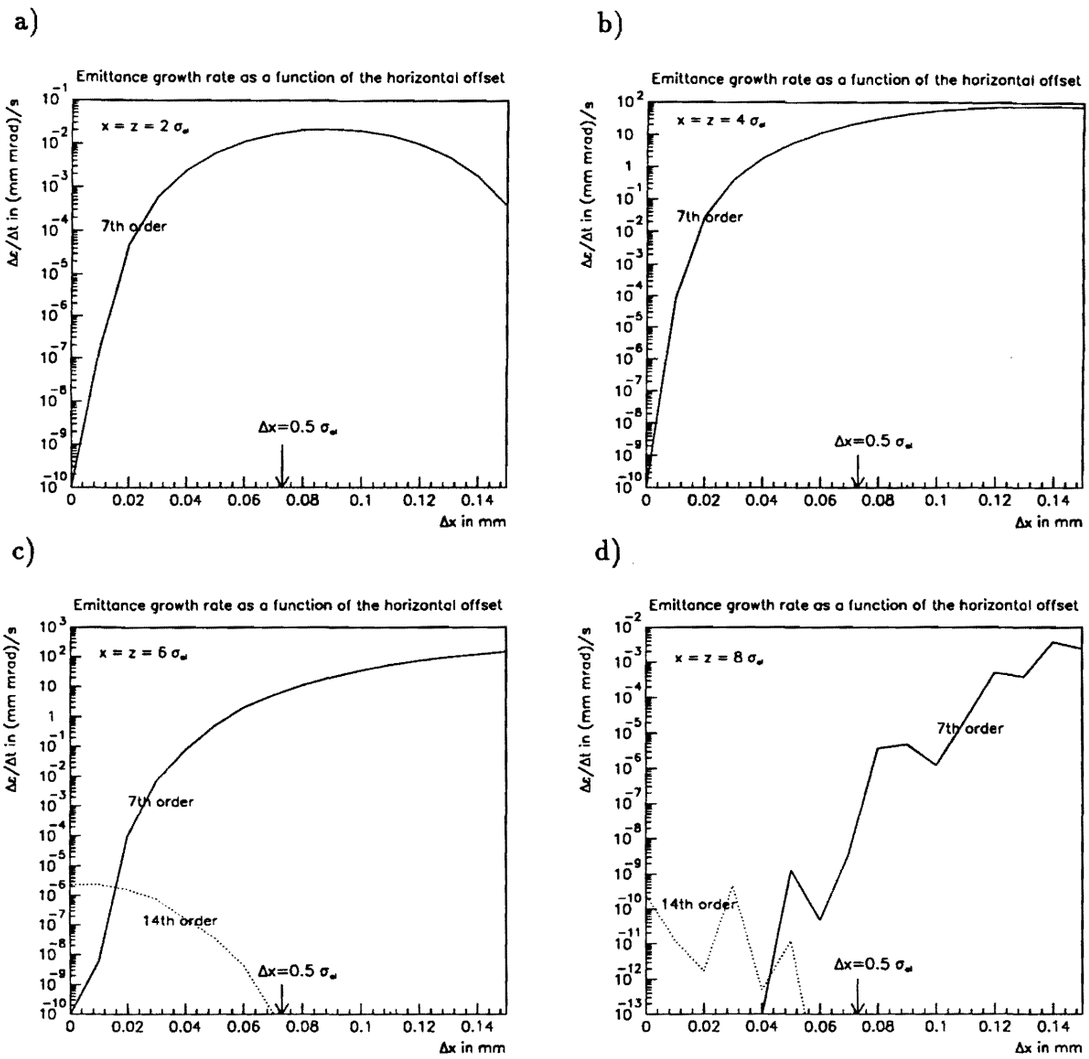

Figure 6.5: Emittance growth rates $< \overline{\Delta\epsilon}/\Delta t >$ close to a 7th and a 14th order resonance as a function of the horizontal displacement Δx between the two beams for various amplitudes $x = z$; the diagrams refer to a modulation frequency of 50 Hz.

Chapter 7

Multiple Proton-Electron Scattering

7.1 Emittance Growth Rate

In this section the effect of multiple proton-electron scattering on the proton beam emittance is estimated. For small four-momentum transfer q, $q^2 \ll 2m_{proton}^2 c^2$, the cross section for elastic electron-proton scattering is given by the Rutherford formula, which in covariant form reads

$$\frac{d\sigma}{dq^2} = \frac{\alpha^2 h^2}{\pi q^4}. \tag{7.1}$$

Here α is the fine structure constant and h is Planck's constant. For small scattering angles the four-momentum transfer can be written as

$$q^2 \approx p_p^2 \theta_p^2. \tag{7.2}$$

In this approximation, p_p is the momentum and θ_p is the scattering angle of the proton in the laboratory frame. Note that the transverse momentum transfer $|\Delta p_{p,\perp}| = |\Delta p_{e,\perp}| \approx p_p \theta_p$ is invariant under Lorentz transformations in the longitudinal direction and thus has the same value in the center-of-mass frame or in the rest frame of the proton. Integration of (7.1) yields the total cross section for proton-electron scattering,

$$\sigma_{tot} = \int_{q_{min}}^{q_{max}} \frac{d\sigma}{dq^2}\, dq^2, \tag{7.3}$$

where q_{min} and q_{max} are suitably chosen limits. The mean squared momentum transfer for scattering of a proton on a single electron is then given by

$$< q^2 >_{single} \approx \frac{1}{\sigma_{tot}} \int_{q_{min}}^{q_{max}} \frac{d\sigma}{dq^2} q^2\, dq^2. \tag{7.4}$$

To compute the mean squared momentum transfer per unit time and per proton for scattering on all electrons of the opposite bunch, the expression (7.4) has to be multiplied by the luminosity L, the total cross section σ_{tot} and the number of interaction points N_{IP}, and it has to be divided by the total number N_p of colliding protons. Hence we get [73]

$$\frac{< q^2 >}{\Delta t} \approx \frac{N_{IP} L}{N_p} \int_{q_{min}}^{q_{max}} \frac{d\sigma}{dq^2} q^2\, dq^2. \tag{7.5}$$

Inserting the cross section (7.1) and performing the integration, one is left with

$$\frac{< q^2 >}{\Delta t} \approx \frac{\alpha^2 h^2 N_{IP} L}{\pi N_p} \ln\left(\frac{q^2_{max}}{q^2_{min}}\right). \tag{7.6}$$

The dependence of $< q^2 > /\Delta t$ (7.6) on the limits of integration is weak. A reasonable value for the maximum four-momentum transfer is deduced from the (horizontal) acceptance A_x,

$$q^2_{max} = p_p^2 \theta^2_{pmax} = p_p^2 \frac{A_x}{\beta^x_{IP}}, \tag{7.7}$$

β^x_{IP} being the horizontal proton beta function at the interaction point. An estimate of the lower limit q_{min} is obtained from the uncertainty principle [73]

$$q^2_{min} = \frac{\hbar^2}{\sigma^2_{el}}, \tag{7.8}$$

where σ_{el} is the electron beam size at the collision point and $\hbar$ is h divided by 2π. Then the horizontal emittance growth rate becomes [73]

$$\begin{aligned} \frac{\Delta\epsilon_x}{\Delta t} &= \frac{1}{2}\beta^x_{IP} N_{IP} \frac{< \theta_p^2 >}{\Delta t} = \frac{1}{2}\beta^x_{IP} \frac{N_{IP}}{p_p^2} \frac{< q^2 >}{\Delta t} \\ &= \frac{1}{2}\beta^x_{IP} \frac{N_{IP}}{p_p^2} \frac{\alpha^2 h^2 L}{\pi N_p} \ln\left(\frac{p_p^2 A_x \sigma^2_{el}}{\beta^x_{IP} \hbar^2}\right). \end{aligned} \tag{7.9}$$

Here the factor $\frac{1}{2}$ takes account of the projection of the scattering space angle θ_p onto the horizontal plane. The vertical emittance growth rate is about ten times smaller ($\beta^z_{IP} \approx \frac{1}{10}\beta^x_{IP}$) and may, therefore, be disregarded. Inserting the actual values of 1992,

$$\begin{aligned} N_{IP} &= 2, \\ p_p &= 820 \text{ GeV/c}, \\ L &\approx 2 \cdot 10^{29} \text{ cm}^{-2}\text{s}^{-1}, \\ N_p &\approx 25 \cdot 10^{10}, \\ \beta^x_{IP} &= 7 \text{ m}, \\ A_x &\approx 0.2 \text{ mm mrad}, \\ \sigma_{el} &\approx 0.2 \text{ mm}, \end{aligned}$$

equation (7.9) yields

$$\frac{\Delta\epsilon_x}{\Delta t} \approx 10^{-10} \text{ mm mrad s}^{-1}. \tag{7.10}$$

Chapter 8

Residual Gas Scattering

8.1 Introduction

During the first commissioning period of the HERA proton ring in March/April 1991, the beam lifetime was limited to about 30 minutes at the injection energy of 40 GeV. Some insight into the underlying loss process was gained by beam profile measurements, which showed that the beam always filled the available aperture completely. However the source of the lifetime limitation is still an unresolved question. In the following we will investigate whether interactions with the residual gas could have been responsible for the short lifetime [1]. By-products of this study are an estimate of the emittance growth rate due to multiple scattering and a calculation of the beam lifetime, if it were limited only by nuclear interactions with the residual gas.

8.2 Lifetime for One Degree of Freedom

We first describe the one-dimensional treatment. This corresponds to a situation, where the aperture in one direction is large compared to the other. In order to determine the distribution function $f(\epsilon, t)$ for either the horizontal or vertical emittance we start from a Fokker-Planck equation (see appendix E)

$$\frac{\partial}{\partial t} f(\epsilon, t) = -\frac{\partial}{\partial \epsilon} \frac{< \Delta\epsilon >}{\Delta t} f(\epsilon, t) + \frac{1}{2} \frac{\partial^2}{\partial \epsilon^2} \frac{< (\Delta\epsilon)^2 >}{\Delta t} f(\epsilon, t). \tag{8.1}$$

In this equation $< \Delta\epsilon > / \Delta t$ denotes the mean emittance change per unit time. Similarly $< (\Delta\epsilon)^2 > / \Delta t$ is the mean squared emittance change per unit time. A projected scattering angle θ causes a change in emittance $\Delta\epsilon(\theta) = 2(\alpha x + \beta x')\theta + \beta\theta^2$. Averaging over the circumference and over the angular coordinate in phase space yields

$$< \Delta\epsilon >_{\Phi,s} = < \beta > \theta^2 , \tag{8.2}$$

where $< \beta >$ is the mean value of the beta function around the machine. Correspondingly we obtain

$$< (\Delta\epsilon)^2 >_{\Phi,s} \approx 2\epsilon < \beta > \theta^2 . \tag{8.3}$$

[1] Studies of beam gas scattering lifetimes have previously been performed at CERN and at Fermilab [74, 75].

Here terms proportional to θ^4 have been neglected. Now the Fokker-Planck equation (8.1) can be solved via a separation ansatz $f(\epsilon,t) = \exp(-t/\tau)\cdot F(\epsilon)$. Introducing the abbreviation

$$1/b \equiv \tau < \beta >< \theta^2 > /\Delta t,$$

the differential equation for the function $F(\epsilon)$ reads

$$\epsilon F'' + F' + bF = 0\,. \tag{8.4}$$

The projected mean squared scattering angle per unit time can be approximated by the expression [2] [76]

$$\frac{< \theta^2 >}{\Delta t} = \left(\frac{14.1\mathrm{MeV/c}}{p}\right)^2 \frac{\rho c}{X_0}\,, \tag{8.5}$$

where p is the momentum of the protons, X_0 is the radiation length of the traversed medium in g/cm^2 and ρ is its density. Introducing the normalized amplitude $\hat{y} \equiv \sqrt{\epsilon}$ of the betatron oscillation, equation (8.4) can be rewritten in terms of a distribution function $G(\hat{y})$ as

$$4b\hat{y}G + G' + \hat{y}G'' = 0\,. \tag{8.6}$$

This equation is solved by a Bessel function of zeroth order, $\mathrm{G}(\hat{y}) = \mathrm{J}_0(\sqrt{4b}\hat{y})$. At the physical acceptance $\hat{y}^2_{max} = A_y$ the argument of J_0 should be identical to the first zero $u_0 \approx 2.4$ of J_0 . We thus arrive at the following expression for the beam lifetime τ

$$\tau_{1\mathrm{d}} = \frac{4}{u_0^2}\frac{A_y}{<\beta>}\left(\frac{p}{14.1\mathrm{MeV/c}}\right)^2 \frac{X_0}{\rho c}\,. \tag{8.7}$$

The lifetime is proportional to the ratio of acceptance A_y and average beta function $<\beta>$. It is inversely proportional to the mean pressure via the density ρ.

The discussion is restricted to the largest possible time constant τ, whereas, in principle, an infinite number of solutions to equation (8.6) exists. Each solution, labeled by the subscript j, is characterized by a different time constant $\tau_j \propto 1/(u_{0,j})^2$, where $u_{0,j}$ denotes the jth zero of J_0 [75]. The solutions form a complete set, in the sense that an arbitrary beam distribution f can be expanded into them, $f(\epsilon,t) = \sum_j F_j(\epsilon)\exp(-t/\tau_j)$. For large values of t the first term ($j = 1$) is dominant, since the time constant τ_2 is considerably smaller than τ_1 ($\tau_2 = (u_{0,1})^2/(u_{0,2})^2\cdot\tau_1 \approx 0.2\cdot\tau_1$) and the contributions for $j > 2$ decay even faster. In addition, two observations suggest to disregard all terms besides $j = 1$: Firstly, in April of 1991 the beam profile had a cosine-like (or Bessel-function-like) shape, which did not change over periods comparable to the beam lifetime. Secondly, the time-dependence of the current was almost perfectly exponential and there was no evidence for a superposition of several time constants.

8.3 Lifetime for Two Degrees of Freedom

To describe a more general situation, (8.1) has to be replaced by a two-dimensional Fokker-Planck equation

$$\frac{\partial}{\partial t}f(\epsilon_x,\epsilon_z,t) = -\frac{\partial}{\partial\epsilon_x}\frac{<\Delta\epsilon_x>}{\Delta t}f(\epsilon_x,\epsilon_z,t) - \frac{\partial}{\partial\epsilon_z}\frac{<\Delta\epsilon_z>}{\Delta t}f(\epsilon_x,\epsilon_z,t) +$$

[2] The approximation is accurate to a few percent for time intervals $\Delta t > 10^{-3}\cdot X_0/(\rho c)$. At an average hydrogen pressure $5\cdot 10^{-7}$ mbar and a temperature $T = 300$ K this amounts to $\Delta t > 50$ sec.

$$+\frac{1}{2}\frac{\partial^2}{\partial\epsilon_x^2}\frac{<(\Delta\epsilon_x)^2>}{\Delta t}f(\epsilon_x,\epsilon_z,t)+\frac{1}{2}\frac{\partial^2}{\partial\epsilon_z^2}\frac{<(\Delta\epsilon_z)^2>}{\Delta t}f(\epsilon_x,\epsilon_z,t)+$$
$$+\frac{\partial^2}{\partial\epsilon_x\partial\epsilon_z}\frac{<(\Delta\epsilon_x\Delta\epsilon_z)>}{\Delta t}f(\epsilon_x,\epsilon_z,t)\,. \tag{8.8}$$

Again neglecting terms proportional to θ^4 and assuming that the average values of the horizontal and vertical beta functions are equal, i. e. $<\beta_x>=<\beta_z>\equiv<\beta>$, one can proceed exactly as in the one-dimensional case. The two-dimensional analogue to (8.6) reads

$$4bG+\frac{1}{\hat{x}}\frac{\partial G}{\partial\hat{x}}+\frac{\partial^2 G}{\partial\hat{x}^2}+\frac{1}{\hat{z}}\frac{\partial G}{\partial\hat{z}}+\frac{\partial^2 G}{\partial\hat{z}^2}=0\,. \tag{8.9}$$

For uncoupled motion, equation (8.9) can be solved by factorizing the distribution function $G(\hat{x},\hat{z})=g_1(\hat{x})g_2(\hat{z})$. After separation of variables one arrives at the following two equations, where λ is the separation constant,

$$\hat{x}^2g_1''+\hat{x}g_1'+(1-\lambda)4b\hat{x}^2g_1 = 0 \tag{8.10}$$
$$\hat{z}^2g_2''+\hat{z}g_2'+\lambda 4b\hat{z}^2g_2 = 0\,. \tag{8.11}$$

These equations are mathematically equivalent to (8.6). Accordingly their solution is given by

$$g_1(\hat{x}) = \mathrm{J}_0(\sqrt{4b(1-\lambda)}\hat{x}) \tag{8.12}$$
$$g_2(\hat{z}) = \mathrm{J}_0(\sqrt{4b\lambda}\hat{z})\,. \tag{8.13}$$

Denoting the horizontal and vertical acceptance by A_x and A_z respectively, the boundary conditions lead to the following set of equations

$$1-\lambda = \frac{u_0^2}{4b}\cdot\frac{1}{A_x} \tag{8.14}$$
$$\lambda = \frac{u_0^2}{4b}\cdot\frac{1}{A_z}\,. \tag{8.15}$$

Elimination of λ yields an expression for the lifetime

$$\tau_{2d}=\frac{4}{u_0^2}\frac{1}{<\beta>}\frac{A_xA_z}{A_x+A_z}\left(\frac{p}{14.1\mathrm{MeV/c}}\right)^2\frac{X_0}{\rho c}\,. \tag{8.16}$$

Note, that (8.16) reduces to (8.7) in the limiting case $A_x \gg A_z$ or $A_z \gg A_x$. However, if the horizontal and vertical acceptances are equal, (8.16) predicts a lifetime which is a factor two lower than in the one-dimensional case.

8.4 Lifetime on the Coupling Resonance

On the coupling resonance, the distribution function f depends only on the single invariant of motion

$$\epsilon_{\mathrm{ges}}=\epsilon_1+\epsilon_2\,. \tag{8.17}$$

In this case the Fokker-Planck equation can be reduced to a one-dimensional differential equation. To this end we choose as a new independent variable the invariant quantity $r\equiv\sqrt{\epsilon_{\mathrm{ges}}}$.

Then equation (8.9) (with $\hat{x}, \hat{z}$ replaced by $\hat{y}_1, \hat{y}_2$) is transformed to an equation for the distribution function $F(r)$

$$4bF + \frac{3}{r}\frac{\partial F}{\partial r} + \frac{\partial^2 F}{\partial r^2} = 0 \,. \tag{8.18}$$

To solve this equation, we try the ansatz $F(r) = R(r)/r$. The differential equation for $R(r)$ becomes

$$r^2 R'' + rR' + 4br^2 R - R = 0 \,. \tag{8.19}$$

Its solution is given by the Bessel function of first order

$$R(r) = \mathrm{J}_1(\sqrt{4b}r) \,. \tag{8.20}$$

The boundary condition requires that $R(r)$ is zero at

$$r^2_{max} = A \equiv \min(A_x, A_z) \,. \tag{8.21}$$

Denoting the first zero of J_1 by u_1 ($u_1 \approx 3.8$), we find

$$\tau_{\text{coupling}} = \frac{4}{u_1^2}\frac{A}{<\beta>}\left(\frac{p}{14.1\text{MeV/c}}\right)^2 \frac{X_0}{\rho c} \,. \tag{8.22}$$

8.5 Comparison with Experimental Observations

In the HERA proton ring, the vacuum-pressure effects in the beam pipe are dominated by the warm straight sections. Under normal operating conditions the main contribution to the pressure comes from hydrogen [77]. Other molecules — such as H_2O, CO and CO_2 — merely constitute a small fraction of the residual gas. If the lifetime at injection energy were caused by gas scattering, it is decribed by (8.16). Inserting the parameter values, $u_0 \approx 2.4$, $p = 40\text{GeV/c}$, $T = 300\,\text{K}$, $<\beta> \approx 50\,\text{m}$ and, assuming that hydrogen is the dominant compound, $X_{0\ \mathrm{H_2}} \approx 61\text{g/cm}^2$, $\rho_{\mathrm{H_2}} \approx p_{\mathrm{H_2}} m_{\mathrm{H_2}}/(kT)$, equation (8.16) is reduced to

$$\tau_{\mathrm{H_2}} \approx 2830 \frac{\text{mbar}\cdot\text{s}}{\text{m}} \frac{A_x A_z}{A_x + A_z} \frac{1}{p_{\mathrm{H_2}}} \,. \tag{8.23}$$

From the vacuum gauges an average hydrogen pressure of $4 \cdot 10^{-9}$ mbar was deduced [78]. In April of 1991 the measured acceptances were $A_x \approx 2.1$ mm mrad , $A_z \approx 0.4$ mm mrad [3]. The lifetime calculated according to (8.23) is approximately 66 hours. To explain the very low observed value of about 30 minutes, one would have to postulate an average pressure of $p_{\mathrm{H_2}} \approx 5 \cdot 10^{-7}$ mbar, which seems extremely unlikely.

In view of the great discrepancy between prediction and measurement the attention should be directed to molecules with higher atomic masses. For instance, to obtain a rather pessimistic estimate of the lifetime, the measured pressure values could completely be ascribed to carbon dioxide. Taking into account the different radiation length and density, $X_{0\ \mathrm{CO_2}} \approx 36\text{g/cm}^2$, $\rho_{\mathrm{CO_2}} \approx p_{\mathrm{CO_2}} m_{\mathrm{CO_2}}/(kT)$, equation (8.23) is replaced by

$$\tau_{\mathrm{CO_2}} \approx 76 \frac{\text{mbar}\cdot\text{s}}{\text{m}} \frac{A_x A_z}{A_x + A_z} \frac{1}{p_{\mathrm{CO_2}}} \,. \tag{8.24}$$

[3]The bad vertical acceptance was caused by a misplaced monitor.

The vacuum gauge data would correspond to an average pressure $p_{CO_2} = 10^{-9}$ mbar at a temperature of 300 K [78]. Using the same value for the acceptances as above the predicted lifetime is about 7 hours. To reduce it to 30 minutes, an average pressure of $p_{CO_2} = 1.4 \cdot 10^{-8}$ mbar has to be assumed. Although this pressure value is smaller by a factor 35 than the one required for hydrogen, it still seems highly improbable.

In order to finally settle this question, a complementary experiment has been performed. After careful minimization of linear coupling, the working point was set on the coupling resonance at $Q_x = Q_z = 0.19$. Subsequently the dependence of the proton beam lifetime on the aperture was measured by applying a local horizontal orbit bump of varying amplitude. Under the assumption that residual gas scattering is responsible for the short lifetime τ, (8.22) predicts the following dependence of τ on the acceptance,

$$\tau_{H_2}^{\text{coupling}} \approx 1130 \frac{\text{mbar} \cdot \text{s}}{\text{m}} \frac{A}{p_{H_2}} \tag{8.25}$$

$$\text{with} \quad A = \min\left(\frac{(a_{\max} - a_{\text{bump}})^2}{\beta_{x,\text{bump}}}, A_x, A_z\right).$$

Here A_x and A_z denote the horizontal and vertical acceptances of the machine without the orbit bump. The lifetime should be constant at small bump amplitudes (for a_{bump} below 17 mm), i. e. as long as the overall aperture limitation is given by the small vertical acceptance and not by the local bump. A typical result of the March/April run is shown in Fig. 8.1, where $\sqrt{\tau}$ is plotted versus the bump amplitude a_{bump}. The measured data differ significantly from the theoretical curves. Moreover, the required pressure value is again highly inconsistent with the vacuum gauge data. The possibility, that residual gas scattering caused the short lifetime, becomes even more improbable in view of the following two observations [79]:

- In April 1991 the best lifetime was obtained on the coupling resonance, whereas (8.16) and (8.22) predict a decrease of the lifetime on the coupling resonance by about a factor $u_0^2/u_1^2 \cdot (1 + A_z/A_x) \approx 0.5$, if the limitation was caused by gas scattering.
- In the second commissioning run of HERA from July to December 1991 typical lifetimes of several hours have been reached at injection energy, while the vacuum gauge data for the two runs have been identical.

The strong disagreement between multiple scattering theory and the observed data together with the experience of the second commissioning run imply that multiple scattering has not been the dominant lifetime limiting effect in spring 1991. Up to now no convincing explanation of the short lifetime has been proposed.

8.6 Estimate of Emittance Growth Rates

An estimate of the emittance growth rate due to multiple scattering is obtained from (8.2) and (8.5)

$$\frac{<\Delta\epsilon>}{\Delta t} = <\beta> \frac{<\theta^2>}{\Delta t} = <\beta> \left(\frac{14.1\text{MeV/c}}{p}\right)^2 \frac{\rho c}{X_0}. \tag{8.26}$$

For an average hydrogen pressure of $5 \cdot 10^{-10}$ mbar we get

$$\frac{<\Delta\epsilon>}{\Delta t} = 1.2 \cdot 10^{-7} \text{ mm mrad s}^{-1} \text{ at 40 GeV}, \tag{8.27}$$

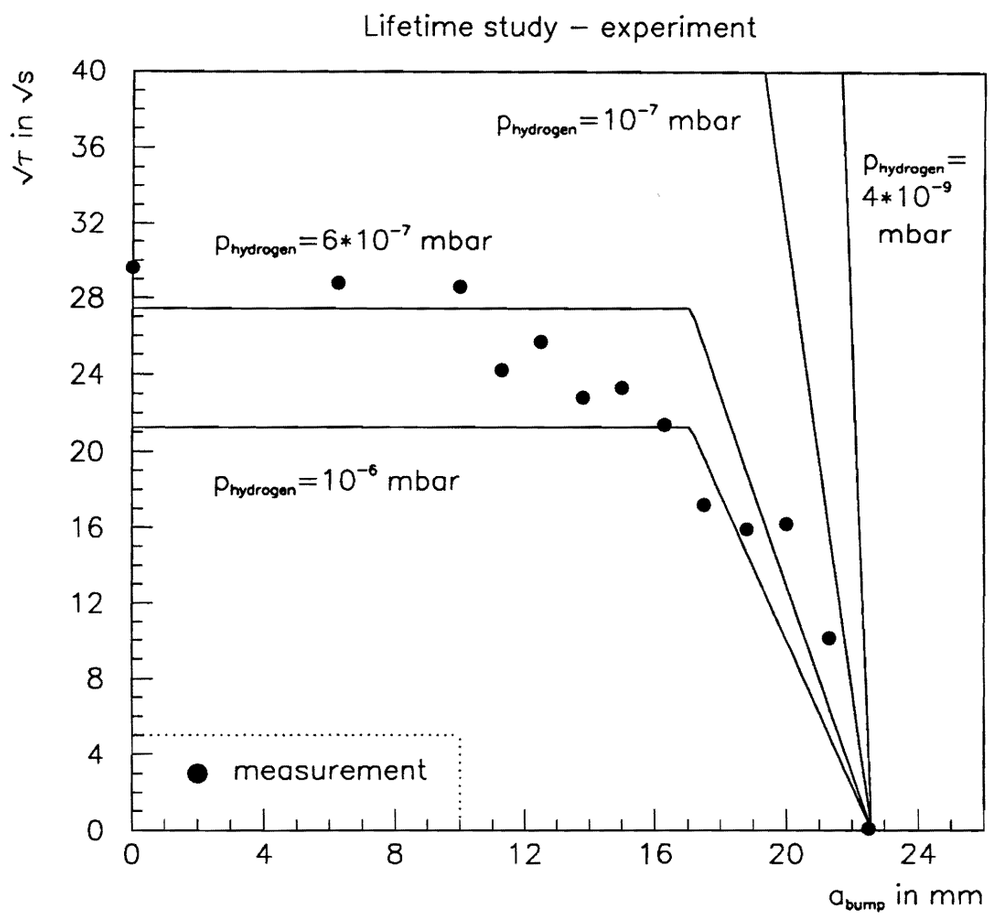

Figure 8.1: Square root of the lifetime versus the amplitude a_{bump} of a horizontal orbit bump. The pressure values refer to a temperature of 300 K. Equivalent carbon dioxide pressures are smaller by a factor 35. The beta function at the bump maximum is $\beta_x = 76$ m.

$$\frac{<\Delta\epsilon>}{\Delta t} = 3.0 \cdot 10^{-10} \text{ mm mrad s}^{-1} \text{ at 820 GeV.} \tag{8.28}$$

At 820 GeV the effect of multiple gas scattering is negligible.

8.7 Nuclear Interactions

A nuclear interaction between a proton and a nucleus of a residual gas molecule will almost certainly lead to a particle loss. The corresponding beam lifetime τ is given by

$$\frac{1}{\tau} = -\frac{1}{N}\frac{dN}{dt} = \rho_{\text{mol}} c \sigma_{\text{p,mol}} , \tag{8.29}$$

that is

$$\tau = \frac{kT}{cp_{\text{mol}}} \frac{1}{\sigma_{\text{p,mol}}} . \tag{8.30}$$

We again consider only hydrogen and carbon dioxide as extreme cases. The total nuclear interaction cross sections for these two molecules are [76]

$$\sigma_{\text{p,H}_2} \approx 4 \cdot 10^{-26} \text{cm}^2 \tag{8.31}$$

$$\sigma_{\text{p,CO}_2} \approx 7.5 \cdot 10^{-25} \text{cm}^2 . \tag{8.32}$$

At a temperature of 300 K we obtain

$$\tau_{\text{H}_2} \approx 3.4 \cdot 10^{-2} \frac{1}{p[\text{mbar}]} s \tag{8.33}$$

$$\tau_{\text{CO}_2} \approx 1.8 \cdot 10^{-3} \frac{1}{p[\text{mbar}]} s . \tag{8.34}$$

To account for a lifetime of half an hour, one would need an average hydrogen pressure of $2 \cdot 10^{-5}$ mbar or a carbon dioxide pressure of 10^{-6} mbar. These values exceed the ones calculated for multiple scattering by at least a factor of 30. Thus it is clear, that nuclear interactions had no influence on the beam lifetime in 1991.

Nuclear interactions with the residual gas lead to a lifetime limitation which is almost independent of the beam energy. This limit is, however, of no practical importance, because it is larger than one year for a mean hydrogen pressure of 10^{-9} mbar.

Chapter 9

Comparison of Lifetime Limiting Processes

In this chapter the various effects that increase the emittance and reduce the beam lifetime are compared regarding their magnitude and significance.

Naturally one can distinguish between effects that lead to an immediate particle loss, such as nuclear interactions with the residual gas, and processes that primarily cause an increase in emittance. If the latter is very large and gives rise to a quasi-stationary proton distribution it will also limit the beam lifetime τ, roughly according to

$$\tau \approx \frac{A}{\Delta\epsilon/\Delta t}, \tag{9.1}$$

where A is the available acceptance. A situation of this kind has been investigated in the treatment of multiple Coulomb scattering on the residual gas. More likely, however, multiple scattering processes will only affect the luminosity lifetime and not the beam current. They are characterized by a uniform emittance growth rate.

Quite different is the chaotic particle transport driven by field nonlinearities or by the beam-beam interaction, which cause a strongly amplitude-dependent emittance growth rate and lead to a loss of the outermost particles.

The contribution of individual processes to the total emittance growth rate is not necessarily additive. For instance, multiple scattering transfers particles between regular and chaotic regions of the phase space and may thereby enhance the chaotic diffusion due to nonlinearities, in addition to its direct effect on the emittance. Quite generally the total growth rate satisfies the inequality

$$\left.\frac{\Delta\epsilon}{\Delta t}\right|_{\text{total}} \geq \sum_i \left(\frac{\Delta\epsilon}{\Delta t}\right)_i \tag{9.2}$$

where the subindex 'i' denotes the separate phenomena.

In the following we summarize the results obtained so far and present some numbers for comparison with other effects.

9.1 Intra-Beam Scattering

A significant limitation of the proton beam lifetime is imposed by intra-beam scattering, which is a multiple Coulomb scattering process between particles within the same bunch [71, 72]. Intra-beam scattering is mainly important in the longitudinal phase space, but contributes to

the horizontal emittance growth as well. The effect has been estimated in [80] assuming a normalized emittance of 20 mm mrad and a Gaussian bunch shape. From reference [80], a mean emittance growth rate of about

$$\frac{<\Delta\epsilon_x>}{\Delta t} \approx 1.6 \cdot 10^{-6} \text{ mm mrad s}^{-1} \qquad \text{at 40 GeV} \tag{9.3}$$

can be deduced, while the initial emittance growth rate is

$$\frac{<\Delta\epsilon_x>}{\Delta t} \approx 1.9 \cdot 10^{-7} \text{ mm mrad s}^{-1} \qquad \text{at 820 GeV.} \tag{9.4}$$

The value at 820 GeV is smaller by a factor of ten than the value at injection, but note that the actual emittance is smaller as well, by a factor 20. The emittance growth rate is proportional to the number of protons per bunch. The quoted values refer to the design number of 10^{11}.

The emittance growth rate of a single test particle $\Delta\epsilon_x/\Delta t$ is proportional to the effective proton density seen during a full betatron oscillation. For a Gaussian bunch shape it can be written in the form

$$\frac{\Delta\epsilon_x}{\Delta t}(\epsilon_x, \epsilon_z) = c_{IB}\frac{1}{(2\pi)^2}\int_0^{2\pi} \exp\left(-\frac{2\epsilon_x}{\bar{\epsilon}_x}\cos^2\phi_x\right) d\phi_x \int_0^{2\pi} \exp\left(-\frac{2\epsilon_z}{\bar{\epsilon}_z}\cos^2\phi_z\right) d\phi_z, \tag{9.5}$$

where $\epsilon_{x,z}$ is the emittance of a single particle and the barred quantity $\bar{\epsilon}_{x,z}$ is the two-sigma beam emittance. The latter equals two times the average emittance of the bunch

$$<\epsilon_{x,z}> = \frac{\bar{\epsilon}_{x,z}}{2} = \frac{2\sigma^2_{p,x,z}}{\beta_p}. \tag{9.6}$$

The coefficient c_{IB} is obtained by requiring that the integral of $\Delta\epsilon_x/\Delta t$ over the bunch distribution yields the mean emittance growth rate,

$$\int_0^\infty \int_0^\infty \rho(\epsilon_x, \epsilon_z)\frac{\Delta\epsilon_x}{\Delta t}(\epsilon_x, \epsilon_z)\, d\epsilon_x\, d\epsilon_z = \frac{<\Delta\epsilon_x>}{\Delta t} \stackrel{!}{=} \frac{\bar{\epsilon}_x}{\tau_x}, \tag{9.7}$$

where τ_x is defined by

$$\frac{1}{\tau_x} = \frac{1}{\sigma_x}\frac{d\sigma_x}{dt}. \tag{9.8}$$

The value of τ_x is adopted from [80]. The integration is done numerically and the resulting normalization constant c_{IB} is

$$c_{IB} \approx 3.0 \cdot 10^{-6} \text{ mm mrad s}^{-1} \qquad \text{at 40 GeV}$$
$$\text{and} \quad c_{IB} \approx 3.8 \cdot 10^{-7} \text{ mm mrad s}^{-1} \qquad \text{at 820 GeV.}$$

In Fig. 9.1 the amplitude-dependent emittance growth rate $\Delta\epsilon_N/\Delta t$ (9.5) at 820 GeV and at 40 GeV is depicted as a function of the normalized emittance $\epsilon_N \equiv \gamma\epsilon \equiv \gamma(\epsilon_x + \epsilon_z)$ for the special case of equal horizontal and vertical emittance.

9.2 Tune Modulation and Field Errors at 40 GeV

The emittance growth caused by the interplay of tune modulation and high-order resonances has been estimated in chapter 5. From (5.10), we expect a single-particle emittance growth rate of about

$$\frac{\Delta\epsilon}{\Delta t} \approx 1 \cdot 10^{-11} \text{ mm mrad s}^{-1} \tag{9.9}$$

at an emittance $\epsilon = 1.2$ mm mrad, while we have

$$\frac{\Delta\epsilon}{\Delta t} \approx 2 \cdot 10^{-4} \text{ mm mrad s}^{-1} \tag{9.10}$$

at an emittance $\epsilon = 4.0$ mm mrad, assuming a modulation frequency of 50 Hz.

9.3 Gas Scattering and Proton-Electron Scattering

According to (8.28), an average hydrogen pressure of $5 \cdot 10^{-10}$ mbar causes an emittance growth rate due to multiple Coulomb scattering of about

$$\frac{<\Delta\epsilon>}{\Delta t} = 1.2 \cdot 10^{-7} \text{ mm mrad s}^{-1} \qquad \text{at 40 GeV,} \tag{9.11}$$

$$\frac{<\Delta\epsilon>}{\Delta t} = 3.0 \cdot 10^{-10} \text{ mm mrad s}^{-1} \qquad \text{at 820 GeV.} \tag{9.12}$$

The growth rate is inversely proportional to the mean pressure around the ring. Hence, for a hydrogen pressure of $4 \cdot 10^{-9}$ mbar the quoted numbers have to be multiplied by 8. The effect of nuclear interactions with the residual gas is considerably less important (see chapter 8).

From chapter 7, multiple proton-electron scattering gives rise to an emittance growth rate of

$$\frac{\Delta\epsilon_x}{\Delta t} \approx 10^{-10} \text{ mm mrad s}^{-1}, \tag{9.13}$$

which thus is about a factor 3–20 and a factor 2000 smaller than the average emittance increase due to residual gas scattering and intra-beam scattering, respectively.

9.4 Tune Modulation and Beam-Beam Interaction

During commissioning and operation of HERA it has been verified that the beam-beam interaction can lead to substantial particle losses and can reduce the proton beam lifetime to less than one hour. The lifetime is short, if the collision parameters are not optimized, for instance if the two beams do not collide centered, if the beams collide with a vertical crossing angle or if the proton tunes come too close to the seventh order resonance at $Q_x \approx Q_z \approx 0.286$. Even under good conditions, when the beam lifetime exceeds 24 hours, the beam-beam effect causes a significant amplitude-dependent transverse proton diffusion rate, which can be measured by the collimation system [64].

Computer simulations suggest a typical emittance growth rate in the order of

$$\frac{\Delta\epsilon}{\Delta t} \approx 4 \cdot 10^{-5} \text{ mm mrad s}^{-1}, \tag{9.14}$$

close to a 14th order resonance, if a random tune drift of $\Delta Q_{\text{rms}} = 5 \cdot 10^{-4}$ is included in the model [33].

The effect of a harmonic tune modulation with a frequency of 50 Hz has been studied in chapter 6 of this thesis. Close to an 8th order resonance it may cause an average emittance growth rate of

$$\frac{\Delta\epsilon}{\Delta t} \approx 0.01 \text{ mm mrad s}^{-1} \tag{9.15}$$

at an amplitude of about $x = z \approx 2.7\sigma_{el}$ ($\approx 2.7\sigma_p$). For a 10th order resonance the growth rate is smaller by a factor 50 000 and the higher-order resonances are suppressed even stronger (see Table 6.2).

If the collision is not centered, odd order resonances are excited too. The predicted emittance growth rates close to a 7th order resonance depend strongly on the displacement between both beams (chapter 6). At the amplitude $x = z \approx 2.7\sigma_{el}$, the emittance growth rate is about

$$\frac{< \Delta\epsilon >}{\Delta t} \approx 5 \cdot 10^{-4} \text{ mm mrad s}^{-1} \tag{9.16}$$

for a horizontal beam separation $\Delta x = 0.1\sigma_{el}$, while for the larger separation $\Delta x = 0.3\sigma_{el}$ the local growth rate is as high as

$$\frac{< \Delta\epsilon >}{\Delta t} \approx 0.2 \text{ mm mrad s}^{-1}. \tag{9.17}$$

The collision adjustment has to be better than $0.1\,\sigma_{el}$ to guarantee a satisfactory proton beam lifetime.

9.5 Comparison of Growth Rates

Table 9.5 summarizes the predicted emittance growth rates due to the various effects both at a proton energy of 40 GeV and of 820 GeV.

Fig. 9.2 shows typical emittance growth rates at injection energy due to nonlinear field errors, intra-beam scattering and residual gas scattering as a function of the single-particle emittance. The dominant effect at small amplitudes is intra-beam scattering, followed by residual gas scattering, which is already a factor three to four less important for the customary vacuum pressure values. The combination of tune modulation and persistent-current field errors generates chaotic regions in phase space and determines the dynamic aperture of the storage ring. It is responsible for very large emittance growth rates beyond about 2 mm mrad, in comparison to which all other processes become negligible.

Fig. 9.3 depicts emittance growth rates at 820 GeV caused by intra-beam scattering and by the beam-beam interaction close to a 10th order resonance as a function of the particle emittance. In the (unavoidable) presence of tune modulation the beam-beam interaction is the major source of transverse diffusion. So far the prediction is in agreement with the observations, but a detailed measurement of diffusion coefficients in the machine is still missing. If the beams do not collide centered the transverse proton diffusion can be much larger than indicated in the figure. For non-colliding beams, intra-beam scattering contributes mostly to the overall emittance growth.

effect	emittance growth during one second in mm mrad	comment
Injection Energy (40 GeV)		
nonlinear resonances & tune modulation	$2 \cdot 10^{-4}$	at 4.0 mm mrad
	$1 \cdot 10^{-8}$	at 2.0 mm mrad
	$1 \cdot 10^{-11}$	at 1.2 mm mrad
intra-beam scattering	$2 \cdot 10^{-6}$	[80]
residual gas scattering	$5 \cdot 10^{-7}$	hydrogen pressure $2 \cdot 10^{-9}$ mbar
	$1 \cdot 10^{-7}$	hydrogen pressure $5 \cdot 10^{-10}$ mbar
Luminosity Energy (820 GeV)		
beam-beam interaction	harmonic tune modulation, modulation frequency 50 Hz, $x = z \approx 2.7\,\sigma_{el}$	
	$2 \cdot 10^{-1}$	7th order resonance and $\Delta x = 0.3\,\sigma_{el}$
	$3 \cdot 10^{-2}$	7th order resonance and $\Delta x = 0.2\,\sigma_{el}$
	$1 \cdot 10^{-2}$	8th order resonance
	$5 \cdot 10^{-4}$	7th order resonance and $\Delta x = 0.1\,\sigma_{el}$
	$2 \cdot 10^{-7}$	10th order resonance
	$6 \cdot 10^{-20}$	12th order resonance
	random tune drift, $\Delta Q_{\mathrm{rms}} = 5 \cdot 10^{-4}$,	
	$4 \cdot 10^{-5}$	14th order resonance [33]
intra-beam scattering	$2 \cdot 10^{-7}$	initially [80]
	$7 \cdot 10^{-8}$	after 10 hours [80]
residual gas scattering	$1 \cdot 10^{-9}$	hydrogen pressure $2 \cdot 10^{-9}$ mbar
	$3 \cdot 10^{-10}$	hydrogen pressure $5 \cdot 10^{-10}$ mbar
multiple pe scattering	$1 \cdot 10^{-10}$	actual lumi parameters

Table 9.1: Comparison of the predicted emittance growth rates at injection energy and at 820 GeV. The values for the beam-beam interaction with random tune drift and for the intra-beam scattering have been adopted from [33] and [80].

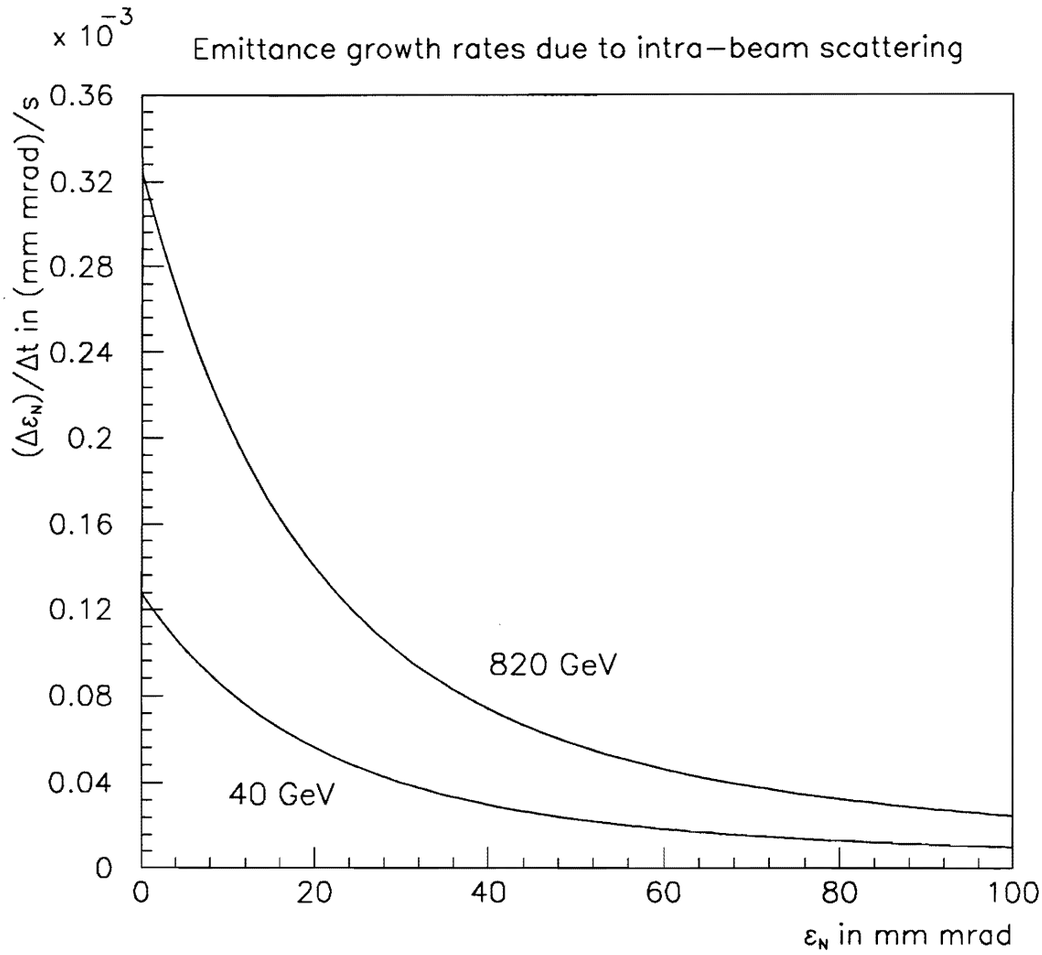

Figure 9.1: Emittance growth rate $\Delta\epsilon_N/\Delta t$ due to intra-beam scattering at 40 GeV and at 820 GeV as a function of the normalized emittance ϵ_N.

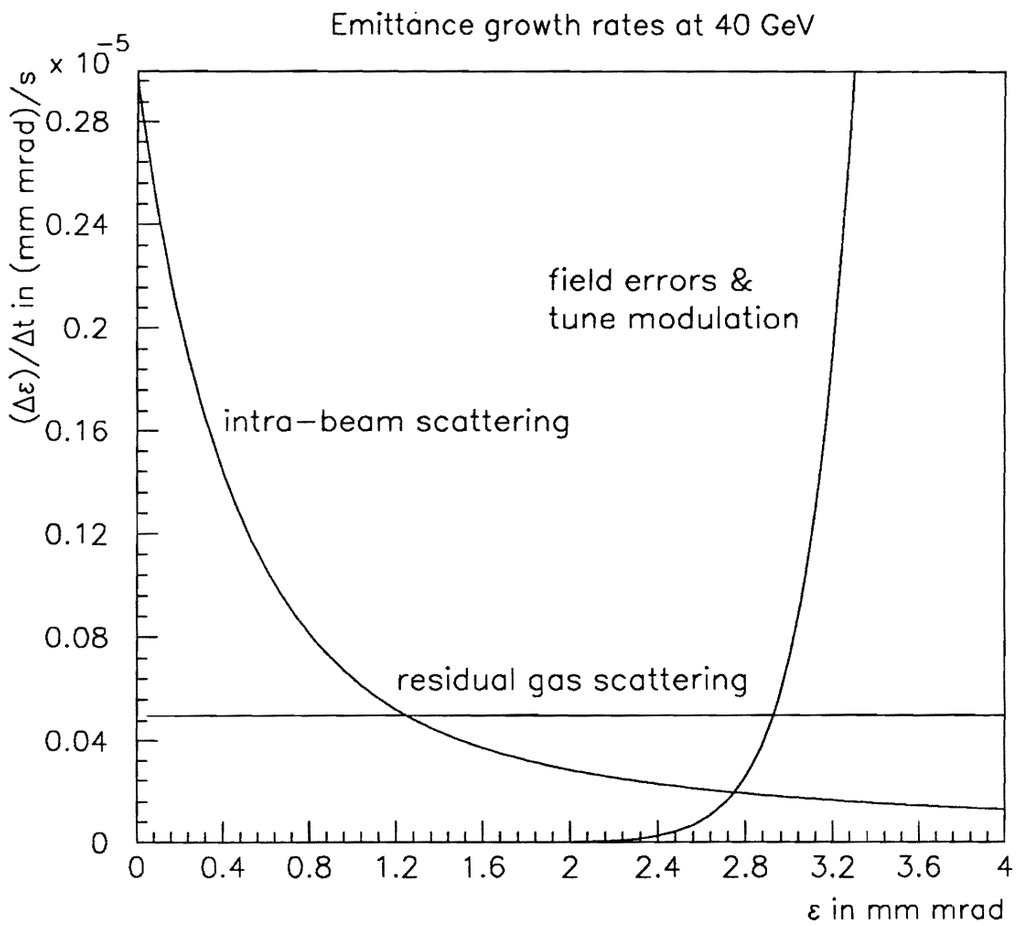

Figure 9.2: Emittance growth rates $\Delta\epsilon/\Delta t$ at 40 GeV as a function of the particle emittance ϵ. The values represent a typical situation.

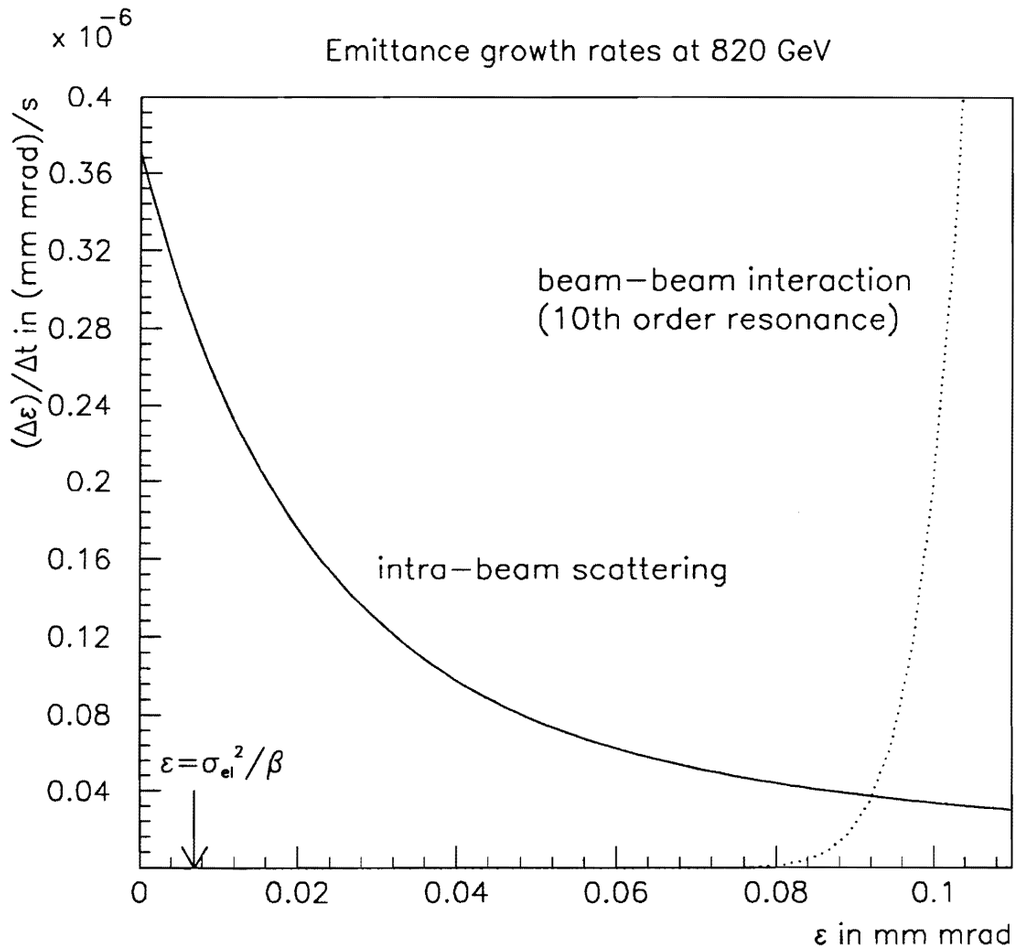

Figure 9.3: Emittance growth rates $\Delta\epsilon/\Delta t$ at 820 GeV as a function of the particle emittance ϵ. The values represent a typical situation.

Chapter 10

Conclusions

The observed dynamic aperture of about 1.2 mm mrad in the HERA proton ring at 40 GeV is in good agreement with the results of computer simulations and analytical calculations which include the effect of the measured nonlinear field errors of all superconducting magnets and an additional modest tune modulation.

Techniques to facilitate the simulation studies have been proposed and investigated in detail. The use of Lyapunov exponents in the postprocessing analysis of tracking data and the application of truncated or symplectified Taylor maps are promising and fast new methods.

Differential-algebra and Lie-algebra software packages have been installed, which provide the possibility to investigate analytically the high-order resonances in the HERA proton ring. It was shown for the first time that a suitable combination of normal-form and factorization processes permits the extraction of parameters for resonances including 11th order inside the whole dynamic aperture of a complex storage ring such as HERA.

A detailed theory describing the effect of an additional tune modulation in a nonlinear Hamiltonian system has been developed. This theory applies to the nonlinear magnet errors at injection energy as well as to the beam-beam interaction. It provides expressions for the chaotic fraction of phase space and for the amplitude-dependent emittance growth rate.

Emittance growth rates due to various sources have been evaluated and compared. At 40 GeV intra-beam scattering is the dominant diffusion-causing process inside the dynamic aperture. For large amplitudes the emittance-dependent diffusion rate due to the nonlinear field errors grows exponentially. The growth rate owing to residual gas scattering is not much smaller than the effect of intra-beam scattering and is prevailing in an intermediate amplitude range.

At 820 GeV the beam-beam interaction strongly affects the proton beam lifetime. Emittance growth rates are predicted for working points close to resonances of various order. In addition the excitation of the 7th order resonance near the actual working point has been studied as a function of the displacement between both beams. The beam displacement at the collision point should be smaller than $0.1\sigma_{el}$ in order not to lead to an unacceptable emittance growth and transverse diffusion. The necessity to adjust the collisions to such a high precision is consistent with the experience of HERA operation available up to now.

If the beams do not collide, intra-beam scattering is the main source of emittance growth also at 820 GeV. The diffusion rates resulting from multiple scattering with atoms of the residual gas and with electrons of the opposite bunch are smaller by about two or three orders of magnitude.

Stimulated by a serious lifetime limitation in the first commissioning run of HERA the effect of residual gas scattering on the beam lifetime has been analysed carefully. Starting from a Fokker-Planck equation, general expressions of the beam lifetime have been derived for several vacuum chamber geometries and including coupling. Residual gas scattering can be ruled out as a possible cause of the short beam lifetime in spring 1991.

The predicted dependence of the diffusion rates on the transverse amplitude will have to be compared with future collimator measurements.

Acknowledgements

I would like to express my deep gratitude to the DESY directorate for the possibility to participate in the commissioning of HERA, for the generous hospitality at DESY, and for financial support.

This thesis would not have been possible without the guidance and encouragement by Dr. F. Willeke, to whom I am very grateful.

I want to thank Dr. F. Schmidt for his continued interest in the progress of my work and for several useful advices. He also deserves my gratitude for the provision of his tracking code and for his co-operation in creating a differential-algebra version of the same.

I am grateful to Prof. P. Schmüser for his strong support and for various helpful discussions.

It is a pleasure to thank Prof. D. Edwards and Dr. H. Edwards for encouragement and for interesting conversations.

I am especially grateful to Dr. É. Forest. He taught me many details of differential algebra and normal-form algorithms. Furthermore he provided the software to perform the normal-form transformations and the Irwin factorization. I also want to thank him for the hospitality experienced at LBL.

I am very much indebted to Mr. K. Heinemann for a lot of stimulating discussions.

I am grateful to the AP group of the CERN SL division, in particular to Dr. J. Gareyte and to Dr. F. Schmidt, for several invitations, for hospitality and for generous support.

I would like to thank Dr. H. Edwards, Prof. P. Schmüser, Prof. B. Wiik and Dr. F. Willeke, who provided the possibility to visit Fermilab and LBL.

Dr. S. Peggs deserves my appreciation for the hospitality at Fermilab.

I am grateful to the SLAC directorate and to Dr. M. Zisman for an invitation to the Stanford B-factory workshop and for support.

I want to acknowledge financial support and hospitality experienced at Brookhaven National Laboratory on the occasion of the workshop on the stability of particle motion in storage rings. Especially I would like to thank Dr. A. Ruggiero, who made it possible for me to attend that conference.

Dr. A. Chao, Dr. M. Syphers and Dr. Y. Yan provided the opportunity to visit the Superconducting Supercollider. They deserve my thanks for support, hospitality and organization.

Moreover, I am grateful to Prof. M. Berz for the invitation to his workshop on high order effects in accelerators, for the received support and for the friendly provision of his differential-algebra package.

The help of the DESY magnet measuring group, which made available the multipole data of the HERA magnets, is also gratefully acknowlegded.

I want to thank a lot of people from DESY and elsewhere for their kind help and co-operation, for answering my questions and for hospitality, respectively. Among these are

Dr. R. Bacher, Dr. K. Balewski, Dr. D. Barber, Dr. A. Bazzani, Mr. S. Berg, Dr. W. Bialowons, Mr. M. Böge, Dr. G. Bourianoff, Dr. R. Brinkmann, Mr. O. Brüning, Dr. W. Chou, Mr. W. Decking, Dr. D. Degèle, Mr. H.-J. Eckoldt, Dr. J. Feikes, Dr. K. Flöttmann, Dr. M. Furman, Dr. W. Gabella, Dr. F. Galluccio, Dr. A. Gamp, Dr. E. Gianfelice-Wendt, Mr. M. Giovannozzi, Dr. S. Herb, Dr. J. Holt, Dr. B. Holzer, Dr. J. Irwin, Dr. G. Jackson, Dr. E. Karantzoulis, Dr. R. Kleiss, Mr. C. Kluth, Prof. R.-D. Kohaupt, Dr. J.-P. Koutchouk, Dr. S. Machida, Dr. J. Maidment, Dr. H. Mais, Dr. S. Mane, Dr. K.-H. Mess, Mr. O. Meincke, Mrs. A. Pauluhn, Mr. M. Pekeler, Dr. J. Petersen, Dr. F. Pilat, Dr. A. Piwinski, Dr. G. Ripken, Dr. D. Robin, Dr. J. Roßbach, Mr. T. Satogata, Dr. W. Scandale, Mr. D. Schulte, Dr. W. Schütte, Mr. M. Seidel, Dr. J. Shi, Dr. D. Trines, Mr. R. Wagner, Dr. R. Warnock, Mrs. K. Wipf, Mrs. S. Wipf, Mr. K. Wittenburg, Dr. S. Wolff, Dr. Y. Yan, Dr. V. Ziemann and many others...

I would like to thank the physicists and engineers, who have been spending their time with me on shifts in the control room, for the relaxed and co-operative atmosphere.

I greatly appreciate many illuminating discussions with members of H1 and ZEUS.

Furthermore, I am grateful to Dr. D. Barber, Prof. D. Edwards, Prof. E. Lohrmann, Dr. G. Ripken, Prof. P. Schmüser and Dr. F. Willeke for a careful reading of the manuscript and for several useful suggestions.

Finally, I want to thank Mrs. B. Lücke, Mrs. I. Nikodem, Mrs. U. Brebbermann, Mrs. A. Verweinen, Mrs. M. P. Colin, Mrs. M. Harvey, Mrs. P. Manning and Mrs. Y. Edwards for their assistance and valuable help.

Appendix A

Differential Algebra and Normal-Form Methods

A.1 Introduction

Differential Algebra (DA) [12] provides the basis for an automated perturbative treatment in terms of Taylor series which allows calculations of storage ring beam dynamics up to very high orders (say above 10th order) [23]. The DA-based perturbation treatment consists of two steps:

- Firstly, the formal power series map for a complex accelerator is extracted from a conventional tracking code like SIXTRACK [19].

- Secondly, this map is analysed by a normal-form algorithm in Lie-algebraic language. All the Lie-algebraic manipulations are very efficiently performed making use of the ability to calculate derivatives of arbitrary order with differential-algebra routines.

The normal-form procedure results in explicit expressions for important dynamical quantities. For example it provides the formal Pseudo-Hamiltonian, detuning and driving terms, island tunes, resonance widths and non-linear invariants. A by-product is a transformation A^{-1}, which can be used to transform particle tracking data into a new coordinate system. In this normal-form coordinate frame, regular motion shows up nearly as a 'circle'.

An advantage of this approach is that the analysis is done with a map obtained from the original tracking code. Thus there is a direct link between conventional tracking on the one side and analytical treatment on the other. For instance, to ensure, that the normal-form algorithm is still convergent at a specific amplitude, one can always cross-check with tracking. A comparison of the tunes deduced from tracking and the ones predicted by the Pseudo-Hamiltonian allows to verify the well behaving of the transformation. An alternative test of the convergence is a transformation of the tracking data by A^{-1}. Like every perturbative method the normal-form analysis breaks down at an amplitude where the first relevant resonance is crossed. This shortcoming is reflected by a divergence of A^{-1}.

Repeatedly another application of differential algebra has been advocated, namely to use the extracted Taylor map instead of the original code for tracking. The problems arising in this approach are dicussed in chapter 2.

A.2 Examples of Differential-Algebra Operations

Differential Algebra can be viewed as an application of nonstandard analysis or, more prosaically, as an efficient implementation of the Leibniz rule for derivatives. Here it will only be indicated by a few examples how the DA operations are performed.

The first component of a DA vector is the actual value of the considered quantity. The second component is the first derivative with respect to one of the independent variables. The further components contain Taylor series coefficients with respect to other variables or of higher order. In addition to a scalar multiplication and an addition, which are defined in the usual way, for DA vectors of first order and one independent variable a multiplication is introduced by

$$(a_0, a_1) \cdot (b_0, b_1) = (a_0 \cdot b_0, a_0 \cdot b_1 + b_0 \cdot a_1).$$

Let us consider the function

$$f(x) = x^2.$$

Starting with the DA vector

$$\vec{x} = (5, 1)$$

and applying the above multiplication rule the resulting vector is

$$\vec{f} = (5 \cdot 5, 5 \cdot 1 + 5 \cdot 1) = (25, 10).$$

Its components are the value of the function and the value of the first derivative at $x = 5$. The DA package is an elegant formulation of this basic idea. Every special function, that occurs in standard Fortran, is internally expressed as a power series, for which the described algebraic differentiation rules are then well defined. The generalization of commonly supported functions, like exponential function and square root, to differential algebra is facilitated by a remarkable property. According to the multiplication rules, nth order DA vectors of the special form $\vec{v} = (0, \vec{a}_{1 \to n})$, i. e. with zero value in the first vector component, vanish if taken to the $(n+1)$th power

$$(0, \vec{a}_{1 \to n})^i = (0, 0, \ldots, 0) \text{ for } i > n. \tag{A.1}$$

As a consequence the extension of ordinary functions in the differential-algebraic sense requires only the evaluation of finite sums (for more details see [12]). Note also that differential algebra operations always act on numbers and not on abstract variables.

For the more general case of two variables and second order the product $\vec{c} = \vec{a} \cdot \vec{b} = (c_0, c_1, c_2, \ldots, c_5)$ of the two DA vectors $\vec{a} = (a_0, a_1, a_2, \ldots, a_5)$ and $\vec{b} = (b_0, b_1, b_2, \ldots, b_5)$ is defined as follows

$$\begin{aligned}
c_0 &= a_0 \cdot b_0 \\
c_1 &= a_0 \cdot b_1 + a_1 \cdot b_0 \\
c_2 &= a_0 \cdot b_2 + a_2 \cdot b_0 \\
c_3 &= a_0 \cdot b_3 + a_1 b_1 + a_3 \cdot b_0 \\
c_4 &= a_0 \cdot b_4 + a_1 b_2 + a_2 \cdot b_1 + a_4 \cdot b_0 \\
c_5 &= a_0 \cdot b_5 + a_2 b_2 + a_5 \cdot b_0
\end{aligned} \tag{A.2}$$

A two-dimensional map consisting of a sequence of sextupole kicks and rotations may serve as an example, namely

$$\begin{pmatrix} x_j \\ p_j \end{pmatrix} = \begin{pmatrix} \cos 2\pi Q_1 & \sin 2\pi Q_1 \\ -\sin 2\pi Q_1 & \cos 2\pi Q_1 \end{pmatrix} \begin{pmatrix} x_i \\ p_i + x_i^2 \end{pmatrix}$$

followed by

$$\begin{pmatrix} x_f \\ p_f \end{pmatrix} = \begin{pmatrix} \cos 2\pi Q_2 & \sin 2\pi Q_2 \\ -\sin 2\pi Q_2 & \cos 2\pi Q_2 \end{pmatrix} \begin{pmatrix} x_j \\ p_j + x_j^2 \end{pmatrix} \tag{A.3}$$

The map (A.3) may be considered as a simple model storage ring in one degree of freedom. This miniature accelerator consists of a linear machine to which two separated sextupoles of equal strength have been added. In this interpretation the sum $Q_1 + Q_2$ corresponds to the tune of the storage ring, whereas the individual angles $2\pi Q_1$ and $2\pi Q_2$ are the phase advances between the two sextupoles.

To apply differential algebra, the initial values of the two DA vectors $\vec{x}$ and $\vec{p}$ are chosen as

$$\vec{x}_i = (0,1,0,0,0,0) \text{ and } \vec{p}_i = (0,0,1,0,0,0), \tag{A.4}$$

where the derivative of x and p with respect to itself has been set to one and all other components to zero. The multiplication rules defined above lead to

$$\begin{aligned}
\vec{x}_i^2 &= (0,0,0,2,0,0) \\
\vec{x}_j &= (0, \cos 2\pi Q_1, \sin 2\pi Q_1, \sin 2\pi Q_1, 0, 0) \\
\vec{p}_j &= (0, -\sin 2\pi Q_1, \cos 2\pi Q_1, \cos 2\pi Q_1, 0, 0) \\
\vec{x}_j^2 &= (0,0,0, \cos^2 2\pi Q_1, 2\sin 2\pi Q_1 \cos 2\pi Q_1, \sin^2 2\pi Q_1) \\
\vec{x}_f &= (0, \cos 2\pi(Q_1+Q_2), \sin 2\pi(Q_1+Q_2), \sin 2\pi(Q_1+Q_2) \\
&\quad + \sin 2\pi Q_2 \cos^2 2\pi Q_1, 2\sin 2\pi Q_2 \sin 2\pi Q_1 \cos 2\pi Q_1, \sin 2\pi Q_2 \sin^2 2\pi Q_1) \\
\vec{p}_f &= (0, -\sin 2\pi(Q_1+Q_2), \cos 2\pi(Q_1+Q_2), \cos 2\pi(Q_1+Q_2) \\
&\quad + \cos 2\pi Q_2 \cos^2 2\pi Q_1, 2\cos 2\pi Q_2 \sin 2\pi Q_1 \cos 2\pi Q_1, \cos 2\pi Q_2 \sin^2 2\pi Q_1)
\end{aligned} \tag{A.5}$$

Note that the matrix elements $\cos 2\pi Q_{1,2}$ and $\pm \sin 2\pi Q_{1,2}$ of the rotation are treated as scalar quantities and not as DA vectors. The components in the final DA vectors $\vec{x}_f$ and $\vec{p}_f$ are related to the derivatives of the coordinates x_f and p_f with respect to the initial ones x_i, p_i up to second order. More precisely, they agree with the coefficients c_{kl} in the Taylor series

$$x_f = \sum_{k,l=0}^{\infty} c_{kl}^x x_i^k p_i^l \text{ and } p_f = \sum_{k,l=0}^{\infty} c_{kl}^p x_i^k p_i^l \tag{A.6}$$

In our example the Taylor map coefficients are

$$\begin{aligned}
c_{00}^x &= 0 & c_{00}^p &= 0 \\
c_{10}^x &= \cos 2\pi(Q_1+Q_2) & c_{10}^p &= -\sin 2\pi(Q_1+Q_2) \\
c_{01}^x &= \sin 2\pi(Q_1+Q_2) & c_{01}^p &= \cos 2\pi(Q_1+Q_2) \\
c_{20}^x &= \sin 2\pi(Q_1+Q_2) & c_{20}^p &= \cos 2\pi(Q_1+Q_2) \\
&\quad + \sin 2\pi Q_2 \cos^2 2\pi Q_1 & &\quad + \cos 2\pi Q_2 \cos^2 2\pi Q_1 \\
c_{11}^x &= 2\sin 2\pi Q_2 \sin 2\pi Q_1 \cos 2\pi Q_1 & c_{11}^p &= 2\cos 2\pi Q_2 \sin 2\pi Q_1 \cos 2\pi Q_1 \\
c_{02}^x &= \sin 2\pi Q_2 \sin^2 2\pi Q_1 & c_{02}^p &= \cos 2\pi Q_2 \sin^2 2\pi Q_1.
\end{aligned}$$

For an actual storage ring a Taylor map representation is obtained in the same way. The closed orbit is chosen as the starting value for the first components of a four- or six-dimensional DA vector, the derivative with respect to itself is initially set to one and all other components are zero. If this vector is transformed through the model of the accelerator, the vector components after one turn are the coefficients of the Taylor map.

A.3 Normal-Form Analysis

Let f and g be arbitrary functions of phase space variables and A, B and C be arbitrary noncommuting operators. Denoting the Poisson bracket operator by $: f :$, i. e.

$$: f : g \equiv [f, g] \equiv \frac{\partial f}{\partial \vec{x}} \frac{\partial g}{\partial \vec{p}} - \frac{\partial f}{\partial \vec{p}} \frac{\partial g}{\partial \vec{x}}$$

the following theorems apply [26, 28, 20].

$$\begin{aligned} e^{:f:} e^{:g:} e^{:-f:} &= \exp(: e^{:f:} g :) && \text{(A.7)} \\ \exp(A)\exp(B) &= \exp(C) \\ \text{with } C &= A + B + \{A, B\}/2 + \{A, \{A, B\}\}/12 + \{B, \{B, A\}\}/12 + \cdots && \text{(A.8)} \\ \{: f :, : g :\} &= : [f, g] : . && \text{(A.9)} \end{aligned}$$

Theorems (A.7)–(A.9) are the fundamental relations used in the normal-form analysis. Formulae (A.7) and (A.8) allow to perform a composition of Lie transformations. Relation (A.9) describes an important homomorphism between the commutator algebra of Lie operators and the Poisson-bracket algebra of functions and is implicitly used in the normalization process. Because of its ability to evaluate derivatives, differential algebra offers the possibility to calculate Poisson brackets to arbitrary order. Let us assume, that we have extracted a Taylor series description of an accelerator

$$v_j^f = T^1_{jk} v_k^i + T^2_{jk_1k_2} v_{k_1}^i v_{k_2}^i + \ldots \equiv M_j(\vec{v}^i), \tag{A.10}$$

where the subscripts j or k denote the components of the phase space coordinate vector $\vec{v} \equiv (x, z, \sigma, p_x, p_z, \eta)$ and the superscripts i or f refer to the initial and final coordinates, respectively. The Taylor series M agrees with a symplectic map up to the truncation order. As described in detail in [23, 26, 27] the map M can be transformed into normal form N up to order $(no - 1)$ by a transformation A

$$M = A^{-1} N A \tag{A.11}$$

The transformation A is of the form

$$A = A_{no} \ldots A_4 A_3 A_2 A_1 \equiv e^{:f_{no}:} \ldots e^{:f_3:} A_2 A_1, \tag{A.12}$$

where A_1 and A_2 are the transformation to the closed orbit and the transformation to Courant-Snyder variables, respectively. The f_n are homogeneous polynomials of degree n in $x_k = \sqrt{2I_k}\cos\phi_k$ and $p_k = -\sqrt{2I_k}\sin\phi_k$. The normalized map N only contains action variables I_k and is independent of the phases ϕ_k,

$$N = \exp(: -\vec{\mu} \cdot \vec{I} + D(\vec{I}) :). \tag{A.13}$$

Here $D(\vec{I})$ denotes the nonlinear part of the exponent. The quantity $A^{-1}[\vec{\mu}\cdot\vec{I} - D(\vec{I})]$ is the formal Pseudo-Hamiltonian.

The normal-form result is well-behaved only inside a resonance-free domain around zero, because the transformation A^{-1} diverges close to resonances. A way to overcome this problem is to construct a partial normal-form by excluding harmful resonances from the transformation. Such a reduced normalization does not transform away completely the ϕ - dependent terms in the map M. On the one hand this is unfavorable because it prevents the construction of a global, only action-dependent Hamiltonian, but on the other hand a partial normalization offers the possibility to calculate driving terms for specified resonances. This scheme allows the evaluation of island widths and other resonance parameters (see chapter 3 and 5).

If all resonances are excluded from the transformation, the normalization process leads to a Dragt-Finn factorization [20] of the map $\tilde{M} \equiv A_2 A_1 M A_2^{-1} A_1^{-1}$

$$\tilde{M} = e^{:h_2:} e^{:h_3:} e^{:h_4:} \ldots e^{:h_{n_o}:} + \mathcal{O}(n_o), \tag{A.14}$$

where the h_n denote homogeneous polynomials of degree n in x_k and p_k.

A.4 Example of a Normal-Form Transformation

As an illustration the transformation to normal form is performed for a two-dimensional map M (compare also [28]) consisting of a rotation

$$\begin{pmatrix} x \\ p \end{pmatrix}_f = \begin{pmatrix} \cos 2\pi Q & \sin 2\pi Q \\ -\sin 2\pi Q & \cos 2\pi Q \end{pmatrix} \begin{pmatrix} x \\ p \end{pmatrix}_i \equiv R \begin{pmatrix} x \\ p \end{pmatrix}_i \tag{A.15}$$

and an octupolar kick

$$p_f = p_i + k_o x_i^3, \tag{A.16}$$

where the parameter k_0 is a measure of the octupole strength. In this example the closed orbit is zero and the linear part of the map is already independent of the beta function. Consequently the transformations A_1 and A_2 of (A.12) are identity transformations. Introducing action and angle variables I and ϕ by

$$x = \sqrt{2I}\cos\phi \qquad \text{and} \qquad p = -\sqrt{2I}\sin\phi \tag{A.17}$$

the rotation R (A.15) can be written as

$$R = e^{-:2\pi Q I:}. \tag{A.18}$$

The octupolar kick (A.16) is expressed by the Lie transformation $e^{:k_0 \frac{x^4}{4}:}$, so that the complete map is

$$M = e^{-:2\pi Q I:} e^{:k_0 \frac{x^4}{4}:}. \tag{A.19}$$

Equation (A.19) already agrees with the Dragt-Finn factorization (A.14) of the map M ($M = \tilde{M}$). In the following the octupole strength k_0 is considered as a smallness parameter of an order-by-order perturbative calculation. For later convenience, the abbreviation f is introduced for the nonlinear term in the exponent

$$f \equiv \frac{x^4}{4} = \frac{1}{8} I^2 (\cos 4\phi + 4\cos 2\phi + 3). \tag{A.20}$$

To construct a transformation A_3, that brings M into normal form N to first order in k_0,

$$N = A_3 M A_3^{-1}, \tag{A.21}$$

we make the ansatz

$$A_3 = e^{:k_0 F:}, \tag{A.22}$$

where the exponent F has to be determined. Combining (A.19)–(A.22) leads to

$$\begin{aligned} A_3 M A_3^{-1} &= \\ &= e^{:k_0 F:} R e^{:k_0 f:} e^{-:k_0 F:} && \text{(A.23)} \\ &= R R^{-1} e^{:k_0 F:} R e^{:k_0 f:} e^{-:k_0 F:} && \text{(A.24)} \\ &= R e^{:k_0 R^{-1} F:} e^{:k_0 f:} e^{-:k_0 F:} && \text{(A.25)} \\ &= R e^{:k_0 (R^{-1} F + f - F):} + \mathcal{O}(k_0^2). && \text{(A.26)} \end{aligned}$$

In the step from (A.25) to (A.26) use has been made of theorem (A.7). Equation (A.26) is obtained by applying the Baker-Campbell-Hausdorff theorem (A.8). It is beneficial to decompose the function f into two parts

$$f = f_0(I) + f_r(I, \phi), \tag{A.27}$$

where f_0 is purely action-dependent. The operator $(1 - R^{-1})$ can only be inverted on the angle-dependent part $f_r(I, \phi)$, because $(1 - R^{-1}) f_0(I) = 0$. If the function F is chosen such that

$$F = (1 - R^{-1})^{-1} f_r \tag{A.28}$$

the transformed map N is in normal form to first order in k_0,

$$N = R e^{:k_0 f_0(I):} + \mathcal{O}(k_0^2) = R e^{:k_0 \frac{3}{8} I^2:} + \mathcal{O}(k_0^2). \tag{A.29}$$

In this example F is given by

$$F = \frac{I^2}{16} \left(\cos 4\phi + \frac{\sin 4\phi \sin 8\pi Q}{1 - \cos 8\pi Q} + 4 \cos 2\phi + 4 \frac{\sin 2\phi \sin 4\pi Q}{1 - \cos 4\pi Q} \right). \tag{A.30}$$

It is typical that small denominators of the form $1/(1 - \cos n 2\pi Q)$ are present, which cause a divergence of the transformation A_3 near resonances $nQ \approx p$.

In the next step a second order normal-form transformation

$$A_4 = e^{:k_0^2 G:} \tag{A.31}$$

is applied to the first-order normalized map N (A.29). The exponent G is determined in the same way as F [23, 28]. The order-by-order transformation can be performed up to an order as high as 11 and is finally terminated by a divergence due to resonances.

A.5 Comparison of the Map and the Hamiltonian

The octupole kick map, defined by (A.15) and (A.16), may also serve to illustrate the differences between the Hamiltonian picture and the map picture in the analysis of a single resonance [29].

A.5.1 Hamiltonian

The octupole kick map is derived from the Hamiltonian

$$H(I,\phi,\theta) = QI - \delta(\theta)\frac{k_o}{4}x^4$$

where

$$x = \sqrt{2I}\cos\phi \text{ and } p = -\sqrt{2I}\sin\phi. \tag{A.32}$$

Inserting these relations and the series expansion of the delta function we have

$$H(I,\phi,\theta) = QI - \frac{1}{2\pi}\frac{k_o}{8}I^2\sum_m[\cos(4\phi+m\theta)+4\cos(2\phi+m\theta)] - \frac{1}{2\pi}\frac{3k_o}{8}I^2\sum_m e^{im\theta}. \tag{A.33}$$

Near the resonance $4Q = 1$ we neglect all oscillating terms except for the resonant one (corresponding to an averaging over θ) and obtain

$$H(I,\phi,\theta) = QI - \frac{1}{2\pi}\frac{k_o}{8}I^2\cos(4\phi-\theta) - \frac{1}{2\pi}\frac{3k_o}{8}I^2. \tag{A.34}$$

A canonical transformation $(I,\phi) \to (J,\tilde{\phi})$ generated by

$$F(J,\phi) = J\cdot\left(\phi - \frac{1}{4}\theta\right), \tag{A.35}$$

eliminates the explicit theta-dependence of the Hamiltonian. The new Hamiltonian becomes

$$H(J,\tilde{\phi}) = \left(Q - \frac{1}{4}\right)J - \frac{1}{2\pi}\frac{k_o}{8}J^2\cos(4\tilde{\phi}) - \frac{1}{2\pi}\frac{3k_o}{8}J^2. \tag{A.36}$$

A.5.2 Lie-Algebraic Treatment

In the Lie algebraic language the map is written as

$$M = e^{:-\pi Q(x^2+p^2):}e^{:+\frac{k_o}{4}x^4:} = Re^{:+\frac{k_o}{4}x^4:}, \tag{A.37}$$

where R denotes the rotation by an angle $2\pi Q$. Introducing action and angle coordinates I, ϕ via

$$h^+ = x + ip = \sqrt{2I}e^{-i\phi}, \tag{A.38}$$

$$h^- = x - ip = \sqrt{2I}e^{+i\phi}, \tag{A.39}$$

one can rewrite x^4 as

$$\begin{aligned} x^4 &= \left(\frac{h^+ + h^-}{2}\right)^4 \\ &= \frac{3}{2}I^2 + \frac{1}{2}I^2\cos(4\phi) + 2I^2\cos(2\phi) \end{aligned} \tag{A.40}$$

By excluding the fourth integer resonance from the normal-form procedure, a transformation A_{res} is constructed with

$$N_{res} \equiv A_{res}Re^{:+\frac{k_o}{4}x^4:}A_{res}^{-1} = Re^{:+\frac{k_oI^2}{8}\cos(4\phi)+\frac{3k_oI^2}{8}:} + \mathcal{O}(k_o^2). \tag{A.41}$$

In analogy to the Hamiltonian treatment it is possible to transform to a rotating coordinate frame [30]. To this end a co-moving map N_c is introduced by

$$\begin{aligned} N_c &\equiv \exp\left(: \frac{2\pi I}{4} :\right) \cdot N_{res} \\ &= \exp\left(: -2\pi \left(Q - \frac{1}{4}\right) I :\right) \exp\left(: +\frac{k_o I^2}{8} \cos(4\phi) + \frac{3k_o I^2}{8} :\right) + \mathcal{O}(k_o^2). \end{aligned} \tag{A.42}$$

Close to the resonance the difference $\delta \equiv Q - 1/4$ is a small quantity. Therefore the two exponents can be combined into one. Neglecting terms of order $(\delta \cdot k_o)$ (A.42) becomes

$$N_c \approx \exp\left(: -2\pi \left(Q - \frac{1}{4}\right) I + \frac{k_o I^2}{8} \cos(4\phi) + \frac{3k_o I^2}{8} :\right) + \mathcal{O}(\delta k_o) + \mathcal{O}(k_o^2). \tag{A.43}$$

The transformation to the co-moving frame is necessary for creating a small quantity δ such as to allow the combination of the exponents. To first order in k_o, the Pseudo-Hamiltonian $\tilde{H}$ of (A.43), defined by $N_c \equiv \exp(: -2\pi\tilde{H} :)$, is identical to the Hamiltonian (A.36) obtained earlier.

A.6 Examples of Normal-Form Results

To illustrate the possibilities of the implemented normal-form algorithms [12, 23, 26, 30], some results are presented for two maps similar to the Hénon map [31].

We first deal with the octupole kick map as defined by (A.15) and (A.16). Let us choose $k_o = -4$ and $Q = 0.245$. Fig. A.1 a) shows the original tracking data for five trajectories, three of which (near the separatrix) can hardly be distinguished. In Fig. A.1 b), a seventh order transformation A^{-1} is applied to the original data. The transformation diverges close to the resonance. If the resonance $4Q = 1$ is excluded from the normalization process, a reduced transformation A_R^{-1} is obtained. The trajectories transformed by A_R^{-1}, in Fig. A.1 c), are very similar to the original trajectories of Fig. A.1 a), apart from a somewhat greater 90-degree symmetry.

From (A.36), the action value at the stable fixed point of the fourth integer resonance is

$$J_r = -\pi \left(Q - \frac{1}{4}\right).$$

This is positive only for values of Q below 0.25. For larger values of Q, the negative resonant action corresponds to imaginary coordinates x and p. Because the convergence behavior of a Taylor series is controlled by singularities in the whole complex plane, the divergence of the normal-form analysis can also be caused by such 'imaginary resonances'. To illuminate this point, we present results, analogous to Fig. A.1, for the case $Q = 0.255$ in Fig. A.2. In Fig. A.2 a) no islands are visible, but in Fig. A.2 b) the convergence of the perturbation series is disturbed by the same 4th integer resonance as in Fig. A.1 b). Therefore, even if no resonances are visible in the original phase space diagram, it is not guaranteed that the normal-form algorithm converges properly. Again, if the resonance $4Q = 1$ is excluded from the transformation, the divergence is removed, in Fig. A.2 c).

Fig. A.3 a) shows the amplitude-dependence of the tune obtained from the full transformation A^{-1} and from the reduced transformation A_R^{-1} (resonance $4Q = 1$ excluded) in the case $Q = 0.245$. In Fig. A.3 b), the cosine-like driving term of the 4th integer resonance is depicted. The results can be compared with a conventional first order perturbation theory applied to the

Hamiltonian (A.36). Using the relation $J = x_{start}^2/2$, a detuning by 0.06 and a driving term of about $1.24 \cdot 10^{-3}$ are expected at $x_{start} = 0.5$. This agrees with the normal-form result of the reduced transformation, which was to be expected.

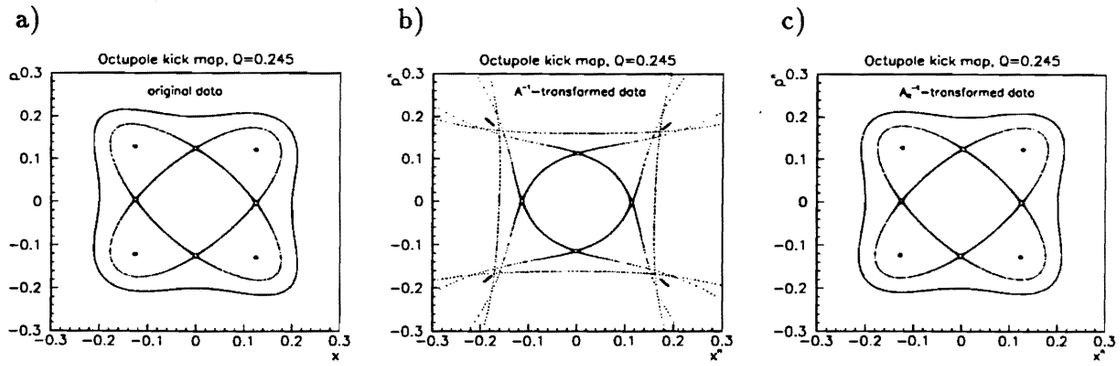

Figure A.1: Original and transformed phase space diagram for the octupole kick map with $Q = 0.245$.

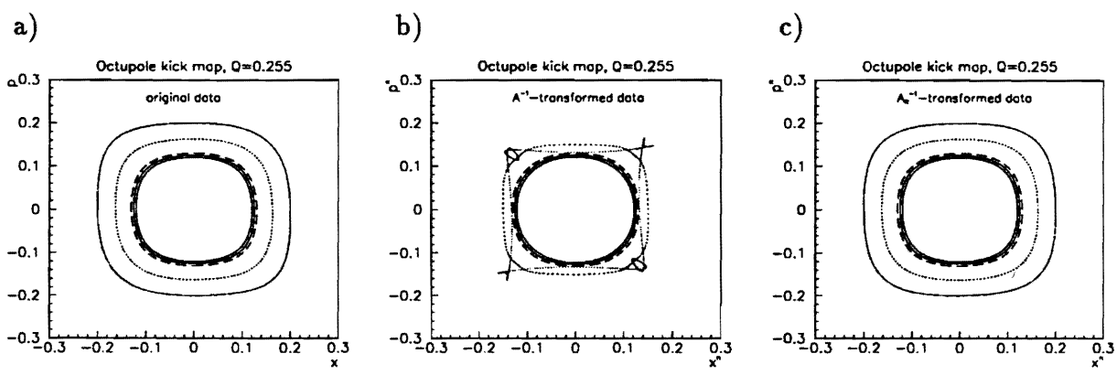

Figure A.2: Original and transformed phase space diagram for the octupole kick map with $Q = 0.255$.

As a second example we consider a four-dimensional map consisting of a rotation

$$\begin{pmatrix} x \\ p_x \\ z \\ p_z \end{pmatrix}_f = \begin{pmatrix} \cos 2\pi Q_x & \sin 2\pi Q_x & 0 & 0 \\ -\sin 2\pi Q_x & \cos 2\pi Q_x & 0 & 0 \\ 0 & 0 & \cos 2\pi Q_z & \sin 2\pi Q_z \\ 0 & 0 & -\sin 2\pi Q_z & \cos 2\pi Q_z \end{pmatrix} \begin{pmatrix} x \\ p_x \\ z \\ p_z \end{pmatrix}_i \tag{A.44}$$

and of a sextupolar and an octupolar-like kick

$$\begin{aligned} p_{xf} &= p_{xi} + k_n(x_i^2 - z_i^2) - 2k_s x_i z_i + k_o x_i^3 \\ p_{zf} &= p_{zi} + k_s(z_i^2 - x_i^2) - 2k_n x_i z_i \end{aligned} \tag{A.45}$$

Let us, arbitrarily, choose the values $Q_x = 0.245$, $Q_z = 0.29$, $k_n = k_s = -1$ and $k_o = -4$. Fig. A.4 a) and d) show the original phase space data in the x-p_x- and in the z-p_z-plane for five different regular trajectories. A normal-form analysis up to 7th order has been performed for the (in this case exact) corresponding Taylor map. In Fig. A.4 b) and e), the normal-form transformation A^{-1} is applied to the original coordinates. At small amplitudes the motion is almost perfectly decoupled and circular. As expected the transformation A^{-1} is strongly

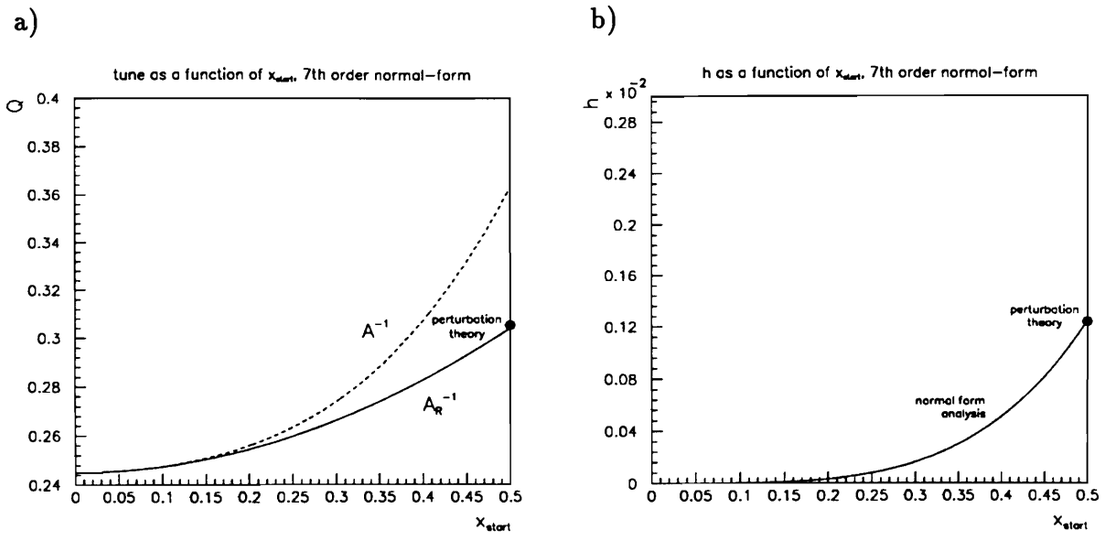

Figure A.3: Normal-form analysis for the octupole kick map: a) tune as a function of starting amplitude for the reduced transformation A_R^{-1} (solid curve) and the full transformation A^{-1} (dotted curve); b) driving term $h(I)$ of the $4Q = 1$ resonance as a function of starting amplitude (solid curve). Also shown is the result of a conventional first order perturbation theory for $x_{start} = 0.5$ (closed circle).

divergent close to the resonance $4Q_x = 1$. In Fig. A.4 c) and f), we depict data transformed by A_R^{-1}, in the construction of which the resonance $4Q_x = 1$ has been excluded. No divergence is observed for this reduced transformation. The price is that the motion at small amplitudes is not completely circular, but exhibits a more distinct residual 4-fold structure in the horizontal plane, in Fig. A.4 c), as compared with Fig. A.4 b).

As indicated in chapter 3, to study the effect of tune modulation on a single resonance, the island tune, the detuning function $g(I_x, I_z)$ and its derivatives as well as the driving term $h(I_x, I_z)$ have to be known [1]. For the four-dimensional map (A.44)–(A.45), the tunes Q_x and Q_z are depicted as a function of the starting amplitudes x_{start} and z_{start} in Fig. A.5. Fig. A.6 shows the cosine-like driving term of the $4Q_x = 1$ resonance as a function of x_{start}. There is no sine-like driving term in this particular case. The second derivatives of the detuning function g with respect to the action variables I_x and I_z are presented in Fig. A.7 a) and b). The curves shown illustrate that a Taylor map may provide detailed informations on resonance islands.

The resonance parameters of an arbitrary Taylor map can be computed in two steps. First, the amplitude values are determined at which a particular resonance condition is fulfilled. Afterwards, for these amplitudes the driving term h of the resonance and the second derivatives of the detuning function g are evaluated, which enter into the expressions for the island tune, for the island width and for the width of the stochastic layer (see chapter 3). Results for HERA are quoted in chapter 5 and in appendix B.

[1]The functions $h(I_x, I_z)$ and $g(I_x, I_z)$ are defined in equation (3.57).

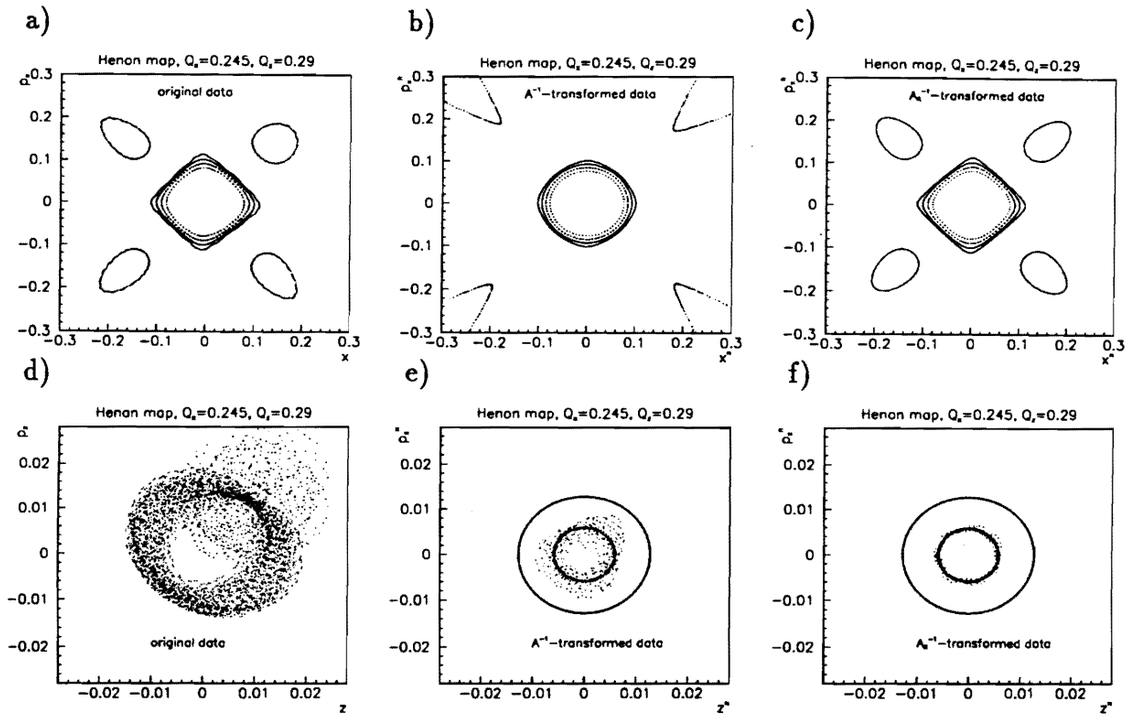

Figure A.4: Original and transformed phase space diagrams of the map (A.44)–(A.45); a)–c) horizontal plane, d)–f) vertical plane.

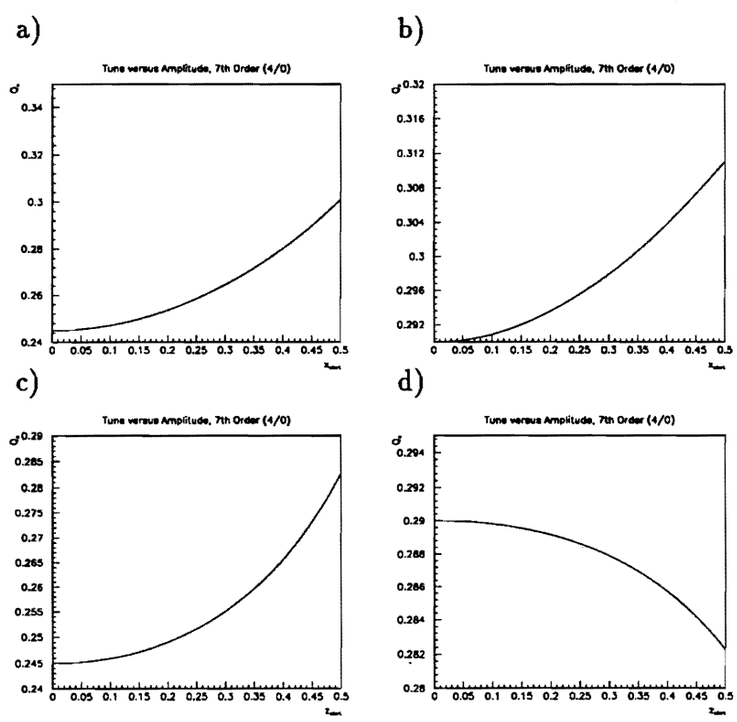

Figure A.5: Tune as a function of amplitude for the map (A.44)–(A.45); a) tune Q_x as a function of x_{start}, b) tune Q_z as a function of x_{start}, c) tune Q_x as a function of z_{start}, d) tune Q_z as a function of z_{start}.

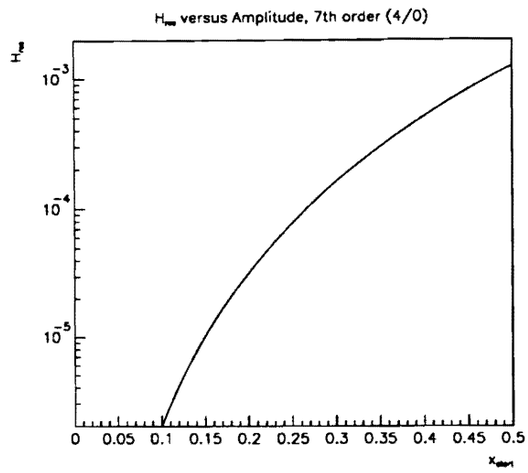

Figure A.6: Driving term $h(I)$ of the $4Q_x = 1$ resonance for the map (A.44)–(A.45) as a function of starting amplitude x_{start}.

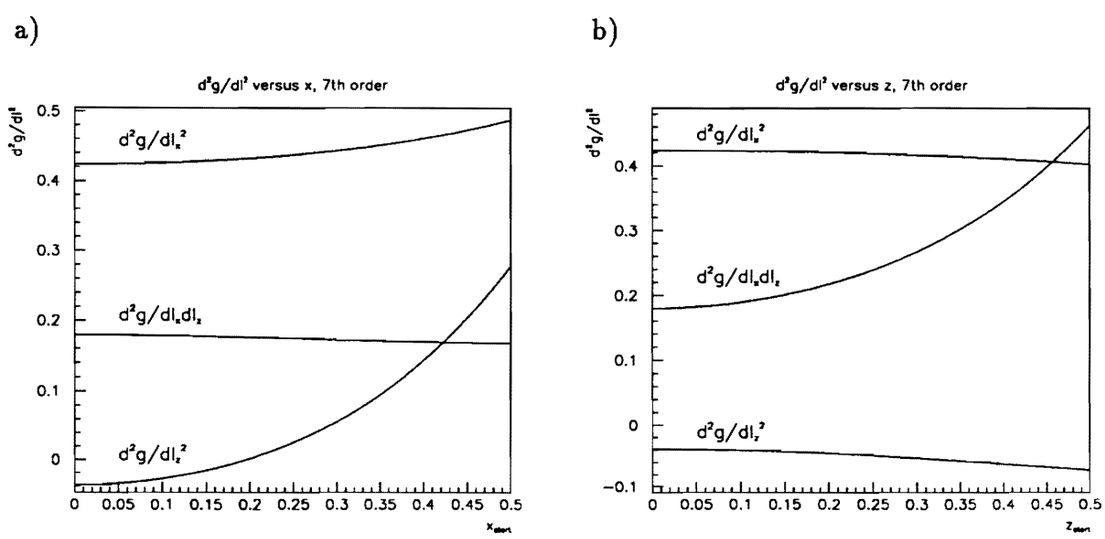

Figure A.7: Second derivative of the detuning function $g(I)$ for the map (A.44)–(A.45); a) $\partial^2 g/\partial I_{x,z}^2$ as a function of starting amplitude x_{start}, b) $\partial^2 g/\partial I_{x,z}^2$ as a function of starting amplitude z_{start}.

A.7 Description of the Beam-Beam Interaction by Differential Algebra

While differential algebra is adequate for the treatment of nonlinear multipole kicks, which are polynomials, this is not necessarily the case for other nonlinear forces. In this section we give a counterexample, which simultaneously shows that a discrepancy between the DA-based normal-form results and tracking is not always related to small denominators and resonance crossing. If the force is not properly represented by a Taylor series, the DA approach may already fail at a relatively small amplitude, far from any resonance. This is unfortunately true for the highly nonlinear beam-beam force.

It is not difficult to extract a Taylor map description of the beam-beam force even for the case of colliding flat beams, which is of importance for HERA. As is well known the general beam-beam kick can be rewritten in terms of the complex error function [32]. However, in order to apply the methods of differential algebra the beam-beam kick has to be expressed by a set of standard functions, which are supported by the employed DA package [12]. A practical solution is to represent the complex error function by a sum of fractions [33], similar to a Padé approximation. This representation is suitable for a differential-algebra treatment. For simplicity a model as in [33] was examined, consisting only of a 4-dimensional rotation followed by a beam-beam kick, that combines the effect of two collision points.

For our present purpose it is, however, sufficient to discuss only the collision of two round beams, which is a possible option for future HERA operation. Fig. A.8 compares the tune as a function of amplitude obtained by tracking with the result of an 8th order normal-form analysis and a subsequent 11th order Dragt-Finn factorization — a combination, which proves to be very useful in studying the effect of nonlinear field errors in HERA (see chapter 5). A strong discrepancy is observed at amplitudes above 0.3 mm, corresponding to two standard deviations $\sigma_{x,z}$ of either beam.

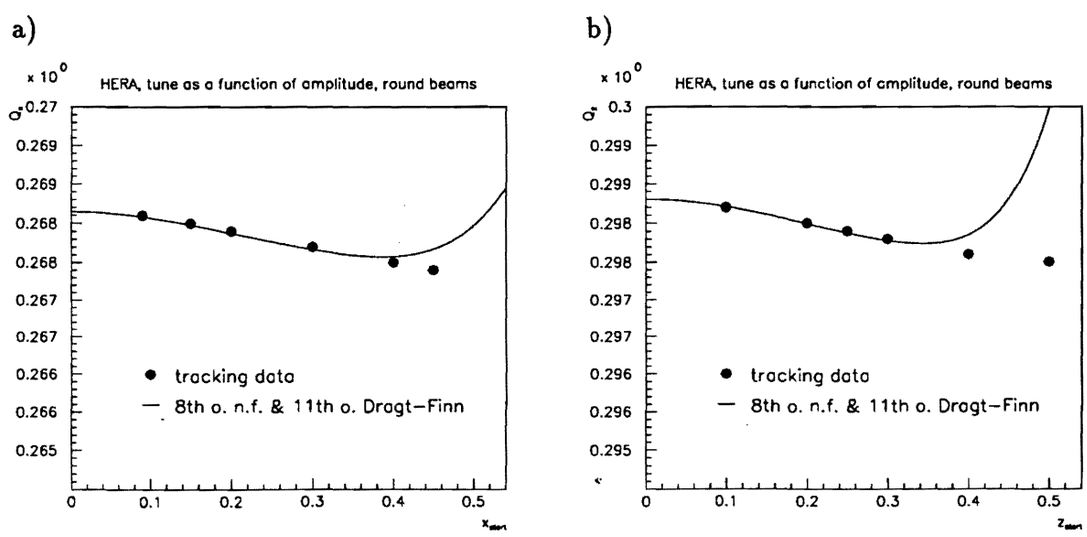

Figure A.8: Result of normal-form analysis for the beam-beam interaction: a) tune Q_x as a function of x_{start}, b) tune Q_z as a function of z_{start}. The maximum amplitude corresponds to about 3.5σ of either beam.

The proton beam-beam kick due to a round electron beam is given by

$$\theta_x = -\frac{8\pi\bar{\xi}_p\sigma_{el}^2}{\beta^*}\frac{x}{x^2+z^2}\left(1-\exp\left(-\frac{x^2+z^2}{2\sigma_{el}^2}\right)\right), \tag{A.46}$$

where β^* is the proton beta function at the interaction point, σ_{el} is the electron beam size and $\bar{\xi}_p$ is the proton beam-beam tune shift, which is expressed in terms of the beam size σ_{el} and the number of electrons per bunch N_{el} as

$$\bar{\xi}_p = \frac{\beta_p^* N_{el} e^2}{(4\pi)^2 \varepsilon_0 m_p c^2 \gamma_p \sigma_{el}^2}$$

The reason for the discrepancy observed in Fig. A.8 is evident from Fig. A.9. The beam-beam kick (A.46) (solid curve) is badly reproduced by 9th and even 11th order Taylor maps, which both diverge at about $2\sigma_{el}$. The results of a differential-algebra application to the flat beam collision show no qualitative difference to the round beam case.

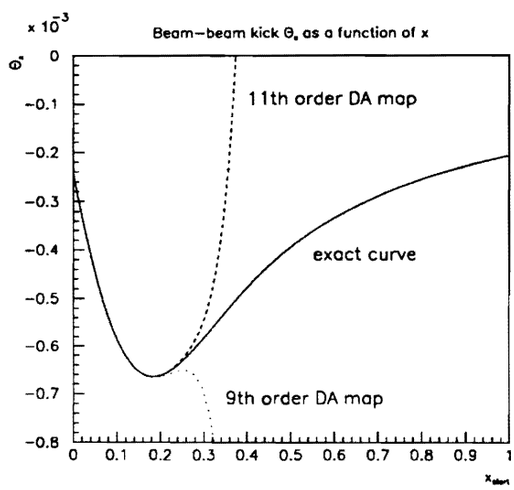

Figure A.9: Beam-beam kick θ_x caused by a round opposite beam of size $\sigma \approx 0.15$ mm versus initial amplitude x_{start}.

At amplitudes below $2\sigma_{el} \approx 2\sigma_p$ the Taylor map description and also the subsequent normal-form transformation may still work well. This implies that high-order resonances are, in principle, still accessible inside the two-sigma region. Here, the corresponding island parameters could be determined in the same way as for the evaluation of the dynamic aperture in chapter 5. In HERA, however, the nominal proton beam-beam tune shift per interaction point is 0.0012 and for the chosen working points no resonances of order up to 11 are crossed at amplitudes below $2\sigma_p$. Such a statement need not necessarily be true for proton colliders, which may have beam-beam tune shifts as large as 0.005 per interaction point.

Because it is impossible to extract the required information on resonances by use of differential algebra, another approach is needed to study the effect of tune modulation on the beam-beam interaction. An analytical treatment is presented in chapter 6.

Appendix B

Parameters of High-Order Resonances in HERA

The parameters of resonances through 11th order in an emittance range up to $\epsilon_x = \epsilon_z = 4$ mm mrad are listed in Tables B.1–B.3 for the actual HERA proton ring (model I). Each table refers to a slightly different working point. The amplitude values x and z are quoted for a position with a horizontal and vertical beta function of $\beta_x \approx 28.5$ m and $\beta_z \approx 3.8$ m, respectively.

Table B.4 shows analogous resonance-parameters for model II, which differs from model I by the increased 20-pole coefficient in the quadrupole magnets (see chapter 5). For the single working point investigated, 18 resonances are crossed as compared with 6–11 resonances for model I. The larger number of resonance-crossings reflects the additional detuning due to the enhanced 20-pole component.

x	z	Resonance	$\partial^2 g/\partial I_x^2$	$\partial^2 g/\partial I_x \partial I_z$	$\partial^2 g/\partial I_z^2$	h	Q_I
0.000	2.720	$-3Q_x + 6Q_z = 100$	$0.5 \cdot 10^{-2}$	$-0.4 \cdot 10^{-2}$	$0.26 \cdot 10^{-3}$	$0.2 \cdot 10^{-10}$	$2 \cdot 10^{-6}$
0.000	2.780	$6Q_x - 2Q_z = 123$	$0.5 \cdot 10^{-2}$	$-0.4 \cdot 10^{-2}$	$0.29 \cdot 10^{-3}$	$0.13 \cdot 10^{-14}$	$1.9 \cdot 10^{-8}$
0.000	2.800	$9Q_x + 2Q_z = 346$	$0.5 \cdot 10^{-2}$	$-0.4 \cdot 10^{-2}$	$0.30 \cdot 10^{-3}$	$0.14 \cdot 10^{-23}$	$6.1 \cdot 10^{-13}$
0.000	2.840	$3Q_x + 4Q_z = 223$	$0.55 \cdot 10^{-2}$	$-0.4 \cdot 10^{-2}$	$0.32 \cdot 10^{-3}$	$0.13 \cdot 10^{-9}$	$2.3 \cdot 10^{-6}$
0.000	3.960	$8Q_x + 3Q_z = 347$	$0.8 \cdot 10^{-2}$	$-0.57 \cdot 10^{-2}$	$0.18 \cdot 10^{-1}$	$0.33 \cdot 10^{-20}$	$2.9 \cdot 10^{-11}$
4.290	0.000	$7Q_x - 3Q_z = 122$	$0.33 \cdot 10^{-2}$	$-0.27 \cdot 10^{-2}$	$-0.71 \cdot 10^{-4}$	$0.9 \cdot 10^{-12}$	$5 \cdot 10^{-7}$
6.105	0.000	$-4Q_x + 7Q_z = 101$	$0.31 \cdot 10^{-2}$	$-0.22 \cdot 10^{-2}$	$-0.17 \cdot 10^{-3}$	$0.3 \cdot 10^{-16}$	$2 \cdot 10^{-9}$
7.150	0.000	$11Q_x = 344$	$0.30 \cdot 10^{-2}$	$-0.20 \cdot 10^{-2}$	$-0.19 \cdot 10^{-3}$	$0.11 \cdot 10^{-7}$	$6.3 \cdot 10^{-5}$
5.720	2.080	$7Q_x - 3Q_z = 122$	$0.39 \cdot 10^{-2}$	$-0.24 \cdot 10^{-2}$	$-0.27 \cdot 10^{-3}$	$0.16 \cdot 10^{-6}$	$2.2 \cdot 10^{-4}$
6.490	2.360	$-4Q_x + 7Q_z = 101$	$0.39 \cdot 10^{-2}$	$-0.21 \cdot 10^{-2}$	$-0.36 \cdot 10^{-3}$	$0.31 \cdot 10^{-6}$	$2.24 \cdot 10^{-4}$
8.415	3.060	$11Q_x = 344$	$0.38 \cdot 10^{-2}$	$-0.13 \cdot 10^{-2}$	$-0.62 \cdot 10^{-3}$	$0.77 \cdot 10^{-7}$	$1.9 \cdot 10^{-4}$

Table B.1: Characteristics of high-order resonances in model I of HERA as a function of starting amplitudes x and z, for the working point $Q_x = 31.27$, $Q_z = 32.30$.

x	z	Resonance	$\partial^2 g/\partial I_x^2$	$\partial^2 g/\partial I_x \partial I_z$	$\partial^2 g/\partial I_z^2$	h	Q_I
0.000	3.300	$7Q_x - 3Q_z = 122$	$0.40 \cdot 10^{-2}$	$-0.12 \cdot 10^{-2}$	$0.70 \cdot 10^{-3}$	$0.1 \cdot 10^{-16}$	$1.6 \cdot 10^{-9}$
3.080	0.000	$10Q_x + Q_z = 345$	$0.34 \cdot 10^{-2}$	$-0.18 \cdot 10^{-5}$	$-0.70 \cdot 10^{-5}$	$0.28 \cdot 10^{-13}$	$9.8 \cdot 10^{-8}$
7.150	0.000	$11Q_x = 344$	$0.29 \cdot 10^{-2}$	$-0.78 \cdot 10^{-4}$	$-0.23 \cdot 10^{-3}$	$0.11 \cdot 10^{-7}$	$6.2 \cdot 10^{-5}$
3.025	1.100	$10Q_x + Q_z = 345$	$0.34 \cdot 10^{-2}$	$-0.89 \cdot 10^{-4}$	$-0.21 \cdot 10^{-4}$	$0.60 \cdot 10^{-12}$	$4.5 \cdot 10^{-7}$
6.820	2.480	$11Q_x = 344$	$0.29 \cdot 10^{-2}$	$-0.14 \cdot 10^{-3}$	$-0.45 \cdot 10^{-3}$	$0.72 \cdot 10^{-8}$	$5.0 \cdot 10^{-5}$
10.835	3.940	$3Q_x + 4Q_z = 223$	$0.16 \cdot 10^{-2}$	$0.68 \cdot 10^{-3}$	$-0.14 \cdot 10^{-2}$	$0.39 \cdot 10^{-4}$	$5.7 \cdot 10^{-4}$

Table B.2: Characteristics of high-order resonances in model I of HERA as a function of starting amplitudes x and z, for the working point $Q_x = 31.27$, $Q_z = 32.295$.

x	z	Resonance	$\partial^2 g/\partial I_x^2$	$\partial^2 g/\partial I_x \partial I_z$	$\partial^2 g/\partial I_z^2$	h	Q_I
0.000	1.700	$9Q_x + 2Q_z = 346$	$0.41 \cdot 10^{-2}$	$-0.32 \cdot 10^{-2}$	$0.10 \cdot 10^{-3}$	$0.28 \cdot 10^{-28}$	$2.5 \cdot 10^{-15}$
0.000	2.680	$7Q_x - 3Q_z = 122$	$0.50 \cdot 10^{-2}$	$-0.33 \cdot 10^{-2}$	$0.29 \cdot 10^{-3}$	$0.13 \cdot 10^{-18}$	$2.2 \cdot 10^{-10}$
0.000	3.100	$8Q_x + 3Q_z = 347$	$0.56 \cdot 10^{-2}$	$-0.35 \cdot 10^{-2}$	$0.54 \cdot 10^{-3}$	$0.20 \cdot 10^{-23}$	$6.2 \cdot 10^{-13}$
0.000	3.900	$6Q_x - 2Q_z = 123$	$0.68 \cdot 10^{-2}$	$-0.43 \cdot 10^{-2}$	$0.17 \cdot 10^{-2}$	$0.25 \cdot 10^{-14}$	$3.0 \cdot 10^{-8}$
4.455	0.000	$10Q_x + Q_z = 345$	$0.32 \cdot 10^{-2}$	$-0.26 \cdot 10^{-2}$	$-0.11 \cdot 10^{-3}$	$0.19 \cdot 10^{-11}$	$7.1 \cdot 10^{-7}$
7.095	0.000	$Q_x + 6Q_z = 225$	$0.29 \cdot 10^{-2}$	$-0.18 \cdot 10^{-2}$	$-0.29 \cdot 10^{-3}$	$0.66 \cdot 10^{-13}$	$4.4 \cdot 10^{-8}$
7.205	0.000	$11Q_x = 344$	$0.29 \cdot 10^{-2}$	$-0.28 \cdot 10^{-2}$	$-0.30 \cdot 10^{-3}$	$0.11 \cdot 10^{-7}$	$6.2 \cdot 10^{-5}$
5.775	2.100	$Q_x + 6Q_z = 225$	$0.38 \cdot 10^{-2}$	$-0.22 \cdot 10^{-2}$	$-0.25 \cdot 10^{-3}$	$0.44 \cdot 10^{-6}$	$1.2 \cdot 10^{-4}$
6.490	2.360	$10Q_x + Q_z = 345$	$0.39 \cdot 10^{-2}$	$-0.19 \cdot 10^{-2}$	$-0.32 \cdot 10^{-3}$	$0.27 \cdot 10^{-8}$	$3.1 \cdot 10^{-5}$
8.085	2.940	$11Q_x = 344$	$0.37 \cdot 10^{-2}$	$-0.13 \cdot 10^{-2}$	$-0.51 \cdot 10^{-3}$	$0.43 \cdot 10^{-7}$	$1.4 \cdot 10^{-4}$
10.120	3.680	$7Q_z = 219$	$0.28 \cdot 10^{-2}$	$-0.47 \cdot 10^{-3}$	$-0.89 \cdot 10^{-3}$	$0.60 \cdot 10^{-5}$	$5.1 \cdot 10^{-4}$

Table B.3: Characteristics of high-order resonances in model I of HERA as a function of starting amplitudes x and z, for the working point $Q_x = 31.27$, $Q_z = 32.29$.

x	z	Resonance	$\partial^2 g/\partial I_x^2$	$\partial^2 g/\partial I_x \partial I_z$	$\partial^2 g/\partial I_z^2$	h	Q_I
0.000	2.448	$-3Q_x + 6Q_z = 100$	$0.5 \cdot 10^{-2}$	$-0.4 \cdot 10^{-2}$	$0.1 \cdot 10^{-2}$	$0.4 \cdot 10^{-10}$	$3 \cdot 10^{-6}$
0.000	2.592	$6Q_x - 2Q_z = 123$	$0.5 \cdot 10^{-2}$	$-0.4 \cdot 10^{-2}$	$0.15 \cdot 10^{-2}$	$0.27 \cdot 10^{-14}$	$2.7 \cdot 10^{-8}$
0.000	2.692	$9Q_x + 2Q_z = 346$	$0.5 \cdot 10^{-2}$	$-0.5 \cdot 10^{-2}$	$0.2 \cdot 10^{-2}$	$0.3 \cdot 10^{-23}$	$8 \cdot 10^{-13}$
0.000	3.636	$Q_x + 9Q_z = 322$	$0.8 \cdot 10^{-2}$	$-0.1 \cdot 10^{-1}$	$0.1 \cdot 10^{-1}$	$0.36 \cdot 10^{-7}$	$1.5 \cdot 10^{-4}$
0.000	3.660	$-2Q_x + 5Q_z = 99$	$0.8 \cdot 10^{-2}$	$-0.1 \cdot 10^{-1}$	$0.1 \cdot 10^{-1}$	$0.8 \cdot 10^{-7}$	$2 \cdot 10^{-4}$
0.000	3.672	$5Q_x - Q_z = 124$	$0.8 \cdot 10^{-2}$	$-0.1 \cdot 10^{-1}$	$0.1 \cdot 10^{-1}$	$0.3 \cdot 10^{-12}$	$3 \cdot 10^{-7}$
0.000	3.680	$8Q_x + 3Q_z = 347$	$0.8 \cdot 10^{-2}$	$-0.1 \cdot 10^{-1}$	$0.1 \cdot 10^{-1}$	$0.1 \cdot 10^{-19}$	$3 \cdot 10^{-11}$
0.000	3.996	$-6Q_x + 5Q_z = -26$	$0.9 \cdot 10^{-2}$	$-0.15 \cdot 10^{-1}$	$0.18 \cdot 10^{-1}$	$0.35 \cdot 10^{-15}$	$2.4 \cdot 10^{-8}$
4.059	0.000	$7Q_x - 3Q_z = 122$	$0.3 \cdot 10^{-2}$	$-0.27 \cdot 10^{-2}$	$-0.44 \cdot 10^{-4}$	$0.5 \cdot 10^{-12}$	$3.6 \cdot 10^{-7}$
5.841	0.000	$-4Q_x + 7Q_z = 101$	$0.34 \cdot 10^{-2}$	$-0.26 \cdot 10^{-2}$	$-0.7 \cdot 10^{-4}$	$0.2 \cdot 10^{-10}$	$2 \cdot 10^{-6}$
6.765	0.000	$11Q_x = 344$	$0.38 \cdot 10^{-2}$	$-0.27 \cdot 10^{-2}$	$0.45 \cdot 10^{-5}$	$0.15 \cdot 10^{-7}$	$9 \cdot 10^{-5}$
10.560	0.000	$4Q_x + 3Q_z = 222$	$0.13 \cdot 10^{-1}$	$-1 \cdot 10^{-2}$	$0.25 \cdot 10^{-2}$	$0.4 \cdot 10^{-8}$	$6 \cdot 10^{-6}$
5.489	1.996	$7Q_x - 3Q_z = 122$	$0.37 \cdot 10^{-2}$	$-0.25 \cdot 10^{-2}$	$-0.34 \cdot 10^{-3}$	$0.1 \cdot 10^{-6}$	$1.7 \cdot 10^{-4}$
6.215	2.260	$-4Q_x + 7Q_z = 101$	$0.35 \cdot 10^{-2}$	$-0.24 \cdot 10^{-2}$	$-0.6 \cdot 10^{-3}$	$0.16 \cdot 10^{-6}$	$1.6 \cdot 10^{-4}$
7.568	2.752	$3Q_x + 4Q_z = 223$	$0.29 \cdot 10^{-2}$	$-0.23 \cdot 10^{-2}$	$-0.17 \cdot 10^{-2}$	$0.56 \cdot 10^{-5}$	$5.6 \cdot 10^{-4}$
9.856	3.584	$2Q_x + 5Q_z = 224$	$-0.85 \cdot 10^{-3}$	$-0.35 \cdot 10^{-2}$	$-0.80 \cdot 10^{-2}$	$0.39 \cdot 10^{-4}$	$3.2 \cdot 10^{-3}$
10.540	3.832	$Q_x + 6Q_z = 225$	$-0.3 \cdot 10^{-2}$	$-0.5 \cdot 10^{-2}$	$-0.12 \cdot 10^{-1}$	$0.35 \cdot 10^{-4}$	$4 \cdot 10^{-3}$
10.920	3.972	$7Q_z = 226$	$-0.5 \cdot 10^{-2}$	$-0.6 \cdot 10^{-2}$	$-0.15 \cdot 10^{-1}$	$0.32 \cdot 10^{-5}$	$2 \cdot 10^{-3}$

Table B.4: Characteristics of high-order resonances in model II of HERA as a function of starting amplitudes x and z. In model II the 20-pole coefficients b_{10} in the quadrupole magnets are a factor of ten larger than the actual values (see chapter 5). The chosen working point is $Q_x = 31.27$, $Q_z = 32.30$.

Appendix C

Jacobi-Anger Expansion

The generating function of the Bessel coefficients is given by [81]

$$e^{\frac{1}{2}z(t-\frac{1}{t})} = \sum_{k=-\infty}^{\infty} t^k J_k(z).$$

An immediate consequence is the Jacobi-Anger expansion [1] [2]

$$e^{iz\sin\theta} = J_0(z) + 2\sum_{k=1}^{\infty} J_{2k}(z)\cos(2k\theta) + 2i\sum_{k=0}^{\infty} J_{2k+1}(z)\sin((2k+1)\theta),$$

which allows the following conversion

$$\begin{aligned}
\cos\left(n\phi + \frac{nq}{Q_m}\sin Q_m\theta - p\theta\right) &= \Re(e^{i(n\phi-p\theta)}e^{i\frac{nq}{Q_m}\sin Q_m\theta}) = \\
&= \sum_{k=-\infty}^{\infty} J_{2k}\left(\frac{nq}{Q_m}\right)\cos(n\phi - p\theta)\cos(2kQ_m\theta) - \\
&\quad - \sum_{k=-\infty}^{\infty} J_{2k+1}\left(\frac{nq}{Q_m}\right)\sin(n\phi - p\theta)\sin((2k+1)Q_m\theta)) = \\
&= \sum_{k=-\infty}^{\infty} J_{2k}\left(\frac{nq}{Q_m}\right)\frac{1}{2}\left[\cos(n\phi - p\theta - 2kQ_m\theta) + \cos(n\phi - p\theta + 2kQ_m\theta\right] - \\
&\quad - \sum_{k=-\infty}^{\infty} J_{2k+1}\left(\frac{nq}{Q_m}\right)\frac{1}{2}\left[\cos(n\phi - p\theta - (2k+1)Q_m\theta) - \cos(n\phi - p\theta + (2k+1)Q_m\theta\right] = \\
&= \sum_{k=-\infty}^{\infty} J_k\left(\frac{nq}{Q_m}\right)\cos(n\phi + kQ_m\theta - p\theta),
\end{aligned}$$

where in the last step use has been made of the relation $J_{-k}(x) = (-1)^k J_k(x)$. We have thus derived the formula applied in section 3.3.

[1] C. G. J. Jacobi, Journal für Math. xv. (1836), p. 12. [Ges. Math. Werke, vi (1891), p. 2].
[2] C. T. Anger, Neueste Schriften der Naturf. Ges. in Danzig, v. (1855), p. 2

Appendix D

Melnikov-Arnold Integral

Following [39] the Melnikov-Arnold integral $\mathcal{A}_m(\lambda)$ refers to the following expression

$$\mathcal{A}_m(\lambda) = \int_{-\infty}^{\infty} dt \cos\left(\frac{1}{2}m\phi_{sx} - \lambda t\right), \tag{D.1}$$

where

$$\phi_{sx}(t) = 4\arctan(e^t) - \pi \tag{D.2}$$

corresponds to the motion along the pendulum separatrix. The integral depends on the two parameters m and λ. If m is an integer, it is possible to specify a solution in terms of residues. Note that the integral can be rewritten as [39]

$$\mathcal{A}_m(\lambda) = \int_{-\infty}^{\infty} dt[e^{\frac{1}{2}m\phi_{sx}-\lambda t}] \tag{D.3}$$

$$= \int_{-\infty}^{+\infty} dt e^{-i\lambda t}\left(\frac{1+ie^t}{i+e^t}\right)^m. \tag{D.4}$$

The integrand has poles at

$$t_p = -\frac{1}{2}i\pi - 2\pi i n, \text{ for } n \in \mathcal{Z}. \tag{D.5}$$

Assuming that $\lambda > 0$, we can close the integral contour in the lower complex half plane, for instance along the lines $\Re(t) = \pm T$, $\Im(t) < 0$. The integral along these lines is, however, not zero, but oscillating as $\sin(\frac{1}{2}m\pi - \lambda T)$ for $T \to \infty$. The definition of the Melnikov-Arnold integral consists in neglecting these periodic oscillations and retaining the aperiodic part only [39, 46, 47, 48]. Introducing the new variable $z = t - t_p$, an evaluation of the residues yields

$$\mathcal{A}_m(\lambda) = -\frac{2\pi i}{i^m(m-1)!}e^{-\frac{\pi\lambda}{2}} \lim_{z\to 0} \frac{d^{m-1}}{dz^{m-1}}\left(e^{-i\lambda z}\left(\frac{1+e^z}{1-e^z}z\right)^m\right)\sum_{n=0}^{\infty} e^{-2\pi\lambda n}. \tag{D.6}$$

In particular, for $m = 2$ one finds

$$\mathcal{A}_2(\lambda) = 4\pi\lambda\frac{e^{\frac{\pi\lambda}{2}}}{\sinh(\pi\lambda)}. \tag{D.7}$$

Appendix E

Fokker-Planck Equation

The Fokker-Planck equation was introduced by A. D. Fokker [82] and M. Planck [83] early in this century. Here it is derived from some basic principles and assumptions in accordance with [85]. More rigorous discussions and additional informations can be found elsewhere [84, 85].

If the emittance growth is caused by a process which can be described by a random force, the distribution function f at a time $t+\tau$ is related to the distribution at time t by an equation of the form

$$f(\epsilon, t+\tau) = \int d\mu W_\tau(\epsilon-\mu,\mu) f(\epsilon-\mu, t). \tag{E.1}$$

Here $W_\tau(\epsilon,\mu)$ is the probability for a change in emittance ϵ by an amount μ after a time τ. Equation (E.1) is an identity, which can be formulated for all stochastic processes. For a very large class of processes another important property applies: the Markov assumption. In this case the distribution at a specific time t completely determines the future evolution, independent of the situation at former times.

To allow a description by a Fokker-Planck equation, the following additional mathematical conditions have to be satisfied. *For all* $\delta > 0$:

$$\lim_{\tau\to 0} \frac{1}{\tau} W_\tau(\epsilon,\mu) = 0\,, \text{ if } |\mu| > \delta, \tag{E.2}$$

$$\frac{<\Delta\epsilon>}{\Delta t} = \lim_{\tau\to 0} \frac{1}{\tau} \int_{|\mu|<\delta} d\mu\, \mu\, W_\tau(\epsilon,\mu) \;=\; A(\epsilon) + \mathcal{O}(\delta) \tag{E.3}$$

$$\frac{<(\Delta\epsilon)^2>}{\Delta t} = \lim_{\tau\to 0} \frac{1}{\tau} \int_{|\mu|<\delta} d\mu\, \mu^2\, W_\tau(\epsilon,\mu) \;=\; B(\epsilon) + \mathcal{O}(\delta). \tag{E.4}$$

The last two limites are understood as being uniform in ϵ, μ and τ. If these equations apply, all higher order expressions of the same form, like $<(\Delta\epsilon)^3>/\Delta t\ldots$, must vanish. The physical interpretation is as follows. Equation (E.2) excludes jumps in the emittance, i. e. sample trajectories show continuous emittance changes only. The quantity $A(\epsilon)$ defined in (E.3) describes a systematic drift, and $B(\epsilon)$ introduced in (E.4) a superimposed diffusion. Specifically, if $B(\epsilon)$ is zero, the motion is purely deterministic.

Differentiation of equation (E.1) with respect to time yields

$$\frac{\partial}{\partial t} f(\epsilon,t) = \lim_{\tau\to 0} \frac{1}{\tau} \left\{ \int d\mu\, W_\tau(\epsilon-\mu,\mu)\, f(\epsilon-\mu,t) - f(\epsilon,t) \right\}. \tag{E.5}$$

If the integrand is expanded with respect to μ where μ occurs in the combination $\epsilon - \mu$ and if implicit use is made of conditions (E.2) to (E.4), equation (E.5) simplifies to

$$\begin{aligned}
\frac{\partial}{\partial t} f(\epsilon,t) &= \lim_{\tau\to 0}\frac{1}{\tau}\left\{\int d\mu\left[-\frac{\partial}{\partial\epsilon}\left(W_\tau(\epsilon,\mu)\,f(\epsilon,t)\right)\mu + \frac{1}{2}\frac{\partial^2}{\partial\epsilon^2}\left(W_\tau(\epsilon,\mu)\,f(\epsilon,t)\right)\mu^2\right]\right\} \\
&= -\frac{\partial}{\partial\epsilon}\lim_{\tau\to 0}\frac{1}{\tau}\left\{\int d\mu\, W_\tau(\epsilon,\mu)\,f(\epsilon,t)\mu\right\} + \frac{1}{2}\frac{\partial^2}{\partial\epsilon^2}\lim_{\tau\to 0}\frac{1}{\tau}\left\{\int d\mu\, W_\tau(\epsilon,\mu)\,f(\epsilon,t)\mu^2\right\} \\
&= -\frac{\partial}{\partial\epsilon}\frac{<\Delta\epsilon>}{\Delta t}f(\epsilon,t) + \frac{1}{2}\frac{\partial^2}{\partial\epsilon^2}\frac{<(\Delta\epsilon)^2>}{\Delta t}f(\epsilon,t), \qquad \text{(E.6)}
\end{aligned}$$

which is the Fokker-Planck equation.

The importance of the Fokker-Planck equation lies in the following fact. If, for a specific process under consideration, the mean change and mean squared change of the emittance during a small time intervall can be calculated, the Fokker-Planck equation describes the long-time evolution of the distribution. In this spirit it has for instance been employed in [86] to derive the electron beam lifetime due to quantum fluctuations and damping. Similarly it has been used in chapter 8 to discuss the effect of multiple proton gas scattering.

Appendix F

Diffusion Equation

The Fokker-Planck equation, for later convenience expressed in terms of action instead of emittance, reads

$$\frac{\partial}{\partial t}f(I,t) = -\frac{\partial}{\partial I}\frac{<\Delta I>}{\Delta t}f(I,t) + \frac{1}{2}\frac{\partial^2}{\partial I^2}\frac{<(\Delta I)^2>}{\Delta t}f(I,t). \tag{F.1}$$

Under certain conditions the Fokker-Planck equation can be reduced to a diffusion equation [46]. To show the connection, a universal relation between the mean action change per unit time $<\Delta I>/\Delta t$ and the mean squared action change $<(\Delta I)^2>/\Delta t$ is derived in this chapter, valid for an arbitrary nearly-integrable Hamiltonian system.

In many cases it is justified to assume a randomization in phase (compare also the discussion of the Lyapunov exponent method in chapter 2). This assumption requires the absence of large island structures. The evolution in the action variable (or in the emittance) is comparatively slow and can be obtained by phase averaging of the equations of motion [46].

The change of action during the time Δt is expressed by a Taylor series of the form

$$\Delta I = \dot{I}\cdot\Delta t + \frac{1}{2}\ddot{I}\cdot(\Delta t)^2 + \ldots \tag{F.2}$$

From the equations of motion we have

$$\dot{I} = -\frac{\partial H}{\partial \phi} \tag{F.3}$$

$$\begin{aligned}\ddot{I} &= -\frac{\partial^2 H}{\partial \phi^2}\frac{\partial H}{\partial I} + \frac{\partial^2 H}{\partial \phi \partial I}\frac{\partial H}{\partial \phi} \\ &= -\frac{\partial}{\partial \phi}\left(\frac{\partial H}{\partial I}\frac{\partial H}{\partial \phi}\right) + \frac{\partial}{\partial I}\left(\frac{\partial H}{\partial \phi}\right)^2\end{aligned} \tag{F.4}$$

Inserting these expressions into the expansion (F.2) and performing an average over the angle ϕ, denoted by brackets $<\ldots>$, it is found

$$\frac{<\Delta I>}{\Delta t} = \frac{1}{2}\frac{\partial}{\partial I}\left\langle\left(\frac{\partial H}{\partial \phi}\right)^2\right\rangle\cdot\Delta t + \mathcal{O}((\Delta t)^2) \tag{F.5}$$

$$\frac{<(\Delta I)^2>}{\Delta t} = \left\langle\left(\frac{\partial H}{\partial \phi}\right)^2\right\rangle\cdot\Delta t + \mathcal{O}((\Delta t)^2). \tag{F.6}$$

Use has been made of the equality $< \partial f/\partial\phi >= 0$ for an arbitrary function f of $x = \sqrt{2I}\cos\phi$ and $p = -\sqrt{2I}\sin\phi$. Equations (F.5) and (F.6) provide an interesting relation between the two coefficients in the Fokker-Planck equation, which reads

$$\frac{< \Delta I >}{\Delta t} = \frac{1}{2}\frac{\partial}{\partial I}\frac{< (\Delta I)^2 >}{\Delta t}. \tag{F.7}$$

It allows to reduce the more general equation (F.1) to a diffusion equation of the form

$$\frac{\partial f}{\partial t} = \frac{\partial}{\partial I}\left(D(I)\frac{\partial f}{\partial I}\right) \tag{F.8}$$

with the *diffusion coefficient* $D(I)$ defined by

$$D(I) = \frac{1}{2}\frac{< (\Delta I)^2 >}{\Delta t}. \tag{F.9}$$

Equation (F.8) is the basis of the diffusion model proposed in chapter 3 and has been employed to describe the emittance growth due to persistent current field errors and due to the beam-beam interaction in chapter 5 and 6, respectively.

Bibliography

[1] H. Brück, R. Meinke, F. Müller, P. Schmüser, "Field distortions from Persistent Currents in the Superconducting HERA Magnets", *DESY* **89-041** (1989).

[2] C. Daum et al. , "The Superconducting Quadrupole and Sextupole Correction Coils for the HERA Proton Ring", *DESY HERA* **89-09** (1989).

[3] R. Brinkmann and F. Willeke, "Persistent Current Field Errors and Dynamic Aperture of the HERA Proton Ring", *DESY HERA* **88-08** (1988).

[4] F. Willeke and F. Zimmermann, "The Impact of Persistent Current Field Errors on the Stability of the Proton Beam in the HERA Proton Ring", *Proc. of the IEEE Particle Accelerator Conference, San Francisco*, 2483 (1991).

[5] S. Herb, O. Meincke, P. Schmüser, F. Willeke, F. Zimmermann, "Experience with Persistent Current Field Errors in the HERA Proton Ring", to be published in the *Proceedings of the 1992 High Energy Accelerator Conference, Hamburg* (1992).

[6] F. Zimmermann, R. Brinkmann, J. Feikes, S. Herb, A. Piwinski, J. Roßbach, F. Willeke, "First Experience with the Asymmetric Beam-Beam Interaction in the 1991 Luminosity Runs of HERA", *DESY HERA* **92-09**, published in the *Proceedings for B factories: the State of the Art in Accelerators, Detectors, and Physics, Stanford, California, SLAC-400*, 125 (1992).

[7] D.P. Barber, G. Ripken, F. Schmidt, "A non-linear canonical formalism for the coupled synchro-betatron motion of protons with arbitrary energy", *DESY* **87-036** (1987).

[8] V.I. Oseledec, "A multiplicative ergodic theorem. Ljapunov characteristic numbers for dynamical systems", *Trans. Moscow Math. Soc.* **19**, 197 (1968).

[9] P. Schmüser, "Basic Course on Accelerator Optics", CERN Accelerator School, Aarhus 1986, *CERN* **87-10** (1987).

[10] D. A. Edwards and M. J. Syphers, "An Introduction to the Physics of High Energy Accelerators", John Wiley (1993).

[11] S.K. Kaufmann, D.M. Ritson, and Y. Yan, "Implementation of one-turn maps in SSCTRK using Zlib", *SSCL Report SSCL*-**321** (1990);
Y. Yan and C. Yan, "Zlib—A Numerical Library for Differential Algebra," *SSCL Report SSCL*-**300** (1990);
Y. Yan, T. Sen, A. Chao, G. Bourianoff, A. Dragt, and É. Forest, "Comments on round-off errors and on one-turn Taylor maps", *SSCL Report SSCL*-**301** (1990).

[12] M. Berz, "Differential-algebraic description of beam dynamics to very high orders", *Part. Acc.* **24**, 109 (1989).

[13] R. Kleiss, F. Schmidt, Y. Yan and F. Zimmermann, "On the Feasibility of Tracking with Differential-Algebra Maps in Long-Term Stability Studies for Large Hadron Colliders", *DESY HERA* **92-01**, *CERN SL/***92-02** (AP), and *SSCL Report SSCL-***564** (1992).

[14] J. Irwin, "A Multi-kick Factorization Algorithm for Nonlinear Maps", *SSC Report SSC-***228** (1989).

[15] R. Kleiss, F. Schmidt, F. Zimmermann, "Experience with a simple Method to 'Symplectify' Differential Algebra Maps", *DESY HERA* **92-16**, *CERN SL/***92-31** (AP) (1992).

[16] R. Kleiss, F. Schmidt, F. Zimmermann, "The Use of Truncated Taylor Maps in Dynamic Aperture Studies", *DESY HERA* **92-21**, *CERN SL/***92-47** (AP), to be published in *Part. Acc.* (1992).

[17] M. Hénon and C. Heiles, "The Applicability of the Third Integral of Motion: Some Numerical Experiments", *Astron. J.* **69**, 73 (1964).

[18] F. Schmidt, F. Zimmermann and F. Willeke, "Comparison of Methods to Determine Long-Term Stability in Proton Storage Rings", *DESY HERA* **91-07**, *CERN SL/***91-14** (AP), published in *Part. Acc.* **35**, 249 (1991).

[19] F. Schmidt, "SIXTRACK, Version 1.1, Single Particle Tracking Code treating Transverse Motion with Synchrotron Oscillations in a Symplectic Manner", *CERN SL/***90-52** (AP) (1991).

[20] A. J. Dragt and J. M. Finn, "Lie Series and Invariant Functions for Analytic Symplectic Maps", *J. Math. Phys.* **17**, 2215-2227 (1976).

[21] É. Forest, "On the Implementation of the Irwin Factorization in the DALIE Package of Programs", private communication (1992).

[22] J. Irwin, private communication (1992).

[23] É. Forest, M. Berz and J. Irwin, "Normal form methods for complicated periodic systems: a complete solution using differential algebra and Lie operators", *Part. Acc.* **24**, 91 (1989).

[24] The LHC Study Group, "Design study of the large hadron collider (LHC): A multiparticle collider in the LEP tunnel", *CERN* **91-03** (1991).

[25] H. Brück, R. Meinke et al., private communication (1990).

[26] É. Forest, "A Hamiltonian-free description of single-particle dynamics for hopelessly comlex periodic systems", *LBL preprint LBL-***28471**, *J. Math. Phys.* **31**, 1133-1144 (1990).

[27] A. J. Dragt and J. M. Finn, "Normal Form for Mirror Machine Hamiltonians", *J. Math. Phys.* **20**, 2649-2660 (1979).

[28] K. La Mon, "Lie Series in an Extended Region of Phase Space", *J. Phys. A: Math. Gen.* **23**, 3875-3884 (1990).

[29] É. Forest, private communication (1992).

[30] É. Forest and J. Irwin, "Single Resonance Theory with Maps", *LBL preprint LBL-***28931**, *Proceedings of the Workshop on Non-linear Problems in Future Particle Accelerators, Capri*, Italy 1990 (1990).

[31] M. Hénon, "Numerical Study of Quadratic Area-Preserving Mappings", *Quart. Appl. Math.* **27** 291 (1969); "A Two Dimensional Map with a Strange Attractor", *Commun. Math. Phys.* **50**, 69 (1976).

[32] M. Bassetti and G. A. Erskine, "Closed Expression for the Electrical Field of a Two-dimensional Gaussian Charge", *CERN-ISR-TH/***80-06** (1980).

[33] R. Brinkmann, "A Simulation Study for the Beam-Beam Interaction of Protons with a Flat Electron Beam in HERA", *DESY HERA* **89-24** (1989).

[34] R. Bacher, K. H. Meß and M. Seidel, "Transmission Line Characteristics of the Superconducting HERA Dipole and Quadrupole String", to be published in the *Proceedings of the 1992 High Energy Accelerator Conference, Hamburg* (1992).

[35] J. Roßbach, "Fast Ground Motion at HERA", *DESY* **89–023** (1989);
K. Flöttmann, Diploma Thesis, University of Hamburg, in German, *DESY HERA* **90-09** (1990);
W. Decking, Diploma Thesis, University of Hamburg, in German, *DESY HERA* **90-13** (1990).

[36] T. Chen and S. Peggs, "Beam-Beam Tune Modulation, the Driven Gravity Pendulum, and Josephson Junctions", *Proceedings of the third ICFA beam dynamics workshop, Novosibirsk* (1989).

[37] S. Peggs, "Hadron Collider Behavior in the Nonlinear Numerical Model EVOL", *Part. Acc.* **17** (1985).

[38] G. N. Watson, "A Treatise on the Theory of Bessel Functions", Cambridge 1966, p. 199 (1966).

[39] B. V. Chirikov, "A Universal Instability of Many-Dimensional Oscillator Systems", *Physics Reports* **52**, No 5 (1979).

[40] L. R. Evans, J. Gareyte, "The Beam-Beam Effect in the SPS", *CERN SPS/***82-8** (DI-MST) (1982).

[41] L. R. Evans, "The Beam-Beam Interaction", CERN Accelerator School "Antiprotons in Colliding Beam Facilities", Geneva 1984, *CERN* **84-15** (1984).

[42] A. Schoch, "Theory of linear and nonlinear perturbations of betatron oscillations in alternating gradient synchrotrons", *CERN* **57-21** (PS Division) 55-56 (1958).

[43] J. D. Jackson, "Classical Electrodynamics", 2nd edition, John Wiley, p. 316 (1975).

[44] A. W. Chao and M. Month, "Particle Trapping during Passage through a High-Order Nonlinear Resonance", *Nucl. Instr. Meth.* **121**, 129-138 (1974).

[45] M. Cornacchia and Y. Chin, "A Study of the Dynamic Aperture Limit in Tristan", *Part. Acc.* **17**, 191-213 (1985).

[46] A. J. Lichtenberg, M. A. Lieberman, "Regular and Stochastic Motion", Springer Verlag (1983).

[47] V. I. Arnold, *Dokl. Akad. Nauk SSSR* **144**, 747 (1962); **148**, 1257 (1963).

[48] V. K. Melnikov, *Dokl. Akad. Nauk SSSR* **156**, 9 (1964).

[49] L. D. Landau, *Zh. Eksp. Teor. Fiz.* **7**, 203 (1937).

[50] T. Satogata and S. Peggs, private communication (1992).

[51] J.-P. Jensen, private communication (1993).

[52] H.-J. Eckoldt, private communication (1992).

[53] R. Bacher, private communication (1992).

[54] H.-J. Eckoldt, "Simulation of Transmissionline Effects within an Octant of the Superconducting HERA Proton Ring during an Energy Dump", to be published in the *Proceedings of the 1992 High Energy Accelerator Conference, Hamburg* (1992).

[55] The major part of this measurement was done by H.-J. Eckoldt.

[56] H. Kaden, "Wirbelströme und Schirmung in der Nachrichtentechnik", *Technische Physik in Einzeldarstellungen* **10**, Springer Verlag (1959).

[57] P. Schmüser, private communication (1991).

[58] D. Trines, private communication (1992).

[59] D. Brandt et al., "Influence of power supply ripple on the dynamic aperture of the SPS in the presence of strong nonlinear fields", *CERN SL/***90-67** (AP) (1990).

[60] F. Zimmermann, Diploma Thesis, University of Hamburg, in German, *DESY HERA* **91-03** (1991).

[61] K. Wittenburg, "Transversal Emittance Measurement", *Proc. of the Bad Lauterberg seminar on HERA commissioning, DESY HERA* **92-07** (1992).

[62] G. Ripken, F. Willeke, "Methods of Beam Optics", *DESY* **88-114** (1988).

[63] F. Zimmermann and F. Willeke, "Long Term Stability and Dynamic Aperture of the HERA Proton Ring", *DESY HERA* **91-08** (1991).

[64] M. Seidel, "The HERA-p Collimation System and First Experience with a Single Collimator", *Proc. of the Bad Lauterberg seminar on HERA commissioning, DESY HERA* **92-07** (1992).

[65] T. Chen et al. , "Measurements of a Hamiltonian System and Their Description by a Diffusive Model", *Phys. Rev. Lett.* **68**, 33 (1992).

[66] A. Gerasimov, "Diffusion Phenomenology of Transverse Beam Dynamics and Losses in Hadronic Colliders", unpublished note (1991).

[67] R. Brinkmann, "Note on Beam Optics and Interaction Parameters for the '92 HERA Run", internal note (1992).

[68] M. Abramowitz and I. Stegun, "Handbook of Mathematical Functions", National Bureau of Standards, p. 228 (1964).

[69] The Numerical Algorithms Group Limited, "The NAG Fortran Library Manual, Mark 14" (1990).

[70] A. Gerasimov, "The Applicability of Diffusion Phenomenology to Particle Losses in Hadron Colliders", *CERN SL/***92-30** (AP) (1992).

[71] A. Piwinski, "Intra-Beam Scattering", *Proc. of the 9th Int. Conf. on High Energy Accelerators, Stanford 1974*, Springfield 1975, 405-409 (1975).

[72] A. Piwinski, "Intra-Beam Scattering", CERN Accelerator School, Nordwijkerhout 1992, *CERN* **92-01** (1992).

[73] E. Lohrmann, private communication (1993).

[74] W. Hardt, "A few simple expressions for checking vacuum requirements in a proton synchrotron", *ISR-300/GS/***68-11** (1968).

[75] M. J. Syphers, "Beam-gas scattering lifetimes in the Fermilab Main Ring", *FN-***484** (1988).

[76] Particle Data Group, "Review of Particle Properties", *Phys. Review D* **45** (1992).

[77] D. Trines, "The HERA cold bore vacuumsystem", *DESY HERA* **85-22** (1985).

[78] D. Trines, private communication (1992).

[79] D. Trines, private discussion (1992).

[80] E. Karantzoulis and J. R. M. Maidment, "Estimates of Intra-beam Scattering in HERA", *DESY HERA* **85-12** (1985).

[81] Reference [38], p. 14.

[82] A. D. Fokker, *Ann. Phys.* (Leipzig) **43**, 310 (1915).

[83] M. Planck, *Sitzungsber. Preuss. Akad. Wiss. Phys. Math. Kl.* **325** (1917).

[84] N. G. van Kampen, "Stochastic Processes in Physics and Chemistry", North-Holland, Amsterdam, New York, Oxford (1981).

[85] C. W. Gardiner, "Handbook of Stochastic Methods", 2nd edition, Springer-Verlag, Berlin, Heidelberg, New York (1985).

[86] A. Piwinski, "Beam losses and lifetime", CERN Accelerator School, Gif-sur-Yvette 1985, *CERN* **85-19** (1985).

[87] M. Month, "Beam-Beam Resonances in Head-On Collisions of Electrons and Positrons", *BNL* **19583** (1975).